Geo-exploration of strategic mineral deposits along Varkala-Kovalam coast, South-West India using hyperspectral remote sensing

Thesis Submitted to AcSIR for the Award of the Degree of DOCTOR OF PHILOSOPHY in Physical Sciences

By

REJITH. R. G

Registration No: 10PP15A39016

Under the guidance of

Dr. M. SUNDARARAJAN

Materials Science and Technology Division

CSIR-National Institute for Interdisciplinary Science and Technology

(CSIR–NIIST)

Thiruvananthapuram-695 019, Kerala, India

June 2020

Dedicated to
my beloved family.....

16th June, 2020

DECLARATION

I hereby declare that the Ph.D. thesis entitled **"Geo-exploration of strategic mineral deposits along Varkala-Kovalam coast, South-West India using hyperspectral remote sensing"** is an independent work carried out by me under the supervision of **Dr. M. Sundararajan** at the Minerals section, Materials Science and Technology Division, CSIR–National Institute for Interdisciplinary Science and Technology (CSIR–NIIST), Thiruvananthapuram and it has not been submitted anywhere else for any other degree or diploma.

Rejith. R. G

National Institute for Interdisciplinary Science and Technology (NIIST)

Council of Scientific & Industrial Research (CSIR)
Industrial Estate P.O., Trivandrum - 695 019
Kerala, INDIA

Dr. M. Sundararajan
Principal Scientist, CSIR-NIIST
Associate Professor, AcSIR

Tel: (91)-471-2515250
E-mail:sundararajan@niist.res.in
rajanmsundar77@yahoo.com

16th June, 2020

CERTIFICATE

This is to certify that the work incorporated in this Ph.D. thesis entitled **"Geo-exploration of strategic mineral deposits along Varkala-Kovalam coast, South-West India using hyperspectral remote sensing"** submitted by **Mr. Rejith. R. G** to Academy of Scientific and Innovative Research (AcSIR) in fulfillment of the requirements for the award of the Degree of Doctor of Philosophy in Physical Sciences, embodies original research work under my supervision and guidance. I further certify that this work has not been submitted to any other University or Institution in part or full for the award of any degree or diploma. Research material obtained from other sources has been duly acknowledged in the thesis. Any text, illustration, table, etc. used in the thesis from other sources, have been duly cited and acknowledged. It is also certified that this work done by the student, under my supervision, is plagiarism free.

Rejith. R. G
(Student)

Dr. M Sundararajan
(Thesis Supervisor)

ACKNOWLEDGEMENTS

It is with great respect and immense pleasure that I express my profound thanks and deep sense of gratitude to my research supervisor Dr. M Sundararajan for his excellent guidance, constant encouragement, daily discussions, and also allowed me to work with full freedom, wholehearted help at any time and also for teaching me every small things regarding Geology and minerals, constructive comments and valuable suggestions throughout my research work.

I would like to acknowledge Dr. A. Ajayaghosh, Director, CSIR-NIIST and the former Directors Dr. Suresh Das and Dr. Gangan Prathap for providing the laboratory facilities to carry out the research work.

I owe a deep sense of gratitude to Dr. S. Savithri (present), Dr. K. Harikrishna Bhat, Dr. P. Prabhakar Rao, Dr M.L.P. Reddy (former) HODs of Material Science and Technology Division, CSIR-NIIST for all the facilities and constant advice to complete my research work.

I take this opportunity to express my honor to Dr. Suresh C H (present), Dr. Luxmi Varma, and Dr. Mangalam S.Nair (former), AcSIR Coordinators at CSIR-NIIST for their timely help and advice regarding all academic procedures of AcSIR.

I express my sincere thanks to my Doctoral Advisory Committee members Dr. L Gnanappazham (IIST, Trivandrum), Dr. Savithri S and Dr. Rajan T P D for their immense support towards completion of my research work.

I express my profound thanks and deep sense of gratitude to Dr. L Gnanappazham, Associate Professor, IIST, Trivandrum for her valuable guidance, and wholehearted help at any time for completing all Remote sensing analysis of my research work, also providing the facilities of Remote sensing Lab at IIST to carry out the research work successfully.

I thank Dr. Ramaswamy S, Mr. Velusamy and Mr. Sashibhooshanan for their laboratory assistance and their constant encouragement and guidance throughout my work.

I owe a debt of gratitude to Mr. Manohar Kumar and Mr. Nithin D. Pillai (IIST, Trivandrum) for collecting spectral signatures of minerals, Dr. Kaustabh Kumar Maiti and Dr. K B Jinesh (IIST, Trivandrum) for Raman spectroscopy, Dr. M Satyanarayanan (CSIR-NGRI,

Hyderabad) for high resolution inductively coupled plasma mass spectrometry (HR-ICP-MS) analysis, Indian Rare Earths Limited-Research Centre, Kollam, Kerala for mineral separation, Dr. Saju Pillai for XPS analysis, Dr. Subrata Das and Mr. Prithviraj for XRD analysis, Mr. Peer Mohamed A for UV-Vis-NIR studies, Mr. Harish Raj V for SEM-EDAX, Mr.Kiran Mohan for TEM analysis, Mr. Robert Philip and Ms. Anju for FTIR analysis, and Ms. Saharuba P M for flame photometry.

I express my sincere thanks to my labmates Mr. Arun Chand, Mr. Arun Kumar, Mr. Silambarasan S, Mr. Rahul V J, Ms. Haritha, Mr. Renjith R A, Mr. Prasanna M, Mr. Vinoth M K, Mr. Sravan Raj. K and Mr. Arun for their great companionship during my research life in CSIR-NIIST.

I would like to acknowledge my other friends, scientists, technical staff, security staff, housekeeping staff at CSIR-NIIST, for their moral support, motivation and to make my life at NIIST memorable.

I express my sincere thanks to staff of administration, stores, canteen and library of NIIST, Trivandrum.

I am grateful to Dept. of Science & Technology (DST) for INSPIRE fellowship.

I dedicate this work to my parents, brothers, family members and to my teachers for having always believed in me, and for their support and constant encouragement.

Above all, Thanks to Almighty God for my life.

Rejith. R. G

CONTENTS

List of Figures

Sl. No. **Page No.**

List of Tables

S. No. **Page No.**

List of Abbreviations

Al	:	Aluminium
$A1_2SiO_5$	:	Chemical composition of aluminosilicate minerals like sillimanite
Al_2O_3	:	Aluminium oxide
A_g/A_u	:	Mulliken Symbols
ANN	:	Artificial neural network
APMDC	:	Andhra Pradesh Mineral Development Corporation Limited
ASTER	:	Advanced Spaceborne Thermal Emission and Reflection Radiometer
ASCII	:	American Standard Code for Information Interchange
a.u.	:	Arbitrary units
AVIRIS-NG	:	Airborne Visible InfraRed Imaging Spectrometer - Next Generation
B	:	Backward looking
B_{10}	:	Band 10
Ba	:	Barium
BE	:	Binary encoding
Be	:	Beryllium
B_g/B_u	:	Mulliken Symbols
BR	:	Band ratio
C	:	Carbon
Ca	:	Calcium
CaO	:	Calcium oxide
CaCO3	:	Calcium Carbonate
cc	:	Cubic Centimeter
CdO	:	Cadmium oxide
Ce	:	Cerium
Ce_2O_3	:	Cerium oxide
CI	:	Carbonate Index
cm	:	Centimetre
Co	:	Cobalt
Cr	:	Chromium
Cs	:	Caesium
CS	:	Coarse skewed

Cu	:	Copper
D_2O	:	Heavy water
Dy	:	Dysprosium
E	:	East
ED-XRF	:	Energy dispersive X-ray fluorescence
E_g/E_u	:	Mulliken Symbols
EnMAP	:	Environmental Mapping and Analysis Program
ENVI	:	Environment for Visualizing Images
EO	:	Earth-Observing
Er	:	Erbium
Eu	:	Europium
ETM	:	Enhanced Thematic Mapper
F	:	Fluorine
FCC	:	False colour composite
Fe	:	Iron
Fe_2O_3	:	Ferric oxide
$FeTiO_3$	:	Chemical composition of ilmenite
FS	:	Finely Skewed
FLAASH	:	Fast line-of-sight Atmospheric Analysis of Spectral Hypercubes
FOV	:	Field of view
g	:	Gram
Ga	:	Gallium
Gar	:	Garnet
Gd	:	Gadolinium
Ge	:	Germanium
GIS	:	Geographical Information System
Govt.	:	Government
GPR	:	Ground penetration Radar
GPS	:	Global Positioning System
GSI	:	Grain size index
Hf	:	Hafnium
HSI	:	Hue-saturation-intensity
HMC	:	Heavy mineral concentrate
Ho	:	Holmium

HR-ICP-MS	:	High resolution inductively coupled mass spectrometer
ICA	:	Independent component analysis
ICP-MS	;	Inductively coupled plasma mass spectrometry
IDW	:	Inverse Distance Weighted
IDL	:	Interactive Data Language
Ilm	:	Ilmenite
IR	:	Infrared
IREL	:	Indian Rare Earths Limited
KG	:	Graphic kurtosis
km	:	Kilometer
KV	:	Kappil-Varkala
La	:	Lanthanum
LA-ICP-MS	:	Laser Ablation Inductively Coupled Plasma Mass Spectrometry
Leu	:	Leucoxene
Li	:	Lithium
LK	:	Leptokurtic
LM	:	Light minerals
LSU	:	Linear spectral unmixing
LPI	:	local polynomial interpolation
Lu	:	Lutetium
M	:	Image spectrum
m	:	Meter
m^3	:	Cubic metre
MAGI	:	Mineral and Gas Identifier
MAE	:	Mean absolute error
MF	:	Matched filter
Mg	:	Magnesium
MgO	:	Magnesium oxide
MK	:	Mesokurtic
MLA	:	Machine learning algorithms
MLC	:	Maximum likelihood classification
mm	:	Millimeter
MNF	:	Minimum Noise Fraction
MnO	:	Manganese(II) oxide

Mon	:	Monazite
MS	:	Moderately sorted
MTMF	:	Mixture tuned match filtering
Mt	:	Metric ton
Mtry	*:*	*N*umber of predictive variables in RF
MWS	:	Moderately well sorted,
Mz	:	Graphic mean
N	:	North
N	:	Nadir looking
NASA	:	National Aeronautics and Space Administration
Nb	:	Niobium
Nd	:	Neodymium
n-D	:	n-Dimensional
NDSI	:	Normalized Difference Snow Index
Ni	:	Nickel
nm	:	nanometer
NN	:	Neural network
NS	:	Nearly symmetrical
Ntree	*:*	*N*umber of regression trees
O	:	Oxygen element
O_2	:	Oxygen
OH	:	Hydroxide
OHI_b	:	OH index
OIF	:	Optimum Index Factor
OK	:	Ordinary kriging
OLI	:	Operational Land Imager
OM	;	Other minerals
OOB	:	Out of bag data
P	:	Phosphorus
Pb	:	Lead
PCA	:	Principal components analysis
PC	;	Principle components
PI	:	Pyrophyllite index
PK	:	Platykurtic

PLS-SVM	:	Partial least squares support vector machine
PPI	:	Pixel purity index
ppm	:	Parts per million
Pr	:	Praseodymium
PS	:	Poorly sorted
P_2O_5	:	Phosphorus Pentoxide
QGIS	:	Quantum GIS
QI	:	Quartz Index
R	:	Reference spectrum
R^2	:	Coefficient of Determination
REE	:	Rare Earth elements
REO	:	Rare Earth Oxide
RFC	:	Random forest classifier
Rb	:	Rubidium
RBF	:	radial basis function
RBD	:	Relative absorption-Band Depth
R_b	:	Reflectance values at band bottom
Rc	:	Reflectance values at continuum of the same band
RGB	:	Red Green Blue
Rs	:	Rupees
RS	:	Remote sensing
RMSE	:	Root Mean Square Error
RMS	:	Root Mean Square
ROI	:	Region of interest
Rut	:	Rutile
SAM	:	Spectral Angle Mapper
Sc	:	Scandium
SD	:	inclusive graphic standard deviation
SEM-EDS	:	Scanning electron microscopy Energy Dispersive X-Ray Spectroscopy
SFF	:	Spectral feature fitting
Si	:	Silica
SiO_2	:	Silicon dioxide (silica)
Sill	:	Sillimanite
Sk1	:	Inclusive graphic skewness

SK	:	Shanghumugham-Kovalam
Sm	:	Samarium
Sr	:	Strontium
SVM	:	Support vector machine
SWIR	:	Shortwave infrared region
Ta	:	Tantalum
Tb	:	Terbium
TGA	:	Thermogravimetric analysis
THM	:	Total Heavy Minerals
Th	:	Thorium
ThO_2	:	Thorium dioxide
Ti	:	Titanium
TiO_2	:	Titanium dioxide
TIR	:	Thermal infrared
TIRS	:	Thermal Infrared Sensor
TM	:	Thematic Mapper
Tm	:	Thulium
U	:	Uranium
USGS	:	United States Geological Survey
UV	:	ultraviolet
VCS	:	Very Coarse skewed
V	:	Vanadium
Vis	:	Visible
VFS	:	Very Finely Skewed
VLK	:	Very Leptokurtic
VNIR	:	Visible near-infrared region
VPK	:	Very Platykurtic
WS	:	Well sorted
wt.	:	Weight
XPS	:	X-ray photoelectron spectroscopy
Y	:	Yttrium
Yb	:	Ytterbium
Zn	:	Zinc
Zir	:	Zircon

Zr	:	Zirconium
ZrO_2	:	Zirconium dioxide
^oC	:	Degree Celsius
~	:	Approximate
Γ	:	upper case Greek letter "gamma" indicating modes of vibrations
%	:	Percentage
Φ	:	phi
θ	:	Theta
μm	:	Micrometer
2-D	:	2-dimenisonal

Preface

Identification, exploration and value addition of the strategic minerals plays an important role in the socio-economic development of the nation in supporting nation's low-carbon plans (electric and hybrid vehicles) and will give a boost to our strategic sector such as aerospace, defence, and nuclear energy. Exploring minerals is always a challenge for the miners because there is a possibility for missing rare and scarcely existing minerals and metals, and the process of finding them is an expensive risk. Here makes the remote sensing techniques and satellite data in mineral exploration so important. It provides solid information on exact targeting of mineral occurrences and thereby it reduces field exploration and drilling costs. Remote sensing archives of satellite data which covers large areas on the ground are readily available. The remote sensing techniques have become a guiding and promising tool for mineral exploration and mapping of lithological units. The heavy mineral deposits found in coastal zones are of high quality and high volume. These strategic minerals act as the primary source for the production of titanium products, rare earth elements, etc. The main objective of the present study is to investigate the texture and mineralogy of beach sediments in the coast of Thiruvananthapuram district, Kerala, India using hyperspectral remote sensing techniques. An attempt has been also made to map other strategic minerals like the silica, baryte and Kaolin clay deposits using hyperspectral remote sensing techniques.

The **chapter 1** gives an introduction to remote sensing and its applications in mineral exploration. A literature review on various remote sensing techniques used for mineral exploration is discussed here in detail.

In **chapter 2**, detailed investigation on texture and mineralogy of beach sediments along the coast of Thiruvananthapuram, the southernmost district of Kerala, India have been carried out. The variation in grain size was studied using the spectral indices derived from the visible-NIR-TIR bands of Landsat and ASTER remote sensing data. Further, an attempt has been made to map the distribution of strategic minerals present in beach sands using standardized hyperspectral analysis techniques. Individual heavy minerals of good quality were recovered from beach sands using a judicious combination of magnetic, electrostatic and gravity separation units. The spectral signatures of 10 strategic minerals including beach minerals, silica sand, kaolin clay deposits were measured using ASD Fieldspec® 3 spectroradiometer and used as the reference spectra for mapping these minerals. Grain Size Index maps showing the texture of beach sediments were successfully generated from the satellite imageries. The hyperspectral analysis extracts two endmembers of ilmenite and light

minerals from the Landsat and ASTER imagery, which could be successfully, mapped using the SAM classification algorithm. The same procedure was used for mapping silica deposits from Landsat and ASTER data. The Fullerene bearing Barytes (Mangampet, Andhra Pradesh) and Kaolin deposits (Thonnakkal, Kerala) were successfully derived from Landsat data using hyperspectral analysis followed from MTMF classification method. The satellite-derived maps have been validated with the results of laboratory analysis and field data which shows strong correlation almost in all locations.

In **chapter 3**, the most widely used four machine learning algorithms such as Random Forest classifier (RFC), Artificial neural network (ANN), support vector machine (SVM) and maximum likelihood classifier (MLC) were compared for their efficiency in mapping beach minerals and silica sand deposits using landsat 8 OLI imagery. The image pixels correspond to sampling locations were selected as the training sites. The random forest classifier (RFC) and Support vector machine (SVM) shows the highest Kappa coefficient and overall accuracy for mapping beach sediments and silica sand deposits.

In **chapter 4**, EO-1 Hyperion data was used for mapping the strategic minerals of Cuddalore coast, Tamil Nadu using the hyperspectral analysis techniques followed by SAM classification. The endmembers of garnet, zircon, sillimanite and light minerals (quartz) were derived from the satellite data and compared with spectral library of minerals. The band depth analysis of continuum removed laboratory spectra and image spectra helps to derive a strong correlation between band parameters and the corresponding mineral concentration. This relation was used to quantify minerals with the help of Random Forest Regression technique. Thus the concentration of zircon mineral along the coast of Cuddalore, Tamil Nadu was quantified from Hyperion data.

In **chapter 5**, detailed characterisation on structure, chemistry and surface morphology of beach minerals recovered from the beach sands of the present study area was carried out using advanced characterisation techniques. The crystal structure of the minerals was analysed using Raman spectroscopy and X-ray diffraction. The X-Ray Fluorescence Spectroscopy (XRF), high resolution inductively coupled mass spectrometer (HR-ICP-MS) and X-ray photoelectron spectroscopy (XPS) was used to analyze chemical composition and rare earth chemistry. Thermal properties of the samples were determined using TG-DTA analysis. The surface morphology of mineral grains was also analysed using scanning electron microscope (SEM). Detailed characterisation helps to analyse and compare the grade of the beach minerals with other important placer deposits of India. The characterisation results show good agreement with the reported values for other major placer deposits in India.

Summary of the thesis work with valid conclusions obtained from the present work are given in the **Chapter 6** which also includes the future perspectives.

Chapter 1

Introduction and Literature Review

1.1.Introduction to GIS and Remote sensing

GIS stands for 'Geographic Information System'. It is defined as a computer system designed for collecting, managing, analyzing, and displaying geographically related data or spatial data. Any data that consists of a geographic component (latitude/longitude) which identifies the geographic location of features on the Earth's surface is termed as spatial data or geographically related data. GIS provides a framework for performing few tasks such as collection of spatial data using GPS, satellite, etc., storing the data in a suitable database, analyzing, manipulating, and mainly querying of these data with the help of softwares and finally displaying the data in online platforms as digital maps. There are many sources for spatial data such as remote sensing (RS), photogrammetry, field survey, paper maps and files, etc. Remote sensing is one the most important source of spatial data where the information about the Earth's surface is acquired without being in contact with it. This is achieved with the help of sensors attached to the satellites which move around the Earth in the outer space. Remote sensing is defined as science to some extent, an art of collecting information about Earth's surface.[1]

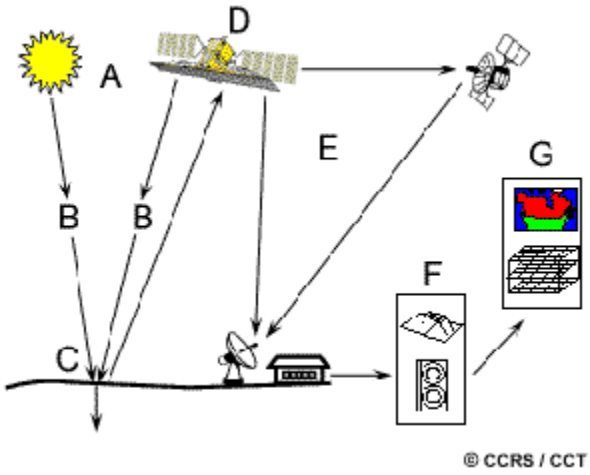

Figure 1.1: Components of remote sensing

The important components of remote sensing are (i) Source of energy source or illumination. Usually sun act as the primary source of energy. It provides electromagnetic energy to the target of interest (A). (ii) While traveling from source to target, the energy gets interacted with the atmosphere where it passes through (B), (iii) Once the energy

reaches the target, an interaction occurs between radiated energy and target. The interaction can be reflection, absorption or transmission (C), (iv) The reflected or emitted light is recorded by the sensor attached remotely, usually in a satellite system in space (D), (v) The recorded energy will be transmitted to processing stations where it is received and processed into an image which is called "satellite imagery" (E), (vi) The satellite data is interpreted using image processing software for extracting solid information regarding the target material (F), (vii) The extracted information regarding the target material is used for an application where it solves a particular problem (G). The seven elements of remote sensing process are shown in Figure 1.1.

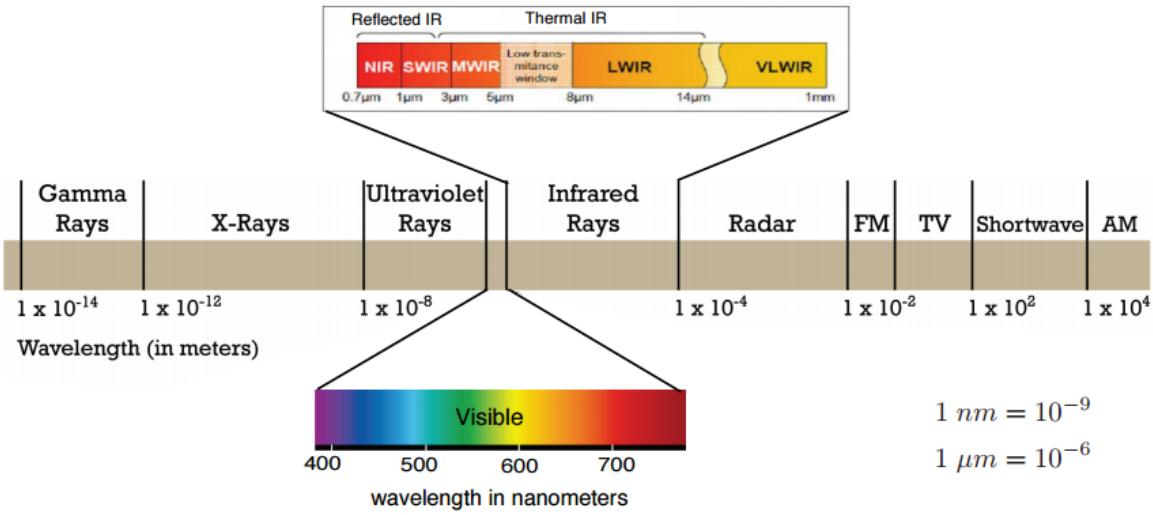

Figure 1.2: Electromagnetic spectrum

The most significant requirement for a remote sensing process is the energy source or source of illumination. The energy is electromagnetic radiation. Based on the wavelength range of electromagnet radiation, the remote sensing can be classified as (i) Optic Remote Sensing, (ii) Thermal Remote Sensing, and (iii) Microwave Remote Sensing. The optic remote sensing uses ultraviolet (UV), visible, and infrared (IR) region. Thermal Remote Sensing uses thermal infrared (TIR) region and Microwave Remote Sensing uses energy in the microwave region. The electromagnetic spectrum is shown in Figure 1.2.

1.2.Remote sensing data

Remote sensing data products ranging from multispectral to hyperspectral and high resolution to low resolution are widely used for mapping mineral deposits and lithological units. The Landsat 8, ASTER and EO-1 Hyperion data were used for the present study.

1.2.1. Landsat imagery

Over the past few decades, the multispectral remote sensing datasets of the Landsat series such as Thematic Mapper (TM), the Enhanced Thematic Mapper (ETM+) and Landsat 8 OLI. A Comparison of the Landsat products are shown in Table 1.1.

Table 1.1: Sensor characteristics for Landsat satellites.[2]

Satellite	**Sensor**	**Band number**	**Band Name**	**Wavelength (µm)**	**Spatial Resolution (m)**	**Radiometric Resolution (bit)**	**Spectral Resolution**
Landsat 8	OLI	1	Coastal aerosol	0.43-0.45	30	12	11
		2	Blue	0.45-0.51			
		3	Green	0.53-0.59			
		4	Red	0.64-0.67			
		5	NIR	0.85-0.88			
		6	SWIR-1	1.57-1.65			
		7	SWIR-2	2.11-2.29			
		8	Panchromatic	0.50-0.68	15		
		9	Cirrus	1.36-1.38	30		
	TIRS	10	TIR-1	10.60-11.19	100		
		11	TIR-2	11.50-12.51			
Landsat 7	ETM+	1	Blue	0.45-0.52	30	9 (8 transmitted)	8
		2	Green	0.52-0.60			
		3	Red	0.63-0.69			
		4	NIR	0.77-0.90			
		5	SWIR1	1.55-1.75			
		6	TIR	10.40-12.50	60		
		7	SWIR2	2.09-2.35	30		
		8	Pan	0.52-0.90	15		
Landsat 5	TM	1	Blue	0.45 - 0.52	30	8	7
		2	Green	0.52 - 0.60			
		3	Red	0.63 - 0.69			
		4	NIR	0.76 - 0.90			
		5	SWIR1	1.55 - 1.75			
		6	TIR	10.4 - 12.5	60		
		7	SWIR2	2.08 - 2.35	30		

(VNIR: Visible near-infrared; SWIR: shortwave infrared; TIR: Thermal Infrared; N: Nadir looking; B: Backward looking, The Swath width for Landsat satellites is 185km)

All these three Landsat products are successfully used for mapping variety of rocks and mineral deposits of particularly alteration minerals like iron oxides and clays associated with hydrothermal altered rocks. The Landsat 7 satellite with Enhanced Thematic Mapper plus (ETM+) sensor consists of seven spectral bands in which the VNIR bands 1-4 and SWIR bands of 5 and 7 and a panchromatic band 8. The Landsat 8 consists of two sensors of Operational Land Imager (OLI) and the Thermal Infrared Sensor (TIRS). It provides images with eleven spectral bands out of which the Visible-NIR-SWIR bands of 1-7 and panchromatic band 8 have the same spatial resolution of 30m as that of ETM+. The band 9 which is used for cirrus cloud detection has a spatial resolution of 30 meters. The thermal Bands 10 and 11 have the resolution of 100 meters. The OLI bands are designed to have optimum spectral range without any influence of atmospheric absorption features observed in ETM+ bands.[3] The water vapour absorption features at 0.825μm exist in the band 4 (0.780-0.900 μm) of ETM+ is removed in OLI by introducing two bands of band 4 and band 5.[4]

1.2.2. ASTER imagery

Another major remote sensing dataset which is also commonly used for mineral mapping especially for alteration minerals is Advanced Spaceborne Thermal Emission and Reflection Radiometer (ASTER) imagery. ASTER was launched using the NASA's TERRA spacecraft.[5] It is an advanced multispectral data consists of 14 bands with three VNIR bands ranging from 0.52 μm – 0.86 μm, six SWIR bands ranging from 1.6 to 2.43 μm and also five TIR bands ranging from 8.125 to 11.65 μm.[6] The SWIR bands have 30meters resolution same as that of Landsat but the VNIR and TIR have the spatial resolution of 15 meters and 90 meters. The alteration minerals show characteristics spectral features in SWIR regions of electromagnetic spectrum. The alteration minerals show relatively high reflectance in SWIR band 5 (1.55-1.75 μm) of Landsat ETM+ and band 4 of ASTER. At the same time they show relatively high absorption in other SWIR bands of Landsat ETM+ and ASTER. The epidote, chlorite, and calcite show high absorption for ASTER band 8, where as the minerals montmorillonite, kaolinite, and muscovite show high absorption for ASTER band 6. The thermal emissivity shown by different rock units corresponds to its silica content. The mafic-ultramafic rock units having low SiO_2 content show high emissivity in shorter wavelengths of ASTER correspond to band 12, 11 or 10 whereas the felsic rock units having high SiO_2 content shows high emissivity in larger wavelengths correspond to ASTER band 13 and 14. So as the rock type changes from felsic to intermediate and finally to ultramafic, the

emissivity increases for ASTER low wavelengths and decreases for ASTER high wavelengths.

1.2.3. EO-1 Hyperion

However, the spatial resolutions of 15 meters and 30 meters are too coarse to recognize small lithological units and mineral resources having very less size. The advent of Hyperion sensor made the beginning of hyperspectral geological remote sensing. Hyperion launched in November 2000 as part of NASA's EO-1 Millennium Mission, is the first spaceborne hyperspectral sensor having the capabilities of acquiring spectral bands in the range of VNIR and SWIR.[7] It covers VNIR and SWIR regions of wavelength 0.36 to 2.58 μm with 242 spectral bands at a spectral resolution of 10nm and spatial resolution of 30m. Comparison of Landsat ETM+, ASTER and Hyperion spectral bands is shown in Figure. 1.3. Sensor features of Hyperion and ASTER are given in Table 1.2.

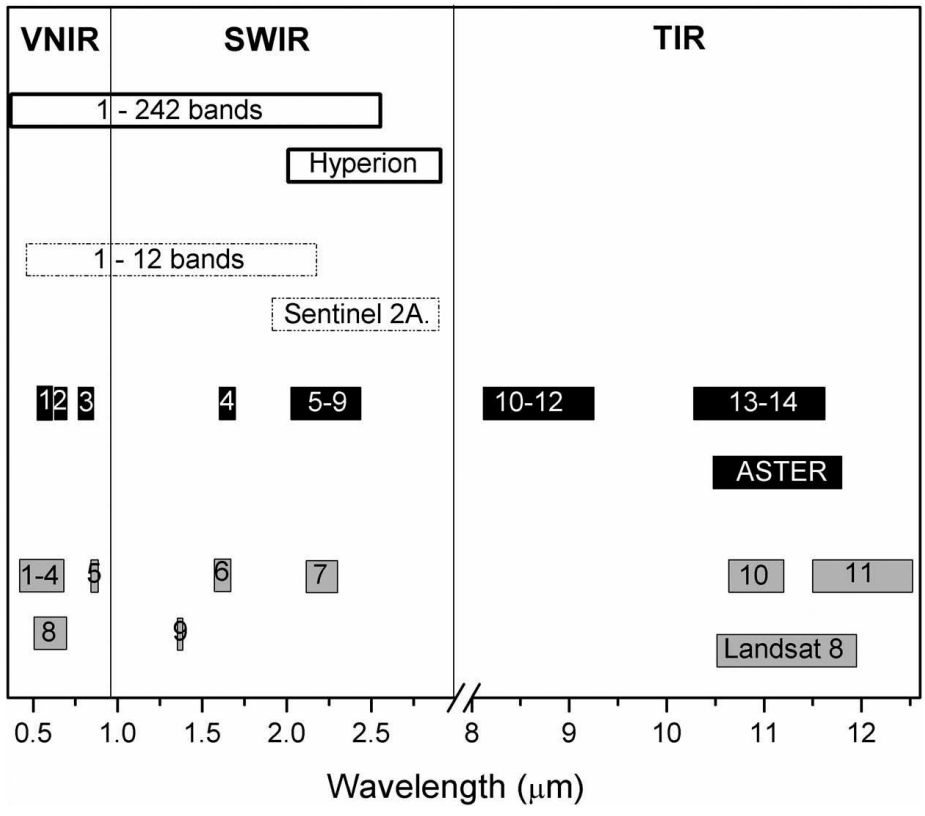

Figure 1.3: Comparison of Landsat 8, ASTER, Sentinel 2A and Hyperion spectral bands.[8,9]

Table 1.2: Sensor details of Hyperion and ASTER.[2,5,10]

Satellite	**Sensor**	**Sub system**	**Band Number**	**Wave length (µm)**	**Spatial Resolution (m)**	**Radio metric Resolution (bit)**	**Spectral Resolution**
EO-1	Hyperion	VNIR	1 – 70	0.36 – 1.06	30	12	242 bands
		SWIR	70– 242	0.85 – 2.58			
Terra	ASTER	VNIR	1	0.52-0.60	15	8	14 bands
			2	0.63-0.69			
			3N	0.76-0.86			
			3B	0.76-0.86			
		SWIR	4	1.600-1.700	30		
			5	2.145-2.185			
			6	2.185-2.225			
			7	2.235-2.285			
			8	2.295-2.365			
			9	2.360-2.430			
		TIR	10	8.125–8.475	90	12	
			11	8.475–8.825			
			12	8.925–9.275			
			13	10.25–10.95			
			14	10.95–11.65			

(The swath width for EO-1 Hyperion data is 7.5km and that of ASTER is 60km; VNIR: visible near-infrared region; SWIR: shortwave infrared region; TIR: Thermal infrared, N: Nadir looking; B: Backward looking)

1.3.Remote sensing for mineral exploration

Remote sensing applications in mineral exploration mainly deal with mapping of lithological units and mineral resources. The structural units like faults and fractures help to easily identify ore deposits. In contrast with field surveys, remote sensing is a cost-effective, less time consuming and efficient method for collecting information from poorly accessible

remote areas like mountainous terrains.[11] All the mineral deposits show characteristic spectral signatures on multispectral and hyperspectral remote sensing systems based on their mineralogy and texture. Even though the hyperspectral images are used in advanced spectral analysis, the freely available multispectral datasets like Landsat imageries are also successfully used for mapping hydrothermally altered mineral deposits like iron oxide and clay minerals which have strong absorption in near and shortwave infrared (NIR and SWIR). The diagnostic spectral characteristics shown by Fe-bearing and hydroxyl-bearing minerals allows mapping of alteration zones. Therefore by accessing the remote sensing techniques like mixture-tuned matched filtering (MTMF), relative band depth (RBD), and band ratio (BR), the six SWIR bands of ASTER data effectively maps Al-OH, Fe-OH and Mg-OH abundances and five VNIR bands of Landsat 8 effectively maps ferric iron alteration minerals.[12–16] The narrower optical bandwidths and high radiometric resolution (16-bit) for Landsat 8 compared to that of Landsat-7 facilitates effective mapping of clay and iron oxide minerals with improved quality. Principle component analysis, band rationing, spectral indices and colour composites have been widely used for mapping mineral abundances from multispectral datasets of Landsat and ASTER.[17] Later it was found out that the combination of remote sensing datasets like ASTER and Landsat8-OLI data together called AO data provides more information regarding the existence of alteration zones and the iron-bearing minerals on applying the same remote sensing techniques such as BR, RBD, and MTMF separately.[3,16]

Recent advances in sensor technology made a breakthrough in the production of satellite imageries with improved spectral, spatial and radiometric resolutions. Hyperspectral imageries like EO-1 Hyperion which have 242 bands would make more easier and efficient for identifying Fe oxide minerals, clay minerals, sulphates and carbonates associated with hydrothermal alteration assemblages using advanced spectral classification techniques.[18,19] The remote sensing techniques are widely used for mapping chromite occurrences[20] carbonatite using HYMap data[21]. Recently an airborne TIR spectrometer called MAGI (Mineral and Gas Identifier) have been introduced for improved discrimination of rocks and mineral types, and more accurately retrieves land-surface temperature.[22] MAGI use 32 contiguous channels to span the TIR spectral region of 7.1 to 12.7μm.

A series of analytical techniques broadly classified into two categories of spectrum matching techniques and subpixel methods were implemented for mapping mineral resources

and lithological units from satellite data.[23,24] The spectrum matching techniques like SAM, SFF, SVM, etc. are used for comparing and validating the reflectance spectra of target materials measured using spectroradiometer and the image spectrum. The maximum likelihood classification (MLC) technique shows better performance than spectral angle mapper (SAM), parallelepiped, Mahalanobis distance, and minimum distance to mean for mapping lithology using ASTER data (Fatima et al. 2013).

The subpixel method finds the spectrally pure pixels with unique signatures of endmembers and then unmixed the mixed pixel spectra as combinations of these endmember spectra. Transformation of multivariate datasets removes the redundancy of spectral information and thereby reduces the computational requirements for further processing. Thus the most commonly used linear transformation techniques like PCA, ICA, MNF, etc. provides a new set of uncorrelated image bands retaining most of the variance. Apart from all these techniques, the band ratios and spectral indices are simple and most widely accepted techniques not used only in the field of mineral exploration but also in other areas of applications. They enhance the spectral differences between the two bands by dividing one spectral band with another. The color composite of band ratios are also used for enhancing the mineral occurrences. Meanwhile researchers also made comparison of different data sets as well as the performance of different techniques for the successful discrimination of mineral resources. Adiri et al. found out that band ratios and PCA outperforms SVM for discriminating lithological units like sandstone, alluvium, etc. The same SVM technique outperformed the SAM technique in mapping the major lithological units of polymictic conglomerate, metabasalt, amphibolite, etc. using Hyperion data.[25]

The software packages PCI Geomatica, ENVI, ERDAS and ArcGIS with more versions and capabilities are used in digital processing, spectral enhancement, and spectral classification. Ground verifications shows good agreement with the obtained results and therefore the accuracy of these latest mapping techniques were also very high. In situ geochemical analyses were also performed using portable X-ray fluorescence (XRF) devices for confirming the minerals.[26] The potential of Remote Sensing (RS) techniques in various geological applications ranging from lithological mapping to exploration of minerals are discussed in detail here. It updates understanding on the subject starting from introducing details on different satellite data products like Landsat, hyperspectral data, ASTER data, etc.

to its application in exploring mineral deposits through different remote sensing techniques. Few case studies were also added under each method.

The selection of remote sensing data products and techniques completely depends on minerals of interest and nature of study area. The major purpose of remote sensing techniques is to narrow the search area and subsequently reduces the cost of exploration and time for the field work.[26] Most widely used remote sensing techniques were discussed with few case studies.

1.3.1. Colour Composites and Band Rationing

Band ratio is used for enhancing the slight variations in the spectral response of lithology and rock units by reducing the effect of topography.[27] It is a simple mathematical operation between two bands given by equation (1.1):

$$\text{Band Ratio} = \frac{B_R}{B_A} \qquad (1.1)$$

Where, B_R corresponds to band consists of high reflectance feature and B_A corresponds to band consists of high absorption feature

Colour composite is an image enhancement method where the bands of satellite images are displayed using the additive colours of red, green and blue, and thus it is known as RGB colour composite. Band ratios and RGB composites of Landsat ETM+ enhances mineral mapping, for example Al-OH have the strong absorption in band 7 and strong reflection in band 5 of ETM+ data, so the band ratio 5/7 enhances hydroxyl-bearing minerals.[28] The band ratio 3/1and 5/4 of Landsat ETM+ highlights iron oxide and ferrous minerals.[29] The alteration zones, vegetation, and the iron oxide zones are displayed as red, violet, and light yellow pixels in a RGB composite image of band ratios 5/7, 3/1, and 4/3.[30]

The Sabins's ratio of R=5/7, G= 3/1, B=3/5 using Landsat ETM+ shows areas with iron oxides and clay minerals.[31,32] On applying Kaufmann ratio, Abrams ratio, and Chica-Olm ratio to the bands of Landsat ETM+, iron and clay minerals are easily identified.[32,33] On applying Abrams ratio (RGB composite of the band ratios 5/7, 3/2, and 4/5), the iron-oxide and clay minerals associated with hydrothermal altered areas were visible in green and red colour. Kaufmann ratio (RGB composite of band ratios 7/4, 4/3 and 5/7) gives red, green and blue colour to iron minerals, vegetated zones and hydroxyl minerals. The Chica-Olma ratio

(RGB composite of band ratios 5/7, 5/4, and 3/1) provides red, green and blue colour to altered clay minerals, iron ions, and ferrous oxide minerals. The RGB composite of 5/7, 4/5 and 3/1 using Landsat ETM+ clearly discriminates the uraniferous alteration zones surrounded by granitic rocks.[28]

The ferric iron oxide minerals show high reflectance in the range 0.63 to 0.69 μm and high absorption in the range 0.45 to 0.52 μm, so the band ratio 4/2 made using the bands 2 and 4 of Landsat 8 clearly depicts the zones rich in iron oxides. The colour composite of bands 6, 5, 4 and band ratios 4/5, 5/6 and 6/7 made using the Landsat 8 data was used to identify iron ores.[34] The colour composites of bands 765 and 752 in RGB and also the band rationing composite of OLI 6/7, 6/4, 4/2 and 6/7, 4/2, 5/4 to RGB, respectively delineates gossanic ridges associated with gold mineralization from Landsat 8.[35] The high grade iron ores are easily detected using the band ratio (4+6)/5of Lansat 8.[10] The band ratios 5/7, 3/1, and 4/3 of Landsat ETM + and 6/7, 4/2, and 5/4 of Landsat 8 in RGB shows iron oxide and hydroxyl-bearing alteration minerals which is sometimes difficult to distinguish from vegetated areas. So the RGB composite of band ratios (5 + 3)/(7 + 1), 3/1, and 5/7 of Landsat ETM+ and band ratios (6 + 4)/(7 + 2), 4/2, and 6/7 of Landsat 8 clearly distinguishes vegetation and alteration areas separately.[36]

ASTER band ratio of 2/1 have been used for delineating iron oxide rich zones [37] and RGB composite of band ratios 4/2, 6/7, 5, and 10 helps in discriminating altered rocks and lithological units.[38] The False color composite (FCC) image of three bands (1, 2 and 9 of ASTER) at the highest Optimum Index Factor OIF index clearly discriminates younger granites.[39] The RGB composite of ASTER bands 3, 2, and 1 clearly distinguishes the faults and lineament structures.[30] The RGB combination of ASTER band ratios 7/6, 5/6, and 9/8 provide yellow to reddish yellow colors to Phyllic zones, green color to argillic zones and light blue to propylitic zones. Here ASTER 5/6 band ratio detects Al–Si–(OH) mineral groups, the band ratio 8/9 shows Mg–Si–(OH) mineral groups and the muscovite rich areas are clearly shown by ASTER 7/6 band ratio images. Also ASTER thermal band ratios 14/12 and 13/14 re used for identifying silicate and carbonate minerals.[40] The lighter and darker tones noticed in FCC composite of band ratios 13/10, 14/10, and 13/12 generated using ASTER data show the rock units contain felsic and mafic minerals.[41] The band ratio of ASTER 4/5 shows alunite mineral, 4/7 shows calcite and 4/6 shows kaolin minerals. So the RGB combination of 4/5, 4/6, and 4/7 shows areas with white pixels indicating the response

of (Al-OH) and (Fe-OH) minerals. Propylitic and phyllic alteration zones are seen in dark green, and yellow color. [42]

Relative absorption-Band Depth (RBD) is computed for each absorption feature by dividing the sum of shoulder bands (Bands 1 and 3) by the nearest band (Band 2) of the absorption feature minimum.[43] The RBD8= (Band 7+Band 9)/Band 8 using the ASTER bands 7, 8 and 9 enhances the pixels showing the abundances of CaCO3 and Mg-O-H minerals like carbonate, chlorite, epidote, etc. since these minerals shows high absorption at Band 8 compared to Band 7 and Band 9 of ASTER data. Similarly RBD6= (Band 5 + Band 7)/Band 6 highlights Al-O-H minerals. The RBD5= (Band 4+Band 6)/Band 5 is used for mapping kaolinite, alunite, and pyrophyllite minerals. The RBD13 highlights mafic and ultramafic rock units due to their high absorption feature in ASTER band 13.[37,44–47]

Spectral indices or Thermal indices are computed using mathematical combinations of bands denoting surface reflectance or emissivity at different wavelengths.[17] The SWIR bands of ASTER are used for deriving OH index (OHI_b) and pyrophyllite index (PI) for mapping Al-OH minerals and pyrophyllite.[48,49] The TIR bands of ASTER data are used for deriving mafic index and mafic-ultramafic index for mapping mafic-ultrmamafic rock units.[49,50] The TIR bands are also used for deriving carbonate index (CI) and quartz index (QI) for mapping carbonate and silicate minerals.[49]

1.3.2. Principal Components Analysis

Principal components analysis (PCA) is an image enhancement technique mostly used for generating a set of uncorrelated variables called principle components or PC bands by the linear transformation of highly correlated original image data. It segregates noise components by inhibiting irradiance effects of the bands and thereby it reduces dimensionality of data.[51] These linear transformation technique have been widely used along with other remote sensing techniques like colour composites, band rationing, crosta technique, hue-saturation-intensity (HSI) colour model, etc. for mapping mineral deposits from multispectral as well as hyperspectral datasets.

The PC bands of Landsat ETM+ (except band 6) and ASTER showed up the hydroxyl minerals and iron oxide minerals. PC4 band of Landsat ETM+ highlights the hydroxyl minerals and PC5 enhances iron oxide minerals. Similar analysis using ASTER data shows that PC2 enhances the hydroxyl-bearing areas.[52] The RGB composite of PC bands of Landsat

ETM+ such as PC1, PC3 and PC2 shows basalt areas with the mineral geosite. Here the PC1 and PC3 were obtained on applying PCA to the first ratio group of band ratios 5/4, 5/1, and 3/7 and PC2 gray level image from the band ratios 3/1, 4/5, and 3/2 of Landsat 7 ETM+.[53] The PCA applied to selected subsets of SWIR ASTER bands detects hydrothermal alteration minerals.[54] Kaolinite mineral shows high reflectance for bands 4 and 7, and strong absorption for band 6 in ASTER data, the PC4 of the SWIR bands can be used for identifying argillic and phyllic alteration zones.[42]

The RGB colour composite of PC3, PC2 and PC1 of ASTER successfully discriminates and characterizes the granitic rocks as younger granites, monzo-granite, older granitoides and also the sediments of metavolcanics, Hamammat sediments, Dokhan volcanic, tertiary sediments and quaternary sediments.[39] Out of nine PC images obtained from ASTER VNIR + SWIR bands, the PC4 image shows iron oxide minerals, PC5 shows the vegetation associated with drainage network, the bright pixels of PC7 image shows the Fe and Mg(OH)-bearing minerals and that of PC6 shows the Al(OH)-bearing minerals. Thus the RGB colour composite of PC bands highlights alteration zones associated with copper deposits.[45] The first three principal components of the PCA image obtained from the ASTER bands covering the visible-NIR-SWIR spectral regions helps to discriminate the geological groups like Cretaceous (limestone, clay, dolomite, etc.), Paleogene (limestone, clay, dolomite, gypsum, etc.), Miocene-Lower Quaternary (conglomerates, silts, ocher, etc.), and Middle Quaternary-Actual(alluvium, silts/gravel, gysum, etc.). Apart from these, the SVM classification of these PC images helps in detailed discrimination of 17 lithological units.[55]

1.3.3. Linear spectral unmixing

Linear spectral unmixing (LSU) considers the reflectance values of pixels in the satellite data as the linear proportion-weighted combination of the reflectance values of all endmembers present within that pixel on the Earth's surface.[56,57] Thus the output of LSU consists of gray-scale images correspond to all the endmembers and a root mean square (RMS) error image. Brighter pixels show higher abundances of the mineral.[58] LSU applied to ASTER data for delineating potassic alteration[30], Phyllic (muscovite), kaolinite (argillic alteration), pyrophylite-alunite (advanced argillic alteration), chlorite-calcite, and epidote (propylitic alterations)[59].

1.3.4. Spectral Information Divergence

Spectral Information Divergence (SID) uses the measures of divergence to match the pixels to a particular reference spectra, similar pixels are classified on the basis of smaller value of divergence. Pixels above a specified divergence threshold is not classified.[60] The spectral variability of a single mixed pixel is calculated based on a probabilistic point of view. Combined SAM and SID classification of ASTER data proved successful mapping of alteration areas consists of calcite, sericite, clay minerals, carbonate, quartz, and pyrite associated with gold mineralization.[61,62]

1.4.Placer deposits and heavy minerals

Placer minerals or placer deposits are formed by the mechanical concentration of mineral particles that get weathered from host rock.[63] Placer deposits are classified into (i) eluvial, (ii) alluvial or fluvial, (iii) aeolian, (iv) beach placers, and (v) fossil placers based on their mode of transportation and site of deposition. The minerals are weathered from parent rocks get transported by streams, reaches the sea and deposited along the coast by the action of waves at suitable locations called beach placer deposits.[64] The geological setting, climate, drainage pattern, and coastal processes are the main driving factors behind the deposition of heavy minerals along the coast of India.[65] The geology of the provenance rocks and the effect geological processes play a vital role in the formation of placer minerals. The weathering of parent rocks is mainly influenced by climatic factors especially the tropical to sub-tropical climate influences largely the chemical weathering along coastal regions. The formation of laterites also favoured pre-concentration of these minerals. The transport of minerals from the provenance to sea is achieved by availability of streams. The dynamic characteristics of coastal processes such as long shore currents, wave velocity, and speed made the transportation, sorting and deposition of sediments along the coasts. The beach sand minerals based on their relative difference in specific gravity are classified into heavy minerals and light minerals. The minerals with the property of high density usually having specific gravity 2.9 or greater are known as Heavy Minerals.[66] It is a mixture of minerals like ilmenite, rutile, leucoxene, zircon, sillimanite, monazite and garnet.[67] The list of most important heavy minerals is shown in Table 1.3.

Table 1.3: List of important heavy minerals

Sl. No	Heavy Mineral	Magnetic Property	Electrostatic Property	Specific Gravity
1	Ilmenite	Magnetic	Conducting	4.7
2	Garnet	Weak to non-magnetic	Non-conducting	3.4-4.2
3	Monazite	Weakly magnetic	Low conducting	4.6-5.4
4	Leucoxene	Weakly magnetic	Conducting	.>2.89
5	Rutile	Non-magnetic	Conducting	4.18-4.25
6	Zircon	Non-magnetic	Non-conducting	4.68
7	Sillimanite	Non-magnetic	Non-conducting	3.23

The light minerals are mostly quartz, dolomite, aragonite, etc., are called light minerals. Heavy minerals in India like ilmenite, rutile, zircon, sillimanite and monazite are named as 'strategic' based on their economic importance and critical applications in many diverse industries. Many researchers also refers the heavy minerals as 'strategic' due to its importance in nation's economy.[68,69]

1.4.1. Placer deposits in India

The important placer deposits of India includes (i) Ratnagiri deposits, Maharashtra, (ii) Chavara deposit, Kerala, (iii) Manavalakurichi deposit , Tamil Nadu, (iv) inland placer deposits (Teri sands), Tamil Nadu, (v) Srikurmam deposit, Andhra Pradesh, and (vi) Chatrapur deposit, Orissa (Figure 1.4).[65] The Chavara deposit in Kollam district of Kerala possesses one of the best ilmenite mineral in the world due to its high TiO_2 content of about 60%. The Neendakara-Kayamkulam deposit contains ilmenite (2.7Mt-35% grade), rutile (1Mt-2.5%), zircon (0.9Mt-2.5%), monazite (0.17Mt-0.5%), and sillimanite (2Mt-7%). The khondalite rocks are the major source of heavy minerals. The charnockites and the outcomes of pegmatites and quartz veins in these rocks also act as the source of heavy minerals. The tertiary sedimentary formations stretched along the coast act as the intermediate source of heavy minerals. The average heavy mineral content of these sedimentary formations are 1%.[70] The Manavalakurichi deposit in Kanyakumari district of Tamil Nadu shows 39% of total heavy mineral content (up to an average depth of 7.5m). Ilmenite mineral (24%) mostly exists followed by garnet (5.5%), sillimanite (3.5%), zircon (2%), rutile (1.8%), monazite (1%), and leucoxene (0.9%).[71] The hinterland is mainly occupied by khondalite rocks of

Archean age. It comprised of quartzite of arenaceous facies, calc silicates, quartz garnet sillimanite graphite schists, etc. Intrusions of charnockites are also noticed in semi-arid places.[72] The Srikurmam deposit in Srikakulam, Andhra Pradesh, predominantly consists of garnet (37.10%), followed by ilmenite (31.94%), rutile (1.3%), zircon (0.96%), sillimanite (24.33%) and monazite (0.24%). The hinterland is mostly dominated by khondalites, and the granulite facies of these khondalite rocks act as the main source of heavy minerals. The southwest of the deposition is mainly occupied by upper Gondwana formations. Charnockites has an only limited occurrence. In Chatrapur mineral sand deposit in the Ganjam district of Orissa, the ilmenite mineral predominantly exist with 5.86-17.45%, followed by garnet (3.78-12.33%), sillimanite (0.78-6.17%), monazite (0.10-0.77%), zircon (0.24-1.09%), rutile (0.40-1.70%), and magnetite (0.06-2.13%). The rocks occupied in Eastern Ghat consist of granites, gneisses, and metasediments of Archean to Proterozoic age, and Gondwanas act as the main provenance for the deposits.[73]

Apart from major placer deposits, many researchers have done detailed studies on texture, mineral distribution and geochemical characterisation of beach sands collected from other parts of the country. The average THM of Kantiaghar beach of Ganjam district, Odisha is 67% with the distribution of majorly sillimanite and ilmenite.[74] The Mulki estuarine beach sands in Karnataka, central west coast consists of ilmenite, magnetite, zircon, etc.[75] The presence of scandium was reported by instrumental neutron activation analysis for the beach sands of eastern coast of Odisha, India.[76] The zircon, garnet, titanite, and opaque non rare earth mineral ilmenite were identified along the Northern Karnataka Coast, India.[77] From Keelakarai to Periyapattinam, Gulf of Mannar, east coast of India, fine grained beach sediments exist with THM content of 5.5 to 31.55%.[78] Coarse grained samples with THM of 0.5 to 16.9% exist in tourist beaches of Chennai in Tamil Nadu.[79] Medium to fine sands present in the beaches of Point Calimere with heavy minerals of pyroxenes, amphiboles, muscovite, etc.[80] Medium to fine grained sand exist with ilmenite exist along the coast of Ullal and Surathkal in Karnataka.[81] The beach sediments of Valapatanam-Azhikode beach in Kerala show 30.32% THM.[82] Medium to fine grained sand exists with an average of 11.8% THM along the coast of Thiruchendur, Tamil Nadu.[67]

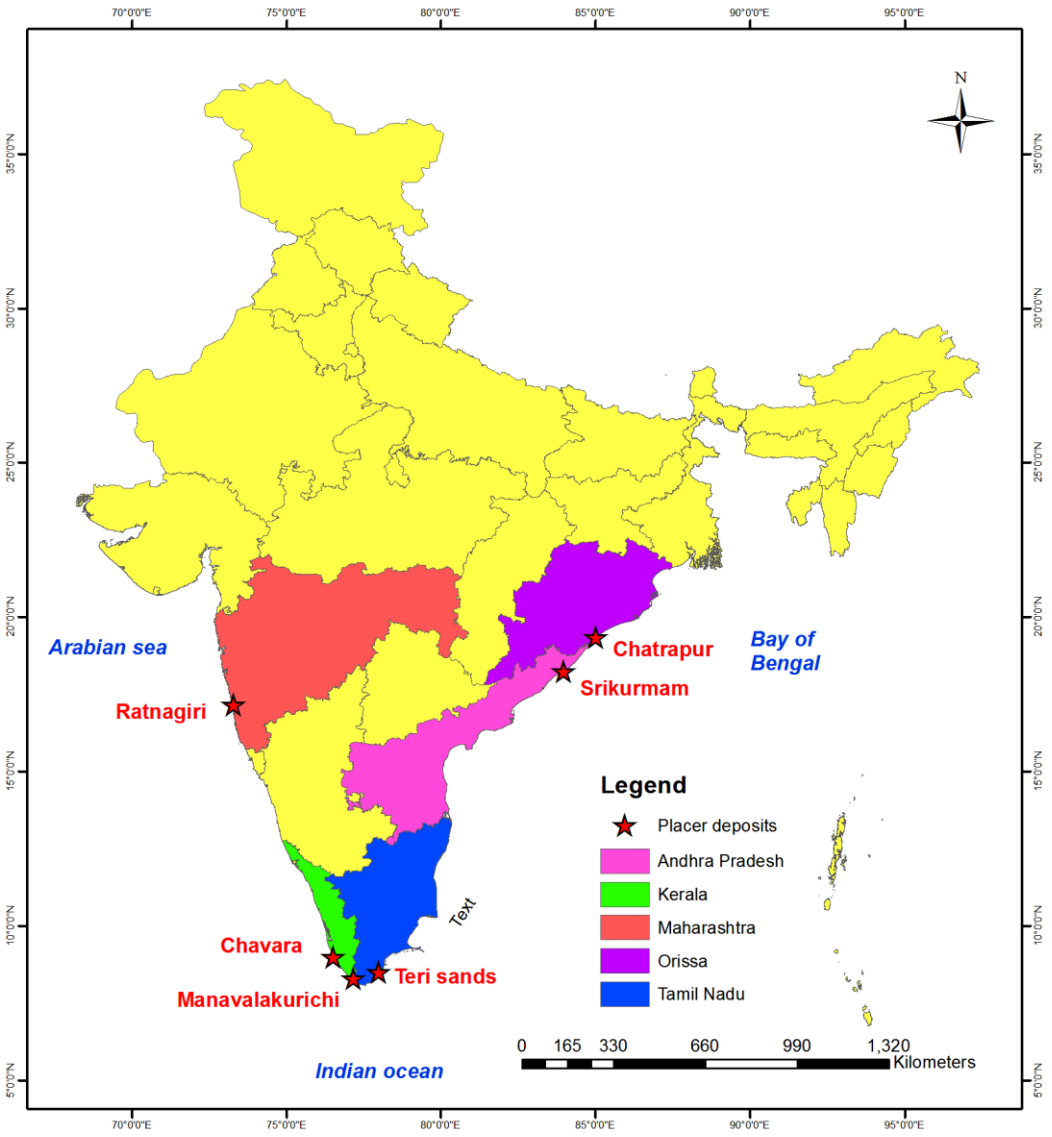

Figure 1.4: Major placer deposits in India.

1.5.Need for the study

Identification, exploration and value addition of the strategic minerals plays a prominent role in the socio-economic development of the nation in supporting Government's low-carbon plans (electric and hybrid vehicles) and will give a boost to our strategic sector such as aerospace, defence, nuclear energy. Exploring minerals is always a challenge for the miners because there is a possibility for missing rare and scarcely existing minerals and metals, and the process of finding them is an expensive risk. Logistic support at high rates may require to access exploration areas due to remoteness or difficult terrain. This all makes remote sensing and remote sensing data (satellite data), a prominent technology for mineral exploration. It provides solid information on exact targeting of mineral occurrences and

thereby it reduces field exploration and drilling costs. Remote sensing archives of satellite data which covers large areas on the ground are readily available. The heavy mineral deposits found in coastal zones are of high quality and high volume. But only limited studies or no systematic and detailed studies have been carried out so far on its identification and exploration. Therefore, consolidation of information on minerals would be complementary to the efforts for improving the deposit utilization. As the first step, all the heavy minerals of strategic/commercial importance should be evaluated quantitatively/geochemically. GIS and remote sensing has emerged as powerful techniques for compiling, storing, integrating and reproducing information on spatial systems. So the aim is to explore strategic mineral deposits through integrated use of geological, remote sensing, and GIS sciences.

1.6.Objectives

- To develop a spectral library of strategic minerals comprising of beach minerals, silica sand, clay deposits and baryte mineral deposits in India.
- To generate potential targets of mineral occurrences using hyperspectral analysis of Landsat 8, ASTER and EO-1 Hyperion datasets.
- To map and quantify mineral abundances through integrated use of machine learning algorithms and EO-1 Hyperion datasets.
- To carryout advanced characterization on structure, chemistry and surface morphology of minerals for quality assessment.

1.7.Strategic mineral deposits and Study area

1.7.1. Beach minerals of Varkala-Kovalam coast, Kerala

Thiruvananthapuram (Trivandrum) is the southernmost district of Kerala (Figure 1.5 and Figure 1.6) with a total of about 78 km coastline along the Arabian Sea on the west (8° 17’ 35”N–8° 51’ 45”N latitudes and 76° 40’ 23”E–77° 17’ 2” E longitudes). The beach sand of Kappil-Varkala (KV) and Shanghumugham-Kovalam (SK) which stretches along the coast of Thiruvananthapuram district shows good THM (Total Heavy Minerals) content. The heavy mineral sand deposits contain an assemblage of predominantly ilmenite followed by sillimanite, monazite, rutile, zircon, leucoxene and garnet. The existence of these minerals as accessories in the provenance rocks act as the geological control, and the rivers originated

from the Western Ghats and flowing westwards to meet the Arabian Sea acts as the geomorphic control together paved the formation of beach sands with heavy mineral content. Geologically the Thiruvananthapuram district has two divisions viz. the eastern Archean crystalline rocks and western coastal periphery filled by Tertiary and Quaternary sediments. The Archaean crystalline rocks comprise of Khondalite, Charnockite and Migmatite groups in which the Khondalites are noticed mainly in the southern part of Kerala and composed of garnetiferous biotite-sillimanite gneiss, with rare presence of calc-granulite and quartzite. Tertiary sedimentary formations exist linearly along the coastal tract and unconformably overlays the crystalline rocks act as the intermediate source of heavy minerals. The laterites formed over khondalite rocks also contain minor contents of sillimanite and graphite whereas those over charnockites contain ilmenite and magnetite. The heavy minerals which form the major part of beach sands are important accessories of khondalite, charnockites and the outcome of pegmatites and quartz veins present in these rocks. The Geological maps of the study areas are prepared using the data collected from Geological Survey of India (GSI).

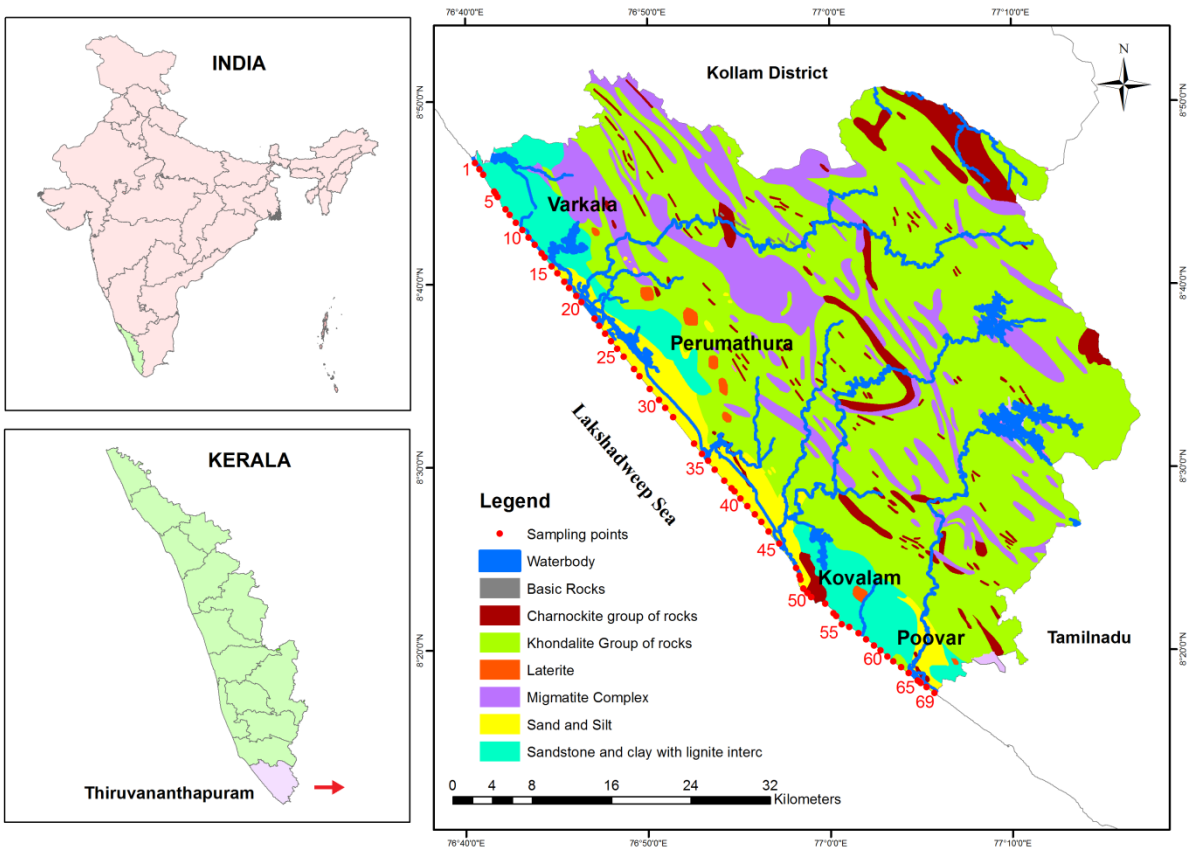

Figure 1.5: Study area map of Varkala-Kovalam coast, Kerala

Figure 1.6: Beach placers of Varkala-Kovalam coast, Kerala

In particular, the khondalites and charnockites are the significant sources of heavy mineral placers in the southern part of Kerala coast. The nature of provenance rocks, climatic conditions, coastal processes, coastal geomorphology, and drainage pattern governed the formation of beach sands. The action of waves and long currents determine the texture of beach sediments as well as the relative sorting of heavy and light minerals.[70]

1.7.2. Beach minerals of Cuddalore coast, Tamil Nadu

The Cuddalore coast situated in the Cuddalore district of Tamil Nadu state in India (see Figure 1.7). The present study is carried out along a coastal stretch of length 50km , bordered with the Bay of Bengal on the east and have the coordinates of 12° 0' 11.53"N- 79° 51' 18.53"E and 11° 33' 52.46"N- 79° 45' 26.95"E. The geology comprises of Mio-Pliocene, Cretaceous deposits, and Quaternary sediments. Uppanar and Gadilam rivers form the major east flowing rivers in the study area. The beaches are characterised by cliffs having a height of about 75–90 cm, which is formed by the erosion of foreshore by high energy waves. The backshore usually has a width of 30m, and that of the foreshore is about 20-30m. The Coastal configuration is N-S, current velocity is 1.8–3.6 m/s, and wave height is 1–1.5m. A detailed study on grain size and mineralogy of the present study area was carried out by many

researchers.[83–86] The heavy mineral analysis shows that the heavies exist in the range of 12.63%- 28.48% comprises mainly of kyanite, garnet, zircon, and opaques. The concentration of kyanite is 1.21% to 32.54%, garnet is 12.03% to 31.76%, and zircon is 4.0% to 20.19%.[83]

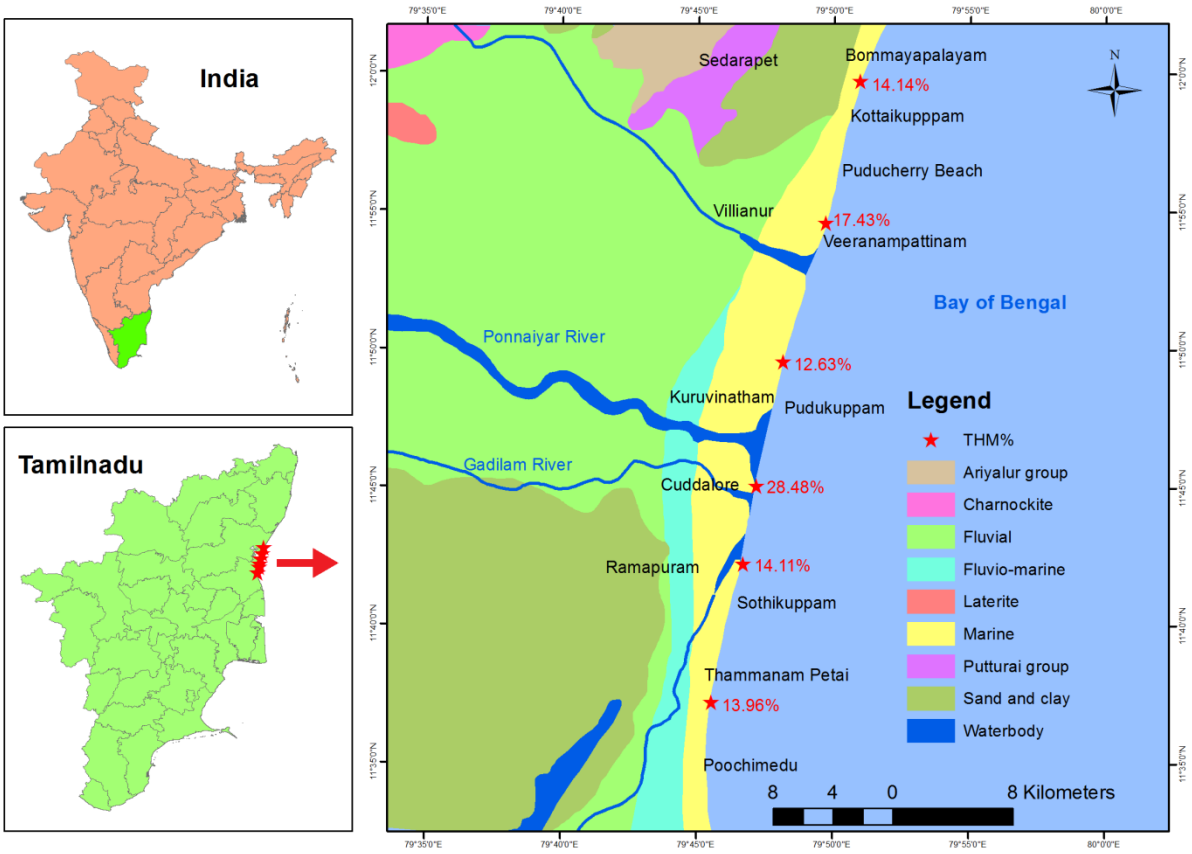

Figure 1.7: Study area map of Cuddalore coast, Tamil Nadu

1.7.3. Silica sand deposits of Cherthala, Kerala

A narrow stretch of land extends over 32km from Arookutti to Cherthala sandwiched by Vembanad lake on one side and Lakshadweep sea on another side, situated in Alappuzha district in Kerala, India is bestowed by large reserves of silica sand deposits of generally flat to gently dipping (Figure 1.8 and Figure 1.9). The geographic location of the study area is 9° 53' 23.50"N -9° 34' 52.29"N latitudes and 76° 16' 15.12"E-76° 23' 55.50"E longitudes. Major silica sand deposits are seen in Cherthala-Alappuzha, Kokothamangalam, and Pallipuram–Panavalli areas.[87] The Palaeo-beach ridges extends from Alappuzha to Nirkunnam contains high concentration of white silica sands which are actually forms the Cherthala sand deposits of 8-9 km length and 1-2 km width.[88]

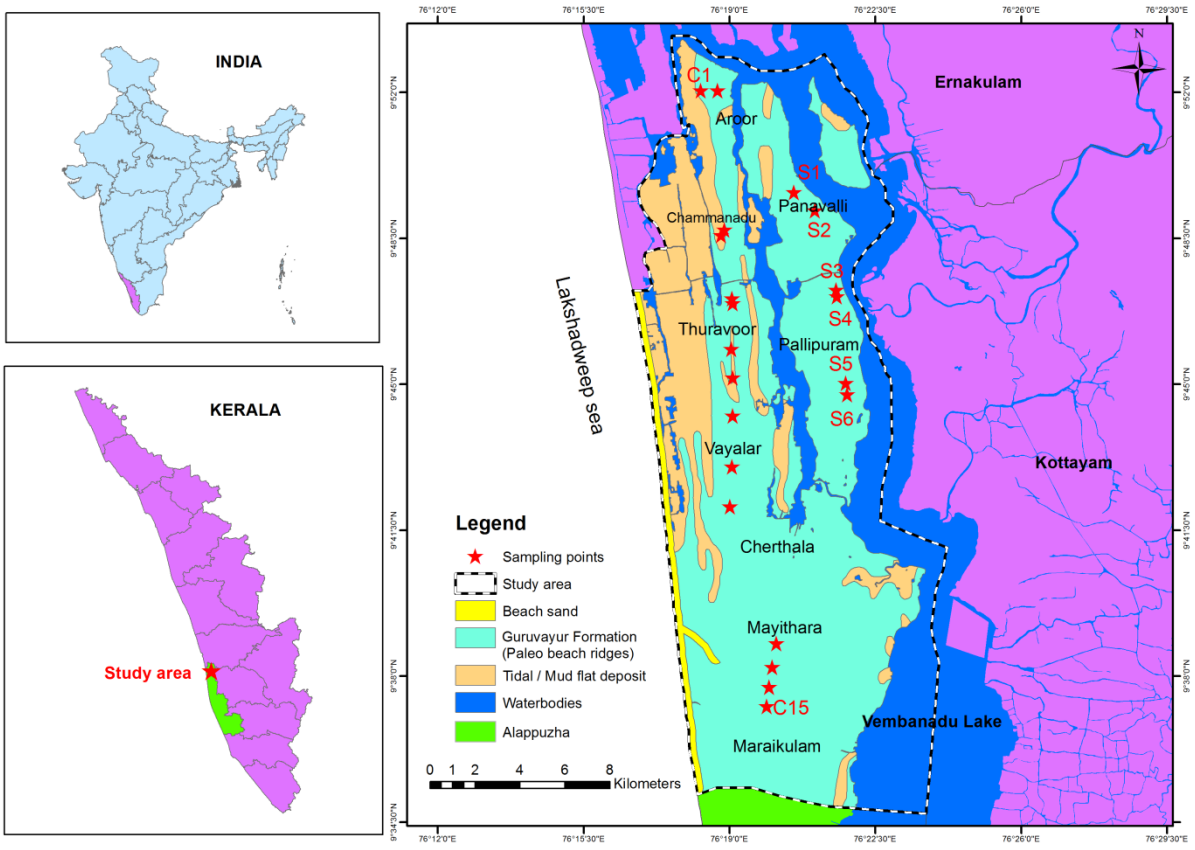

Figure 1.8: Study area map of Cherthala siica sand, Kerala

Figure 1.9: Silica sand deposits in Cherthala, Kerala

The Alappuzha district is mainly comprised of coastal plains with landforms originated by marine, fluvial and also fluvio-marine actions. The deposits are unconsolidated Quaternary sediments in which the sands occupy the upper layer underlain by clay. The quaternary sediments of the study area is mainly occupied by strand line/palaeo beach deposit (Guruvayoor Formation) followed by (Viyyam Formation) and beach deposit (Kadappuram

Formation).[89] The coastal parts of the district experience a moist and hot climate, and towards the interior it becomes slightly cooler and drier. The average annual rainfall received by the district is 2965.4 mm. The district experiences an average annual temperature of 30.7ºC to 23.9 ºC.

1.7.4. Kaolin deposits in Thonnakkal, Kerala

The Kaolin deposits are situated in Thonnakkal located in Thiruvananthapuram district, Kerala, India. It lies at the latitude of 8°37'55.78"N and longitude of 76°51'5.75"E which is approximately 7km away from the west coastline of Kerala (as shown in the Figure 1.10 and Figure 1.11). Geologically the district was divided into two groups of Archean crystalline rocks on the eastern side and tertiary-quaternary sediments on the western coastal side.

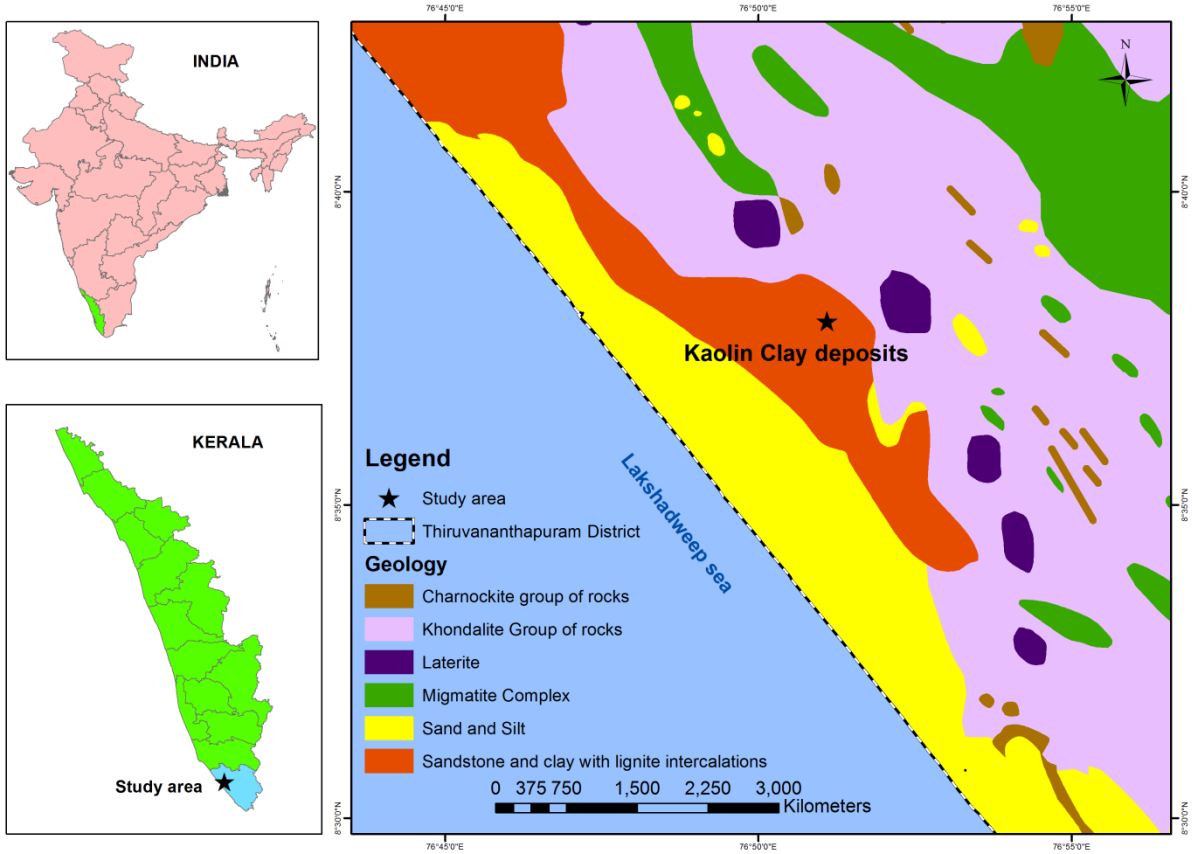

Figure 1.10: Study area map of Thonnakkal Kaolin clay deposits, Kerala

The Archean crystalline rocks comprise of Khondalite, Charnockite, and Migmatite Group of rocks. The Khondalite group comprises of garnetiferous biotite-sillimanite gneiss, with occasional stretches of calc-granulite and quartzite. Apart from these crystalline rocks,

Cenozoic sediments are occupied along the coastal react overlain the Precambrian crystalline.[89] The Kaolin deposits at Thonnakkal also forms a part of Cenozoic sediments. It is a Tertiary Warkalli formation situated between the Tertiary formation on the western side and at the periphery of khondalite belt.[90]

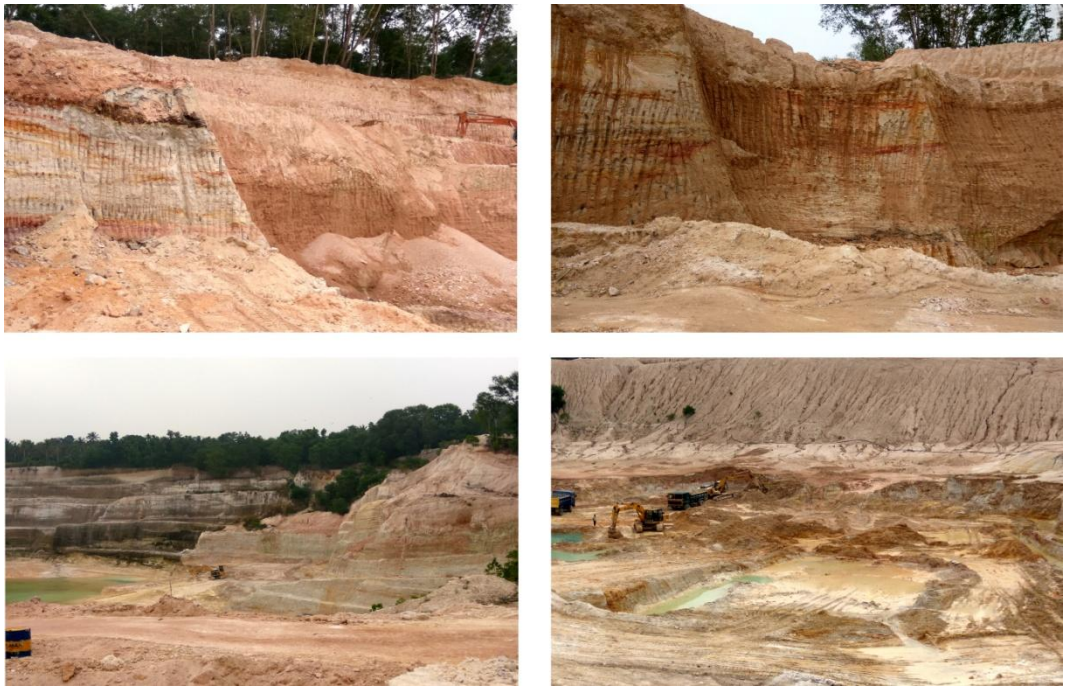

Figure 1.11: Kaolin deposits at Thonnakkal, Kerala

1.7.5. Fullerene bearing Mangampet baryte mine, Andhra Pradesh

The Mangampet baryte mine is located in the southern part of Kadapa District of state Andhra Pradesh in India (Figure 1.12 and Figure 1.13). In India, fullerene bearing shungite rocks were discovered in the Mangampet baryte mine located in Kadapa District, Andhra Pradesh. [91] The interlayered thick black coloured slates of carbonaceous shales exist in barite mines are confirmed that of shungite suite of rocks by carbon-hydrogen-sulphur composition. Further, ICP-MS analysis indicates the presence of Be, Co, Ga, Ge, Y, Zr, etc. The laser desorption/ionization mass spectrometry gives the main peaks near m/z= 720amu and 840 amu indicating the presence of C_{60} and C_{70}. It is estimated to about 74 million tonnes of reserves which is known to be the largest in the World. The Andhra Pradesh Mineral Development Corporation Limited (APMDC) is presently engaged in mining of barytes and achieved a turnover of Rs. 2.13 billion in the year 2009-10 through the sale and exports (alone accounts over 92%). The geographic location is 14°1'46.21"N latitude and 79°18'52.34"E longitude. Belongs to structurally configured “pull apart” Proterozoic

Cuddapah Basin. Lithology dominated by quartzites, shales, dolomites, with intercalations of chert, limestone, dolerites, and basalts.

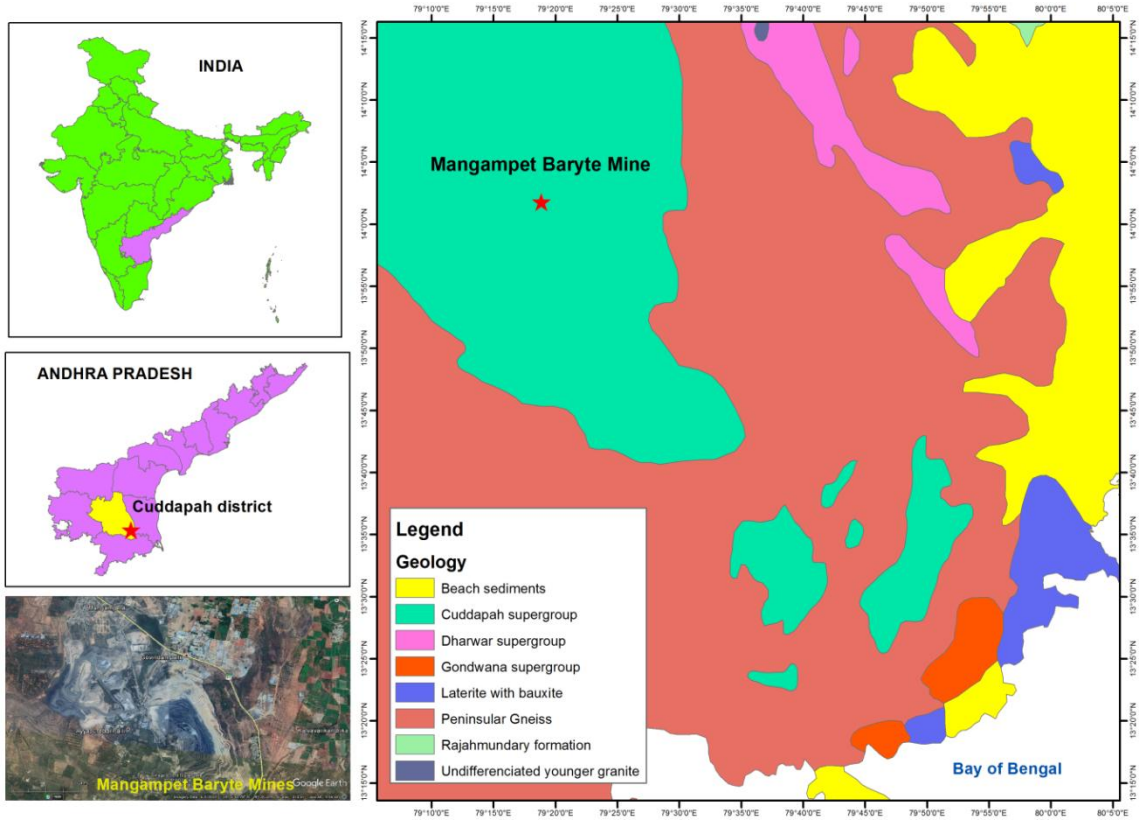

Figure 1.12: Study area map of Mangampet baryte mine, Andhra Pradesh

Figure 1.13: Mangampet baryte mine in Andhra Pradesh, India

The rock strata of Cuddapah Supergroup consists of arenaceous and argillaceous sediments overlain by carbonate sediments associated with Kurnool Group with upper part covered by clastics. Barytes mineralization is attributed to the hydrothermal solution and

contact metamorphism in contact zones of dolomites with the igneous sill intrusive. The bya zone of lapilli barite is considered as one of the economically important deposit and it is over lined by granular barite beds seen in upper Carbonaceous tuff zone of Cuddapah Supergroup. It is also occurred in association with copper mineralization zones of pyrite, chalcopyrite, azurite, etc. The Proterozoic Cuddapah Basin having a crescent-shaped structure is formed over the high grade Archaean crust of the Eastern Dharwar Craton. The sub-basins are formed by large dolerite dykes. The basin is filled with strategic minerals like baryte, asbestos, high-grade limestone, phosphorites, uranium, and diamond.[92]

1.8.References

(1) CCRS. *Fundamentals of Remote Sensing*; Canada Centre for Remote sensing, 2004.

(2) Rull, F.; Martinez-Frias, J.; Rodríguez-Losada, J. A. Micro-Raman Spectroscopic Study of El Gasco Pumice, Western Spain. *J. Raman Spectrosc.* **2007**, *38* (2), 239–244.

(3) Zhang, T.; Yi, G.; Li, H.; Wang, Z.; Tang, J.; Zhong, K.; Li, Y.; Wang, Q.; Bie, X. Integrating Data of ASTER and Landsat-8 OLI (AO) for Hydrothermal Alteration Mineral Mapping in Duolong Porphyry Cu-Au Deposit, Tibetan Plateau, China. *Remote Sens.* **2016**, *8* (11), 890.

(4) Irons, J. R.; Dwyer, J. L.; Barsi, J. A. The next Landsat Satellite: The Landsat Data Continuity Mission. *Remote Sens. Environ.* **2012**.

(5) Abrams, M.; Hook, S. Summary for Policymakers. In *Climate Change 2013 - The Physical Science Basis*; Intergovernmental Panel on Climate Change, Ed.; Cambridge University Press: Cambridge, 2002; pp 1–30.

(6) Abrams, M.; Hook, S. J. Simulated Aster Data for Geologic Studies. *IEEE Trans. Geosci. Remote Sens.* **1995**, *33* (3), 692–699.

(7) Pearlman, J. S.; Barry, P. S.; Segal, C. C.; Shepanski, J.; Beiso, D.; Carman, S. L. Hyperion, a Space-Based Imaging Spectrometer. *IEEE Trans. Geosci. Remote Sens.* **2003**, *41* (6), 1160–1173.

(8) Kääb, A.; Huggel, C.; Paul, F.; Wessels, R.; Raup, B. H.; Kieffer, H.; Kargel, J.

Glacier Monitoring from ASTER Imagery: Accuracy and Applications. In *Proceedings of EARSeL-LISSIG-Workshop Observing our Cryosphere from Space, Bern, March 11-13, 2002*; 2002.

(9) Waldhoff, G.; Bubenzer, O.; Bolten, A.; Koppe, W.; Bareth, G. Spectral Analysis of Aster, Hyperion, and Quickbird Data for Geomorphological and Geological Research in Egypt (Dakhla Oasis, Western Desert). In *International Archives of the Photogrammetry, Remote Sensing and Spatial Information Sciences - ISPRS Archives*; 2008.

(10) Ducart, D. F.; Silva, A. M.; Toledo, C. L. B.; De Assis, L. M. Mapping Iron Oxides with Landsat-8/OLI and EO-1/Hyperion Imagery from the Serra Norte Iron Deposits in the Carajás Mineral Province, Brazil. *Brazilian J. Geol.* **2016**.

(11) Gad, S.; Kusky, T. ASTER Spectral Ratioing for Lithological Mapping in the Arabian-Nubian Shield, the Neoproterozoic Wadi Kid Area, Sinai, Egypt. *Gondwana Res.* **2007**.

(12) Yamaguchi, Y.; Fujisada, H.; Kudoh, M.; Kawakami, T.; Tsu, H.; Kahle, A. .; Pniel, M. ASTER Instrument Characterization and Operation Scenario. *Adv. Sp. Res.* **1999**, *23* (8), 1415–1424.

(13) Rull, F.; Martinez-Frias, J.; Rodríguez-Losada, J. A. Micro-Raman Spectroscopic Study of El Gasco Pumice, Western Spain. *J. Raman Spectrosc.* **2007**, *38* (2), 239–244.

(14) Hewson, R. D.; Cudahy, T. J.; Mizuhiko, S.; Ueda, K.; Mauger, A. J. Seamless Geological Map Generation Using ASTER in the Broken Hill-Curnamona Province of Australia. *Remote Sens. Environ.* **2005**, *99* (1–2), 159–172.

(15) Hewson, R.; Cudahy, T. Issues Affecting Geological Mapping with ASTER Data: A Case Study of the Mt Fitton Area, South Australia. In *Remote Sensing and Digital Image Processing*; 2011.

(16) Pour, A. B.; Hashim, M. Hydrothermal Alteration Mapping from Landsat-8 Data, Sar Cheshmeh Copper Mining District, South-Eastern Islamic Republic of Iran. *J. Taibah Univ. Sci.* **2015**.

(17) San, B. T.; Sumer, O.; Gurcay, B. Comparison of Band Rationing and Spectral Indices Methods for Detecting Alunite and Kaolinite Minerals Using Aster Data in Biga Region, Turkey. *Proc. ISPRS* **2004**.

(18) Bhattacharya, S.; Majumdar, T. J.; Rajawat, A. S.; Panigrahy, M. K.; Das, P. R. Utilization of Hyperion Data over Dongargarh, India, for Mapping Altered/Weathered and Clay Minerals along with Field Spectral Measurements. *Int. J. Remote Sens.* **2012**, *33* (17), 5438–5450.

(19) Kumari, S. K.; Debashish, C.; Pulakesh, D.; Jatisankar, B. Hyperion Image Analysis for Iron Ore Mapping in Gua Iron Ore Region. *Int. Res. J. Earth Sci.* **2014**, *1*, 1–6.

(20) Othman, A.; Gloaguen, R. Improving Lithological Mapping by SVM Classification of Spectral and Morphological Features: The Discovery of a New Chromite Body in the Mawat Ophiolite Complex (Kurdistan, NE Iraq). *Remote Sens.* **2014**, *6* (8), 6867–6896.

(21) Zimmermann, R.; Brandmeier, M.; Andreani, L.; Mhopjeni, K.; Gloaguen, R. Remote Sensing Exploration of Nb-Ta-LREE-Enriched Carbonatite (Epembe/Namibia). *Remote Sens.* **2016**, *8* (8), 620.

(22) Hall, J. L.; Boucher, R. H.; Buckland, K. N.; Gutierrez, D. J.; Hackwell, J. A.; Johnson, B. R.; Keim, E. R.; Moreno, N. M.; Ramsey, M. S.; Sivjee, M. G.; Tratt, D. M.; Warren, D. W.; Young, S. J. MAGI: A New High-Performance Airborne Thermal-Infrared Imaging Spectrometer for Earth Science Applications. *IEEE Trans. Geosci. Remote Sens.* **2015**, *53* (10), 5447–5457.

(23) van der Meer, F. The Effectiveness of Spectral Similarity Measures for the Analysis of Hyperspectral Imagery. *Int. J. Appl. Earth Obs. Geoinf.* **2006**, *8* (1), 3–17.

(24) van der Meer, F. D.; van der Werff, H. M. A.; van Ruitenbeek, F. J. A.; Hecker, C. A.; Bakker, W. H.; Noomen, M. F.; van der Meijde, M.; Carranza, E. J. M.; Smeth, J. B. de; Woldai, T. Multi- and Hyperspectral Geologic Remote Sensing: A Review. *Int. J. Appl. Earth Obs. Geoinf.* **2012**, *14* (1), 112–128.

(25) Rani, N.; Mandla, V. R.; Singh, T. Performance of Image Classification on Hyperspectral Imagery for Lithological Mapping. *J. Geol. Soc. India* **2016**.

(26) Zeinelabdein, K. A. E.; Halim, A.; Nadi, H. El. The Use of Landsat 8 OLI Image for the Delineation of Gossanic Ridges in the Red Sea Hills of NE Sudan. *Am. J. Earth Sci.* **2014**, *1* (3), 62–67.

(27) Langford, R. L. Temporal Merging of Remote Sensing Data to Enhance Spectral Regolith, Lithological and Alteration Patterns for Regional Mineral Exploration. *Ore Geol. Rev.* **2015**.

(28) Ramadan, T. M.; Ibrahim, T. M.; Said, A. D.; Baiumi, M. Application of Remote Sensing in Exploration for Uranium Mineralization in Gabal El Sela Area, South Eastern Desert, Egypt. *Egypt. J. Remote Sens. Sp. Sci.* **2013**, *16* (2), 199–210.

(29) Mehdi, S. M.; Pant, N. C.; Saini, H. S.; Mujtaba, S. A. I.; Pande, P. Identification of Palaeochannel Configuration in the Saraswati River Basin in Parts of Haryana and Rajasthan, India, through Digital Remote Sensing and GIS. *Episodes* **2016**, *39* (1), 29–38.

(30) Sojdehee, M.; Rasa, I.; Nezafati, N.; Abedini, M. V. Application of Spectral Analysis to Discriminate Hydrothermal Alteration Zones at Daralu Copper Deposit, SE Iran. *Arab. J. Geosci.* **2016**, *9* (1), 41.

(31) SABINS, F. F. *Remote Sensing : Principles and Interpretation*; New Yark: WH Freeman and Company, 1997.

(32) Khidir, S. O. El; Babikir, I. a a. Digital Image Processing and Geospatial Analysis of Landsat 7 ETM + for Mineral Exploration , Abidiya Area , North Sudan. *Int. J. Geomatics Geosci.* **2013**, *3* (3), 645–658.

(33) Mia, B.; Fujimitsu, Y. Mapping Hydrothermal Altered Mineral Deposits Using Landsat 7 ETM+ Image in and around Kuju Volcano, Kyushu, Japan. *J. Earth Syst. Sci.* **2012**, *121* (4), 1049–1057.

(34) Bersi, M.; Saibi, H.; Chabou, M. C. Aerogravity and Remote Sensing Observations of an Iron Deposit in Gara Djebilet, Southwestern Algeria. *J. African Earth Sci.* **2016**, *116*, 134–150.

(35) Zeinelabdein, K. A. E.; El Nadi, A. H. H. The Use of Landsat 8 OLI Image for the

Delineation of Gossanic Ridges in the Red Sea Hills of NE Sudan. *Am. J. Earth Sci.* **2014**, *1* (3), 62–67.

(36) Masoumi, F.; Eslamkish, T.; Honarmand, M.; Abkar, A. A. A Comparative Study of Landsat-7 and Landsat-8 Data Using Image Processing Methods for Hydrothermal Alteration Mapping. *Resour. Geol.* **2017**, *67* (1), 72–88.

(37) Bhadra, B. K.; Pathak, S.; Karunakar, G.; Sharma, J. R. ASTER Data Analysis for Mineral Potential Mapping Around Sawar-Malpura Area, Central Rajasthan. *J. Indian Soc. Remote Sens.* **2013**, *41* (2), 391–404.

(38) Beiranvand Pour, A.; Hashim, M.; Pournamdari, M. CHROMITITE PROSPECTING USING LANDSAT TM and ASTER REMOTE SENSING DATA. In *ISPRS Annals of the Photogrammetry, Remote Sensing and Spatial Information Sciences*; Copernicus GmbH, 2015; Vol. 2, pp 99–103.

(39) Gemail, K.; Abd-El Rahman, N. M.; Ghiath, B. M.; Aziz, R. N. Integration of ASTER and Airborne Geophysical Data for Mineral Exploration and Environmental Mapping: A Case Study, Gabal Dara, North Eastern Desert, Egypt. *Environ. Earth Sci.* **2016**, *75* (7), 592.

(40) Pour, A. B.; Hashim, M. Hydrothermal Alteration Mapping from Landsat-8 Data, Sar Cheshmeh Copper Mining District, South-Eastern Islamic Republic of Iran. *J. Taibah Univ. Sci.* **2015**, *9* (2), 155–166.

(41) Matar, S. S.; Bamousa, A. O. Integration of the ASTER Thermal Infra-Red Bands Imageries with Geological Map of Jabal Al Hasir Area, Asir Terrane, the Arabian Shield. *J. Taibah Univ. Sci.* **2013**.

(42) Mahdevar, M. R.; Ketabi, P.; Saadatkhah, N.; Rahnamarad, J.; Mohammadi, S. S. Application of ASTER SWIR Data on Detection of Alteration Zone in the Sheikhabad Area, Eastern Iran. *Arab. J. Geosci.* **2015**, *8* (8), 5909–5919.

(43) Crowley, J. K.; Brickey, D. W.; Rowan, L. C. Airborne Imaging Spectrometer Data of the Ruby Mountains, Montana: Mineral Discrimination Using Relative Absorption Band-Depth Images. *Remote Sens. Environ.* **1989**, *29* (2), 121–134.

(44) Rull, F.; Martinez-Frias, J.; Rodríguez-Losada, J. A. Micro-Raman Spectroscopic Study of El Gasco Pumice, Western Spain. *J. Raman Spectrosc.* **2007**, *38* (2), 239–244.

(45) Pour, A. B.; Hashim, M. Identification of Hydrothermal Alteration Minerals for Exploring of Porphyry Copper Deposit Using ASTER Data, SE Iran. *J. Asian Earth Sci.* **2011**, *42* (6), 1309–1323.

(46) Abedi, M.; Gholami, A.; Norouzi, G.-H. A Stable Downward Continuation of Airborne Magnetic Data: A Case Study for Mineral Prospectivity Mapping in Central Iran. *Comput. Geosci.* **2013**, *52*, 269–280.

(47) Rejith, R. G.; Sundararajan, M. Mapping of Mafic-Ultramafic Rock Units in Late Archean Bhavani Complex, Southern India Using ASTER Thermal Bands. In *Shear Zones and Crustal Blocks of Southern India*; 2018; pp 34–40.

(48) Son, Y.-S.; Kang, M.-K.; Yoon, W.-J. Pyrophyllite Mapping in the Nohwa Deposit, Korea, Using ASTER Remote Sensing Data. *Geosci. J.* **2014**, *18* (3), 295–305.

(49) Ninomiya, Y.; Fu, B.; Cudahy, T. J. Detecting Lithology with Advanced Spaceborne Thermal Emission and Reflection Radiometer (ASTER) Multispectral Thermal Infrared "Radiance-at-Sensor" Data. *Remote Sens. Environ.* **2005**, *99* (1–2), 127–139.

(50) Ding, C.; Liu, X.; Liu, W.; Liu, M.; Li, Y. Mafic-Ultramafic and Quartz-Rich Rock Indices Deduced from ASTER Thermal Infrared Data Using a Linear Approximation to the Planck Function. *Ore Geol. Rev.* **2014**.

(51) SINGH, A.; HARRISON, A. Standardized Principal Components. *Int. J. Remote Sens.* **1985**, *6* (6), 883–896.

(52) Ranjbar, H.; Honarmand, M.; Moezifar, Z. Application of the Crosta Technique for Porphyry Copper Alteration Mapping, Using ETM+ Data in the Southern Part of the Iranian Volcanic Sedimentary Belt. *J. Asian Earth Sci.* **2004**, *24* (2), 237–243.

(53) Corumluoglu, O.; Vural, A.; Asri, I. Determination of Kula Basalts (Geosite) in Turkey Using Remote Sensing Techniques. *Arab. J. Geosci.* **2015**, *8* (11), 10105–10117.

(54) Farahbakhsh, E.; Shirmard, H.; Bahroudi, A.; Eslamkish, T. Fusing ASTER and QuickBird-2 Satellite Data for Detailed Investigation of Porphyry Copper Deposits Using PCA; Case Study of Naysian Deposit, Iran. *J. Indian Soc. Remote Sens.* **2016**.

(55) Gasmi, A.; Gomez, C.; Zouari, H.; Masse, A.; Ducrot, D. PCA and SVM as Geo-Computational Methods for Geological Mapping in the Southern of Tunisia, Using ASTER Remote Sensing Data Set. *Arab. J. Geosci.* **2016**, *9* (20), 753.

(56) Smith, M. O.; Ustin, S. L.; Adams, J. B.; Gillespie, A. R. Vegetation in Deserts: I. A Regional Measure of Abundance from Multispectral Images. *Remote Sens. Environ.* **1990**, *31* (1), 1–26.

(57) Ramak, R.; Valadan Zouj, M. J.; Mojaradi, B. IMPROVING LINEAR SPECTRAL UNMIXING THROUGH LOCAL ENDMEMBER DETECTION. *ISPRS - Int. Arch. Photogramm. Remote Sens. Spat. Inf. Sci.* **2015**, *XL-3/W2*, 177–181.

(58) Van Der Meer, F. Spectral Unmixing of Landsat Thematic Mapper Data. *Int. J. Remote Sens.* **1995**, *16* (16), 3189–3194.

(59) Hosseinjani, M.; Tangestani, M. H. Mapping Alteration Minerals Using Sub-Pixel Unmixing of Aster Data in the Sarduiyeh Area, Se Kerman, Iran. *Int. J. Digit. Earth* **2011**.

(60) Chang, C.-I. New Hyperspectral Discrimination Measure for Spectral Characterization. *Opt. Eng.* **2004**, *43* (8), 1777.

(61) El-Magd, I. A.; Mohy, H.; Basta, F. Application of Remote Sensing for Gold Exploration in the Fawakhir Area, Central Eastern Desert of Egypt. *Arab. J. Geosci.* **2015**, *8* (6), 3523–3536.

(62) Amer, R.; El Mezayen, A.; Hasanein, M. ASTER Spectral Analysis for Alteration Minerals Associated with Gold Mineralization. *Ore Geol. Rev.* **2016**, *75*, 239–251.

(63) Bates, R. L.; Jackson, J. A. *Dictionary of Geological Terms*, 3rd ed.; American Geological Institute, Anchor Press, 1984.

(64) Angusamy, N.; Rajamanickam, G. V. Depositional Environment of Sediments along the Southern Coast of Tamil Nadu, India. *Oceanologia* **2006**, *48* (1).

(65) Ali, M. A.; Krishnan, S.; Banerjee, D. C. Beach and Inland Heavy Mineral Sand Investigations and Deposits in India-An Overview. *Explor. Res. At. Miner.* **2001**, *13*, 1–21.

(66) Cheepurupalli, N. R.; Radha, B. A.; Reddy, K. S. N.; Dhanamjayarao, E. N.; Dayal, A. M. Heavy Mineral Distribution Studies in Different Microenvironments of Bhimunipatnam Coast, Andhra Pradesh, India. *Int. J. Sci. Res. Publ.* **2012**, *2* (5).

(67) Rajganapathi, V. C.; Jitheshkumar, N.; Sundararajan, M.; Bhat, K. H.; Velusamy, S. Grain Size Analysis and Characterization of Sedimentary Environment along Thiruchendur Coast, Tamilnadu, India. *Arab. J. Geosci.* **2013**, *6* (12), 4717–4728.

(68) Rao, D. S.; Kumar, T. V. V.; Rao, S. S.; Prabhakarr, S.; Raju, G. B. Characterization of Srikunntan and Navaladi Beach Placer Minerals. **2005**, No. iii, 65–73.

(69) Raju, R. D.; Ravi, G. S.; Shivkumar, K.; Reddy, L. S. R.; Rohatgi, S. WDXRFS Method for Quantification of Heavy Minerals in Sand Samples. *J. Geol. Soc. India* **2005**, *66* (4), 401.

(70) Krishnan, S.; Viswanathan, G.; Balachandran, K. Heavy Mineral Sand Deposits of Kerala. *Explor. Res. At. Miner.* **2001**, *13*, 111–146.

(71) Chandrasekharan, S.; Murugan, C. Heavy Minerals in the Beach and the Coastal Red Sands (TERIS) of Tamil Nadu. *Explor. Res. At. Miner.* **2001**, *13*, 87–109.

(72) Gayathri, G. S.; Rejith, R. G.; Jeelani, S. H.; Sundararajan, M.; Aslam, M. M.; Chidambaram, S. Heavy Mineral Resources In Tamil Nadu, India: An Overview. In *Geochemistry and Mineralogy of Coastal Sediments in Tamil Nadu*; 2017; pp 110–121.

(73) Rao, R. G.; Sahoo, P.; Panda, N. K. Heavy Mineral Sand Deposits of Orissa. *Explor. Res. At. Miner.* **2001**, *2*, 133–146.

(74) Nayak, B.; Mohapatra, R. K.; Mangaraj, M.; Venkatesh, A. S.; Behera, P. N. Mineralogical Characterisation of Beach Placers at Kantiaghar in Ganjam District, Odisha. *J. Geol. Soc. India* **2019**.

(75) Shalini, G.; Hegde, V. S.; Soumya, M.; Korkoppa, M. M. Provenance and Implications

of Heavy Minerals in the Beach Sands of India's Central West Coast. *J. Coast. Res.* **2019**.

(76) Khan, R.; Ghosal, S.; Sengupta, D.; Tamim, U.; Hossain, S. M.; Agrahari, S. Studies on Heavy Mineral Placers from Eastern Coast of Odisha, India by Instrumental Neutron Activation Analysis. *J. Radioanal. Nucl. Chem.* **2019**.

(77) Hegde, V.; G, S.; Gouri, K.; Girish, G.; Lavanya, G.; Krishnaprasad, P.; Bhagwat, T. Potentials of Rare Earth and Other Placer Mineral Occurrence along the Northern Karnataka Coast, India. *Indian J. Geo-Marine Sci.* **2017**, *46* (3), 605–611.

(78) Kannaiyan, N.; Suresh Gandhi, M.; Elango, R.; Sujita, G.; Hussain, S. M. Heavy Minerals and Granulometric Studies in Coastal Sediments from Keelakarai to Periyapattinam, Gulf of Mannar, East Coast of India. In *WATER RESOURCES IN ARID AREAS: THE WAY FORWARD*; 2017; pp 283–294.

(79) Santhiya, G.; Lakshumanan, C.; Jonathan, M. P.; Sundrarajan, M.; Srinivasalu, S.; Viveganandan, S.; Uma-Maheswari, B. Depositional Features in Tourist Beaches of Chennai Metropolis, SE Coast of India: Inferences from Grain Size Studies. *J. Geol. Soc. India* **2016**.

(80) Sundararajan, M.; Natesan, U.; Babu, N.; Seralathan, P. Sedimentological and Mineralogical Investigation of Beach Sediments of a Fast Prograding Cuspate Foreland (Point Calimere), Southeast Coast of India. *Res. J. Environ. Sci.* **2009**.

(81) Sundararajan, M.; Bhat, K. H.; Velusamy, S.; Babu, N.; Janaki, M. E. K.; Sasibhooshanan, S.; Das, P. N. M. Characterization of Ilmenite from Kerala Coastline, India:Implications in the Production of Synthetic Rutile. *J. Miner. Mater. Charact. Eng.* **2009**, *08* (06), 427–438.

(82) Sundararajan, M.; Bhat, K. H.; Velusamy, S. Investigation on Mineralogical and Chemical Characterization of Ilmenite Deposits of Northern Kerala Coast, India. *Res. J. Earth Sci.* **2010**, *2* (2), 36–40.

(83) Angusamy, N.; Dajkumar Sahayam, J.; Suresh Gandhi, M.; Rajamanickam, G. V. Coastal Placer Deposits of Central Tamil Nadu, India. *Mar. Georesources Geotechnol.* **2005**, *23* (3), 137–174.

(84) Suresh, M.; Solai, A.; Kaveri, S.; Kanan, K.; Dhamodharan, V.; Baskar, K.; Rajamanickam, V. Post Tsunami Heavy Mineral Distribution Between Cuddalore to Kanyakumari Along the Tamil Nadu Coast, India – A Review. In *Tsunami - A Growing Disaster*; InTech, 2011.

(85) Suresh Gandhi, M.; Solai, A. Textural and Heavy Mineral Characteristics of Surface and Buried Sediments along the Coast between Cuddalore and Pondicherry, India. *Int. J. Earth Sci. Eng.* **2010**, *3* (6), 886–892.

(86) Viveganandan, S.; Lakshumanan, C.; Sundararajan, M.; Eswaramoorthi, S.; Natesan, U. Depositional Environment of Sediments along the Cuddalore Coast of Tamilnadu, India. *Indian J. Mar. Sci.* **2013**, *42* (3), 375–382.

(87) Poulose, K. V.; Nair, G. B. *Reconnaissance Geological Mapping of the Coastal Tertiaries in Parts of Trivandrum, Quilon, Kottayam, Alleppey and Ernakulam Districts, Kerala State*.; 1965.

(88) Rajan, T. N.; Anil Kumar, P. S. Geology And Mineral Resources Of The States Of India Part Ix – Kerala. *Geol. Surv. India Misc. Publ. No. 30* **2005**.

(89) Soman, K. *Geology of Kerala*; GSI Publications, 1987.

(90) Nakagawa, M.; Santosh, M.; Yoshikura, S.; Miura, M.; Fukuda, T.; Harada, A. Kaolin Deposits at Melthonnakkal and Pallipuram within Trivandrum Block, Southern India. *Gondwana Res.* **2006**, *9* (4), 530–538.

(91) Modabberi, S.; Ahmadi, A.; Tangestani, M. H. Sub-Pixel Mapping of Alunite and Jarosite Using ASTER Data; a Case Study from North of Semnan, North Central Iran. *Ore Geol. Rev.* **2017**, *80*, 429–436.

(92) Nageswara Rao, M.; Dikshitulu, G. R.; Desapati, T.; Krishnan, S.; Mir Azam Ali. A Strategic Placer Mineral Deposit Along Tandava-Varaha River Goastal Area, Visakhapatnam District, Andhra Pradesh. *JOAMS* **2001**, *7*.

Chapter 2

Hyperspectral analysis of Landsat 8 and ASTER data using spectral library of minerals

2.1. Abstract

Detailed analysis on grain size and mineralogy of beach sediments helps to understand their nature of deposition and potential targets of strategic mineral deposits. The beach sediments from the coast of Thiruvananthapuram, the southernmost district of Kerala, India, have been studied to understand the variation in grain size by using the spectral indices as derived from the visible-NIR-TIR bands of Landsat 8 and ASTER remote sensing data. Further, an attempt has been made to map the distribution of strategic minerals present in beach sands using standardized hyperspectral analysis techniques. The grain size shows a remarkable variation from medium sand to fine sand. The THM (Total Heavy Minerals) content was estimated to about 80.04% and 52.33% along the coast of Kovalam and Varkala, respectively. The ilmenite predominantly exists in these areas, followed by monazite, sillimanite, rutile, zircon, garnet, leucoxene, and Kyanite. The hyperspectral analysis extracts two endmembers of ilmenite and light minerals from the Landsat and ASTER imagery, which could be successfully, mapped using the SAM classification algorithm. The hyperspectral analysis applied to Landsat 8 OLI and ASTER could successfully derived the mineral occurrence of silica sand deposits in Cherthala (Kerala), kaolin clay deposits in Thonnakkal (Kerala), and baryte mine in Mangampet (Andhra Pradesh). The satellite-derived maps have been validated with the results of laboratory analysis and shows strong correlation almost in all locations. The present study illustrates the possible applications of satellite remote sensing techniques for exploring natural resources, especially mineral resources.

2.2.Introduction

The advent of advanced satellite image processing techniques and target recognition algorithms made a vital breakthrough in remote sensing applications for mapping mineral occurrences and lithological units. During the initial days of remote sensing, the multispectral remote sensing using Landsat imageries successfully used to map the mineral occurrences above the surface of the Earth.[1] Since 1972, the Landsat series of satellite data products are extensively used in exploring mineral deposits of altered rocks, gold-bearing sulphide rocks,

Li-bearing pegmatites, etc.[2–4] The Landsat 8 completely avoids the water vapour absorption features at 0.825µm of Landsat ETM+[5] which facilitates advanced exploration of clay minerals[6], gold[7], etc. Later other mineral deposits like clays, quartz, carbonates, silica, limestone, mafic rock units, gold occurrences were also identified using advanced multispectral dataset like ASTER.[7–11] Apart from these, remote sensing datasets with increased spatial, spectral, and temporal resolutions like Hyperion, Sentinel, etc. also make a significant contribution to mineral identification.[12] The improvements in satellite sensor technology paralleled with the development of image processing and classification algorithms available in the latest versions of remote sensing software packages made a breakthrough in mineral exploration. The remote sensing techniques for mineral exploration can be broadly classified into two categories of subpixel methods and spectrum matching techniques.[13] Subpixel based mapping methods are widely used for extracting solid information of mineral occurrences from multispectral and hyperspectral satellite data. Many researchers uses LSU, MTMF, and SVM for mapping alteration minerals.[14–18] The spectrum matching techniques like SAM, SVM, SFF, etc. measures the spectral similarity between the reference spectra measured in field or laboratory with the image spectrum derived from satellite imageries.[19,20] Before these, the linear transformation techniques like PCA, ICA, MNF, etc. removes the noise dominated bands by converting the multispectral bands into a set of uncorrelated image bands, which reduces the computational requirements for further processing.[21,22] The spectral classification of images can be successfully achieved using various classification algorithms like MTMF, SAM, SVM, and LSU, etc.[23,24] The widely used image enhancement techniques such as band ratios and spectral indices also help to quickly resolve mineral deposits of varying texture and composition.[9,25] The integration of results derived from various techniques like remote sensing, geophysics, geochemistry, and field data retrieves solid information regarding strategic mineral occurrences and their related host rock.

The beach sands of Kerala are richly bestowed with the presence of heavy minerals, predominantly with ilmenite followed by monazite, rutile, sillimanite, zircon, and garnet. Presently the high degree of weathering causes the alteration of ilmenite to leucoxene[26]. All these minerals are economically significant due to their critical applications in many diverse industries, especially the ilmenite from Chavara deposit in Kerala is World famous for high TiO_2 content. Many researchers have done a systematic analysis of grain size parameters and mineral composition of beach sediments, and also conducted detailed characterisation of beach minerals from the coast of Kerala.[27–30] The complex coastal processes such as waves,

currents, and tides were the actual governing factors behind the size of the sediment grain, and thereby, it determines the depositional environment of beach sediments. This variation in textural characteristics of sediments differentiates the sedimentary environments into beach, dune, and river.[31] Therefore, a systematic granulometric study using textural parameters derived from the beach sediments provides an idea of the nature and energy of agents responsible for the transport and deposition of sediments.

The present study aims to investigate the texture and mineralogy of beach sediments on the coast of Thiruvananthapuram district, Kerala, India using advanced remote sensing techniques. The grain size indices showing the texture of beach sediments were generated using the visible, NIR, and TIR bands of Landsat and ASTER imageries. An attempt has been made to use the advanced hyperspectral analysis techniques followed by SAM and MTMF classification for identifying silica sand deposits (Cherthala, Kerala), kaolin deposits (Thonnakkal, Kerala), and baryte mineral deposits (Mangampet, Andhra Pradesh) from Landsat and ASTER remote sensing datasets.

2.3.Materials and Methods

The flow sheet showing the proposed methodology for mapping the variation in grain size and distribution of beach minerals is shown in Figure 2.1.

2.3.1. Fieldwork and Laboratory analysis

Beach samples were collected to a depth of 1m from 69 sampling stations located at an interval of approximately 1km along the coastline of Thiruvananthapuram district during the pre-monsoon months of March and April. The heavy mineral analysis was carried out for the 1m depth samples, whereas the textural analysis was carried out in a more detailed manner by subdividing the 1m depth samples at 30cm interval and named as “Top”, “Middle” and “Bottom”. Pre-treatment of the collected samples was carried out prior to sieving the samples through ASTM sieves of +18 to +230 mesh sizes (0.5ϕ intervals) using a gyratory sieve shaker.[32] The cumulative weight percentage frequencies of the sieved materials were computed.[33] The textural parameters were determined using the GRAIN software package. All these statistical methods help to understand even the finer differences that may exist within a particular environment of the same geography.[34]

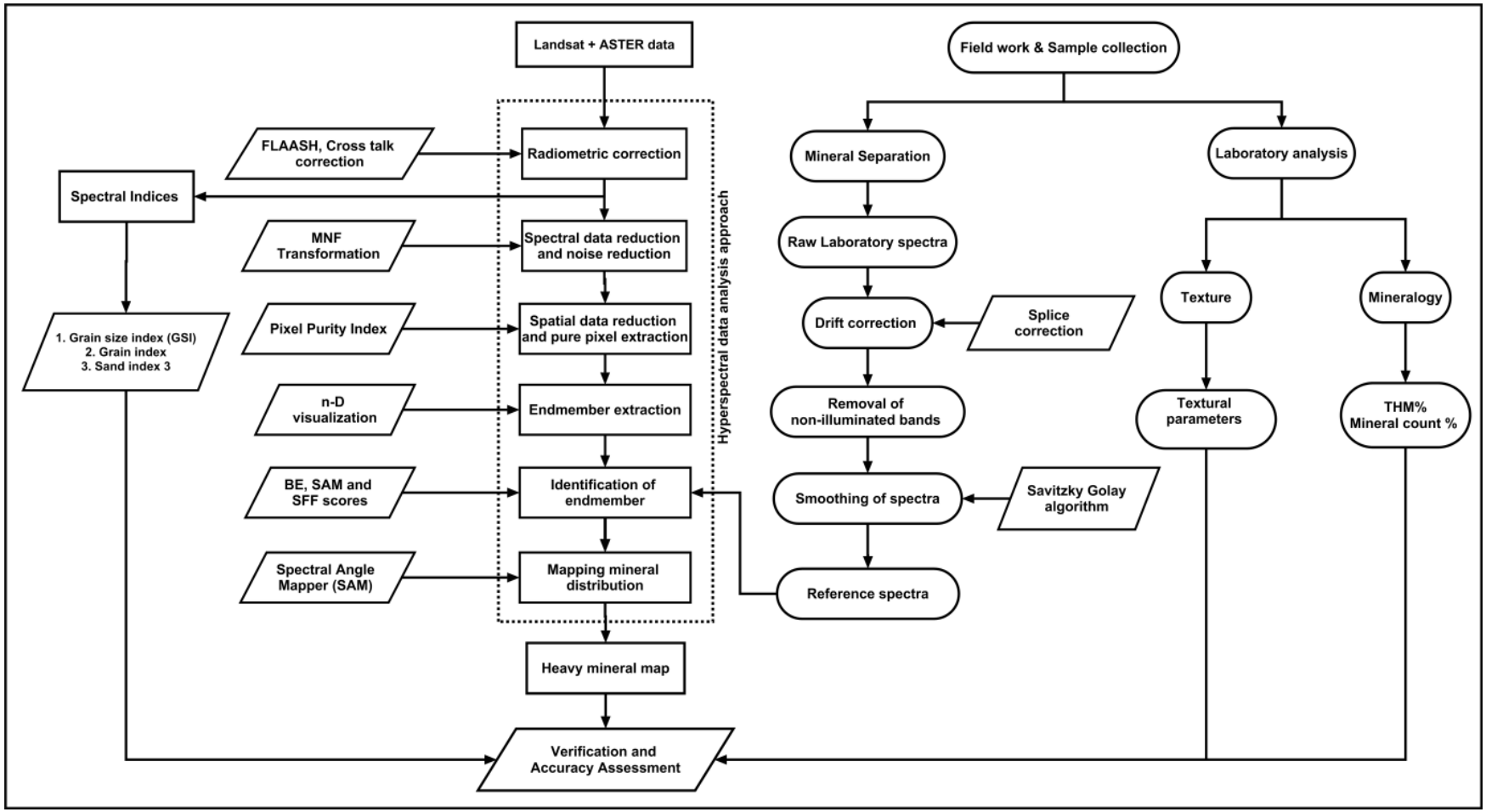

Figure 2.1: Flow diagram of the proposed methodology for mapping the texture and mineralogy of beach sediments.

Separation of heavy minerals from the pre-processed beach sands were carried using bromoform, having a specific gravity of 2.89.[35] Then the grains were subjected to grain counting using Leica petrological microscope for estimating the relative abundances of individual heavy minerals.[36]

In general, IDW with a power factor of 2 is widely used in interpolating with lower prediction error compared to kriging when the number of samples is relatively lesser.[37,38] Spatial variation of total heavy minerals (THM), individual mineral concentration, and also the texture of the beach sediments along the Indian coast were mapped using Inverse Distance Weighted (IDW) interpolation technique.[39,40] Moreover, the predicted values obtained from the widely used interpolation techniques IDW, OK, RBF, and LPI are validated against laboratory data using the statistics such as R^2 , RMSE, and MAE values.[41] The best parameters were selected for the interpolation techniques. The power factors of 1 and 2 were used for IDW. Three semivariograms like circular, exponential, and spherical were used for OK. The regularized spline was selected for RBF, and exponential kernel function was used for LPI. The ArcGIS software is used for generating surface maps showing texture and mineralogy using various interpolation techniques and map generation.

2.3.2. Separation techniques for mineral recovery

Representative raw placer samples of 20 Kg each collected up to a depth of about 1m from Kappil-Varkala (KV) and Sanghumugham – Kovalam (SK) coastal stretches were processed to separate and estimate heavy minerals from the bulk beach sand. A series of mineral separation techniques which include magnetic, electrostatic and gravity methods are used for recovering heavy minerals. Suitable separation techniques were adopted based on the physical properties of minerals. Figure 2.2 shows the flow sheet for the mineral recovery from the beach sands. Laboratory model Carpco rare earth drum magnetic separator, Readings induced roll magnetic, Orekinetics CoronaStat high-tension separator, Mineral Technologies electrostatic plate separator and Mineral Technologies short spiral concentrator separator were used in this study. The samples were weighed and analysed using Leica petrological microscope at the start of the exercise and also at different stages during the process which helps to estimate the weight percentages and also to identify the individual minerals.

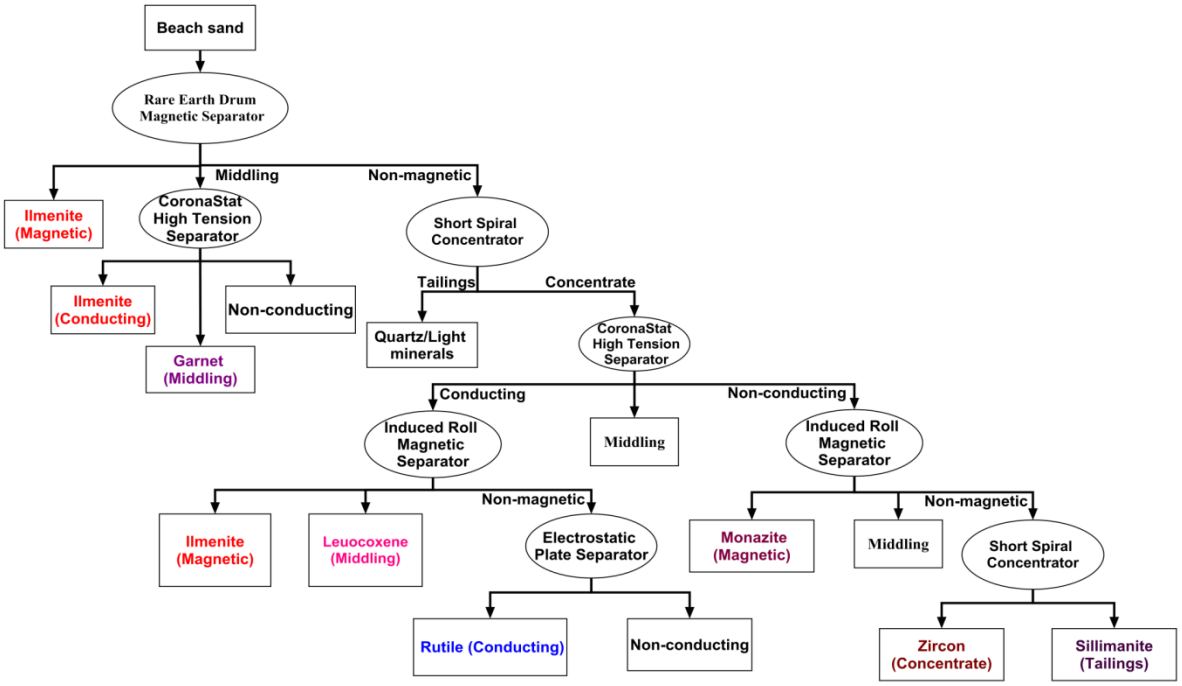

Figure 2.2: Flow sheet showing the recovery of heavy minerals from the beach sands.

The high content of magnetic ilmenite in the raw sand samples suggested the use of rare earth drum magnetic separator. The middlings were collected and subjected to electrostatic separation using CoronaStat high tension separator which separates the remaining magnetic and conducting ilmenite fractions in the bulk sample. The middlings from the CoronaStat high tension separator were again passed through rare earth drum magnetic separator for recovering less magnetic and less conducting garnet. The non magnetic minerals from rare earth drum magnetic separator are fed through a gravity concentration unit, typically known as short spiral concentrator. It effectively separates the remaining heavy minerals from the sand and produces HMC. The HMC was divided into conducting and non conducting fractions, and then passed through a CoronaStat high tension separator. The conducting fractions contain ilmenite, rutile, and leucoxene. These fractions were separated individually by passing through induced roll magnetic separator and electrostatic plate separator. The non conducting fractions may contain monazite, zircon and sillimanite. The non-conducting and magnetic fractions of monazite were recovered by subjected to induced roll magnetic separator. The non magnetic fractions of zircon and sillimanite were separated using gravity method because of their difference in specific gravities. The zircon has high specific gravity compared to sillimanite so they were recovered by passing through short spiral concentrator. The concentrate obtained contains zircon and

tailings contain sillimanite fractions. Further it can be separated in lab using diidomethane liquid having a density of 3.31 g/cc.

The Mineralogical modal analysis was carried out using a Leica petrological optical microscope for estimating count percentages of mineral of interest and other contaminants in the recovered mineral fraction after the separation. The mineral counting had been accomplished by following the method of line counting.[36] The different counts have been converted into percentages and the values were tabulated.

2.3.3. Textural analysis using spectral indices

Retrieval of textural parameters from satellite remote sensing data using Topsoil grain size index (GSI), Normalized Difference Snow Index (NDSI), Asymptotic Radiative Transfer (ART) theory, etc. have been developed for monitoring land desertification and snow cover mapping.[42,43] Here, the visible-NIR-TIR regions of Landsat and ASTER data were used for generating grain size indices showing the clear discrimination in the texture of beach sand. Atmospheric correction and radiometric calibration of Visible, SWIR, and NIR bands of Landsat 8 and ASTER L1B were done using FLAASH modules in the software package ENVI. The atmospheric contributions to thermal infrared radiance data of ASTER image were eliminated using the Thermal Atmospheric Correction technique, and the emissivity is retrieved using the Emissivity Normalization technique. Then the spectral indices such as (i) topsoil grain size index (GSI) (Eq.2.1), (ii) Grain index map (Eq.2.2), and (iii) Sand Index 3 (Eq.2.3) were derived using Visible, SWIR and NIR bands of Landsat 8 and ASTER L1B. All image processing analysis, such as atmospheric correction, textural indices, and hyperspectral analysis were carried out using image processing software ENVI (https://www.harrisgeospatial.com/Software-Technology/ENVI).

The topsoil grain size index (GSI) calculated using the visible bands of the Landsat 8 image clearly discriminates the topsoil with varying grain size.[44]

$$\text{Grain size index (GSI)} = \frac{(B_4 - B_2)}{(B_4 + B_2 + B_3)} \qquad (2.1)$$

where B_2, B_3, and B_4 correspond to blue, green, and red bands of Landsat 8 imagery. The GSI value is near to 0 for the vegetated area, and negative for water bodies.

The Grain index map derived using NIR- SWIR bands of ASTER also helps to discriminate the topsoil with varying grain size.[45,46]

$$\text{Grain Index} = \frac{(B_3 - B_6)}{(B_3 + B_6)} \quad (2.2)$$

where B_3 and B_6 correspond to NIR and SWIR bands of ASTER.

Finally, the TIR bands of ASTER data were also used for deriving the Sand Index, showing the variation in the texture of the sand.[47]

$$\text{Sand Index 3} = \frac{(3 * B_{13})}{(B_{10} + B_{11} + B_{12})} \quad (2.3)$$

where B_{10}, B_{11}, B_{12}, and B_{13} is the emissivity of the given ASTER thermal bands.

2.3.4. Building spectral library of beach minerals

The spectral data of all heavy and light minerals present in the beach sediments of the study area were measured using ASD Fieldspec® 3 spectroradiometer. It records the reflectance values in the ranges of VNIR (350–1000 nm) at a spectral resolution of 3nm and SWIR (1000–2500 nm) at a spectral resolution of 10 nm, respectively.[48] About 150gm of each mineral species were made spread on a black cloth covering the FOV of Fieldspec ® 3's sensor and illuminated using a tungsten filament halogen lamp, which provides a consistent energy source in the range of 400–2500 nm.[49]

Post-processing of collected spectra includes splice correction, removal of measurements ranges in the wavelength of 350nm to 400nm, and smoothing of the spectra. The spectral drifts at 1001 and 1831 nm were corrected using the splice correction function of ASD Viewspec Pro™.[50] The splice correction function generates a new point using the average of tangents at either side of breakpoints for the line to pass through without drift [51]. Since the halogen lamp used as the source of illumination radiates energy in the range of 400 to 2500nm, the spectral measurements range in the wavelength of 350nm to 400nm were removed. The sensor inherent noises were removed by applying a smoothing filter to the data. Savitzky–Golay smoothing algorithm with an optimal degree of polynomial order of 2 and a filter size of 15, which maintains the actual slope of the spectra is used for smoothing the spectra.[49] The mean spectra in ASCII format consist of wavelength, and full-width half-maximum values are imported to the ENVI software for building the spectral library of beach

minerals. The spectral library of minerals was validated using the scores obtained for spectral matching techniques. The spectral matching techniques such as SAM, SFF, and BE are used for comparing the laboratory spectra of minerals with the USGS spectral library. A weight value of 1 is applied to each algorithm.

2.3.5. Hyperspectral analysis of ASTER and Landsat 8

Hyperspectral analysis of ASTER and Landsat 8 data is used for mapping the heavy minerals. Many researchers have successfully integrated multispectral data and hyperspectral techniques for mapping potential mineral occurrences. Using hyperspectral techniques, Masoumi et al. delineated hydrothermally altered areas using Landsat-7, Landsat-8, and ASTER data[4,52], Pal et al. used Landsat ETM+ for mapping minerals over Dalma and Dhanjori in Jharkhand, India.[53] Yousefi et al. mapped alteration minerals (kaolinite, alunite, and quartz) using ASTER data[7]. It is a multi-fold spectral analysis technique consists of six continuous processes such as (i) reflectance calibration and atmospheric correction, (ii) spectral data reduction and noise reduction using minimum noise transformation, (iii) extraction of pure pixels using pixel purity index (PPI), (iv) extraction of endmembers, (v) identification of endmembers using spectral matching techniques, (vi) mineral mapping using classification algorithms.[53] All these techniques were applied to Landsat 8 and ASTER individually for mapping the beach minerals. The complete analysis was carried out using the Spectral hourglass wizard in ENVI software. The FLAASH atmospherically corrected, and reflectance calibrated bands of Landsat and ASTER data were linearly transformed using minimum noise fraction (MNF) transformation for removing the noisy bands and thereby minimizes the spectral dimensionality.[54] Here the highly informative lower MNF bands with least noises will be selected based on the eigenvalues calculated using the noise statistics of the input data. The Pixel purity index (PPI) reduces the spatial dimensionality of the bands by separating the spectrally pure pixels from MNF bands. It generates a PPI image, which clearly shows the pure pixels as bright. These pure pixels are used for generating the spectrally unique target members or endmembers using the n-D visualizer. In the n-D visualizer, the clouds of pure pixels lie at the corners of n-D scatter plot are rotated in different orientations for extracting the target members.[55]

The extracted endmembers are assigned to a particular class of minerals by comparing the image spectra with the spectral library of heavy minerals using spectral matching techniques like SFF, SAM, and BE. Spectral matching algorithms are mainly classified into two types,

(i) deterministic, and (ii) stochastic. The SFF, SAM, and BE come under deterministic in which the geometry and physical aspects of the spectra were considered for calculating the matching.[56] The SAM uses the spectral angle between the image spectra and reference spectra for measuring their similarity, irrespective of their invariance in scale and illumination. SFF is a least-squares technique that uses unique absorption features for measuring the similarity, irrespective of their illumination, and variations in grain sizes. BE uses binary codes of descriptors depicting the spectral and spatial properties of the spectra for matching with the target code.[57] Finally, the true endmembers of the minerals are mapped using spectral classification techniques.

2.3.6. Spectral Angle Mapper (SAM) classifier

The similarities in spectral properties exist between image-derived spectra, and the reference spectra were measured using a spectral angle called n-D angle.[58,59] For measuring the n-D angle, both the spectra were treated as unit vectors in n-dimensional space, and the SAM algorithm measures the angle between them as

$$\theta = \cos^{-1}\left(\frac{\sum_{i=1}^{n} m_i r_i}{\left(\sum_{i=1}^{n} m_i^2\right)^{1/2}\left(\sum_{i=1}^{n} r_i^2\right)^{1/2}}\right) \qquad (2.4)$$

where m is image spectrum, r is reference spectrum, and n represents number of bands in the image. Smaller the spectral angle θ, closer the image spectra to the reference spectra. The accuracy of the proposed methodology for mapping the heavy minerals was accessed using the overall accuracy and kappa coefficient obtained from error matrix calculation. The laboratory results of the textural and mineralogical analysis were used for generating the error matrix.[60] The Kappa coefficient is estimated using entire elements of the error matrix, whereas the diagonal elements are only taken for finding the overall accuracy.[61]

2.3.7. Mixture Tuned Matched Filtering (MTMF)

The true endmembers derived from the satellite data are also mapped using MTMF technique. MTMF is one of the effective image processing technique as well as a partial unmixing process used for mapping minerals that shows remarkable differences from their background.[62,63] It integrates two methods such as matched filter (MF) method and linear spectral mixing theory, therefore possess the advantages of two methods. No prior knowledge regarding the background spectral signature is required for the processing (matched filter

(MF)). The linear combination of individual components exists in each pixel gives spectral signature for that particular pixel (linear spectral mixing theory). Apart from this, it reduces the weakness of individual methods also.[14,64] High and low values for MF and infeasibility ranges from 1 to 0 represents closer matches and indicates high probability for mineral occurrences.[63] Pal et al. successfully delineate alteration minerals from Landsat ETM+ image using MTMF.[53] Moreover, the alteration minerals associate with porphyry copper Deposits were also delineated from Landsat-8 bands[65] and ASTER data.[14]

2.4.Results and Discussion

The textural parameters and weight percentages of heavy mineral species were determined using laboratory analysis. Spectral indices and hyperspectral analysis techniques were used to derive the maps showing the texture and mineralogy of beach minerals, which were cross-validated using laboratory analysis.

2.4.1. Recovery of heavy minerals

The petro-mineralogical analysis of the sample indicates that the sample mainly contains ilmenite followed by sillimanite, zircon, garnet, rutile, monazite and leucoxene. Flow sheets shown in Figure. 2.3 and Figure. 2.4 were also suggested with material balance on the recovery of heavy minerals. The mineralogical assemblage, yield, grade and recovery of the minerals have been tabulated in Table 2.1 and Table 2.2. The feed samples from KV and SK stretches are subjected to a series of separation techniques for recovering the heavy minerals. The data indicate that overall recovery of total heavy minerals is 67.3% and 65.15% for Kappil-Varkala (KV) and Shanghumugham-Kovalam (SK) coastal stretches. The major mineral recovered from the coastal stretch of KV is ilmenite (45.55% yield) followed by sillimanite (8.75%), monazite (5.1%), zircon (2%), rutile (1.3%), leucoxene (0.9%), and garnet (0.05%). The major mineral recovered from the coastal stretch of SK is also the ilmenite (43.6% yield) followed by sillimanite (9.9%), zircon (2.8%), monazite (1.7%), rutile (1.05%), leucoxene (2.6%), and garnet (0.95%). At certain stages of process, small quantities of heavy mineral samples with major content of ilmenite and sillimanite were also obtained which were totally estimated to about 3.65% and 2.55% for KV and SK.

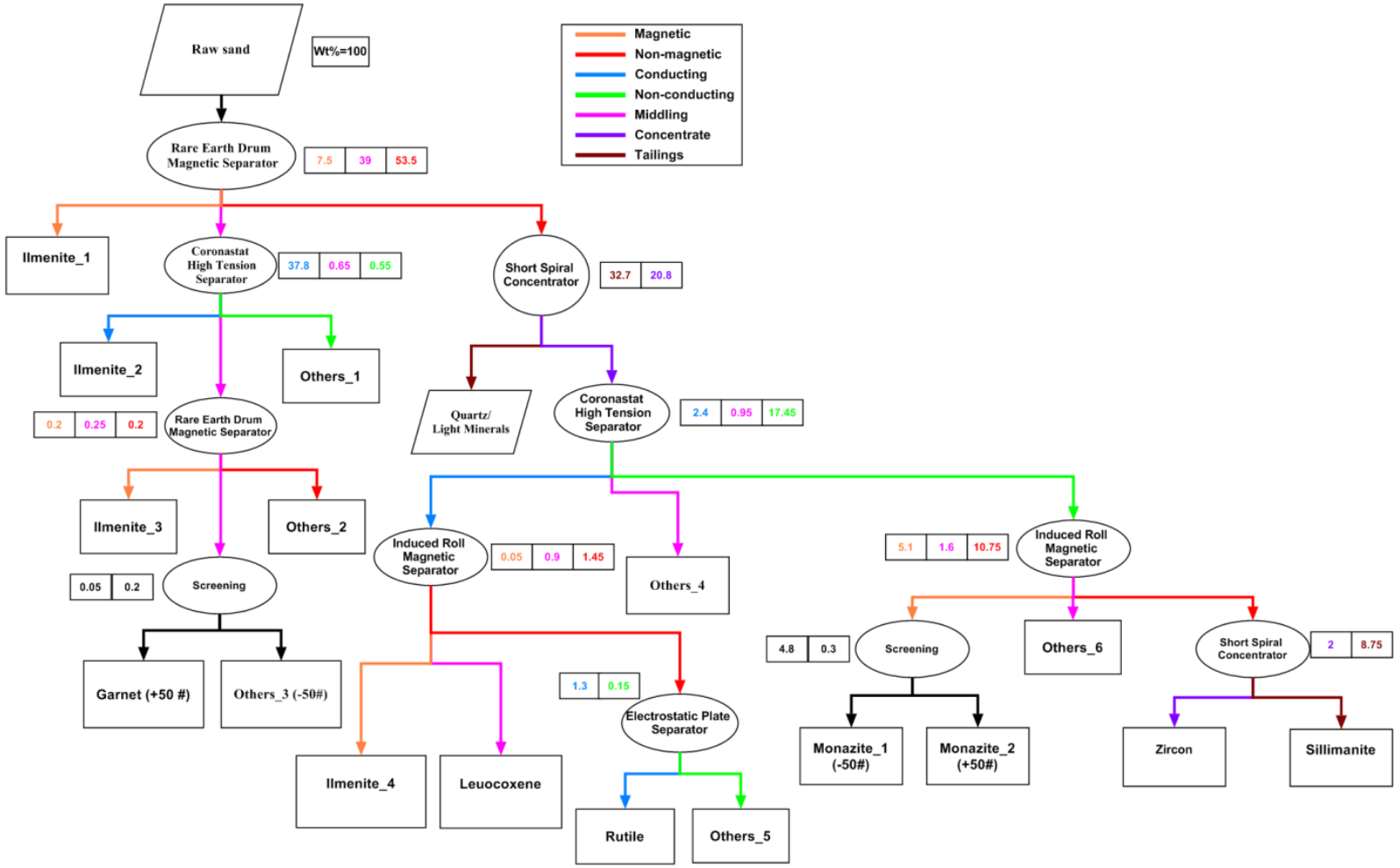

Figure 2.3: Flow sheet with material balance showing the recovery of heavy minerals from the beach sands of Kappil-Varkala Coast.

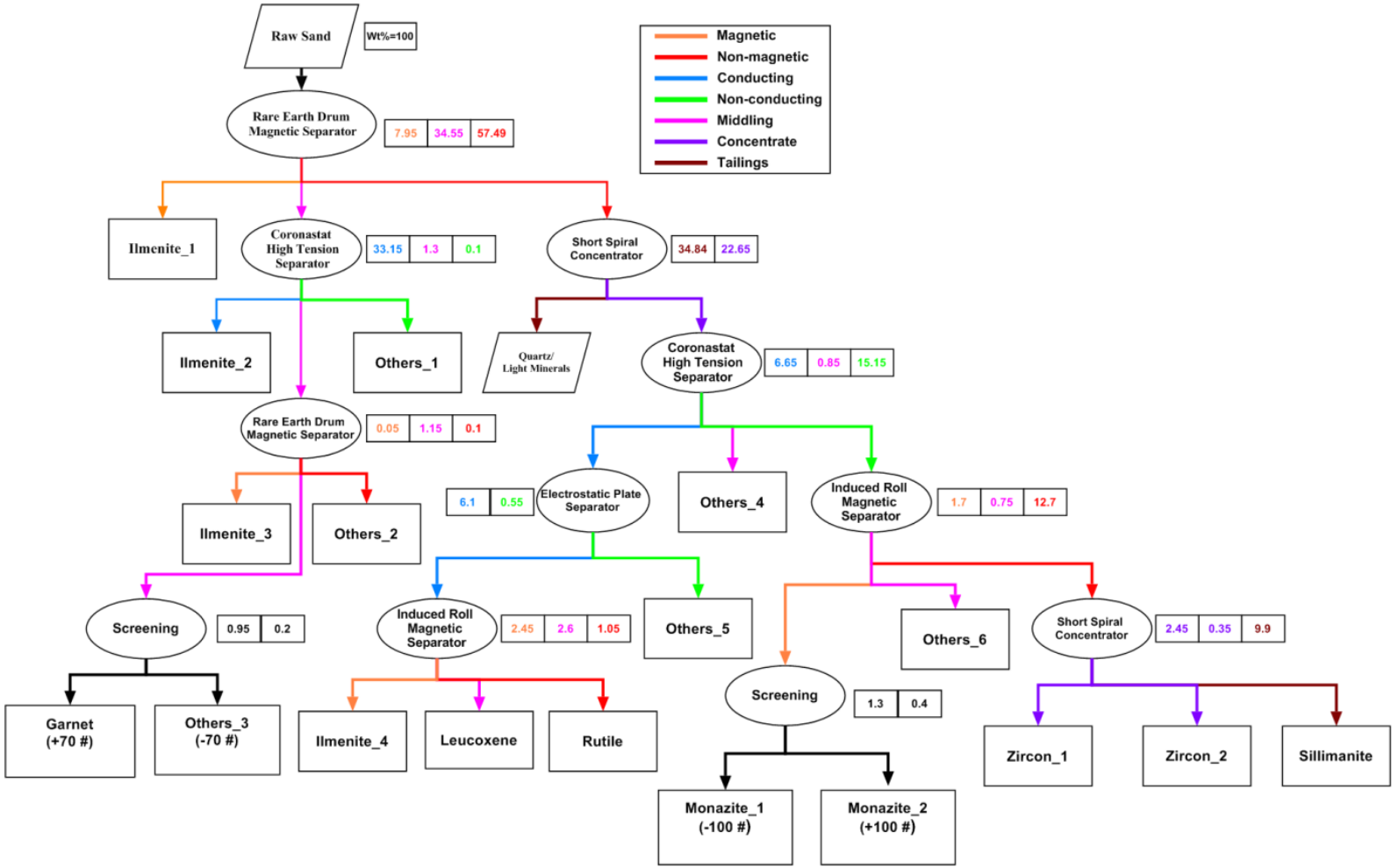

Figure 2.4: Flow sheet with material balance showing the recovery of heavy minerals from the beach sands of Shanghumugham-Kovalam Coast.

Table 2.1: Heavy minerals recovered from the beach sediments of Kappil-Varkala Coast

Heavy Minerals	**Mineral Composition (Grade %)**				**Yield (%)**	**Recovery (%)**
Ilmenite_1	Ilmenite (100)				45.55	97.02
Ilmenite_2	Ilmenite (100)					
Ilmenite_3	Ilmenite (100)					
Ilmenite_4	Ilmenite (100)					
Monazite_1	Monazite (98.12)	Ilmenite (1.88)			5.1	99.98
Monazite_2	Monazite (91.24)	Ilmenite (8.75)				
Sillimanite	Sillimanite (75.90)	Zircon (17.94)	Quartz (6.16)		8.75	75.11
Zircon	Zircon (93.16)	Sillimanite (6.84)			2	50.96
Rutile	Rutile (91.48)	Sillimanite (6.2)	Zircon (2.32)		1.3	99.48
Leucoxene	Leucoxene (90.1)	Monazite (8.52)	Sillimanite (1.38)		0.9	92.26
Garnet	Garnet(88.24)	Ilmenite (9.29)	Monazite (2.47)		0.05	52.13
Others_1	Sillimanite (55.51)	Ilmenite (36.02)	Leucoxene (8.48)		3.65	
Others_2	Sillimanite(86.26)	Zircon (7.17)	Kyanite (5.32)	Garnet (1.24)		
Others_3	Ilmenite (91.88)	Garnet (8.12)				
Others_4	Ilmenite (84.07)	Sillimanite (9.15)	Zircon (4.57)	Leucoxene (2.21)		
Others_5	Ilmenite (68.92)	Sillimanite (26.93)	Rutile (4.14)			
Others_6	Sillimanite (84.80)	Zircon (7.93)	Kyanite (5.89)	Garnet (1.37)		
Total Weight (%)					**67.3**	

Table 2.2: Heavy minerals recovered from the beach sediments of Shanghumugham-Kovalam coast

Heavy Minerals	Mineral Composition (Grade %)				Yield (%)	Recovery (%)
Ilmenite_1	Ilmenite (100)				43.6	96.42
Ilmenite_2	Ilmenite (100)					
Ilmenite_3	Ilmenite (100)					
Ilmenite_4	Ilmenite (100)					
Monazite_1	Monazite (95.51)	Ilmenite (4.49)			1.7	82.17
Monazite_2	Monazite (68.03)	Ilmenite (31.97)				
Sillimanite	Sillimanite (65.64)	Kyanite (10.94)	Zircon (10.44)	Quartz (12.98)	9.9	90.9
Zircon_1	Zircon (100)				2.8	57.66
Zircon_2	Zircon (91.13)	Kyanite (7.52)	Sillimanite (1.35)			
Rutile	Rutile (91.15)	Zircon (8.85)			1.05	94.75
Leucoxene	Leucoxene (92.14)	Garnet (2.74)	Ilmenite (5.12)		2.6	97.95
Garnet	Garnet (90.86)	Ilmenite (7.26)	Rutile (1.88)		0.95	87.76
Others_1	Sillimanite (67)	Ilmenite (28.30)	Kyanite (4.71)		2.55	
Others_2	Sillimanite (82)	Ilmenite (13.07)	Sphene (4.94)			
Others_3	Garnet (49.38)	Ilmenite (33.16)	Monazite (11.76)	Zircon (5.70)		
Others_4	Ilmenite (87.28)	Sillimanite (6.92)	Leucoxene (4.01)	Garnet (1.79)		
Others_5	Ilmenite (90.70)	Rutile (6.38)	Leucoxene (2.02)	Garnet (0.90)		
Others_6	Sillimanite (58.40)	Monazite (41.60)				
Total Weight (%)					**65.15**	

From Table 2.1 and Table 2.2, it is observed that high grades of ilmenite, rutile, leucoxene, zircon, garnet, and monazite were recovered from the beach sands of both the study areas. The sillimanite fractions associated majorly with zircon, kyanite and quartz which can be reprocessed for the recovery of individual mineral concentrates by judicious combination of gravity and flotation processes. Ilmenite along with other heavy minerals like sillimanite, monazite, rutile, zircon, leucoxene, and garnet are the important constituents of beach sand deposits. Initial separation of magnetic minerals like ilmenite and monazite followed by the concentration of other mineral constituents using spiral column and other magnetic and electrostatic separation techniques seemed to be the best route for recovering strategic minerals from the beach sand. The results show that effective recovery of high-grade heavy minerals can be achieved by judicious combination of magnetic, electrostatic, and gravity separation techniques. Previous studies on mineral recovery focuses only on particular categories of minerals like titanium bearing minerals and rare-earth minerals.[66–68] Here we have developed a process flow connecting a series of mineral separation techniques for the successful recovery of seven important heavy minerals of different magnetic and conducting properties from a single feed.

2.4.2. Grain size parameters and bivariant plots

The textural parameters like mean (Mz), sorting (SD), skewness (Ski), and kurtosis (KG) were meticulously used for studying the sediment transport processes as well as the depositional mechanisms in various environments.[69–72] The coastal geomorphology and sedimentology of beach sediments are two critical factors determining the depositional environments of a coastal region.[73] The grain size parameters were calculated for the top, middle, and bottom portion of samples collected from a depth of 1metre from 69 sampling stations, and the values were interpolated using IDW spatial interpolation technique. The maps showing the variation in the grain size statistical parameters were given in Figure 2.5. Samples collected from Perumathura and Poovar regions show coarse to medium-sized grain size, whereas the grain size for the samples from Varkala and Kovalam ranges from medium to fine. The sorting values range from well-sorted to moderately sorted. All the sectors show dominance in strongly coarse skewed to very finely skewed nature, whereas the kurtosis values are dominated from very platykurtic to very leptokurtic.

The Figure 2.6 shows the bivariant plots drawn using the textural parameters. Actually, these plots help to understand the fluid –flow mechanisms result in the movement

and deposition of beach sediments.[74] In the mean versus (Vs.) sorting diagram, clustering can be observed in medium-sized and moderately well sorted. Since the mean size and sorting of sediment grains are hydraulically controlled, the most excellent sorting is always shown by sedimentary environments dominated by fine sized grains. The sorting Vs. skewness diagram clearly depicts that the sediments are moderately well sorted and near symmetric towards the medium fraction. The skewness Vs. kurtosis diagram shows that the majority of the sediments are positively skewed and ranges from lepto to platykutic. The positive skewness indicates the domination of medium-sized grains with subdues of coarse and fine-sized grains.[32] Negative skewness is shown by sediments consists of a small amount of coarser grains.[75] At the same time, the positively or negatively skewed sediments show leptokurtic in nature.[76] Most of the beach sediments collected from the study area also contain one predominant population of medium-sized grains for Perumathura and Poovar sectors except Varkala and Kovalam sectors in which fine sized grains predominantly exist. The change in grain size from coarse to fine leads skewness from negative to positive.

Coastal geomorphology and fluctuation in the physicochemical conditions due to marine interactions are the main factors causing variation in wave energy conditions and thereby variation in textural patterns of beach sediments. In high wave energy environments, the strong winnowing action of waves results in the removal of fine sediments and results in coarser to medium-sized sediments. The positively skewed sediments also indicate low energy condition, whereas the negatively skewed sediments show high energy waves with winnowing action.[77]

In the present study area, the sediments from Varkala and Kovalam show fine-sized, whereas the sediments collected from Perumathura and Poovar show coarse to medium-sized. The beach sediments collected from most of the locations in Kovalam are finer compared to the Varkala region. It further suggests that high wave energy conditions prevail in Permathura and Poovar regions, which results in the strong winnowing of finer sediments. Figure 2.7 developed using sediment trend matrix analysis of McLaren clearly shows the movement and transport of beach sediments.[78] The sediment trend matrix analysis uses representative samples from four important locations, such as Varkala (sampling points 1 to 7), Perumathura (22-24), Kovalam (45-50), and Adimalathura-Poovar (55-57). Total deposition (Case I) and selective deposition (Case III) were noticed for the present study area. If the deposit is finer, better sorted and more negatively skewed than the source, then total

deposition of sediments takes place which is considered as Case I. In case of selective deposition, the deposit is seemed to be finer (Case IIIA) or coarser (Case IIIB), better sorted and more positively skewed than the source.[79,80] The textural analysis clearly shows that the sediments of Kovalam followed by Varkala are finer, well-sorted, or moderately sorted in nature. The sediments of Adimalathura-Poovar coast, followed by Perumathura regions, shows coarse-medium sized grain texture. These results in the deposition of more fine sediments in Kovalam-Varkala regions compared to other areas, which are clearly shown in Figure 2.7.

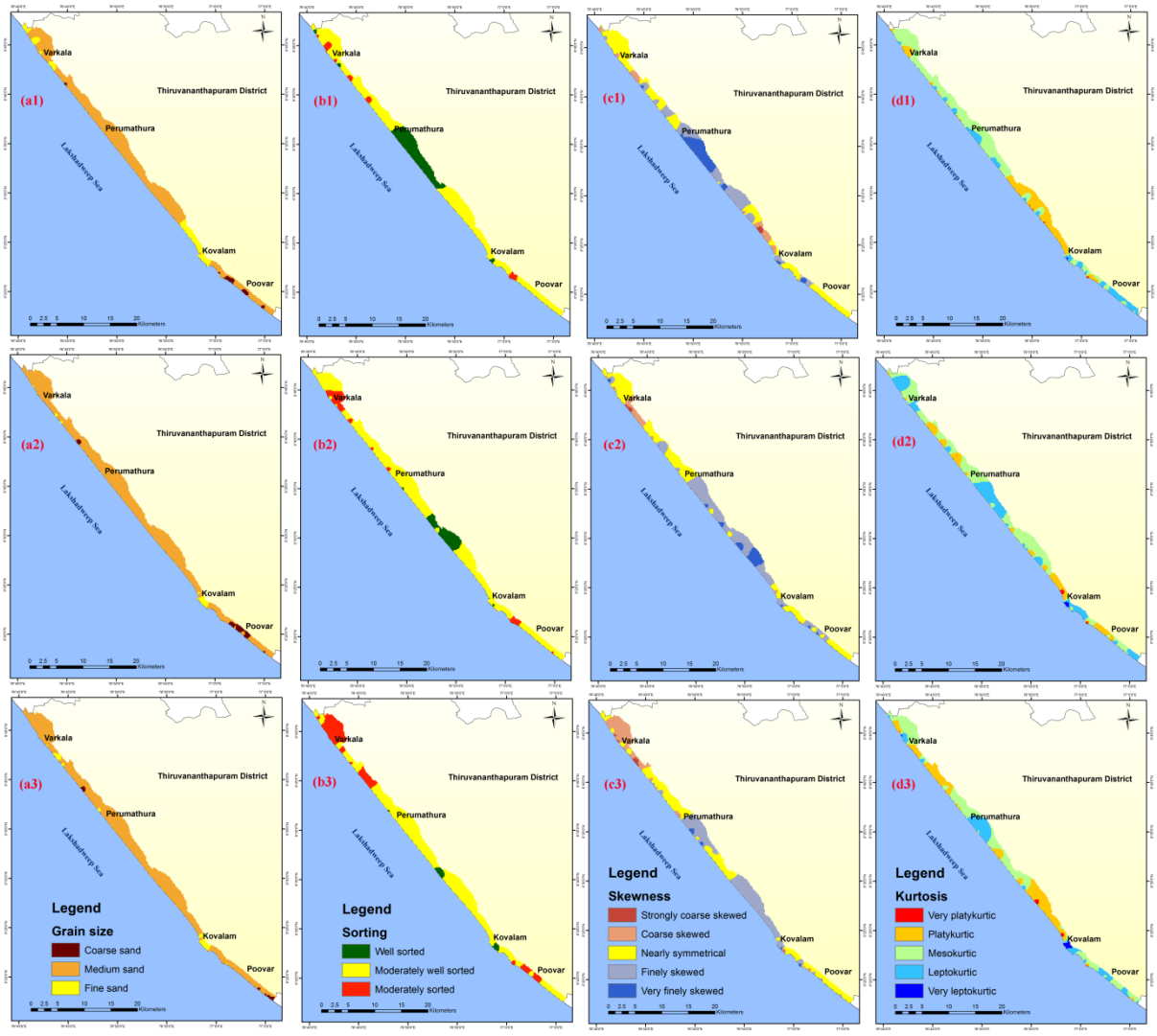

Figure 2.5: Maps showing the variation in the grain size statistical parameters according to Top, Middle and Bottom samples. (a1-a2) Graphic mean; (b1-b3) Graphic standard deviation; (c1-c3) Inclusive graphic skewness; (d1-d3) Graphic kurtosis.

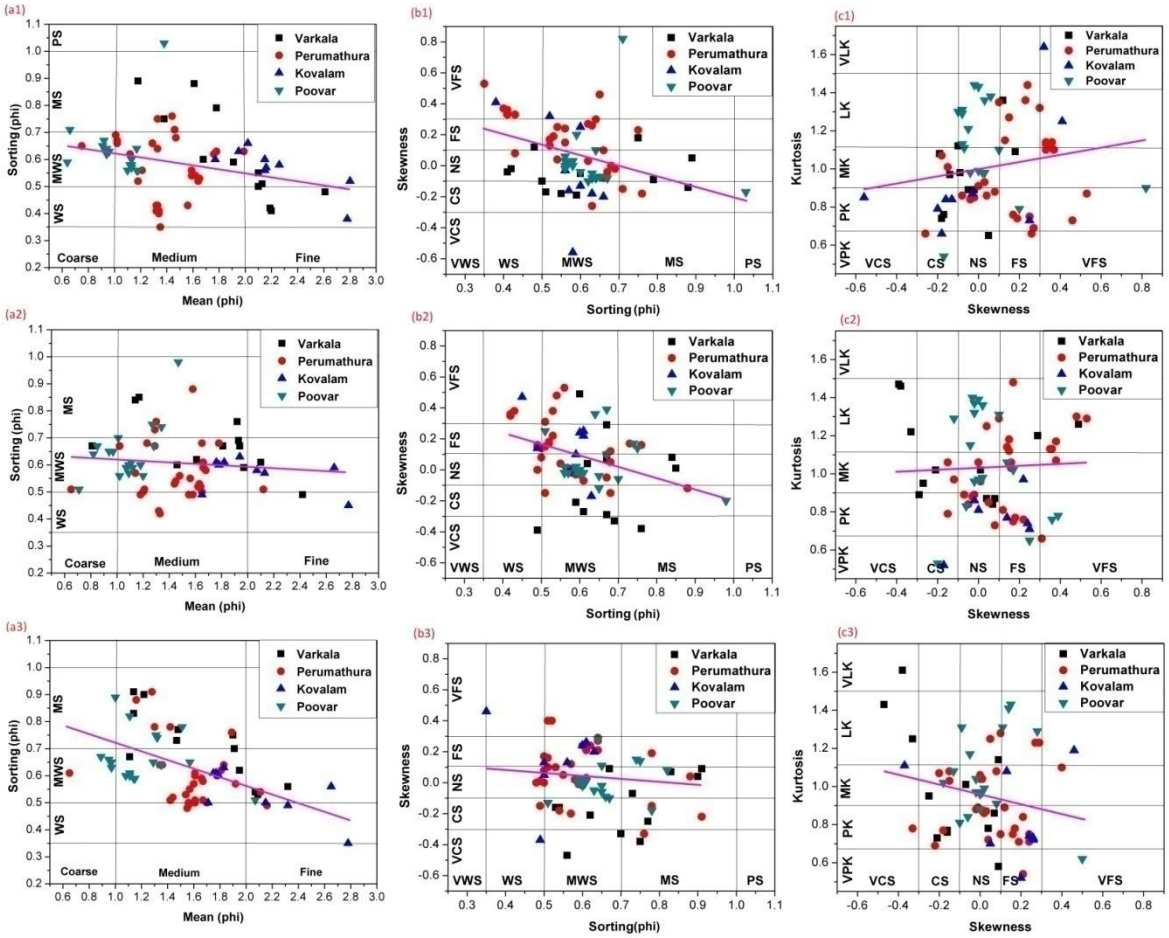

Figure 2.6: Bivariant plots showing the relationship between grain size, sorting, skewness and kurtosis of Top, Middle and Bottom samples. (a1-a3) Mean Vs Sorting corresponds to Top, Middle and Bottom samples; (b1-b3) Sorting Vs Skewness corresponds to Top, Middle and Bottom samples; (c1-c3) Skewness Vs Kurtosis corresponds to Top, Middle and Bottom samples (WS-Well sorted, MWS-Moderately well sorted, MS-Moderately sorted, PS-Poorly sorted, VPK- Very Platykurtic, PK-Platykurtic, MK-Mesokurtic, LK-Leptokurtic, VLK-Very Leptokurtic, VCS-Very Coarse skewed, CS-Coarse skewed, NS-Nearly symmetrical, FS-Finely Skewed, VFS-Very Finely Skewed).

During the south-west monsoon months of June to September, the beach gets eroded due to strong and steep waves. During the time of monsoon, the zero-crossing wave periods were in the range of 5.3 to 13.1s, and the wave direction varied from 220–254. The Valiathura experiences a wave height of 0.78-3.3m.[81] But during the time of fair seasons (November to April), the wave height is low (below 1m).[82] The wave direction varied from 199 to 214. The wave angle actually determines the transport of the sediments. The sediment transport is southwards from June to August and is towards the north for the rest of the year.

So the net transport of the sediments is towards the north, and it's about (0.72–1) × 10^5 m^3/year.[83,84] These are clearly shown in Figure 2.7 where the net movement of fine sediments is towards the north. Sajeev et al. analyzed the daily and monthly wave breaker height and confirmed that the coast of Thiruvananthapuram is an open coast exposed to high wave energy conditions.[85] After the monsoon, the beach building starts, which is a slow process compared to erosion. During the period of 1989–2006, it was reported that the Adimalathura and Perumathura regions experienced a serious accretion whereas the Panathura–Poonthura–Bhimapalli-Kovalam coastal sectors experience major erosion.[84,86] Two major coastal plains, such as Pudukuruchi-Poonthura in the north and Adimalathura-Pozhiyur in the south, are characteristically formed by coarse-medium sized grains. The Vizhinjam–Kovalam coastal stretch is occupied with rocky headlands, but lateritic cliffs are seen in Edava –Varkala beaches. The characteristic features like high energy waves, medium-fine sized texture, steep beach face, and the structural interventions such as gyrones, breakwaters, seawalls, etc. termed as 'artificial morphologies' by Thankappan et al. are the main factors causing the deposition and erosion of coastal sediments.[86]

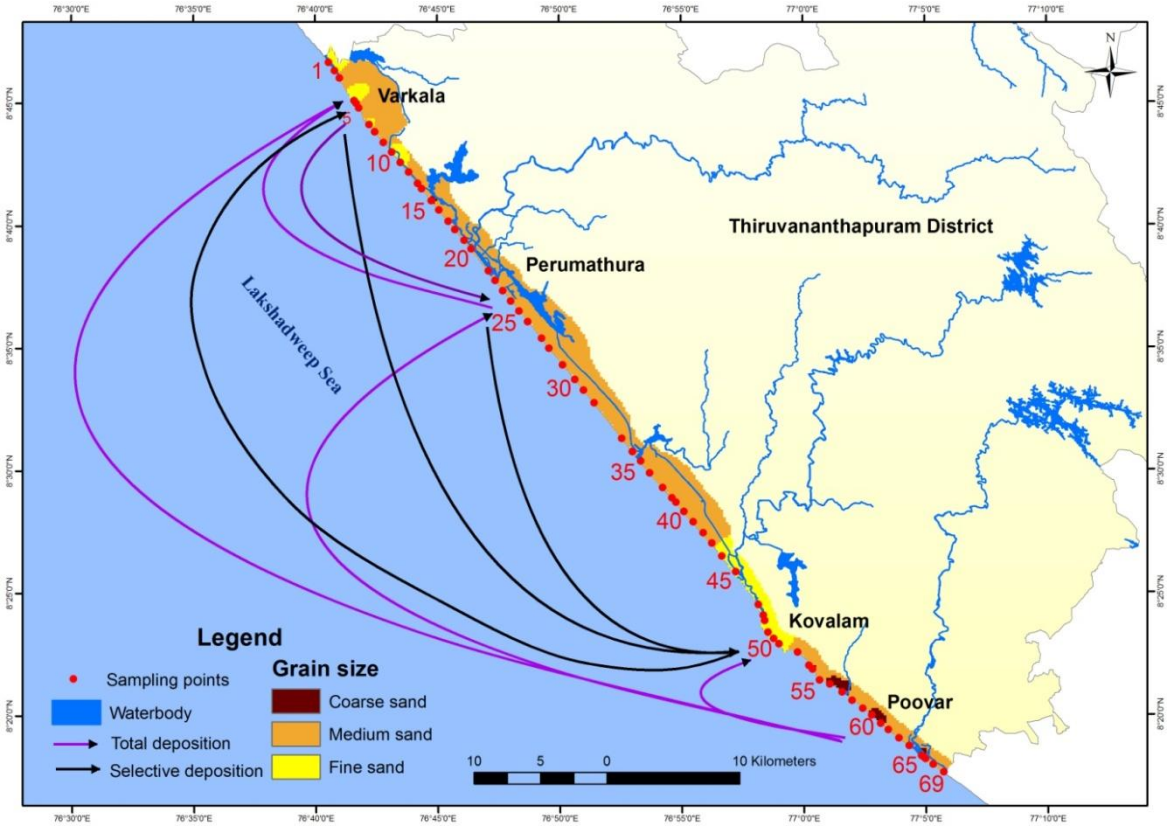

Figure 2.7: Sediment transport/movement map.

2.4.3. Mineralogy of Beach sediments

The total heavy mineral weight percentage (THM%) values obtained from 69 sampling stations are used to generate a THM% map using the IDW interpolation technique, as shown in Figure 2.8(a). The predicted values obtained from four interpolation techniques were validated using R^2, RMSE, and MAE values. It can be noticed that IDW with power factor 2 shows the highest correlation of 0.998, followed by RBF with 0.997, OK (exponential) with 0.955, and finally, the LPI with 0.877. The RMSE and MAE values for IDW with power factor 2 are 0.642 and 0.0024, which seems to be very low compared to any other interpolation techniques. The RBF show RMSE and MAE values of 0.957 and 0.00604 and that of OK (exponential) are 4.267 and 0.0298. The fine-grained sediments show the maximum THM% in the range of 0.21% to 55.54%. The Shanghumugham-Kovalam and Kappil-Varkala coastal regions show the maximum weight percentage of heavy minerals, whereas Perumathura and Poovar show the least THM%.

The THM% of the beach sands in Kovalam and Edava (in Varkala) were estimated to about 80.04% and 52.33%, respectively, whereas the Thumba region shows 0.57% only. The winnowing action of waves causes the deposition of heavy minerals as well as the removal of light minerals, which maintain the high values of THM% along with these areas. Since the heavy minerals possess very high specific gravity as compared to light minerals, high energy waves are needed for transportation and deposition along the coast.[32] The heavy mineral concentrate of Varkala and Kovalam regions were taken for grain counting. The results of grain counting show that the ilmenite predominantly exists in the beach sands of Varkala and Kovalam with a maximum of about 28.14% and 52.86% respectively, followed by monazite, sillimanite, rutile, zircon, garnet, leucoxene and Kyanite.

The ilmenite map derived using IDW interpolation technique is shown in Figure 2.8(b). The Figure 2.8(c) shows the THM% with respect to grain size for the sampling locations. The results of the grain counting of heavy mineral concentrate were shown in Figure 2.8(d) and Figure 2.8(e). Very small quantities of other heavy minerals like hornblende and sphene were also noticed. The leucoxene, which is a product of ilmenite alteration, is also seen in the study area with a maximum of about 0.88%. Table 2.3 renders a summary of the grain counting results of THM concentrate. The major content of ilmenite mineral followed by monazite, sillimanite, etc. along the coast of Varkala-Kovalam coastal stretch was also confirmed by many researchers.[87,88]

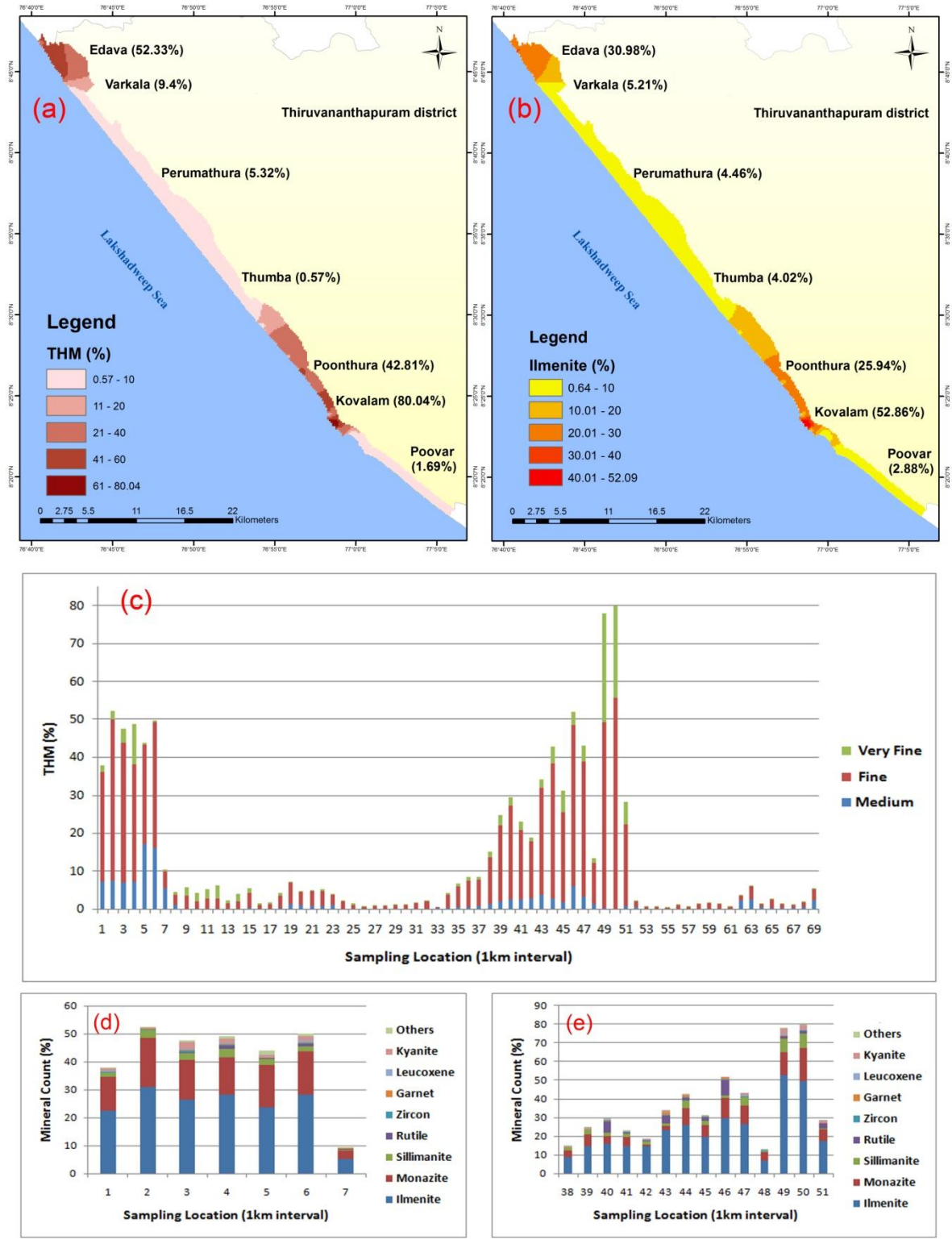

Figure 2.8: Results of heavy mineral analysis. (a) Heavy Mineral map; (b) Ilmenite mineral map (c) Graph showing the THM% with respect to grain size; (d) Graph showing the count percentage of heavy mineral species from Kappil-Varkala coast; (e) Graph showing the count percentage of heavy mineral species from Shanghumugham-Kovalam coast.

Table 2.3: Summary of the results of grain counting of THM concentrate.(Ilm-Ilmenite, Mon-Monazite, Sill-Sillimanite, Rut-Rutile, Zir-Zircon, Gar-Garnet, Leu-Leucoxene, Kya-Kyanite, OM-Other minerals)

			Ilm (%)	**Mon (%)**	**Sill (%)**	**Rut (%)**	**Zir (%)**	**Gar (%)**	**Leu (%)**	**Kya (%)**	**OM (%)**
Kappil- Varkala coast	Medium	Max	9.33	5.92	0.82	0.29	0.21	0.02	0.29	0.68	0.33
		Min	2.86	1.25	0.28	0	0	0	0	0	0
	Fine	Max	25.43	14.32	2.21	1.12	0.82	0.11	0.35	2.20	1.02
		Min	2.11	1.46	0.15	0	0	0	0	0	0.06
	Very Fine	Max	5.65	2.17	1.00	1.05	0.42	0.10	0.20	0.03	0.08
		Min	0.24	0.13	0.02	0	0	0	0	0	0
	Total	Max	30.98	17.44	2.97	1.35	0.90	0.14	0.64	2.51	1.37
		Min	5.21	2.84	0.55	0	0.10	0	0	0.12	0.09
Shanghumugham-Kovalam coast	Medium	Max	3.27	1.88	0.62	0.12	0.02	0.88	0.15	0.28	0.04
		Min	0.10	0.03	0.01	0	0	0	0	0	0
	Fine	Max	34.72	11.72	4.95	8.41	0.17	1.50	0.54	1.92	0.25
		Min	5.88	0	0	0	0	0	0	0.09	0
	Very Fine	Max	21.09	6.30	2.70	2.12	0.11	0.07	0.87	1.17	0.06
		Min	0.61	0.16	0.07	0	0	0	0	0	0
	Total	Max	52.86	18.05	7.48	8.41	0.17	1.50	0.88	3.09	0.31
		Min	7.04	0.84	0.56	0	0	0	0	0.56	0

Geologically the formation of these minerals was supported by the existence of khondalites and charnockites. The study area falls under the southern Kerala, which is composed of khondalites and charnockites. Both these rocks, along with their outcrops of pegmatites and quartz veins, are the important source of heavy minerals.[87] The tertiary sedimentary formations found along the coastal side also act as the provenance of heavy minerals. In the present study area, sandstone and clay with lignite intercalations exist in Varkala and Kovalam regions, which are prominent heavy mineral areas. The sandstone and clay with lignite intercalations fall under tertiary sedimentary formations. The laterites formed over khondalites contain sillimanite, whereas over charnockites contain ilmenite and magnetite. The zircon and monazite are usually seen as confined to granites and pegmatites. High-grade metamorphic rocks of granulite facies contain sillimanite and garnet. All these

minerals were carried down by major rivers, and its minor streams like Kallar, Vamanapuram, Neyar, Poovar, Karamana, Killiyar, etc., and will deposit along the coastal tracts results in a high concentration of heavy minerals. The Karamana River debouches to the Arabian Sea at Poonthura estuary carry a significant amount of heavy minerals, which makes high concentration along the Vizhinjam-Kovalam-Pachaloor coastal tracts. The geology of the study area and the west-flowing rivers are the main reasons behind the high heavy mineral concentration in beach sands.

2.4.4. Grain Size Indices

The maps showing the texture of beach sediments, which were successfully, derived using spectral indices, are shown in Figure 2.9. The Figure 2.9(a), 2.9(b) and 2.9(c) show the GSI map, Grain index map, and Sand index3 map prepared using the Visible-NIR-SWIR-TIR bands of Landsat 8 and ASTER. The parameters used for the FLAASH correction of satellite data are shown in Table 2.4. The Grain size indices show improved correlation with Graphic mean values derived from sixty sampling stations. The scatter plots showing the relationship between grain size indices and Graphic mean values were shown in Figure 2.9 (a1-c1). The GSI shows the best correlation (R^2=0.705) with the grain size, followed by grain index (R^2=0.671) and sand index 3 (R^2=0.646). The spectral indices are statistically significant, with a p-value of less than 0.001. Further, an attempt has been made to estimate the graphic mean values by substituting the values of GSI, Grain index, and Sand index3 in equations of trend lines. The RMSE error calculated between the original and estimated graphic mean values is low for GSI (RMSE= 0.264) compared to Sand Index (RMSE=0.290) and Grain index (RMSE=0.279). The results clearly suggest that the GSI compared to other spectral indices shows the best correlation with the grain size of beach sediments.

The spectral indices show an increasing trend as the texture of the beach sand changes from fine to medium. The Perumathura and Poovar regions show darker pixels with larger values indicating the medium texture of the sand as compared to low values in the Varkala and Kovalam regions consists of fine sand texture. Here the grain size indices detect the medium and fine sand area along the beach, which shows its potential in evaluating the textural characteristics. Table 2.5 renders the summary statistics of textural parameters and grain size indices. The maximum, minimum, and average values of grain size parameters (graphic mean) and spectral indices correspond to different grain sizes estimated for sixty sampling points were used for generating the statistics.

It clearly shows the correlation between graphic mean and spectral indices. The spectral indices show an increase in trend as the size of the sand grains increases. The fine sands always dominate in low wave energy environments while the coarser sediments persist in high wave energy environments. In this area, the action of strong winnowing waves has removed the fine sand.[89]

Table 2.4: Parameters of FLAASH atmospheric correction

Sensor	**Landsat 8 OLI**	**ASTER**
Scene center location	8.6731N, 76.3287E	8.4775N, 76.8821E
Sensor altitude	705	705
Pixel size	30	30
Flight date	2015-11-29	2004-02-24
Flight time	05:12:13.21	05:30:09.56
Atmospheric model	Tropical	Tropical
Aerosol model	Maritime	Maritime
Kaufman-Tanre Upper and lower	Band 7 and 4	NIL
Initial visibility	40	40

Table 2.5: Summary statistics of textural analysis

Grain size	**Graphic Mean**			**GSI**			**Grain Index**			**Sand Index 3**		
	Min	Max	Mean	Min	Max	Mean	Min	Max	Mean	Min	Max	Mean
Coarse	0.64	0.96	0.88	0.25	0.29	0.27	-0.37	-0.34	-0.36	1.06	1.09	1.08
Medium	1.02	1.99	1.41	0.07	0.33	0.23	-0.59	-0.32	-0.41	1.02	1.09	1.06
Fine	2.02	2.80	2.28	0.01	0.14	0.06	-0.72	-0.50	-0.62	1.00	1.05	1.02

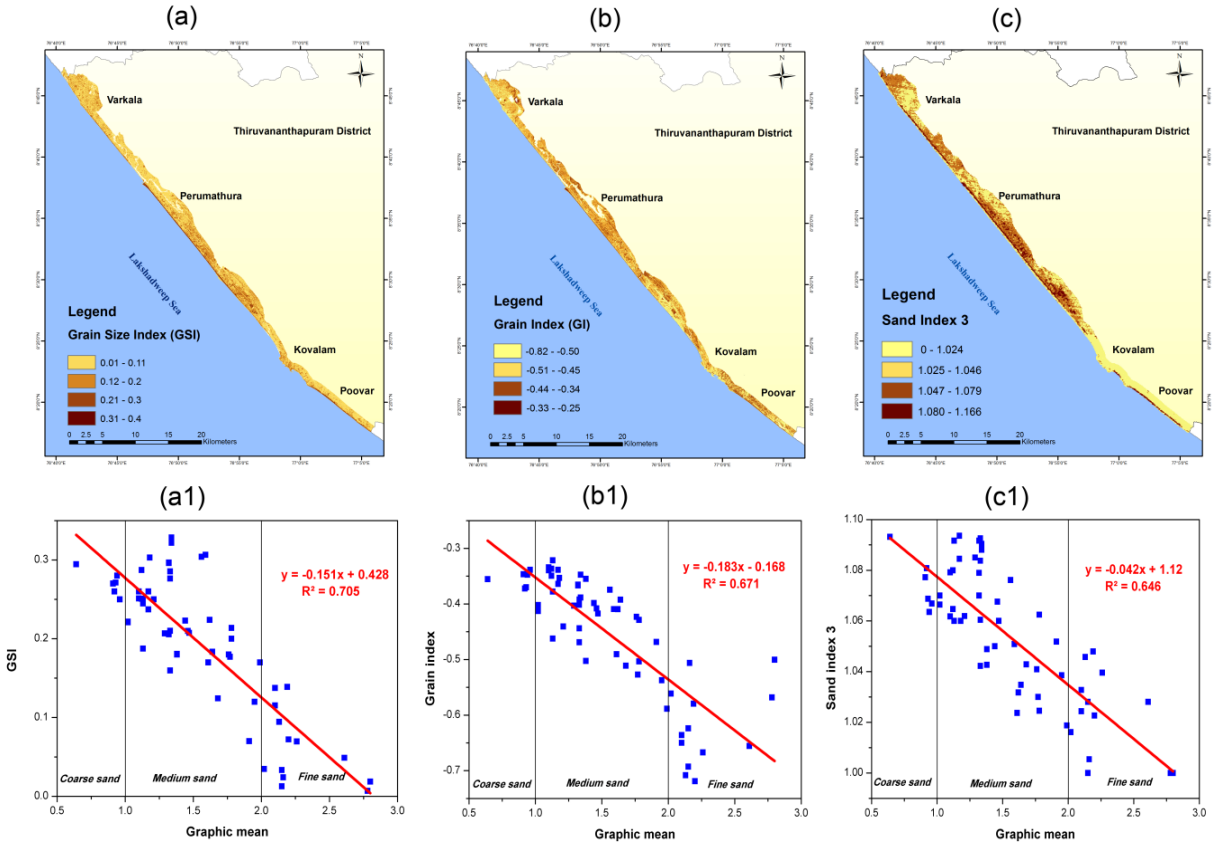

Figure 2.9: Satellite derived maps showing texture of beach minerals. (a) Grain size index (GSI) map; (b) Grain index map; (c) Sand index 3 map; (a1) Scatter plot corresponds to Grain size index (GSI); (b1) Scatter plot corresponds to Grain index map; (c1) Scatter plot corresponds to Sand index 3 map

2.4.5. Mapping of beach minerals in Varkala-Kovalam coast, Kerala

The reflectance calibrated spectral bands of Landsat imagery and ASTER data were linearly transformed using the MNF technique. Spatial data coherency calculated using a threshold value of 0.62 and 0.35 removes the noise dominated and least informative last band of each dataset.

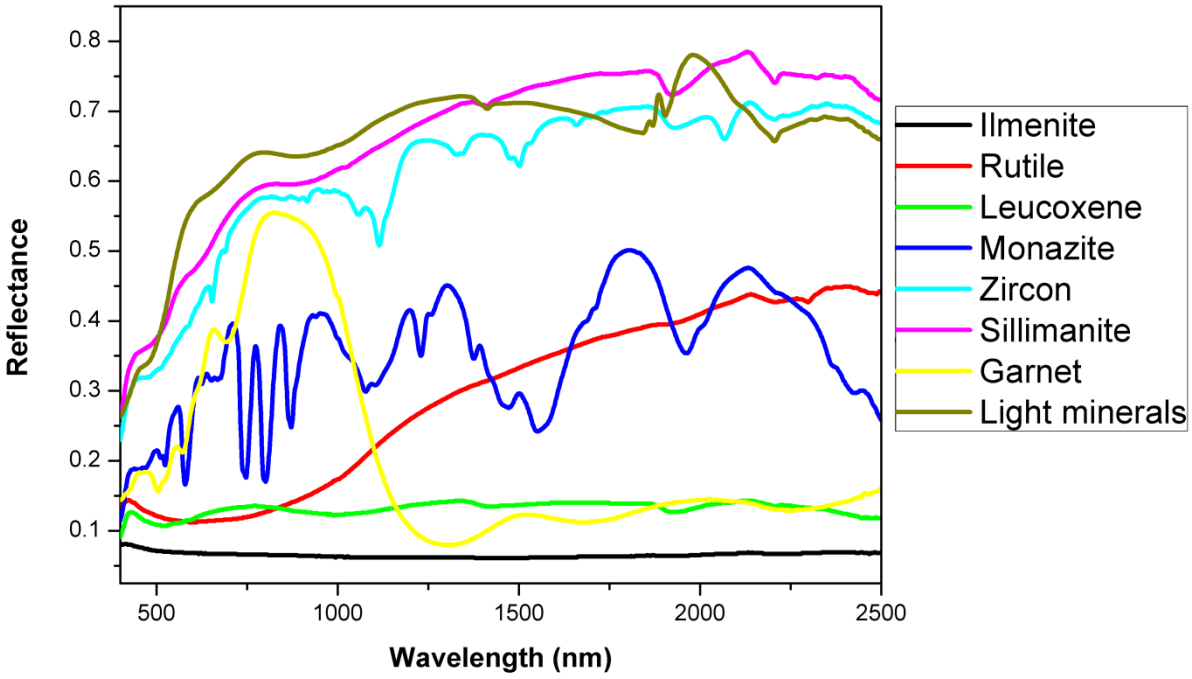

Figure 2.10: Spectral library of beach minerals.

The bright pixels of PPI image obtained using 100 iterations with a threshold value of 3 clearly represent the spectrally extreme pixels. In the case of multispectral datasets, the generation of non-extreme pixels may occur for a higher number of iterations.[53] The 2-D scatter plots of this higher number MNF bands are used to identify the unique target material, and then they were compared with a laboratory-derived spectral library of beach minerals. The spectral library of beach minerals developed after processing the laboratory spectral signatures is shown in Figure 2.10. The mean spectra of beach minerals recovered from Kappil-Varkala and Shanghumugham-Kovalam coastal stretches of the study area are used to develop the spectral library. Post-processing of laboratory collected spectra eliminates the thermal drifts at 1001 and 1831 nm, followed by smoothing of the spectra. Table 2.6 shows the validation results of laboratory spectra. Each mineral produces a maximum score with the corresponding mineral in the USGS library. The score is calculated using the values obtained

for SAM, SFF, and BE methods. The results conclude that the laboratory spectra show the best match with USGS spectral library and can be taken for hyperspectral analysis.

Table 2.6: Validation of laboratory data

Mineral	**USGS Library**	**Score**	**SAM**	**SFF**	**BE**
Ilmenite	Ilmenite HS231.3B	1.775	0.854	0.588	0.333
Rutile	Rutile HS137.3B	2.037	0.602	0 .602	0.833
Monazite	Monazite S255.3B	2.466	0.871	0.762	0.833
Zircon	Zircon WS522	2.947	0.947	1	1
Sillimanite	Sillimanite HS186.3B	3	1	1	1
Garnet	Almandine HS114.3B	2.755	0.886	0.868	1
Light Minerals	Quartz GDS74 Sand Ottawa	2.749	0.916	1	0.833

Table 2.7: Results of spectral matching techniques for beach minerals.

Satellite data	**Date of Acquisition**	**Endmember**	**SAM**	**SFF**	**BE**	**Score**
Landsat 8	2015-11-29	Ilmenite	0.911	0.965	1	2.876
		Light minerals	0.673	0.975	0.833	2.481
ASTER	2004-02-24	Ilmenite	0.242	0.720	0.444	1.406
		Light minerals	0.764	0.847	0.444	2.055

Likewise, the image spectra are also compared with reference spectra using the scores of SAM, SFF, and BE methods. The Table 2.7 shows the scores of SAM, SFF, and BE, showing the highest degree of match between the image-derived endmembers and the laboratory-derived spectral signatures. The endmembers derived from the image spectrum were detected as ilmenite and light minerals. The ilmenite and lights show the maximum

scores compared to other endmembers. The image spectra derived from Landsat show total scores of 2.876 and 2.481 for ilmenite and light minerals. In the case of ASTER data, the scores are 1.406 and 2.055.

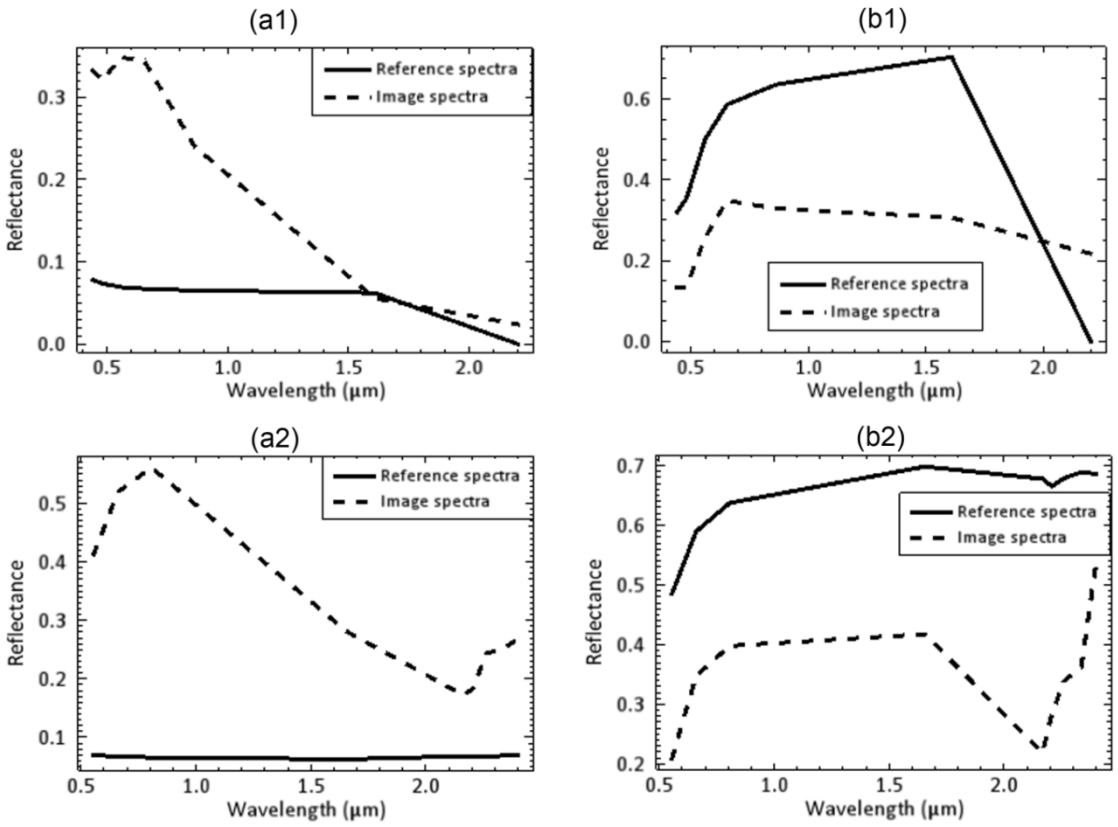

Figure 2.11: Plots of relative reflectance of image spectra and reference spectra for beach minerals. (a1-a2) ilmenite corresponds to Landsat and ASTER data; (b1-b2) Light minerals corresponds to Landsat and ASTER data.

Comparatively, the image spectra derived from Landsat imagery shows more match with the reference spectra. The Plots of relative reflectance of these image spectra with the corresponding reference spectra is shown in Figure 2.11. These identified endmembers were used as the input training data for the SAM algorithm. Figure 2.12 and Figure 2.13 show the SAM classified images of the study area showing the distribution of ilmenite and light minerals derived from Landsat and ASTER data. SAM classified image shows rich deposits of heavy mineral such as ilmenite along the coast of Varkala and Kovalam regions, which clearly indicate the moderate to high energy environmental conditions, exist on these beaches favouring the deposition of minerals.

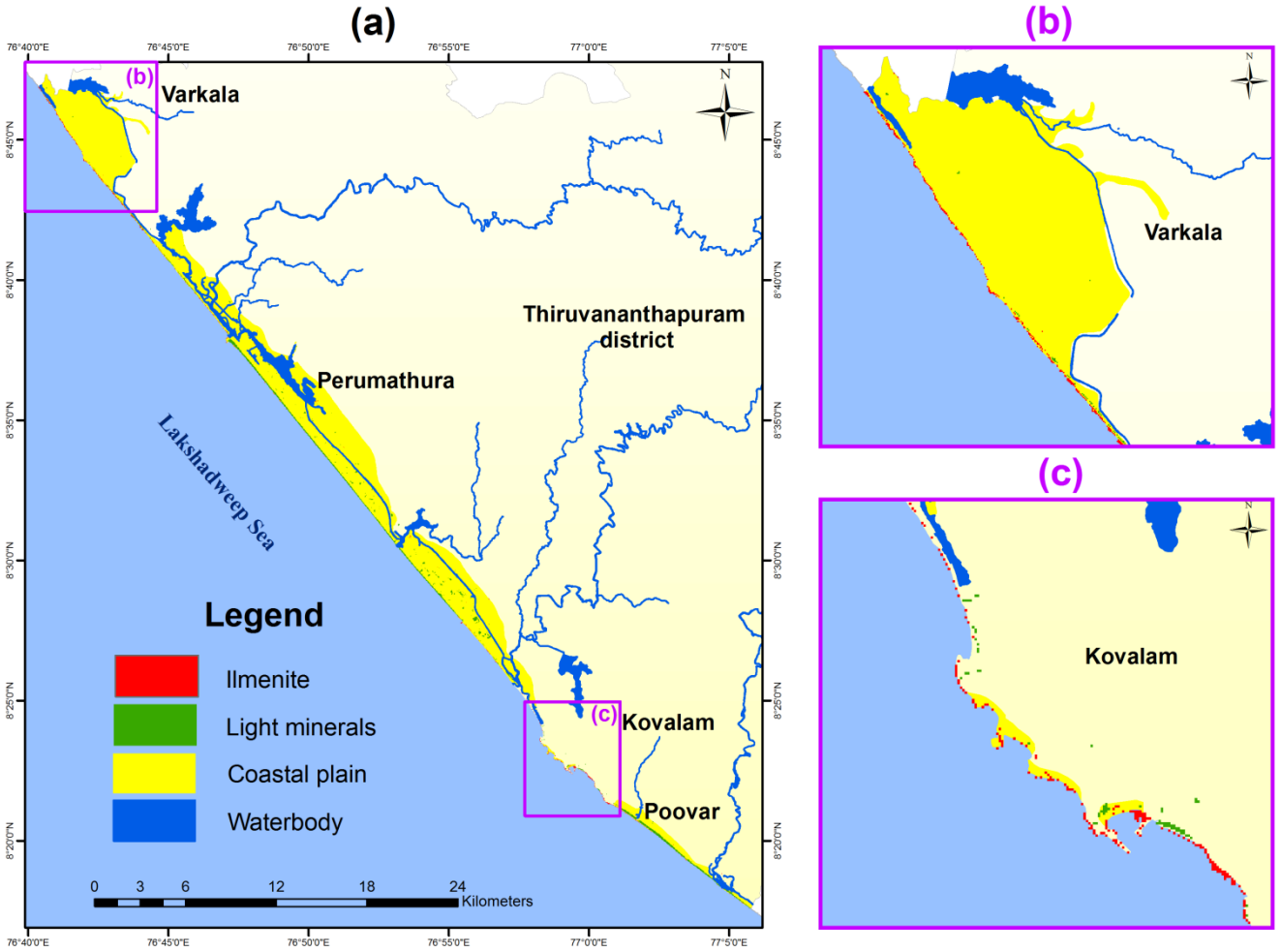

Figure 2.12: SAM classified image of Landsat data showing beach minerals. (a) Thiruvananthapuram district; (b) Varkala coast; (c) Kovalam coast.

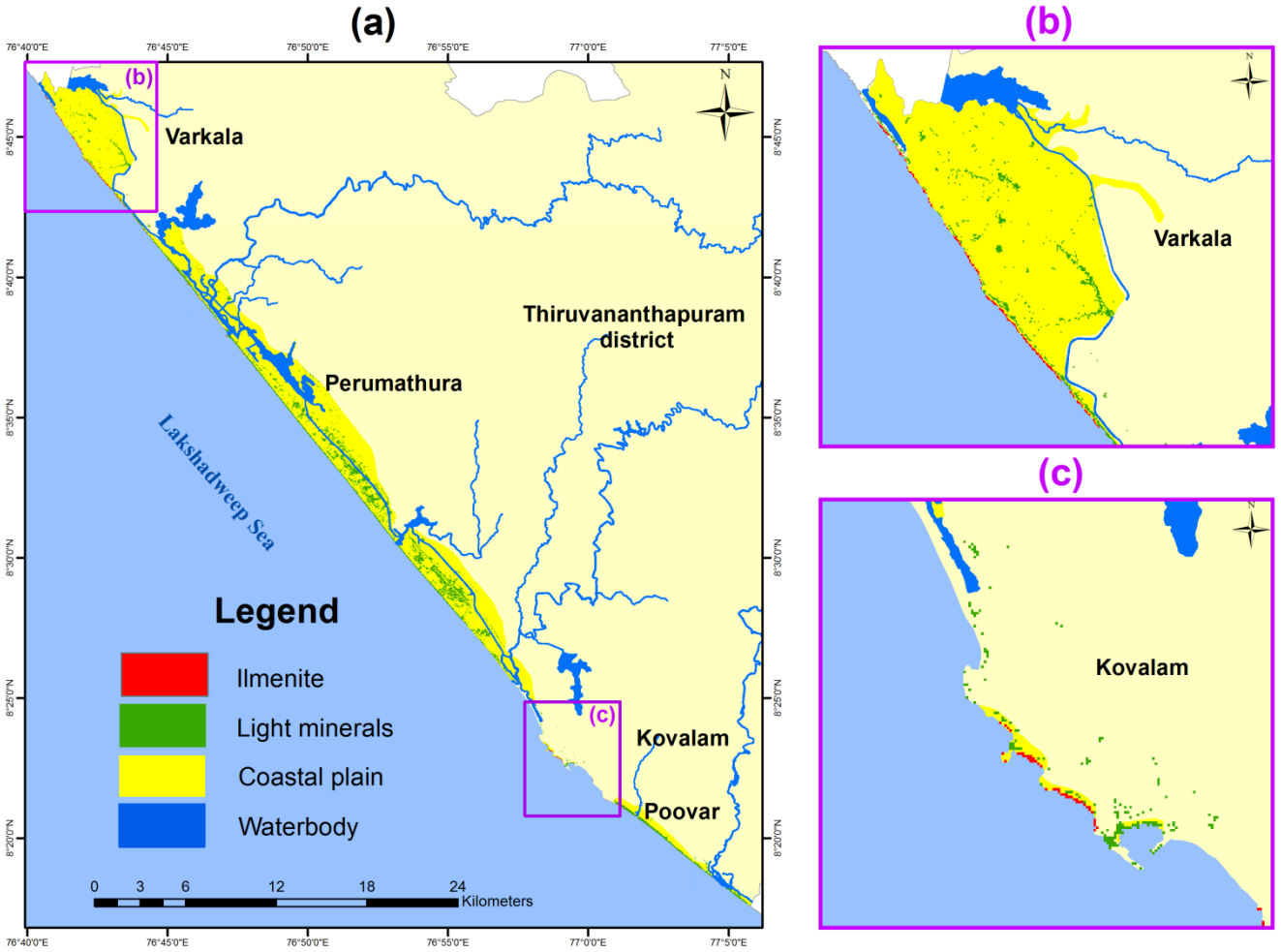

Figure 2.13: SAM classified image of ASTER data showing beach minerals. (a) Thiruvananthapuram district; (b) Varkala coast; (c) Kovalam coast.

Table 2.8: Accuracy assessment matrix for Landsat derived mineral map.

	Reference Data			
Classes	**Ilmenite (>10%)**	**Lights**	**Total**	**User's accuracy**
Unclassified	0	0	0	-
Ilmenite	17	2	19	89.47
Light minerals	2	48	50	96
Total	19	50	69	-

Overall accuracy = 94.20%, Kappa coefficient = 0.85

The action of high energy waves and currents results in the removal of light minerals to the offshore and leaving the heavy minerals on the beach[90]. Apart from beach minerals, endmembers of other geological units, water bodies, vegetation, and land use were also derived from the PPI images of ASTER and Landsat, which were removed for the SAM classification. Here the SAM technique was used successfully for two purposes; it facilitates the comparison of image spectra and reference spectra and also facilitates the sub-pixel mapping of target endmembers in the satellite data.

Table 2.9: Accuracy assessment matrix for ASTER derived mineral map.

	Reference Data			
Classes	**Ilmenite (>10%)**	**Light minerals**	**Total**	**User's accuracy**
Unclassified	1	2	3	-
Ilmenite	10	1	11	90.91
Light minerals	8	47	55	85.45
Total	19	50	69	-

Overall accuracy = 82.61%, Kappa coefficient = 0.60

The accuracy of SAM inferred heavy mineral distribution map is shown in Table 2.8 and Table 2.9, which gives an overall classification accuracy and Kappa coefficient. The accuracy of the SAM classified ilmenite mineral occurrences was cross-checked using the sampling locations having more than 10% ilmenite mineral concentration. The Accuracy assessment matrix for the SAM classified images derived from Landsat and ASTER shows overall

accuracies of 94.20% and 82.61% while the values of the Kappa coefficient are 0.85 and 0.60, which shows a strong correlation between ground truth data and satellite-derived results. The value of the Kappa coefficient clearly demonstrates a relatively high degree of accuracy for the proposed methodology for heavy mineral mapping.[4] Since the ilmenite predominantly exists in the study area, only two mineral spectra of ilmenite and lights were derived from Landsat and ASTER data. But the results obtained from the present study would be helpful for the identification of low concentration minerals from hyperspectral remote sensing datasets using more advanced mapping algorithms.

2.4.6. Mapping of Silica sand deposits in Cherthala, Kerala

The samples collected from six locations (S1 to S6) were used for reference spectra built. The reference spectra of silica sand developed after processing the laboratory spectral signatures are shown in the Figure 2.14. The pre-processed samples are also subjected to spectral data collection. The mean spectrum of six samples collected from the study area is used to develop the reference spectra of silica sand. The sensor inherent errors such as thermal drifts at 1001 and 1831 nm were rectified followed by smoothing of the spectra gives characteristic spectra for silica sand which is used for mapping the potential targets of silica sand deposits. Effective mapping of minerals can be successfully achieved if they show marked variation in their reflectance for different ranges of wavelengths.[90] The spectral-reflectance distribution curve of silica sand reveals reflectance minima at 1.93μm of SWIR region.

The reflectance calibrated nine VNIR-SWIR bands of ASTER and seven bands of Landsat 8 OLI imageries were used for deriving the occurrences of silica mineral. The noise dominated and least informative last bands were removed using MNF transformation by applying suitable threshold values. The PPI image showing spectrally extreme pixels as bright were generated using the 100 iterations with a threshold value of 3. Higher number of iterations for multispectral datasets may generate pixels which are not extreme.[53] The endmember spectra of unique target materials identified using the 2-D scatter plots of higher number MNF bands were compared with reference spectra of silica sand using spectral matching techniques results in successful identification of true endmembers. The scores of spectral matching techniques such as SAM, SFF and BE showing the highest degree of match between the image-derived and the laboratory-derived endmembers were shown in Table 2.10.

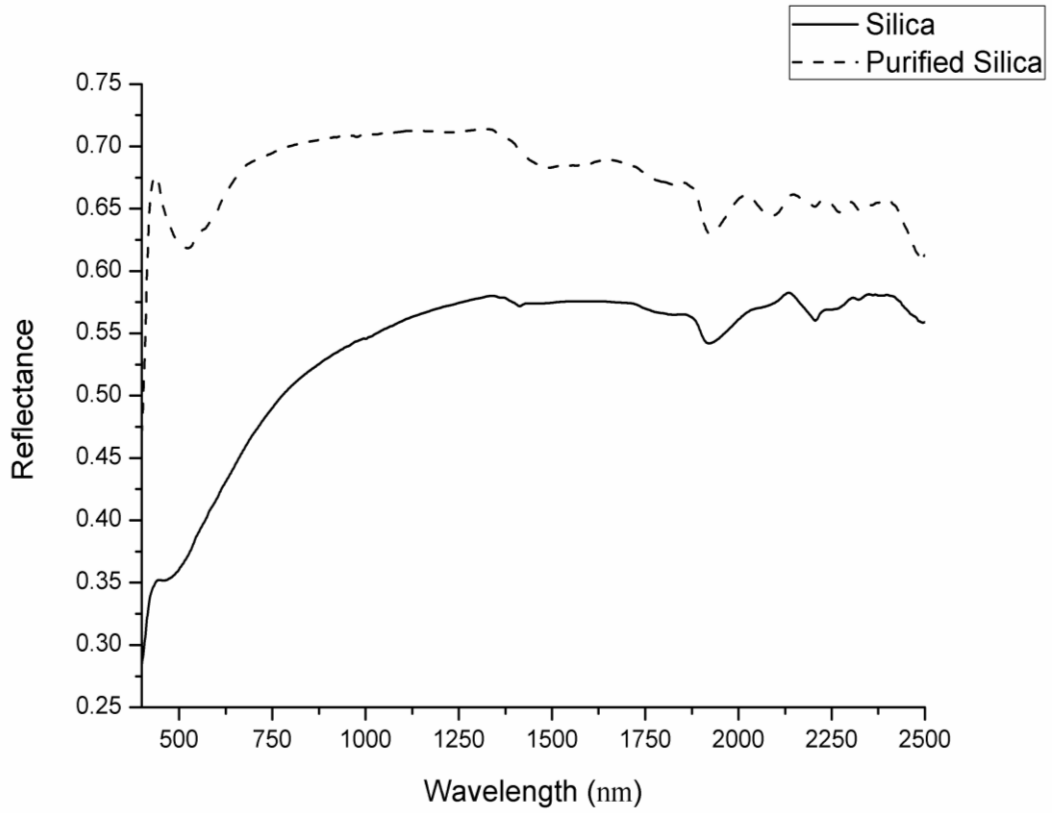

Figure 2.14: Laboratory spectral reflectance plot of silica sand

Table 2.10: Results of spectral matching techniques for silica sand deposits.

Satellite data	**Date of Acquisition**	**Endmember**	**SAM**	**SFF**	**BE**	**Score**
ASTER	2017-12-19	Sillica	0.629	0.968	1	2.597
		Purified Sillica	0.511	0.965	0.222	1.699
	2017-12-19	Sillica	0.717	0.948	1	2.665
		Purified Sillica	0.601	0.947	0.222	1.771
Landsat 8	2017-01-18	Sillica	0.426	0.987	0.714	2.127
		Purified Sillica	0.325	0.950	0.429	1.703

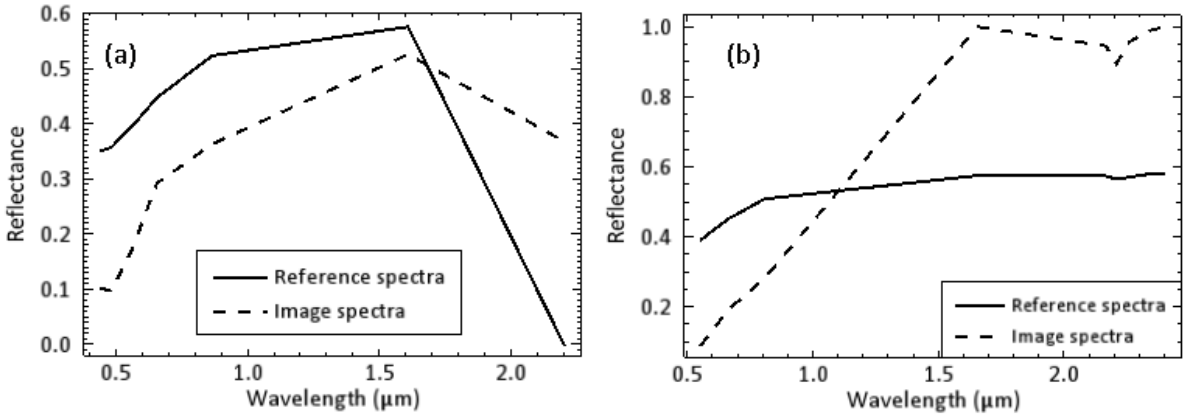

Figure 2.15: Plot of relative reflectance of image spectra and reference spectra for silica sand. (a) Landsat data; (b)ASTER data.

The true endmembers showing the highest degree of match is selected for further analysis. The Landsat data generates six endmembers in which the endmember "n-D Class Mean #2" shows the maximum score of 2.127 is used as the image spectra for mapping the silica sand occurrences. The ASTER scenes generate eight endmenbers each in which the n-D Class Mean #7 and n-D Class Mean #1 show the maximum scores of 2.597 and 2.665. These endmembers were used as the training data for SAM classification. The Figure 2.15(a) and 2.15(b) shows the plots of relative reflectance between the reference spectra and image spectra corresponds to Landsat and ASTER. In addition to these, end members indicating waterbodies, vegetation and other common landforms and lithological structures were also retrieved from the PPI images which were expelled from the further processing of SAM classification. SAM is used successfully for comparing the image spectra to reference spectra and also it is also used for the per-pixel mapping of the target endmembers by measuring the spectral angle between the unit vectors representing the image and reference spectra.[91] The Figure 2.16 and Figure 2.17 shows the SAM classified images of the study area showing the rich distribution of silica sand derived from Landsat and ASTER datasets. On comparing with the Geological map, it is revealed that the inland silica sand deposits are mainly distributed along with the quaternary sediments of strand line/paleo beach deposit (Guruvayoor Formation).

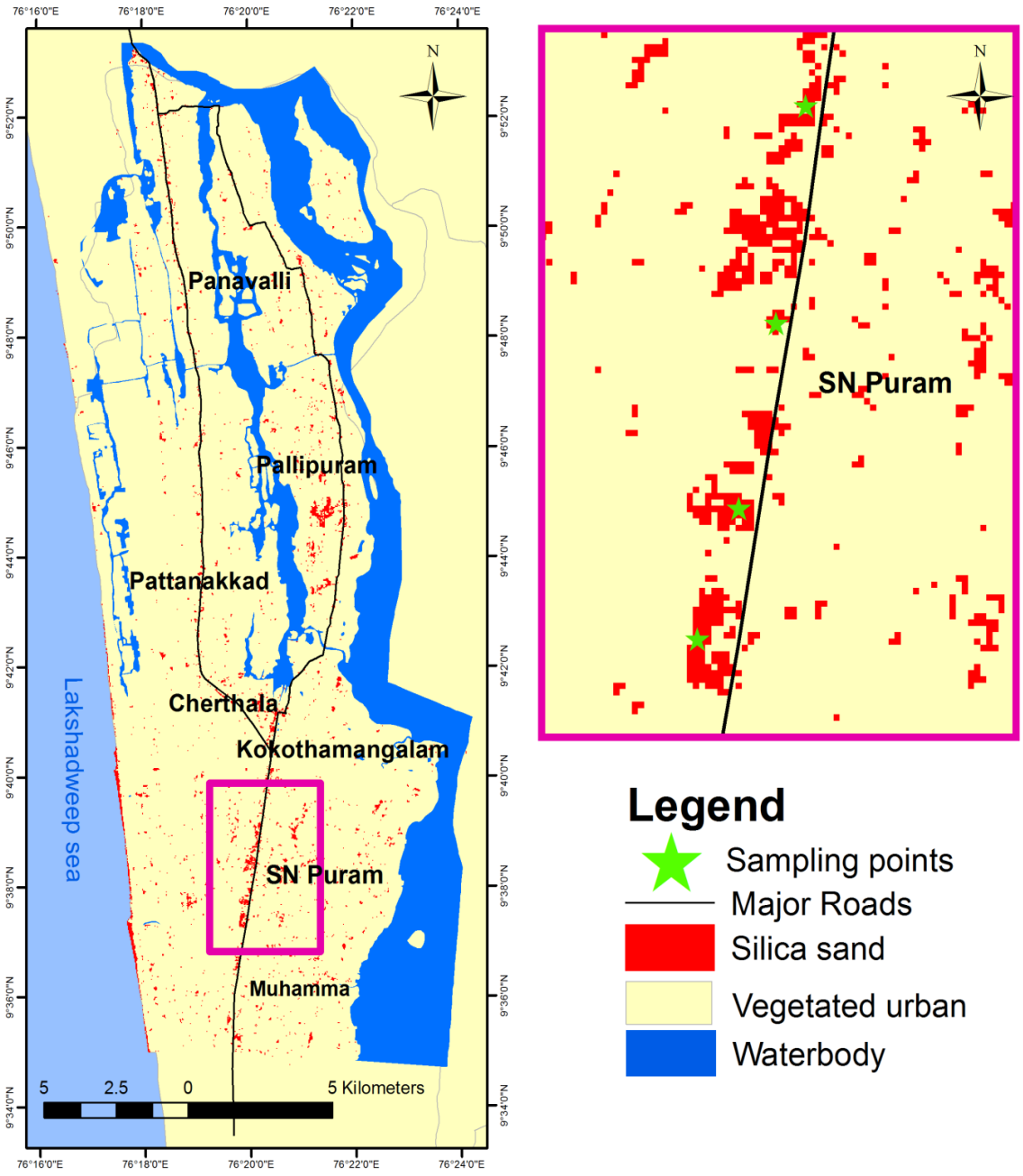

Figure 2.16: SAM classified image of the Landsat data.showing silica sand deposits.

The accuracy of the classification was assessed using the overall accuracy derived using error matrix.[60] Since only one mineral type is taken for the study, Kappa coefficient cannot be calculated. The overall accuracy obtained for the Landsat 8 OLI imagery is 90.476% and that for ASTER data is 80.952%. Accuracy assessment using field observation demonstrates that the mineral occurrences show a high degree of accuracy with the sampling points. The sampling locations show a strong correlation with the pixels of classified images

denoting silica mineral occurrences. The silica sand content of the beach deposit along the coastal side is also clearly seen in the inferred map derived using SAM method.

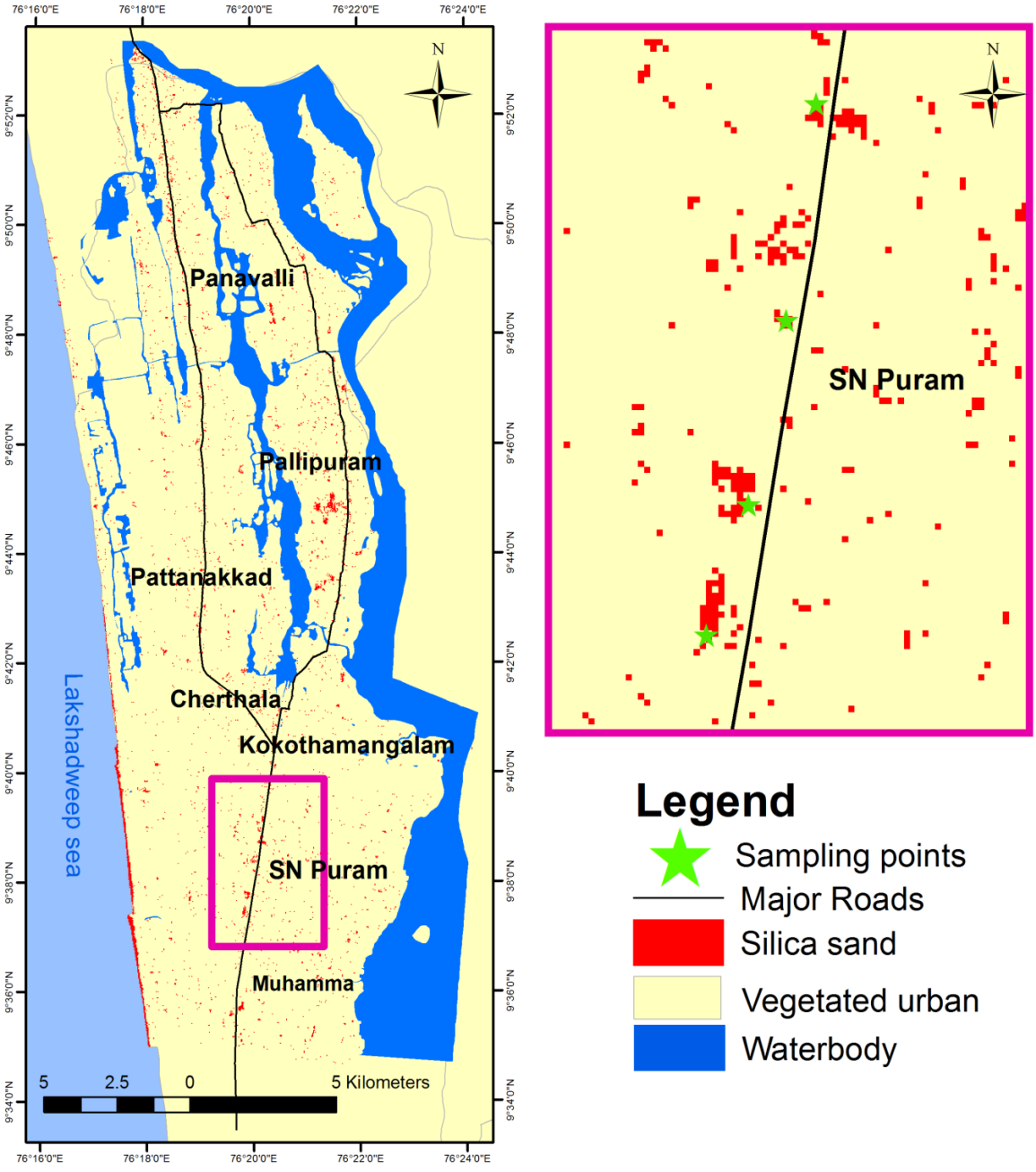

Figure 2.17: SAM classified image of the ASTER data showing silica sand deposits.

2.4.7. **Mapping of Kaolin deposits in Thonnakkal, Kerala**

The laboratory spectral reflectance plot of Kaolin clays are given in Figure 2.18. This is used as the reference spectra for mapping the kaolinite occurrences using the MTMF classification of Landsat 8 OLI imagery. The parameters such as 100 iterations with a threshold value of 3 are used for generating the PPI image. The endmembers derived from n-D visualizer are compared with the laboratory spectral reflectance of kaolin clay deposits.

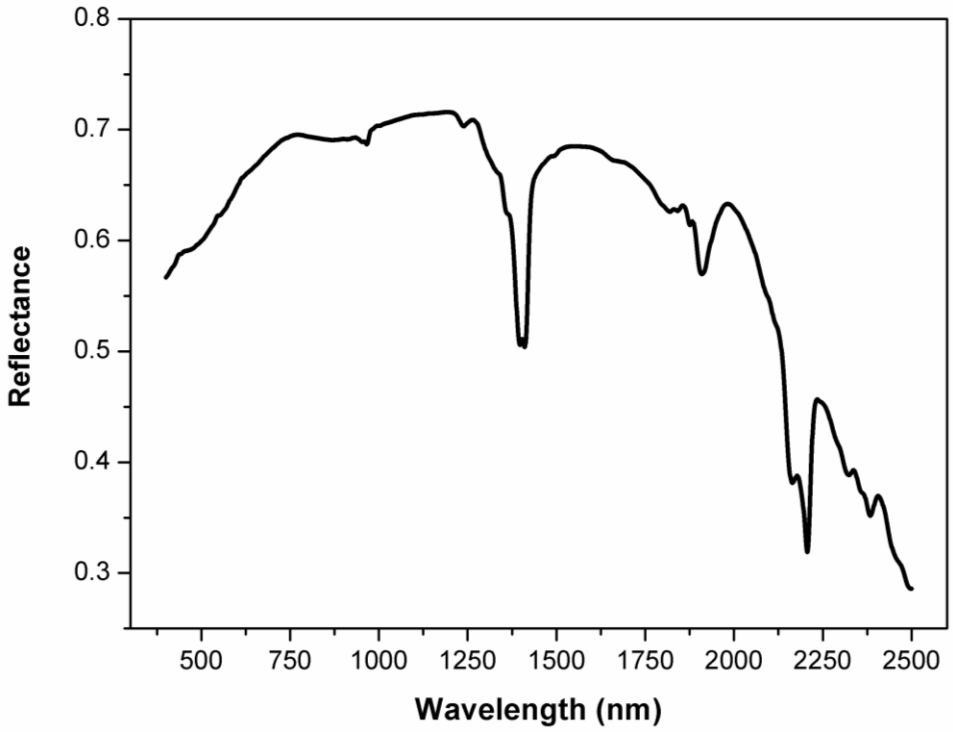

Figure 2.18: Laboratory spectral reflectance plot of Thonnakkal Kaolinite clays.

The scores obtained for the spectral matching techniques are given in Table 2.11. On comparing with the image spectra, the laboratory spectra obtained a total score of 2.638 and thereby the endmeber can be assigned to the class of Kaolin clays. The plots of relative reflectance of endmembers from image and reference spectra are shown in Figure 2.19.

Table 2.11: Results of spectral matching technique for Thonnakkal Kaolinite clays.

Satellite data	**Date of acquisition**	**SAM**	**SFF**	**BE**	**Score**
Landsat 8	2017-01-18	0.791	0.990	0.857	2.638

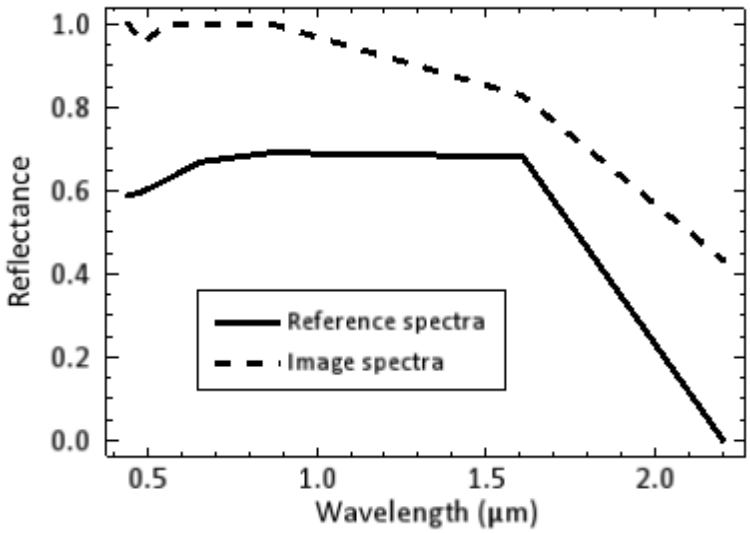

Figure 2.19: Plots of relative reflectance of endmember spectra from Landsat data and reference spectra for Koalin clay deposits.

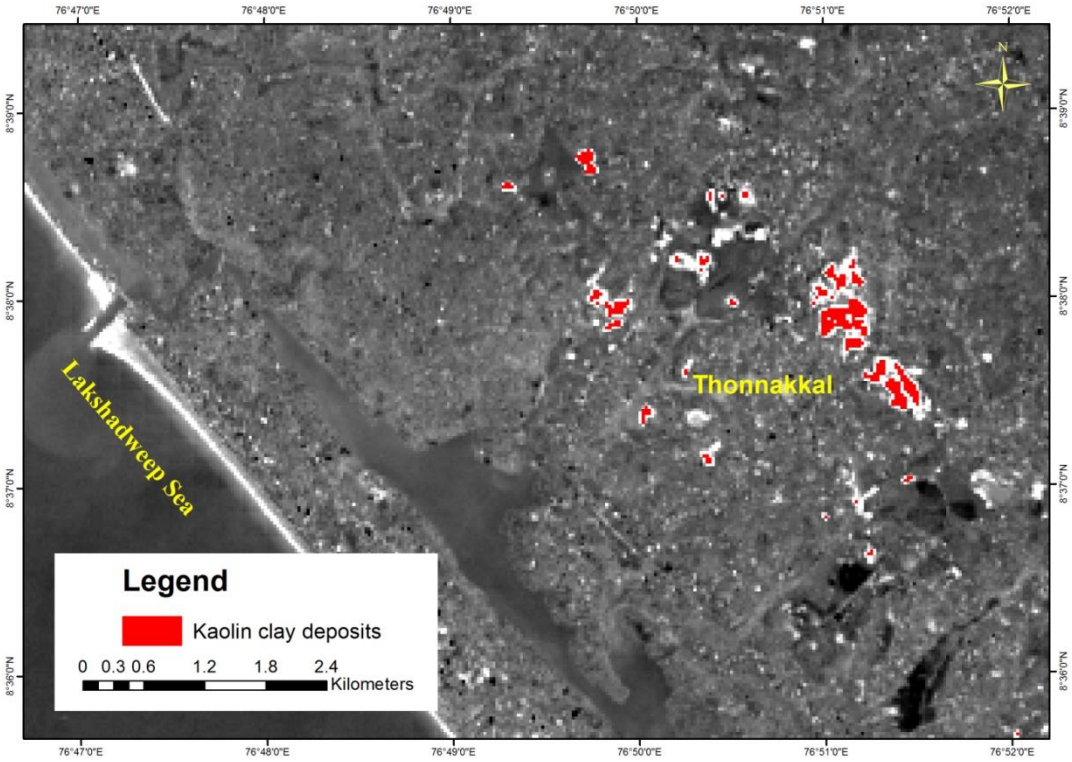

Figure 2.20: Map showing Kaolin clays mines derived from Landsat imagery using MTMF method.

These endmember was used as the traing site for the MTMF algorithm. The classified mineral map obtained from MTMF method is shown in Figure 2.20. Thonnakkal clay deposits were marked in red color. On field verification, it was confirmed that the clay mines in Thonnakkal mines were identified correctly using MTMF metod applied to Landsat 8 imagery.

2.4.8. Mapping of Fullerene bearing Mangampet baryte mine, Andhrapradesh

The reference spectra developed by processing the laboratory spectra collected for the samples is also shown in the Figure 2.21. The reflectance calibrated and FLAASH atmospherically corrected seven VNIR-SWIR bands of Landsat imagery were used for the study.

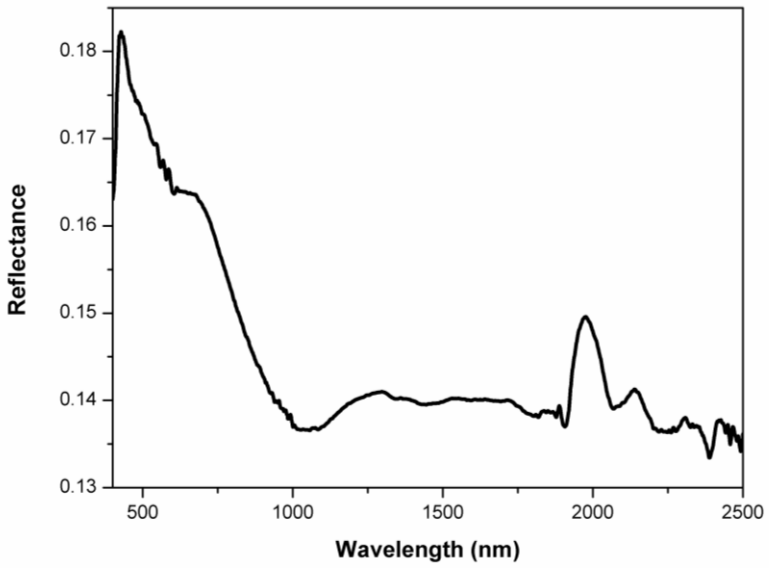

Figure 2.21: Laboratory spectral reflectance plot of baryte mineral

The MNF transformation eliminates the least informative and noisy last band from the satellite data. The PPI image showing extremely pure pixels as bright ones are generated using 100 iterations with a threshold value of 3. The endmembers generated using 2-D plots of MNF bands were compared with reference spectra using spectral matching techniques and true endmembers of shungite rocks were identified. The scores of spectral matching techniques such as SAM, SFF and BE showing the highest degree of match were shown in Table 2.12 and the corresponding plots of relative reflectance is shown in Figure 2.22.

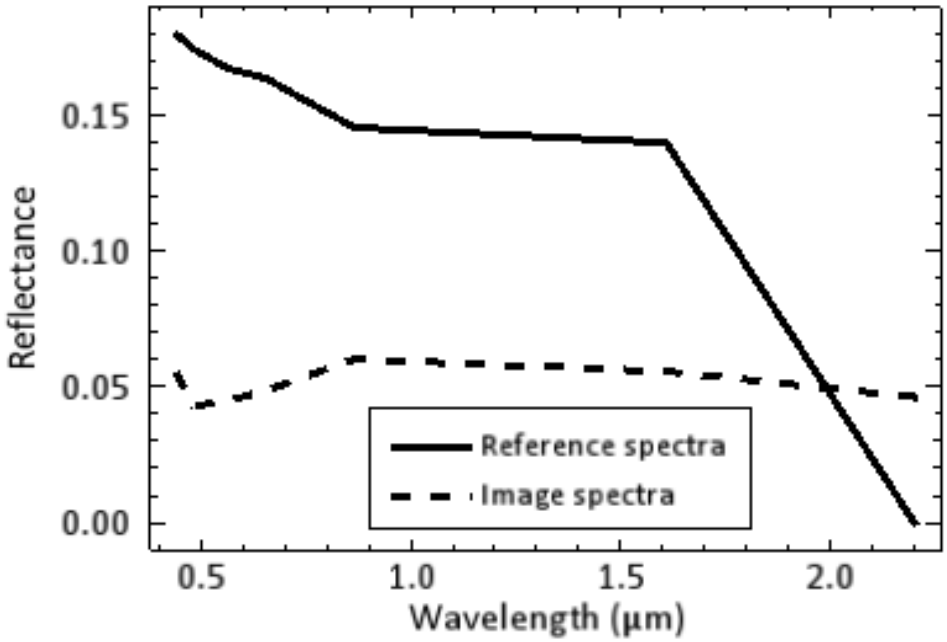

Figure 2.22: Plots of relative reflectance of endmember spectra from landsat data and their corresponding reference spectra.

Table 2.12: Results of spectral matching technique for baryte mineral in Mangampet.

Satellite data	**Date of acquisition**	**SAM**	**SFF**	**BE**	**Score**
Landsat 8	2018-05-06	0.823	0.974	1	2.797

On comparing with the reference spectra, the endmember "n-D class Mean #1" out of six endmembers extracted from the Landsat data shows the maximum score of 2.797 which indicates the maximum similarity with reference spectra. Finally the MTMF algorithm classifies the entire images using these endmember and the bright pixels shown in the MTMF-classified imagery shows the occurrence of fullerene bearing shungite rocks (Figure 2.23). The MTMF gives the most satisfying results when a particular target needs to be identified rather than all the materials in the scene [14].

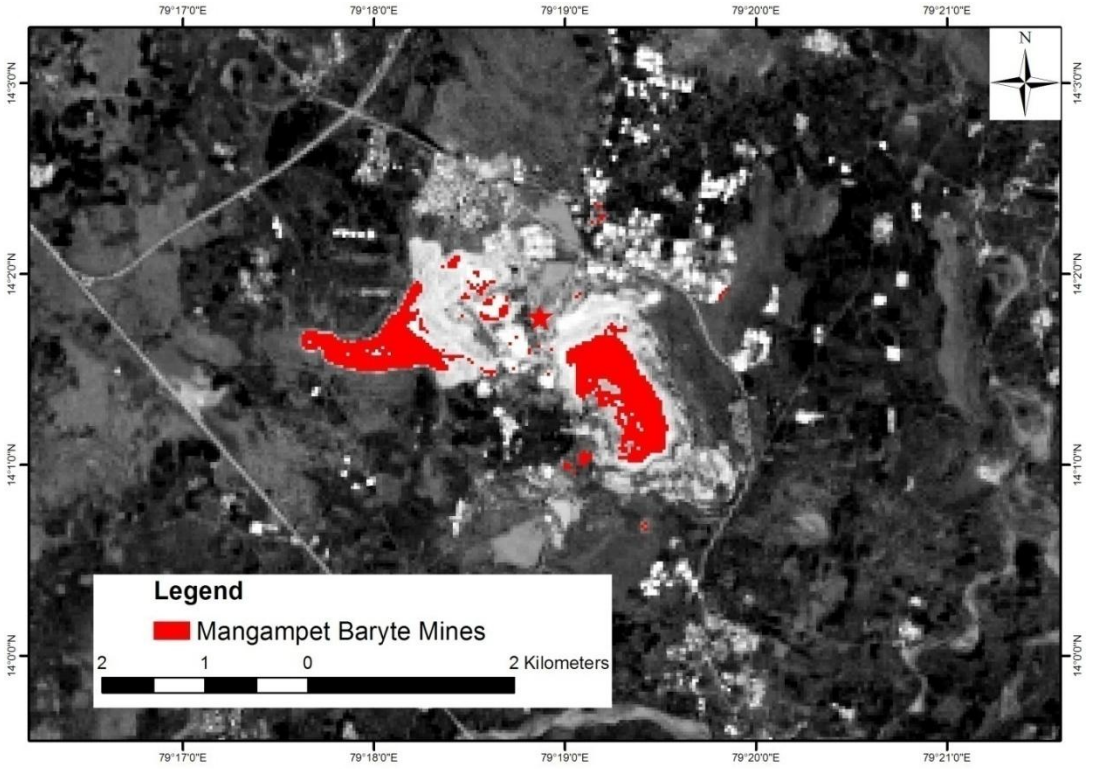

Figure 2.23: Map showing Baryte mines derived from Landsat imagery using MTMF method.

2.5.Conclusion

Investigation on grain size and mineral distribution of beach sediments collected from the coast of Thiruvananathapuram District in Kerala, India, shows the dominance of medium to fine-grained sands with the major content of ilmenite mineral. The spectral indices developed using the bands of ASTER and Landsat clearly detect the abundance of medium to fine sand area. The mineral map developed using hyperspectral analysis of ASTER and Landsat data shows it's ability in demarcating the potential targets of mineral occurrences. Two mineral spectra of ilmenite and lights were successfully extracted from processed Landsat and ASTER data and the spectra were compared using the laboratory spectra of the minerals. Meanwhile, the silica sand deposits in Certhala, Kerala, Kaolin clay deposits in Thonnakkal, Kerala and Baryte mine in Mangampet, Andhrapradesh were also successfully mapped using the hyaperspectral analysis of Lasat and ASTER data. The accuracy of satellite-derived maps has been validated using field measurement that shows strong correlation almost in all locations. Laboratory derived spectral library provides highly accurate information of minerals, which significantly increased the accuracy of image classification. The spectral library is the first of its kind in Indian minerals and covers nine

strategic minerals seen commonly in the beaches and inland areas of the India. On applying hyperspectral analysis techniques to multispectral remote sensing datasets, effective mapping of texture and mineralogy of minerals can be achieved successfully, which has been analysed at first in this study areas. The results clearly illustrate the advanced image processing techniques and multispectral remote sensing datasets are very useful for the eco-friendly and sustainable exploration of strategic mineral resources. Moreover, the results will be helpful in identifying optimal wavelengths in hyperspectral remote sensing datasets for mineral exploration, using advanced mapping techniques and machine learning methods.

2.6.References

(1) Harris, J. R.; Rencz, A. N.; Ballantyne, B.; Sheridon, C. Mapping Altered Rocks Using Landsat TM and Lithogeochemical Data: Sulphurets-Brucejack Lake District, British Columbia, Canada. *Photogrammetric Engineering and Remote Sensing*. 1998.

(2) Ramadan, T. M.; Abdelsalam, M. G.; Stern, R. J. Mapping Gold-Bearing Massive Sulfide Deposits in the Neoproterozoic Allaqi Suture, Southeast Egypt with Landsat TM and SIR-C/X SAR Images. *Photogrammetric Engineering and Remote Sensing*. 2001, pp 491–497.

(3) Suman Babu, P.; Majumdar, T. J.; Bhattacharya, A. K. Study of Spectral Signatures for Exploration of Bauxite Ore Deposits in Panchpatmali, India. *Geocarto Int.* **2015**, *30* (5), 545–559.

(4) Masoumi, F.; Eslamkish, T.; Honarmand, M.; Abkar, A. A. A Comparative Study of Landsat-7 and Landsat-8 Data Using Image Processing Methods for Hydrothermal Alteration Mapping. *Resour. Geol.* **2017**, *67* (1), 72–88.

(5) Zhang, T.; Yi, G.; Li, H.; Wang, Z.; Tang, J.; Zhong, K.; Li, Y.; Wang, Q.; Bie, X. Integrating Data of ASTER and Landsat-8 OLI (AO) for Hydrothermal Alteration Mineral Mapping in Duolong Porphyry Cu-Au Deposit, Tibetan Plateau, China. *Remote Sens.* **2016**, *8* (11), 890.

(6) Nath, B.; Niu, Z.; Mitra, A. K. Observation of Short-Term Variations in the Clay Minerals Ratio after the 2015 Chile Great Earthquake $$(8.3M_{\mathrm{w}})$$ Using Landsat 8 OLI Data. *J. Earth Syst. Sci.* **2019**, *128* (5), 117.

(7) Yousefi, T.; Aliyari, F.; Abedini, A.; Calagari, A. A. Integrating Geologic and Landsat-8 and ASTER Remote Sensing Data for Gold Exploration: A Case Study from Zarshuran Carlin-Type Gold Deposit, NW Iran. *Arab. J. Geosci.* **2018**, *11* (17), 482.

(8) Fereydooni, H.; Mojeddifar, S. A Directed Matched Filtering Algorithm (DMF) for Discriminating Hydrothermal Alteration Zones Using the ASTER Remote Sensing Data. *Int. J. Appl. Earth Obs. Geoinf.* **2017**, *61*, 1–13.

(9) Rejith, R. G.; Sundararajan, M. Mapping of Mafic-Ultramafic Rock Units in Late Archean Bhavani Complex, Southern India Using ASTER Thermal Bands. In *Shear Zones and Crustal Blocks of Southern India*; 2018; pp 34–40.

(10) Rani, N.; Mandla, V. R.; Singh, T. Performance of Image Classification on Hyperspectral Imagery for Lithological Mapping. *J. Geol. Soc. India* **2016**, *88* (4), 440–448.

(11) Basavarajappa, H. T.; Jeevan, L.; Rajendran, S.; Manjunatha, M. C. Aster Mapping of Limestone Deposits and Associated Lithounits of Parts of Chikkanayakanahalli, Southern Part of Chitradurga Schist Belt, Dharwar Craton, India. *J. Indian Soc. Remote Sens.* **2019**, *47* (4), 693–703.

(12) Hu, B.; Xu, Y.; Wan, B.; Wu, X.; Yi, G. Hydrothermally Altered Mineral Mapping Using Synthetic Application of Sentinel-2A MSI, ASTER and Hyperion Data in the Duolong Area, Tibetan Plateau, China. *Ore Geol. Rev.* **2018**.

(13) van der Meer, F. D.; van der Werff, H. M. A.; van Ruitenbeek, F. J. A.; Hecker, C. A.; Bakker, W. H.; Noomen, M. F.; van der Meijde, M.; Carranza, E. J. M.; Smeth, J. B. de; Woldai, T. Multi- and Hyperspectral Geologic Remote Sensing: A Review. *Int. J. Appl. Earth Obs. Geoinf.* **2012**, *14* (1), 112–128.

(14) Hosseinjani, M.; Tangestani, M. H. Mapping Alteration Minerals Using Sub-Pixel Unmixing of Aster Data in the Sarduiyeh Area, Se Kerman, Iran. *Int. J. Digit. Earth* **2011**.

(15) Hosseinjani Zadeh, M.; Tangestani, M. H.; Roldan, F. V.; Yusta, I. Sub-Pixel Mineral Mapping of a Porphyry Copper Belt Using EO-1 Hyperion Data. *Adv. Sp. Res.* **2014**, *53* (3), 440–451.

(16) Modabberi, S.; Ahmadi, A.; Tangestani, M. H. Sub-Pixel Mapping of Alunite and Jarosite Using ASTER Data; a Case Study from North of Semnan, North Central Iran. *Ore Geol. Rev.* **2017**. 80, 429-436.

(17) Salje, E.; Werneke, C. The Phase Equilibrium between Sillimanite and Andalusite as Determined from Lattice Vibrations. *Contrib. to Mineral. Petrol.* **1982**, *79* (1), 56–67.

(18) Abubakar, A. J.; Hashim, M.; Pour, A. B.; Musa, S. I.; Amusuk, D. J. Per-Pixel and Sub-Pixel Mapping of Alteration Minerals Associated with Geothermal Systems Using ASTER SWIR Data. *IOP Conf. Ser. Earth Environ. Sci.* **2018**, *169*, 012086.

(19) Abedi, M.; Norouzi, G.-H.; Bahroudi, A. Support Vector Machine for Multi-Classification of Mineral Prospectivity Areas. *Comput. Geosci.* **2012**, *46*, 272–283.

(20) Eslami, A.; Ghaderi, M.; Rajendran, S.; Pour, A. B.; Hashim, M. Integration of ASTER and Landsat TM Remote Sensing Data for Chromite Prospecting and Lithological Mapping in Neyriz Ophiolite Zone, South Iran. *Resour. Geol.* **2015**, *65* (4), 375–388.

(21) Ranjbar, H.; Honarmand, M.; Moezifar, Z. Application of the Crosta Technique for Porphyry Copper Alteration Mapping, Using ETM+ Data in the Southern Part of the Iranian Volcanic Sedimentary Belt. *J. Asian Earth Sci.* **2004**, *24* (2), 237–243.

(22) Moghtaderi, A.; Moore, F.; Ranjbar, H. Application of ASTER and Landsat 8 Imagery Data and Mathematical Evaluation Method in Detecting Iron Minerals Contamination in the Chadormalu Iron Mine Area, Central Iran. *J. Appl. Remote Sens.* **2017**, *11* (1), 016027.

(23) Kayet, N.; Pathak, K.; Chakrabarty, A.; Sahoo, S. Mapping the Distribution of Iron Ore Minerals and Spatial Correlation with Environmental Variables in Hilltop Mining Areas. *Environ. Earth Sci.* **2018,** 77(8), 308.

(24) Sun, T.; Chen, F.; Zhong, L.; Liu, W.; Wang, Y. GIS-Based Mineral Prospectivity Mapping Using Machine Learning Methods: A Case Study from Tongling Ore District, Eastern China. *Ore Geol. Rev.* **2019**, *109*, 26–49.

(25) Sojdehee, M.; Rasa, I.; Nezafati, N.; Abedini, M. V. Application of Spectral Analysis

to Discriminate Hydrothermal Alteration Zones at Daralu Copper Deposit, SE Iran. *Arab. J. Geosci.* **2016**, *9* (1), 41.

(26) Sundararajan, M.; Bhat, K. H.; Velusamy, S.; Babu, N.; Janaki, M. E. K.; Sasibhooshanan, S.; Das, P. N. M. Characterization of Ilmenite from Kerala Coastline, India:Implications in the Production of Synthetic Rutile. *J. Miner. Mater. Charact. Eng.* **2009**, *08* (06), 427–438.

(27) Rajendran, J.; Balasubramanian, G.; Thampi, P. K. Determination of Rare Earth Elements in Indian Coastal Monazite by ICP-AES and ICP-MS Analysis and Their Geochemical Significance. *Curr. Sci.* **2008**, *94* (10), 1296–1302.

(28) Sundararajan, M.; Bhat, K. H.; Babu, N.; Janaki, M. E. K.; Das, P. N. M. Characterization Studies on Ilmenite of Ullal and Suratkal along Karnataka Coastline, West Coast of India. *J. Miner. Mater. Charact. Eng.* **2009**, *08* (06), 479–493.

(29) Nair, A. G.; Babu, D. S. S.; Damodaran, K. T.; Shankar, R.; Prabhu, C. N. Weathering of Ilmenite from Chavara Deposit and Its Comparison with Manavalakurichi Placer Ilmenite, Southwestern India. *Journal of Asian Earth Sciences*. 2009, pp 115–122.

(30) Sajimol, S.; Rejith, R. G.; Lakshumanan, C.; Sundararajan, M. Sedimentology And Geochemistry Of Heavy Mineral Deposits along the Coast of Kanyakumari District, Tamil Nadu, India. In *Geochemistry and Mineralogy of Coastal Sediments in Tamil Nadu*; 2017; pp 145–161.

(31) Chaudhri, R. S.; Khan, H. M. M.; Kaur, S. Sedimentology of Beach Sediments of the West Coast of India. *Sediment. Geol.* **1981**, *30* (1–2), 79–94.

(32) Rajganapathi, V. C.; Jitheshkumar, N.; Sundararajan, M.; Bhat, K. H.; Velusamy, S. Grain Size Analysis and Characterization of Sedimentary Environment along Thiruchendur Coast, Tamilnadu, India. *Arab. J. Geosci.* **2013**, *6* (12), 4717–4728.

(33) Folk, R. L.; Ward, W. C. Brazos River Bar [Texas]; a Study in the Significance of Grain Size Parameters. *J. Sediment. Res.* **1957**.

(34) Mohan, P. M.; Rajamanickam, G. V. Depositional Environments: Inferred from Grain Size along the Coast of Tamil Nadu. *J. Geol. Soc. India* **1998**, *52* (1), 95–102.

(35) Milner, I. *Sedimentary Petrology Vol 1 & 2*; George Allen and Unwin, London, 1962.

(36) Galehouse, J. S. Counting Grain Mounts; Number Percentage vs. Number Frequency. *J. Sediment. Res.* **1969**, *39* (2), 812–815.

(37) Zarco-Perello, S.; Simões, N. Ordinary Kriging vs Inverse Distance Weighting: Spatial Interpolation of the Sessile Community of Madagascar Reef, Gulf of Mexico. *PeerJ* **2017**, *5*, e4078.

(38) Mathes, S. E.; Rasmussen, T. C. Combining Multivariate Statistical Analysis with Geographic Information Systems Mapping: A Tool for Delineating Groundwater Contamination. *Hydrogeol. J.* **2006**, *14* (8), 1493–1507.

(39) Magesh, N. S.; Chandrasekar, N.; Kaliraj, S. Mapping of Heavy Mineral Placers through Marine GIS Expert System: A Case Study in Kalaignanapuram Coastal Stretch, Southeast Coast of Tamil Nadu, India. *Arab. J. Geosci.* **2015**.

(40) Sundararajan, M. Occurrence, Distribution and Grain Micro-Textures of Light Heavy Placer Minerals in Thiruchendur-Ovari Beaches, South-Eastern Coast of India. *Sundararajan M.* **2018**, *20* (4), 399–411.

(41) Rejith, R. G.; Sundararajan, M.; Kaliraj, S. A Geo-Processing Modeling of Deltaic Suspended Sediment Variability. *J. Geovisualization Spat. Anal.* **2018**, *2* (2), 13.

(42) Dozier, J. Spectral Signature of Alpine Snow Cover from the Landsat Thematic Mapper. *Remote Sens. Environ.* **1989**.

(43) Kokhanovsky, A.; Schreier, M. The Determination of Snow Specific Surface Area, Albedo and Effective Grain Size Using AATSR Space- borne Measurements. *Int. J. Remote Sens.* **2009**, *30* (4), 919–933.

(44) Xiao, J.; Shen, Y.; Tateishi, R.; Bayaer, W. Development of Topsoil Grain Size Index for Monitoring Desertification in Arid Land Using Remote Sensing. *Int. J. Remote Sens.* **2006**, *27* (12), 2411–2422.

(45) Koren, H. *Snow Grain Size from Satellite Images*; 2009.

(46) Haq, M. A. Comparative Analysis of Hyperspectral and Multispectral Data for

Mapping Snow Cover and Snow Grain Size. In *International Archives of the Photogrammetry, Remote Sensing and Spatial Information Sciences - ISPRS Archives*; 2014.

(47) Pilong, S.; Bihong, F.; Thomas, C.; Qiang, G.; Huan, X.; Xiuyan, C.; Yuanxu, M.; Guoliang, X. Desertification Monitoring Using the ASTER Global Emissivity Dataset. In *2017 IEEE International Geoscience and Remote Sensing Symposium (IGARSS)*; IEEE, 2017; pp 4501–4504.

(48) Apple. Aperture 3 User Manual. *ASD Document 600540 Rev. J*. 2010, pp 1–908.

(49) Prasad, K. A.; Gnanappazham, L. Discrimination of Mangrove Species of Rhizophoraceae Using Laboratory Spectral Signatures. In *2014 IEEE Geoscience and Remote Sensing Symposium*; IEEE, 2014; pp 2906–2909.

(50) Beal, D.; Eamon, M. *Preliminary Results of Testing and a Proposal for Radiometric Error Correction Using Dynamic, Parabolic Linear Transformations of "Stepped" Data*; 1996.

(51) Prasad, K. A.; Gnanappazham, L.; Selvam, V.; Ramasubramanian, R.; Kar, C. S. Developing a Spectral Library of Mangrove Species of Indian East Coast Using Field Spectroscopy. *Geocarto Int.* **2015**, *30* (5), 580–599.

(52) Matar, S. S.; Bamousa, A. O. Integration of the ASTER Thermal Infra-Red Bands Imageries with Geological Map of Jabal Al Hasir Area, Asir Terrane, the Arabian Shield. *J. Taibah Univ. Sci.* **2013**, *7* (1), 1–7.

(53) Pal, S. K.; Majumdar, T. J.; Bhattacharya, A. K.; Bhattacharyya, R. Utilization of Landsat ETM+ Data for Mineral-Occurrences Mapping over Dalma and Dhanjori, Jharkhand, India: An Advanced Spectral Analysis Approach. *Int. J. Remote Sens.* **2011**, *32* (14), 4023–4040.

(54) Green, A. A.; Berman, M.; Switzer, P.; Craig, M. D. A Transformation for Ordering Multispectral Data in Terms of Image Quality with Implications for Noise Removal. *IEEE Trans. Geosci. Remote Sens.* **1988**.

(55) Kruse, F. A.; Boardman, J. W.; Huntington, J. F. Comparison of Airborne

Hyperspectral Data and Eo-1 Hyperion for Mineral Mapping. *IEEE Trans. Geosci. Remote Sens.* **2003**, *41* (6), 1388–1400.

(56) Vishnu, S.; Nidamanuri, R. R.; Bremananth, R. Spectral Material Mapping Using Hyperspectral Imagery: A Review of Spectral Matching and Library Search Methods. *Geocarto Int.* **2013**, *28* (2), 171–190.

(57) Shanmugam, S.; SrinivasaPerumal, P. Spectral Matching Approaches in Hyperspectral Image Processing. *Int. J. Remote Sens.* **2014**, *35* (24), 8217–8251.

(58) Kruse, F. A.; Lefkoff, A. B.; Boardman, J. W.; Heidebrecht, K. B.; Shapiro, A. T.; Barloon, P. J.; Goetz, A. F. H. The Spectral Image Processing System (SIPS)—Interactive Visualization and Analysis of Imaging Spectrometer Data. *Remote Sens. Environ.* **1993**, *44* (2–3), 145–163.

(59) De Carvalho, O. .; Meneses, P. R. Spectral Correlation Mapper (SCM): An Improvement on the Spectral Angle Mapper (SAM). In: Summaries of the 9th JPL Airborne Earth Science Workshop. *Summ. 9th JPL Airborne Earth Sci. Work.* **2000**, No. JPL Publication 00-18, 9 p.

(60) Congalton, R. G. A Review of Assessing the Accuracy of Classifications of Remotely Sensed Data. *Remote Sens. Environ.* **1991**, *37* (1), 35–46.

(61) Cohen, J. A Coefficient of Agreement for Nominal Scales. *Educ. Psychol. Meas.* **1960**, *20* (1), 37–46.

(62) Boardman, J. W. Leveraging the High Dimensionality of AVIRIS Data for Improved Sub-Pixel Target Unmixing and Rejection of False Positives: Mixture Tuned Matched Filtering. *7th JPL Airborne Earth Sci. Work.* **1998**.

(63) Goodarzi Mehr, S.; Ahadnejad, V.; Abbaspour, R. A.; Hamzeh, M. Using the Mixture-Tuned Matched Filtering Method for Lithological Mapping with Landsat TM5 Images. *Int. J. Remote Sens.* **2013**.

(64) Boardman, J. W.; Kruse, F. a.; Green, R. O. Mapping Target Signatures via Partial Unmixing of AVIRIS Data. *Summ. JPL Airborne Earth Sci. Work.* **1995**.

(65) Pour, A. B.; Hashim, M. Hydrothermal Alteration Mapping from Landsat-8 Data, Sar

Cheshmeh Copper Mining District, South-Eastern Islamic Republic of Iran. *J. Taibah Univ. Sci.* **2015**, *9* (2), 155–166.

(66) Mohanan, S.; Tripathy, S. K.; Ramamurthy, Y.; Kumar, C. R. Application of High Tension Roll Separator for the Separation of Titanium Bearing Minerals: Process Modeling and Optimization. *J. Miner. Mater. Charact. Eng.* **2012**, *11* (10), 1005–1011.

(67) Laxmi, T.; Srikant, S. S.; Rao, D. S.; Bhima Rao, R. Beneficiation Studies on Recovery and In-Depth Characterization of Ilmenite from Red Sediments of Badlands Topography of Ganjam District, Odisha, India. *Int. J. Min. Sci. Technol.* **2013**, *23* (5), 725–731.

(68) Jordens, A.; Sheridan, R. S.; Rowson, N. A.; Waters, K. E. Processing a Rare Earth Mineral Deposit Using Gravity and Magnetic Separation. *Miner. Eng.* **2014**.

(69) Curtis C. Mason, R. L. F. Differentiation of Beach, Dune, and Aeolian Flat Environments by Size Analysis, Mustang Island, Texas. *SEPM J. Sediment. Res.* **1958**, *Vol. 28*.

(70) Gerald M. Friedman. Dynamic Processes and Statistical Parameters Compared for Size Frequency Distribution of Beach and River Sands. *SEPM J. Sediment. Res.* **1967**.

(71) Hardarshan S. Valia, Barry Cameron. Skewness as a Paleoenvironmental Indicator. *SEPM J. Sediment. Res.* **1977**.

(72) Wang, P.; Davis, R. A.; Kraus, N. C. Cross-Shore Distribution of Sediment Texture under Breaking Waves along Low-Wave-Energy Coasts. *J. Sediment. Res.* **1998**, *68* (3), 497–506.

(73) Angusamy, N.; Rajamanickam, G. V. Coastal Processes of Central Tamil Nadu, India: Clues from Grain Size Studies. *Oceanologia* **2007**.

(74) SUTHERLAND, R. A.; LEE, C.-T. Discrimination between Coastal Subenvironments Using Textural Characteristics. *Sedimentology* **1994**, *41* (6), 1133–1145.

(75) FOLK, R. L. A REVIEW OF GRAIN- SIZE PARAMETERS. *Sedimentology*. 1966.

(76) Friedman, G. M. On Sorting, Sorting Coefficients, and the Lognormality of the Grain-Size Distribution of Sandstones. *J. Geol.* **1962**.

(77) Nageswara Rao, P. V.; Suryam, R. K.; Ranga Rao, V. Depositional Environment Inferred from Grain Size Parameters of the Beach Sediments between False Devi Point to Kottapatnam, Andhra Pradesh Coast. *J. Geol. Soc. India* **2005**, *65*, 317–324.

(78) Patrick McLaren. An Interpretation of Trends in Grain Size Measures. *SEPM J. Sediment. Res.* **1981**, *Vol. 51*.

(79) Rao, S.; Shirlal, K. G.; Rao, N. B. S. Sediment Trend Matrix Analysis along Shore Normal Transects off Surathkal Beach, Karnataka. *J. Geol. Soc. India* **2003**, *61*, 215–219.

(80) Natesan., U.; Sundararajan, M.; Md Sattar Hussain, S. Sediment Transport along Vedaranyam Coast South East India. *Eng. Today* **2007**, *9*, 41–45.

(81) Noujas, V.; Thomas, K. V.; Ajeesh, N. R. Shoreline Management Plan for a Protected but Eroding Coast along the Southwest Coast of India. *Int. J. Sediment Res.* **2017**, *32* (4), 495–505.

(82) Baba, M.; Shahul Hameed, T. S.; Kurian, N. P.; Thomas, K. V.; Harish, C. M.; Rameshkumar, M.; Mohahanan, S. *Long-Term Wave and Beach Data of Kerala Coast.*; Thiruvananthapuram, 1984.

(83) Thomas, K. V.; Kurian, N. P.; Sundar, V.; Sannasiraj, S. A.; Badarees, K. O.; Saritha, V. K.; Abhilash, S.; Sarath, L. G.; Srikanth, K. Morphological Changes Due to Coastal Structures along the Southwest Coast of India. In *Indo-Brazil Workshop*; 2010; pp 125–133.

(84) Noujas, V.; Thomas, K. V.; Sheela Nair, L.; Hameed, T. S. S.; Badarees, K. O.; Ajeesh, N. R. Management of Shoreline Morphological Changes Consequent to Breakwater Construction. *Indian J. Mar. Sci.* **2014**, *43* (1), 54–61.

(85) Sajeev, R.; Chandramohan, P.; Josanto, V.; Sanakaranarayanan, V. N. Studies on Sediment Transport along Kerala Coast,South West Coast of India. *Indian J. Mar. Sci.* **1997**, *26*, 11–15.

(86) Thankappan, N.; Varangalil, N.; Kachapally Varghese, T.; Njaliplackil Philipose, K. Coastal Morphology and Beach Stability along Thiruvananthapuram, South-West Coast of India. *Nat. Hazards* **2018**.

(87) Krishnan, S.; Viswanathan, G.; Balachandran, K. Heavy Mineral Sand Deposits of Kerala. *Explor. Res. At. Miner.* **2001**, *13*, 111–146.

(88) Jayaraju, N. Controls on Formation and Distribution of Heavy Minerals along Southern Tip of India. *J. Ind. Geophys. Union* **2004**, *8* (3), 191–194.

(89) Reineck, H. E.; Singh, I. . *Depositional Sedimentary Environments: With Reference to Terrigenous Clastics Springer Study Edition*; Springer, 1980.

(90) Chandrasekar, N.; Mujabar, P. S.; Rajamanickam, G. V. Investigation of Heavy-Mineral Deposits Using Multispectral Satellite Data. *Int. J. Remote Sens.* **2011**, *32* (23), 8641–8655.

(91) Boardman, J. W.; Huntington, J. F. Mineral Mapping with 1995 AVIRIS Data. In *Summaries of the Sixth Annual JPL Airborne Research Science Workshop*; JPL Publication 96-4, 1996; pp 9–11.

Chapter 3

Mineral mapping using Machine learning algorithms and Landsat 8 imagery

3.1. Abstract

Machine learning algorithms (MLAs) provides a supervised classification of high-dimensional data like satellite imageries for mapping lithological units and mineral occurrences on Earth's surface. Here, four widely used MLAs like RFC, SVM, MLC, and ANN were used for mapping beach minerals and inland sand deposits. The Visible-NIR-SWIR seven bands of multispectral remote sensing dataset Landsat-8 OLI imagery is used in the present study. The accuracy assessment using overall accuracy and Kappa coefficient reveals that RFC and SVM show better performance for mapping beach minerals and inland sand deposits. The results confirm the ability of MLAs to map mineral sands on the Earth's surface.

3.2.Introduction

Since the time of first Landsat data product called Lansat-1 launched in the year 1972 onwards, remote sensing applications have made a breakthrough in the field of mineral exploration and lithological mapping.[1] Geological analysis of Landsat-1 data of Nevada suggests Seventeen (17) areas as favourable targets for mineral exploration, especially limonitic iron oxide.[2] Landsat series of satellite data products such as Landsat 5, Landsat 7, and finally the Landsat 8 have contributed immense information on the lithology and precious minerals and metals on the surface of Earth. Through the years, it can be noticed that the advancements in sensor technology get paralleled with innovations in software and computing technologies. This paved the invention for new image processing algorithms, and target detection algorithms like principal components analysis, band ratio that facilitates the accurate mapping of mineral occurrences. The colour composite, band ratio, and principal components analysis extracts the occurrence of clay alteration in Landsat TM[3], Landsat ETM+[4] and Chromite mineralization from Landsat 8[5]. Mixture tuned matched filtering (MTMF) applied to Landsat TM, Landsat ETM+, and Landsat 8 identifies alteration minerals[6,7] and lithological units[8]. The SAM applied to Landsat TM, Landsat 7, and Landsat 8 data identify hydrothermal alteration minerals[9], lithological mapping[10], sulphide

deposits[11]. Linear spectral unmixing (LSU) applied to Landsat ETM+ identifies Hydrothermal Alteration minerals.[12]

Machine learning algorithms are data-driven algorithms developed based on the input data without relying on any predefined rule as a model. Since it offers an automated means of recognizing patterns in high-dimensional data, today ML algorithms are widely used as an image classification algorithms in remote sensing applications where it easily hands large volumes of satellite data.[13] Different MLC algorithms are compared for mapping mineral occurrences, and the best one will be selected based on cross-validation with testing points. RF classification outperforms Naive Bayes, SVM, *k*-Nearest Neighbors, and ANN for geological mapping using Landsat 7 ETM+ data.[13] The SVM approach provides better results than the ANN for lithological mapping using Landsat 8 OLI.[14] Random Forest shows better performance than Naïve Bayes, k Nearest Neighbour, and SVM for geological mapping using Landsat 4-5 TM.[15] The ML algorithms like NN, SVM, and RF performed better than the maximum likelihood classifier (MLC) on using the Landsat 8 and Landsat 7 data for mapping lithology.[16]

The beach sands of the Indian coast are bestowed with a good concentration of strategic minerals like ilmenite, rutile, monazite, zircon, sillimanite, garnet, and the altered form of ilmenite called leucoxene.[17] These minerals are collectively called heavy minerals due to high specific gravity of about 2.9, and also these minerals are economically important due to their immense applications in wide areas of industries. The rutile and synthetic rutile from ilmenite having high TiO_2 content are used for the production of TiO_2 products such as titania, TiO_2 pulp, metal, etc.[18] Rare earth elements are produced from monazite[19], zirconia from zircon, synthetic mullite from sillimanite for refractories applications, and garnet is as abrasive material used for glass polishing[20]. A combination of magnetic, electrostatic, and gravity separation units is used for recovering these minerals from beach sands. Detailed studies were carried out on the depositional environment, mineralogy[21], and geochemical characteristics[22] of these strategic minerals. An attempt has made for mapping the beach minerals using advanced hyperspectral analysis of Landsat and ASTER data. The silica sand deposits in Cherthala region have the SiO_2 content of 96.5% and are widely used as a 'special grade glass making sand'.[23]

The present study aims to compare the performance of four machine learning algorithms such as Random Forest Classifier, Support Vector Machine, Maximum Likelihood Classifier,

and Artificial Neural Network for mapping the beach minerals and the inland silica sand deposits using multispectral Landsat 8 OLI imagery.

3.3.Materials and Methods

The flow sheet showing the proposed methodology adopted for the present study is given in Figure 3.1.

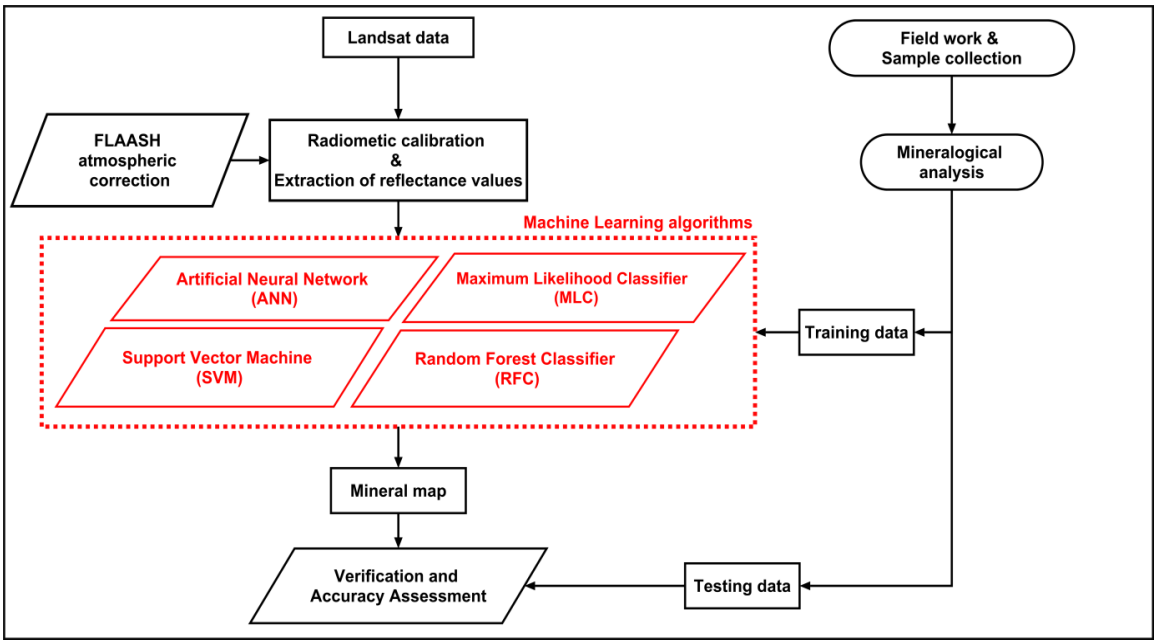

Figure 3.1: Flow sheet showing the proposed methodology adopted for the present study.

3.3.1. Random Forest Classifier

RF is a supervised ensemble algorithm widely used for both classification and regression where it combines the performance of multiple decision trees for generating the results.[24] The Random Forest method was widely used for lithological mapping using Landsat[15,25], AVIRIS-NG[26], Sentinel-2A[27] and also identifying gold deposits from Landsat Thematic Mapper (TM)[28]. The decision trees with the inbuilt nature of feature selection make the RF method one of the most robust classification techniques that can be applied to any large and correlated datasets.[26] Each decision trees will generate results, and based on majority rule, a final class is selected. Decision trees and randomness are two advantages of RF. Apart from other classification techniques, here, a 'forest' is constructed comprises of multiple decision trees instead of a single classifier, which facilitates lower sensitivity towards over-fitting.[29] The training data is selected via random sampling through a process of bootstrap aggregation, known as bagging.[30] At each node of the classifier, a random subset of

variables was selected from the input data and made available to the classifier to split at each node. The split at the node is controlled by the rank assigned to the randomly selected variables based on the value of Gini index calculated at each node.[31] While bagging randomly selects data, some variables will not get selected or duplicates. Usually, about 63.2% if the variable was taken for training the model, which is called training subset, and the remaining "out-of-bag" samples of about 37.8% are used for validation of results.[25] The Random Forest classification was carried out using EnMAP-Box, a free and open-source plug-in available in QGIS desktop software using the parameter number of trees as 500.

3.3.2. Support Vector Machine

Support vector machine (SVM) is a supervised MLA developed based on statistical learning theory.[32] It was proposed by Vapnik and Chervonenkis in 1963[33] and successfully used for pattern recognition and image classification[34]. The SVM provides high classification accuracy for complex spectral class distributions[35] and a small set of learning data compared to traditional methods[14]. The SVM generates a hyperplane for the optimal separation of classes by maximising the separation margin (optimal separator) between them. The classes exist nearest to these margins, or the boundaries of decision are called support vectors. Thus the n-dimensional hyperplane with the optimal margin separated the data into support vectors and misclassified instances. Recently SVM classification has been successfully used for lithological mapping using Landsat[14,15], Sentinel-2A Data[27], ASTER data[36], AVIRIS-NG[26], and also widely used for exploring porphyry-Cu deposits[37,38] and gold deposits[39]. The best performance of SVM truly depends on the selection of parameters, mainly the Kernel function along with the penalty parameter and the gamma kernel. In order to avoid the non-linear relationships between the input data, they were efficiently transformed into a space of higher dimension with the help of widely used kernel functions like linear, polynomial, radial basis function (RBF), and sigmoid. The possible degree of non- linearity exists in SVM model will be handled by gamma parameter, whereas the level of possible error exists in the input data called training errors will be controlled by the penalty Parameter.[40] The RBF kernel with a penalty parameter of 100 and a gamma parameter of inverse of the input band numbers shows the best interpolation capabilities compared to other kernel functions.[41,42] So for the present study, RBF is selected as the kernel, the penalty parameter is 100 and a gamma parameter is 0.167.[14] The SVM classification was performed using the ENVI image processing software.

3.3.3. Maximum Likelihood Classifier

The maximum likelihood classification (MLC) is a widely used supervised classification algorithm developed based on the multivariate distribution (normal /Gaussian) of data.[43] In remote sensing, it was widely used for lithological mapping[27] and mapping pegmatites[44] using Sentinel-2A, ASTER, and Landsat-8 OLI data, also lithological classification using Landsat ETM+ and ASTER images.[45] The classification completely rely on the hypothesis that each class of data follows a multivariate probability density function, and the assignment of the pixel to a class depends on the highest probability of belonging to that particular class.[46] Here not the minimum Euclidean distance, but the direction and shape of hyper-ellipsoids representing the distribution of pixels belong to a unique class, are used for evaluating the probability.[47] The parameters such as location, shape, and size of ellipsoids are defined from statistics of individual classes such as its mean vector and variance-covariance matrices.[48] The probability of belonging to a particular class is defined by a set of concentric ellipses drawn with the centre on the mean vector of the class. The probability of memberships descents away from the mean center. These ellipsoidal "equi-probability contours" act as the decision boundaries in the MLC classifier.[49] In the present study, the MLC classification was applied to the Landsat 8 OLI dataset using the ENVI image processing software.

3.3.4. Artificial Neural Network

Artificial neural network (ANN) also called neural network (NN) is particularly used for pattern recognition, solving complex tasks, generating prediction model from input data and classify image data into unique classes based on artificial intelligence technique.[50,51] It was widely deployed for identifying gold-silver deposits[52,53] and also for lithological mapping using Landsat 8 OLI[14], Sentinel-2A Data[27], etc. Here the algorithm attempts to solve the problems and recognize the patterns by exactly simulating the same way by which the human's brain does.[54] The architecture is similar to a biological neural system where it consists of a large number of simple processing elements called nodes or neurons.[54] It is a multi-layered neural network comprises of three layers, such as an input layer, a middle layer (hidden layer), and an output layer, each consists of one or more nodes or neurons. The nodes are gets linked by weighted connections and perform interactive experiments for generating reasonable results from the given datasets. The input data are multiplied by weighted functions assigned to middle and output layer neurons, and their product is summed up and

processed using a log-sigmoid transfer function to generate the results. Each layer of the network is trained by doing forward and backward computation, commonly known as back-propagation training algorithm, using input data and the obtained results. The back-propagation training algorithm allows the network to adjust the weights of the neurons by analyzing the errors of the output results.[52] Thus it can be seen that the algorithm involves two stages, training stage where the back-propagation algorithm trains the network to achieve a minimal error, and a classifying stage where the data is classified using a feed-forward structure where it generates the output.[55] For the present study, a multi-layer feed-forward ANN method was applied to the Landsat 8 OLI dataset using the ENVI image processing software. The parameters used for executing the ANN includes logistic activation function, training threshold contribution value of 0.9, the training rate of 0.2, the training momentum of 0.9, and the training root mean square (RMS) exit criterion selected was 0.1.[27]

3.3.5. Accuracy evaluation

The commonly used Overall accuracy and Kappa coefficient are used for evaluating ML algorithms for classifying the Landsat 8 OLI data.[56,57] The complete elements in the error matrix are used for generating the Kappa coefficient, whereas only the diagonal elements are used in the case of overall accuracy. The Kappa statistics provide a measure of similarity between the observation datasets and the predicted or classified data using a value ranging from 0 to 1 where 1 represents the best match.[58]

3.4.Results and discussion

3.4.1. Mapping of Beach minerals

The FLAASH atmospherically corrected seven bands (band1 to band 7) of Landsat 8 OLI imagery is used for mapping beach minerals. The average spectra of training ROIs are shown in Figure 3.2. The classification classes used for the present study include vegetation, urban/settlement, waterbody, inland sand deposits and beach sands. The beach sand is again subdivided into beach sand 1(>10% THM) and beach sand 2 (light Minerals). The sampling points where the THM is >10% is taken as beach sand 1 and the remaining locations were assigned to beach sand 2. About 69 sampling stations were used for the present study in which 40 sampling stations were assigned as training sites, and 29 sampling stations were taken as testing sites for checking the accuracy of the mapping algorithms. The sand types such as inland sand deposits (quartz), beach sand 1, and beach sand 2 show almost the same

reflectance in the visible bands, and then it shows an increase in NIR and SWIR 1, which is due to bright white colour and thin surface covering.

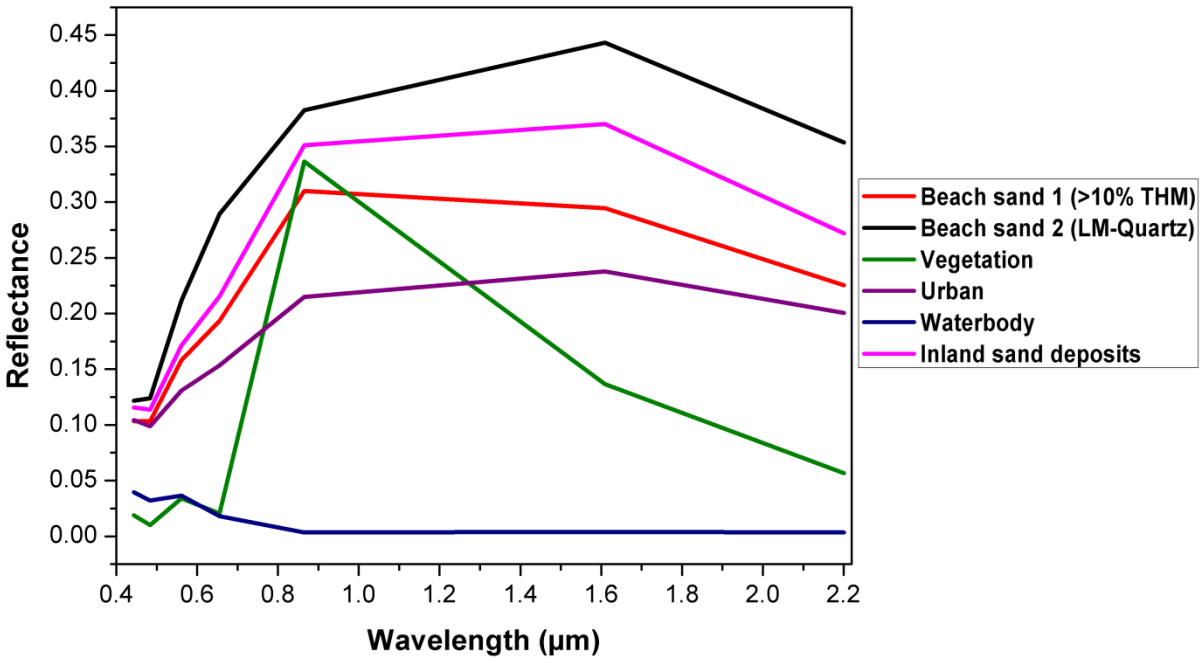

Figure 3.2: Average spectra of training ROIs collected for mapping beach minerals.

The reflectance for heavy minerals shows a decrease from visible bands until reached SWIR2 compared to light minerals due to the addition of high-density heavies such as ilmenite, rutile, etc.[59] The beach minerals correspond to the locations of Varkala and Kovalam contain heavy minerals (THM is about 80.04%) with major content of ilmenite followed by sillimanite, rutile, monazite, zircon, etc. The presence of ferrous oxide minerals makes the beach sand to possess strong absorption in band 7.[14] The accuracy assessment of four ML algorithms for mapping beach minerals is given in Table 3.1. On analysing the accuracy assessment results, it is clear all the ML algorithms show the best results with average values of overall accuracy 84.10488% and Kappa coefficient of 0.813675. Out of four, the RFC provides the best results with an overall accuracy of 84.4925% and Kappa coefficient of 0.8184 followed by ANN with the values of 84.3515% and 0.8162, then comes the SVM with 84.3515% and 0.8161, and finally the MLC with accuracy values of 83.224% and 0.804.

Table 3.1: Results of accuracy assessment for MLAs

Minerals	Machine Learning Algorithms	Overall accuracy (%)	Kappa coefficient
Beach Minerals	Random Forest Classifier	84.4925	0.8184
	Support Vector Machine	84.3515	0.8161
	Maximum Likelihood Classifier	83.224	0.804
	Artificial Neural Network	84.3515	0.8162
Silica sand deposits	Artificial Neural Network	96.9855	0.9411
	Random Forest Classifier	97.7635	0.9563
	Support Vector Machine	97.8242	0.9574
	Maximum Likelihood Classifier	95.7093	0.9181

The mineral classification map showing the distribution of heavy minerals using random forest classifier (RFC) for the study area is shown in Figure 3.3(a-c). The mineral maps correspond to four different ML algorithms for Kovalam coast is shown in Figure 3.4(a-d). The ANN and MLC (Figure 3.4 (b and c)) generate more pixels of heavy minerals apart from actual locations whereas in the case of SVM, very few pixels were noticed. The RFC generates the exact locations with high concentration of heavy minerals compared to others. The best performance of RFC for geological mapping was reported earlier but not in the case of beach minerals. RFC outperforms MLC and SVM for mapping serpentinite, talus and terrace deposits, red argillites, etc. from ASTER data.[60] RF again shows better performance than SVM for geological mapping using Landsat 4-5 TM.[15] Also it performed better than MLC for mapping lithology using Landsat-8 and Landsat-7 data.[16]

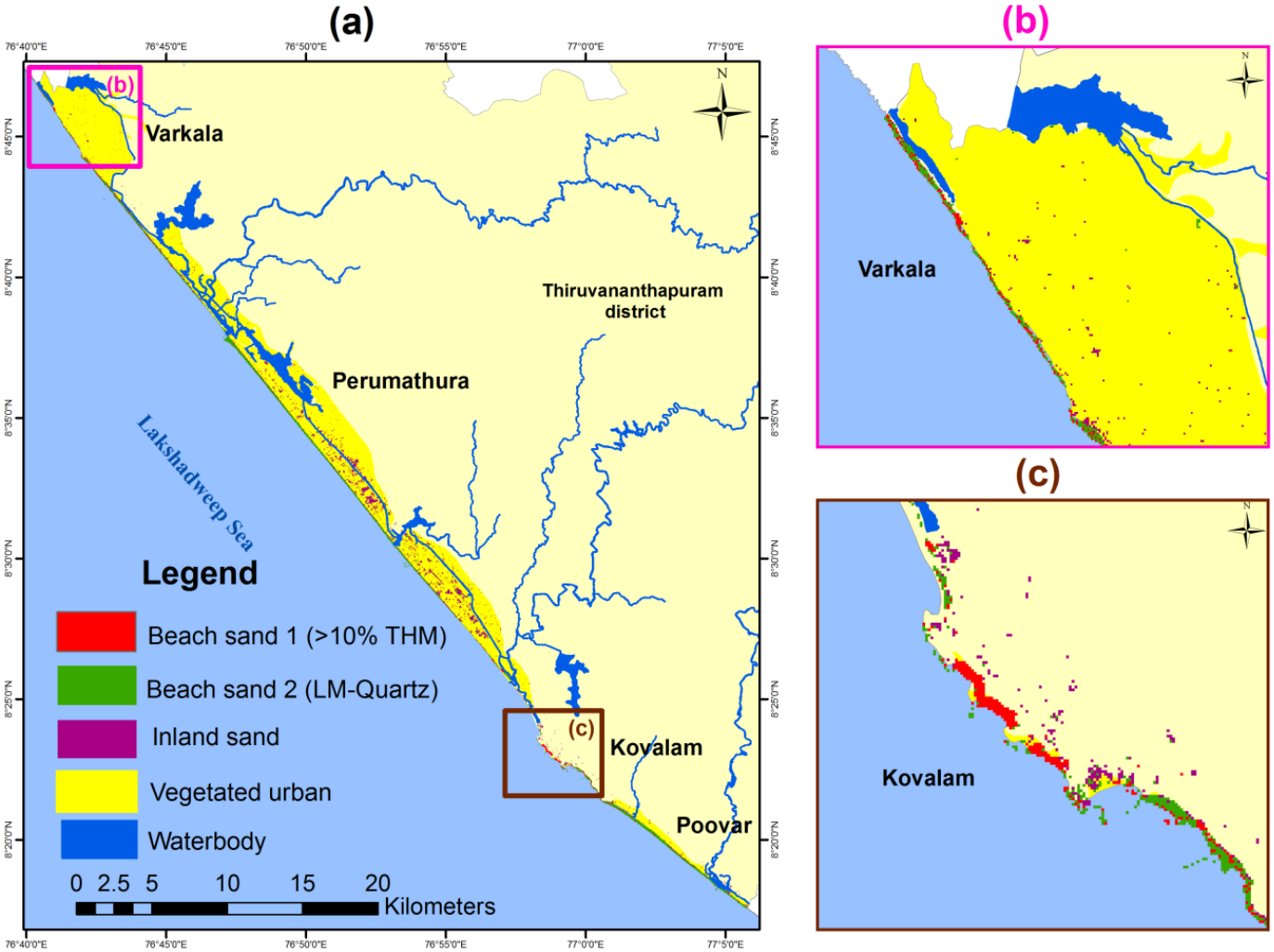

Figure 3.3: Mineral classification map showing distribution of heavy minerals using Random forest classifier (RFC) (a) Thiruvananthapuram district; (b) Varkala coast; (c) Kovalam coast.

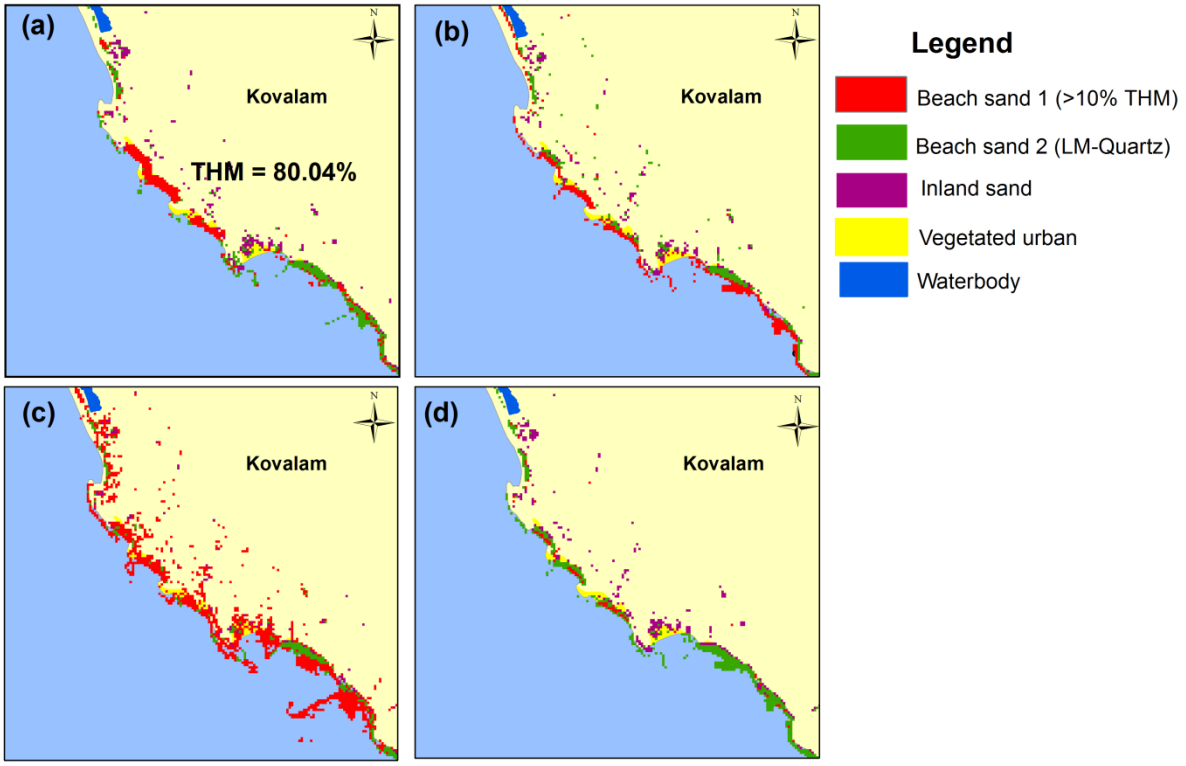

Figure 3.4: Mineral classification map showing distribution of heavy minerals for Kovalam coast using (a) RFC; (b) ANN; (c) MLC; (d) SVM.

3.4.2. Mapping of Silica sand deposits in Cherthala

The FLAASH atmospherically corrected seven bands of Landsat 8 OLI imagery were used for mapping the silica sand deposits. The average spectra of training ROIs selected for mapping the silica sand deposits in Cherthala are shown in Figure 3.5. The classification classes used for the present study are inland silica sand deposits, beach sand, vegetation, urban/settlement, and water body. About 21 sampling stations were used for the present study in which 11 sampling stations were assigned as training sites, and 10 sampling stations were taken as testing sites for checking the accuracy of the mapping algorithms. The sand types such as inland sand deposits (silica) and the beach sand show almost the same reflectance in the visible bands, and then it shows an increase in NIR and SWIR 1which is due to bright white colour and thin surface covering. The reflectance for inland sand deposits show a decrease from visible bands until it reached SWIR 2 compared to beach minerals may be due to the presence of soil particles.[59] The presence of hydroxyl and ferrous oxide minerals also possess strong absorption in band 7.[14]

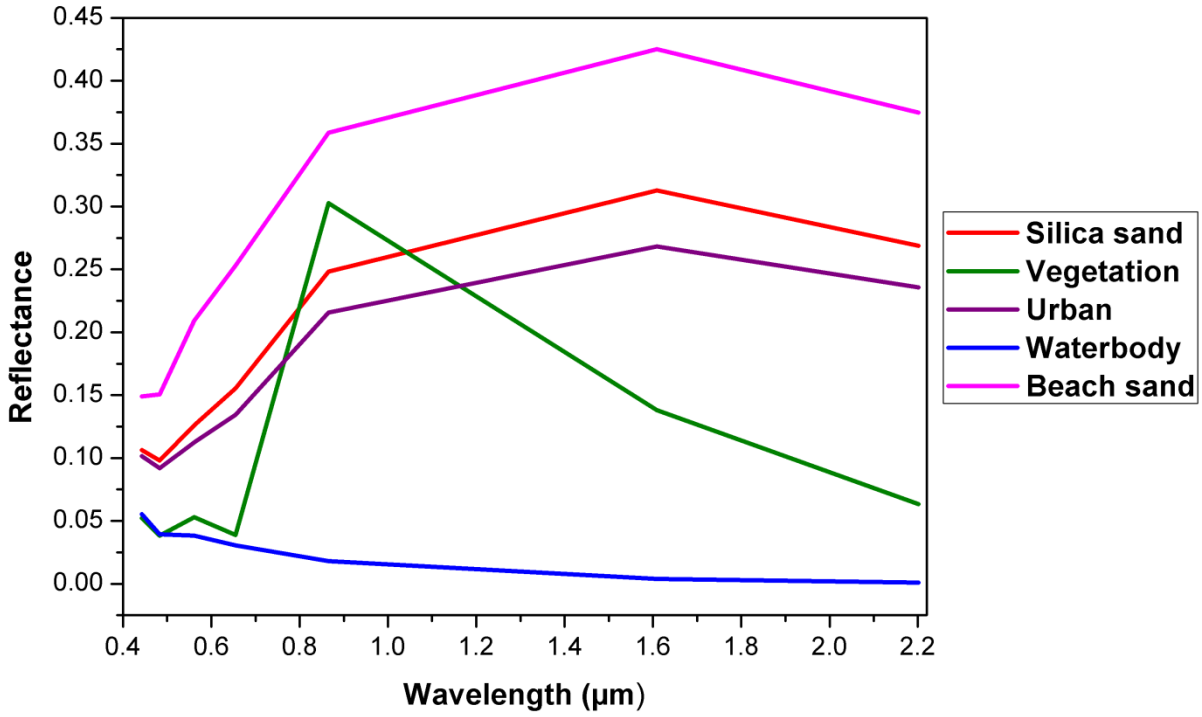

Figure 3.5: Average spectra of training ROIs collected for mapping inland silica sand.

Table 3.1 shows the accuracy results obtained for the four algorithms in mapping the silica sand deposits. The accuracy assessment clearly indicates that all the ML algorithms show good performance in mapping silica sand deposits with average values of overall accuracy and Kappa coefficient of 97.0706% and 0.9432%. The results show that SVM outperforms the other algorithms such as RFC, ANN, and MLC. The SVM shows an overall accuracy and Kappa coefficient of 97.8242% and 0.9574, followed by RFC with values of 97.7635% and 0.9563, ANN with values of 96.9855% and 0.9411, and finally, the least accuracy is shown by MLC with values of 95.7093% and 0.9181. The mineral classification map showing the distribution of inland silica sand deposits using support vector machine (SVM) is shown in Figure 3.6. The mineral classification maps showing the distribution of silica sand deposits in the Cherthala area using different ML algorithms are shown in Figure 3.7(a-d). On analysing the Figure 3.7, it is noticed that all the sampling points in the four classification maps are overlaying the pixels correspond to silica sand deposits. In the less accurate ANN derived Map (Figure 3.7(b)), comparatively more number of misclassification of pixels can be seen. In the case of RFC and MLC (Figure 9(c and d)), other classes like waterbody is not seen. These could able to showcase the accuracy of ANN over other ML algorithms.

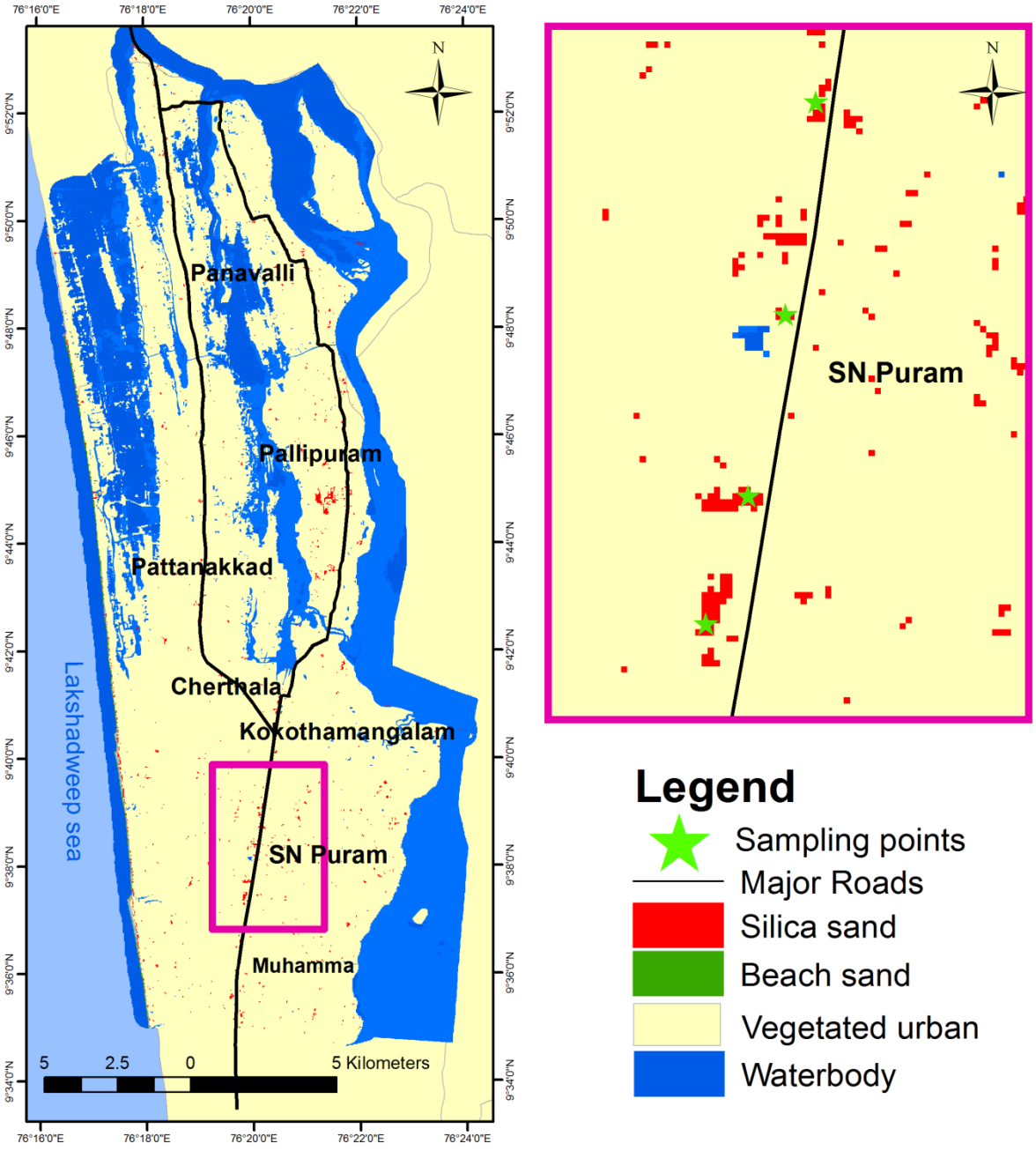

Figure 3.6: Mineral classification map showing distribution of inland silica sand deposits using support vector machine (SVM).

On comparing with others, the SVM map (Figure 3.7(a)) shows the accurate locations of silica sand deposits along with other classes. The better performance of SVM compared to ANN were also reported for mapping lithological units such as limestone, dolostone, andesite, etc. using Landsat 8 OLI data.[14] The SVM and RF performed better than MLC for the Landsat-8 and Landsat-7 data for mapping lithology.[16]

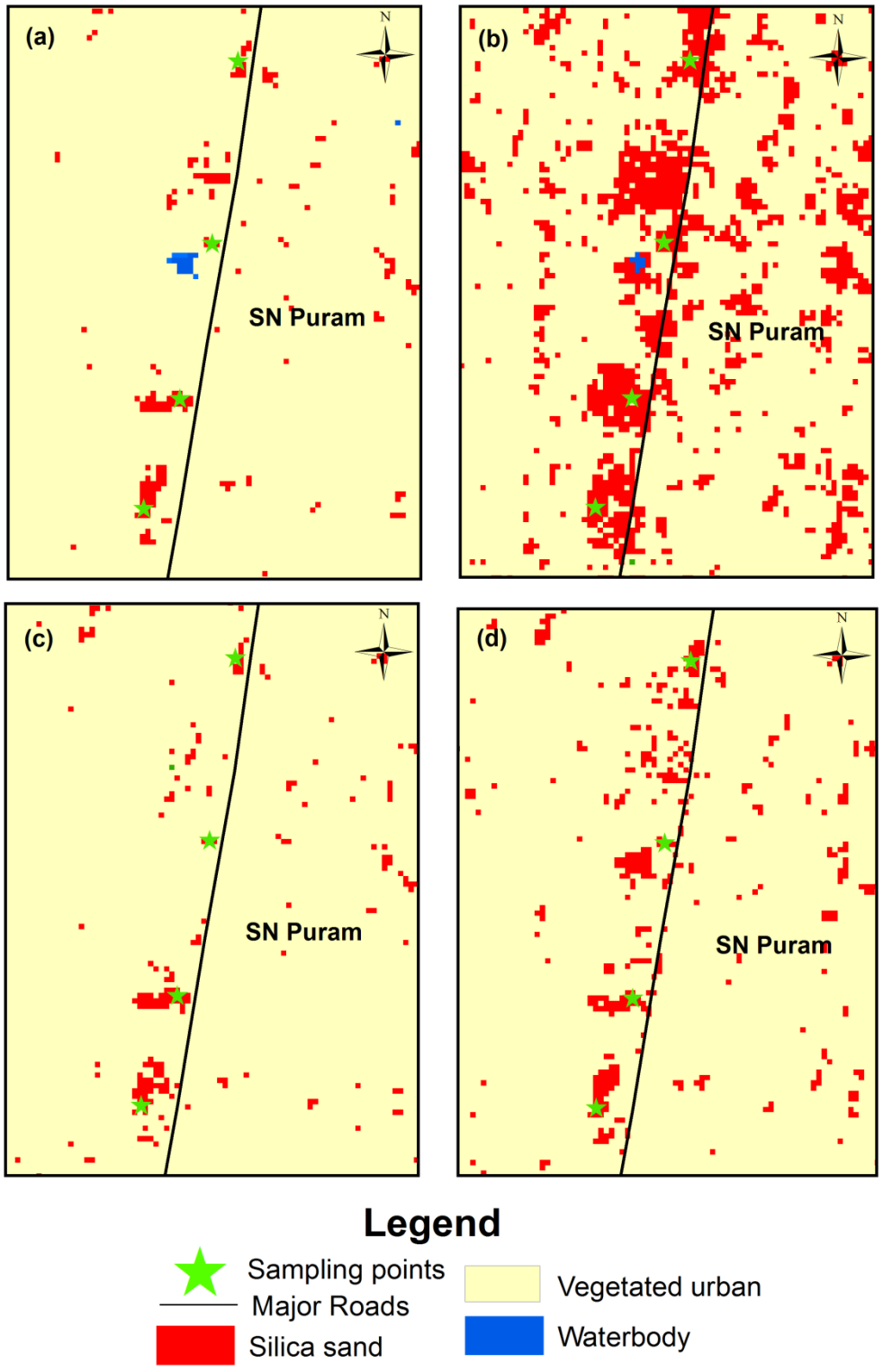

Figure 3.7: Mineral classification maps showing distribution of silica sand deposits in Cherthala area using (a) SVM; (b) ANN; (c) RFC; (d) MLC.

The training set of samples played an important role in the successful classification of minerals especially the sand minerals using multispectral data because there are chances of misclassification due to the presence of vegetation cover, atmospheric effects, soil presence, etc. The similarity in chemical composition, texture, and type of minerals acts as one of the prime hindrances for misclassification.[61] All these factors make a significant contribution to the spectral response of target materials, especially, minerals of sand type, which is not present in bulk as hard rock mineral. The hyperspectral analysis comprises of MNF transformation, pixel purity index (PPI), etc. followed by spectral angle mapper (SAM) classification using reference spectra of beach minerals collected at laboratory via spectroradiometer, reveals perfect mapping of ilmenite mineral (heavy mineral) and light minerals (quartz) along the coast of Varkala and Kovalam from Landsat 8 OLI imagery with overall accuracy and Kappa coefficient of 94.20% and 0.85. The same applied for identifying silica sand deposits of Cherthala reveals an overall accuracy of 90.476%. Both approaches of classification provide best results of above 80%, but on analysing the classified images, it can be concluded that the MLAs provide the accurate and visually satisfying distribution of mineral occurrences. In the case of beach sand minerals, it can be noticed that most of the pixels in the RFC classified image of Kovalam region having the highest heavy mineral concentration of about 80.04% correspond to heavy minerals than that obtained using SAM classification. In the case of silica sand deposits also, the results of SVM are optimized very well to the sampling stations. Here the difference may occur due to the selection of training sites for classification purposes. The RFC classification was carried out using the image spectra directly derived from the image at the sampling location rather than using the reference spectra measured using the minerals in the laboratory.

3.5.Conclusion

On comparing the four widely used MLAs for mapping the mineral sands using Landsat 8 OLI imagery, it can be concluded that the RFC and SVM show better performance for identifying the potential zones of beach minerals and inland sand deposits. The high accuracy confirms the ability of MLAs to map mineral sands using multispectral datasets by providing the best hyperparameters and accurate selection of training sites. In conclusion, MLAs provides an effective mapping of mineral deposits of sand type covering a small area using multispectral data. This study facilitates time and resources savings over geological mapping in this field, which allows eco-friendly and sustainable mineral exploration. Moreover, the

results facilitate the use of optimal wavelengths in hyperspectral remote sensing datasets for mineral classification using MLAs.

3.6.References

(1) Baker, R. N. LANDSAT DATA: A NEW PERSPECTIVE FOR GEOLOGY. *Photogramm. Eng. Remote Sensing* **1975**, *41*, 1233–1239.

(2) Abdel-Gawad, M.; Tubbesing, L. Mineral Target Areas in Nevada from Geological Analysis of LANDSAT-1 Imagery. In *NASA. Lyndon B. Johnson Space Center NASA Earth Resources Surv. Symp.,*; NASA; United States, 1975; pp 1059–1078.

(3) Carranza, E. J. M.; Hale, M. Mineral Imaging with Landsat Thematic Mapper Data for Hydrothermal Alteration Mapping in Heavily Vegetated Terrane. *Int. J. Remote Sens.* **2002**, *23* (22), 4827–4852.

(4) Mia, B.; Fujimitsu, Y. Mapping Hydrothermal Altered Mineral Deposits Using Landsat 7 ETM+ Image in and around Kuju Volcano, Kyushu, Japan. *J. Earth Syst. Sci.* **2012**, *121* (4), 1049–1057.

(5) Abdelaziz, R.; Abd El-Rahman, Y.; Wilhelm, S. Landsat-8 Data for Chromite Prospecting in the Logar Massif, Afghanistan. *Heliyon* **2018**, *4* (2), e00542.

(6) Pour, A. B.; Hashim, M. Hydrothermal Alteration Mapping from Landsat-8 Data, Sar Cheshmeh Copper Mining District, South-Eastern Islamic Republic of Iran. *J. Taibah Univ. Sci.* **2015**.

(7) Pal, S. K.; Majumdar, T. J.; Bhattacharya, A. K.; Bhattacharyya, R. Utilization of Landsat ETM+ Data for Mineral-Occurrences Mapping over Dalma and Dhanjori, Jharkhand, India: An Advanced Spectral Analysis Approach. *Int. J. Remote Sens.* **2011**, *32* (14), 4023–4040.

(8) Goodarzi Mehr, S.; Ahadnejad, V.; Abbaspour, R. A.; Hamzeh, M. Using the Mixture-Tuned Matched Filtering Method for Lithological Mapping with Landsat TM5 Images. *Int. J. Remote Sens.* **2013**.

(9) Masoumi, F.; Eslamkish, T.; Honarmand, M.; Abkar, A. A. A Comparative Study of Landsat-7 and Landsat-8 Data Using Image Processing Methods for Hydrothermal Alteration Mapping. *Resour. Geol.* **2017**, *67* (1), 72–88.

(10) Girouard, G.; Bannari, a. Validated Spectral Angle Mapper Algorithm for Geological Mapping: Comparative Study between QuickBird and Landsat-TM. *XXth ISPRS Congr. …* **2004**.

(11) Van Der Meer, F.; Vazquez-Torres, M.; Van Dijk, P. M. Spectral Characterization of Ophiolite Lithologies in the Troodos Ophiolite Complex of Cyprus and Its Potential in Prospecting for Massive Sulphide Deposits. *Int. J. Remote Sens.* **1997**, *18* (6), 1245–1257.

(12) Honarmand, M.; Ranjbar, H.; Shahabpour, J. Application of Spectral Analysis in Mapping Hydrothermal Alteration of the Northwestern Part of the Kerman Cenozoic Magmatic Arc, Iran. *J. Sci. Islam. Repub. Iran* **2012**.

(13) Cracknell, M. J.; Reading, A. M. Geological Mapping Using Remote Sensing Data: A Comparison of Five Machine Learning Algorithms, Their Response to Variations in the Spatial Distribution of Training Data and the Use of Explicit Spatial Information. *Comput. Geosci.* **2014**, *63*, 22–33.

(14) Bachri, I.; Hakdaoui, M.; Raji, M.; Teodoro, A. C.; Benbouziane, A. Machine Learning Algorithms for Automatic Lithological Mapping Using Remote Sensing Data: A Case Study from Souk Arbaa Sahel, Sidi Ifni Inlier, Western Anti-Atlas, Morocco. *ISPRS Int. J. Geo-Information* **2019**, *8* (6), 248.

(15) Harvey, A. S.; Fotopoulos, G. GEOLOGICAL MAPPING USING MACHINE LEARNING ALGORITHMS. *ISPRS - Int. Arch. Photogramm. Remote Sens. Spat. Inf. Sci.* **2016**, *XLI-B8*, 423–430.

(16) He, J.; Harris, J. R.; Sawada, M.; Behnia, P. A Comparison of Classification Algorithms Using Landsat-7 and Landsat-8 Data for Mapping Lithology in Canada's Arctic. *Int. J. Remote Sens.* **2015**, *36* (8), 2252–2276.

(17) Gayathri, G. S.; Rejith, R. G.; Jeelani, S. H.; Sundararajan, M.; Aslam, M. M.; Chidambaram, S. Heavy Mineral Resources In Tamil Nadu, India: An Overview. In *Geochemistry and Mineralogy of Coastal Sediments in Tamil Nadu*; 2017; pp 110–121.

(18) Sundararajan, M.; Bhat, K. H.; Velusamy, S.; Babu, N.; Janaki, M. E. K.; Sasibhooshanan, S.; Das, P. N. M. Characterization of Ilmenite from Kerala Coastline,

India:Implications in the Production of Synthetic Rutile. *J. Miner. Mater. Charact. Eng.* **2009**, *08* (06), 427–438.

(19) Kumari, A.; Panda, R.; Jha, M. K.; Kumar, J. R.; Lee, J. Y. Process Development to Recover Rare Earth Metals from Monazite Mineral: A Review. *Miner. Eng.* **2015**, *79*, 102–115.

(20) Banerjee, G. Beach and Minerals: A New Material Resource for Glass and Ceramics. *Bull. Mater. Sci.* **1998**, *21* (4), 349–354.

(21) Rajganapathi, V. C.; Jitheshkumar, N.; Sundararajan, M.; Bhat, K. H.; Velusamy, S. Grain Size Analysis and Characterization of Sedimentary Environment along Thiruchendur Coast, Tamilnadu, India. *Arab. J. Geosci.* **2013**, *6* (12), 4717–4728.

(22) Anitha, J. K.; Joseph, S.; Rejith, R. G.; Sundararajan, M. Monazite Chemistry and Its Distribution along the Coast of Neendakara–Kayamkulam Belt, Kerala, India. *SN Appl. Sci.* **2020**, *2* (5), 812.

(23) Raghavan, P.; Ramaswamy, S.; Chandrasekhar, S.; Sundararajan, M. Evaluation for the Beneficiability of Silica Sands from Cherthala Area of Alappuzha District, Kerala, India. *Indian J. Geo-Marine Sci.* **2017**, *46* (08), 1596–1606.

(24) Breiman, L. Random Forests. *Mach. Learn.* **2001**, *45* (1), 5–32.

(25) Kumar, C.; Chatterjee, S.; Oommen, T.; Guha, A. Automated Lithological Mapping by Integrating Spectral Enhancement Techniques and Machine Learning Algorithms Using AVIRIS-NG Hyperspectral Data in Gold-Bearing Granite-Greenstone Rocks in Hutti, India. *Int. J. Appl. Earth Obs. Geoinf.* **2020**, *86*, 102006.

(26) Kumar, C.; Chatterjee, S.; Oommen, T.; Guha, A. Automated Lithological Mapping by Integrating Spectral Enhancement Techniques and Machine Learning Algorithms Using AVIRIS-NG Hyperspectral Data in Gold-Bearing Granite-Greenstone Rocks in Hutti, India. *Int. J. Appl. Earth Obs. Geoinf.* **2020**, *86*, 102006.

(27) Ge, W.; Cheng, Q.; Tang, Y.; Jing, L.; Gao, C. Lithological Classification Using Sentinel-2A Data in the Shibanjing Ophiolite Complex in Inner Mongolia, China. *Remote Sens.* **2018**, *10* (4), 638.

(28) Rodriguez-Galiano, V.; Sanchez-Castillo, M.; Chica-Olmo, M.; Chica-Rivas, M.

Machine Learning Predictive Models for Mineral Prospectivity: An Evaluation of Neural Networks, Random Forest, Regression Trees and Support Vector Machines. *Ore Geol. Rev.* **2015**, *71*, 804–818.

(29) Hastie, T.; Tibshirani, R.; Friedman, J. H. *The Elements of Statistical Learning: Data Mining, Inference and Prediction*; Springer series in statistics, 2009.

(30) Breiman, L. Bagging Predictors. *Mach. Learn.* **1996**, *24* (2), 123–140.

(31) Gordon, A. D.; Breiman, L.; Friedman, J. H.; Olshen, R. A.; Stone, C. J. Classification and Regression Trees. *Biometrics* **1984**, *40* (3), 874.

(32) De Boissieu, F.; Sevin, B.; Cudahy, T.; Mangeas, M.; Chevrel, S.; Ong, C.; Rodger, A.; Maurizot, P.; Laukamp, C.; Lau, I.; Touraivane, T.; Cluzel, D.; Despinoy, M. Regolith-Geology Mapping with Support Vector Machine: A Case Study over Weathered Ni-Bearing Peridotites, New Caledonia. *Int. J. Appl. Earth Obs. Geoinf.* **2018**, *64*, 377–385.

(33) Cortes, C.; Vapnik, V. Support-Vector Networks. *Mach. Learn.* **1995**, *20* (3), 273–297.

(34) Platt, J. Fast Training of Support Vector Machines Using Sequential Minimal Optimization. In *Advances in Kernel Methods --- Support Vector Learning*; 1999.

(35) Okujeni, A.; van der Linden, S.; Tits, L.; Somers, B.; Hostert, P. Support Vector Regression and Synthetically Mixed Training Data for Quantifying Urban Land Cover. *Remote Sens. Environ.* **2013**, *137*, 184–197.

(36) Gasmi, A.; Gomez, C.; Zouari, H.; Masse, A.; Ducrot, D. PCA and SVM as Geo-Computational Methods for Geological Mapping in the Southern of Tunisia, Using ASTER Remote Sensing Data Set. *Arab. J. Geosci.* **2016**, *9* (20), 753.

(37) Abedi, M.; Norouzi, G.-H.; Bahroudi, A. Support Vector Machine for Multi-Classification of Mineral Prospectivity Areas. *Comput. Geosci.* **2012**, *46*, 272–283.

(38) Shabankareh, M.; Hezarkhani, A. Application of Support Vector Machines for Copper Potential Mapping in Kerman Region, Iran. *J. African Earth Sci.* **2017**, *128*, 116–126.

(39) Geranian, H.; Tabatabaei, S. H.; Asadi, H. H.; Carranza, E. J. M. Application of Discriminant Analysis and Support Vector Machine in Mapping Gold Potential Areas

for Further Drilling in the Sari-Gunay Gold Deposit, NW Iran. *Nat. Resour. Res.* **2016**, *25* (2), 145–159.

(40) Damaševičius, R. Structural Analysis of Regulatory DNA Sequences Using Grammar Inference and Support Vector Machine. *Neurocomputing* **2010**, *73* (4–6), 633–638.

(41) Zhu, X.; Zhang, S.; Jin, Z.; Zhang, Z.; Xu, Z. Missing Value Estimation for Mixed-Attribute Data Sets. *IEEE Trans. Knowl. Data Eng.* **2011**, *23* (1), 110–121.

(42) Yang, X. Parameterizing Support Vector Machines for Land Cover Classification. *Photogramm. Eng. Remote Sens.* **2011**, *77* (1), 27–37.

(43) Chen, X.; Warner, T. A.; Campagna, D. J. Integrating Visible, near-Infrared and Short-Wave Infrared Hyperspectral and Multispectral Thermal Imagery for Geological Mapping at Cuprite, Nevada. *Remote Sens. Environ.* **2007**, *110* (3), 344–356.

(44) Gemusse, U.; Lima, A.; Teodoro, A. C. M. Comparing Different Techniques of Satellite Imagery Classification to Mineral Mapping Pegmatite of Muiane and Naipa: Mozambique); 2019.

(45) Fatima, K.; Khan Khattak, M. U.; Kausar, A. B.; Toqeer, M.; Haider, N.; Rehman, A. U. Minerals Identification and Mapping Using ASTER Satellite Image. *J. Appl. Remote Sens.* **2017**.

(46) Scott, A. J.; Symons, M. J. Clustering Methods Based on Likelihood Ratio Criteria. *Biometrics* **1971**, *27* (2), 387.

(47) Marschallinger, R. Automatic Mineral Classification in the Macroscopic Scale. *Comput. Geosci.* **1997**, *23* (1), 119–126.

(48) Kavzoglu, T.; Reis, S. Performance Analysis of Maximum Likelihood and Artificial Neural Network Classifiers for Training Sets with Mixed Pixels. *GIScience Remote Sens.* **2008**.

(49) Tso, B.; Mather, P. M. *Classification Methods for Remotely Sensed Data*; Taylor & Francis: Abingdon, UK, 2001.

(50) Haykin, S.; Network, N. A Comprehensive Foundation. *Neural Networks* **2004**, *2* (2004), 41.

(51) Lee, S.; Ryu, J.-H.; Kim, I.-S. Landslide Susceptibility Analysis and Its Verification Using Likelihood Ratio, Logistic Regression, and Artificial Neural Network Models: Case Study of Youngin, Korea. *Landslides* **2007**, *4* (4), 327–338.

(52) Lee, S.; Oh, H.-J. Application of Artificial Neural Network for Mineral Potential Mapping. In *Artificial Neural Networks - Application*; InTech, 2011.

(53) Rigol-Sanchez, J. P.; Chica-Olmo, M.; Abarca-Hernandez, F. Artificial Neural Networks as a Tool for Mineral Potential Mapping with GIS. *Int. J. Remote Sens.* **2003**, *24* (5), 1151–1156.

(54) Hepner, G. F.; Logan, T.; Ritter, N.; Bryant, N. Artificial Neural Network Classification Using a Minimal Training Set: Comparison to Conventional Supervised Classification. *Photogrammetric Engineering & Remote Sensing*. 1990.

(55) PAOLA, J. D.; SCHOWENGERDT, R. A. A Review and Analysis of Backpropagation Neural Networks for Classification of Remotely-Sensed Multi-Spectral Imagery. *Int. J. Remote Sens.* **1995**, *16* (16), 3033–3058.

(56) Cohen, J. A Coefficient of Agreement for Nominal Scales. *Educ. Psychol. Meas.* **1960**, *20* (1), 37–46.

(57) Lumpkin, G. R. Alpha-Decay Damage and Aqueous Durability of Actinide Host Phases in Natural Systems. *J. Nucl. Mater.* **2001**, *289* (1–2), 136–166.

(58) Congalton, R. G., & Green, K. *Assessing the Accuracy of Remotely Sensed Data. Principles and Practices (2 Edition)*; 2009.

(59) Sadiq, A.; Howari, F. Remote Sensing and Spectral Characteristics of Desert Sand from Qatar Peninsula, Arabian/Persian Gulf. *Remote Sens.* **2009**, *1* (4), 915–933.

(60) Othman, A. A.; Gloaguen, R. Integration of Spectral, Spatial and Morphometric Data into Lithological Mapping: A Comparison of Different Machine Learning Algorithms in the Kurdistan Region, NE Iraq. *J. Asian Earth Sci.* **2017**.

(61) Othman, A.; Gloaguen, R. Improving Lithological Mapping by SVM Classification of Spectral and Morphological Features: The Discovery of a New Chromite Body in the Mawat Ophiolite Complex (Kurdistan, NE Iraq). *Remote Sens.* **2014**, *6* (8), 6867–6896.

Chapter 4

Mineral mapping and quantification using EO-1 Hyperion data and continuum removed band depth analysis

4.1. Abstract

The strategic minerals in beach sands of Cuddalore coast in Tamil Nadu, India were mapped from EO-1 Hyperion data using a series of hyperspectral image processing algorithms. Furthermore, an attempt has been made to develop a Random Forest (RF) regression model to estimate the mineral concentration using Hyperion hyperspectral data characterised by the absorption of the minerals. The SAM algorithm is able to show the distribution of four minerals such as zircon, sillimanite, garnet and quartz (light minerals). The spectral geometric parameters such as band depth and band area corresponding to the spectral range of 1075– 1150nm which has strong absorption characteristics of zircon were derived from the continuum removed spectra of image spectra and laboratory spectra of physical mixtures of zircon samples. The positive correlation between geometric parameters due to absorption and the mineral concentration was used to develop a model using RF technique which shows satisfying results having low RMSE error. Thus our study demonstrates the ability of EO-1 Hyperion data not only for mapping but also for the quantification of mineral occurrences which could be successfully achieved by integration of continuum removal band depth analysis and random forest regression.

4.2.Introduction

The advances in satellite sensor technology get paralleled with the invention of new image processing algorithms, made a significant breakthrough in mineral exploration and mapping of lithological units. With the availability of Landsat multispectral data till the middle of 2010 decade, the potential zones of hydrothermal alteration minerals, Fe-rich minerals, carbonate deposits, uranium deposits, etc. were successfully mapped using the remote sensing techniques like band composites, band ratio, principal component analysis, SAM classification, etc. [1–4] Later the ASTER with 14 bands started playing major role in exploring alteration zones of granitic rocks, gold mineralization, mafic-ultramafic rock units, felsic igneous intrusion using various remote sensing techniques like principal component analysis (PCA), band ratio, colour composites.[5–8]

The Sentinel-2A Data with 12 bands also performed well in mapping hydrothermal alteration, lithofacies mapping, and band ratios using various hyperspectral analysis followed by spectral angle mapper (SAM), and maximum likelihood classifier (MLC).[9,10] The advent of hyperspectral imagery like EO-1 Hyperion with 242 bands made accurate subpixel mapping of alteration minerals using hyperspectral analysis techniques and classification algorithms like SAM and MTMF techniques.[11–13] The mineral type, its distribution and the nature of study area determines the selection of satellite data and the remote sensing techniques for mineral studies. The remote sensing approach will narrow down the expense and time needed for delineating the potential targets for mineral exploration.[14] Recently attempts were also made to formulate quantitative relationships between the mineral concentrations, its geochemistry with reflectance spectra either extracted from the satellite data or measured using spectroradiometer. The reflectance measurements made in the laboratory were used for determining the copper concentration of rocks using Partial least squares support vector machine (PLS-SVM) algorithm[15], quantification of mineral abundances using radiative transfer models[16] and coupling spectral deconvolution[17], carbonate mining waste quantification using Continuum Removal Analysis[18]. The Hyperion image analysis were also carried for determining grades of iron ores using Continuum Removal Analysis.[19]

The beaches of India are bestowed with enormous quantity of strategic minerals like ilmenite, monazite, rutile, zircon, etc.[20] The major beach placer deposits in India like Chavara in Kerala, Manavalakurichi in Tamil Nadu, Ratnagiri in Maharashtra, Bhimunipatnam in Andhra Pradesh, and Chatrapur in Odisha are good sources of these minerals.[21] The wide range of critical applications brought high economic value to these minerals and made them strategic minerals. The ilmenite and rutile act as a primary source of titania products such as TiO_2 pulp, pigment, etc.[22], rare earth elements from monazite[23], High purity zirconia from zircon mineral[24], synthetic mullite from sillimanite[25], etc. Many researchers have studied in detail the depositional environment, heavy mineral distribution and geochemical characterisation of all major placer deposits in India.[26–31] However only few studies had been carried out on mapping these strategic mineral using remote sensing datasets.

Present study aims to map the beach minerals of Cuddalore coast, Tamil Nadu, Southern India from EO-1 Hyperion data using a series of hyperspectral remote sensing techniques followed by SAM image classification. An attempt has also been made to predict

the concentration of minerals by using the random forest regression model developed using band parameters of continuum removed spectra derived from Hyperion data.

4.3.Materials and methods

The flow sheet showing the detailed methodology adopted for the present study is given in Figure 4.1.

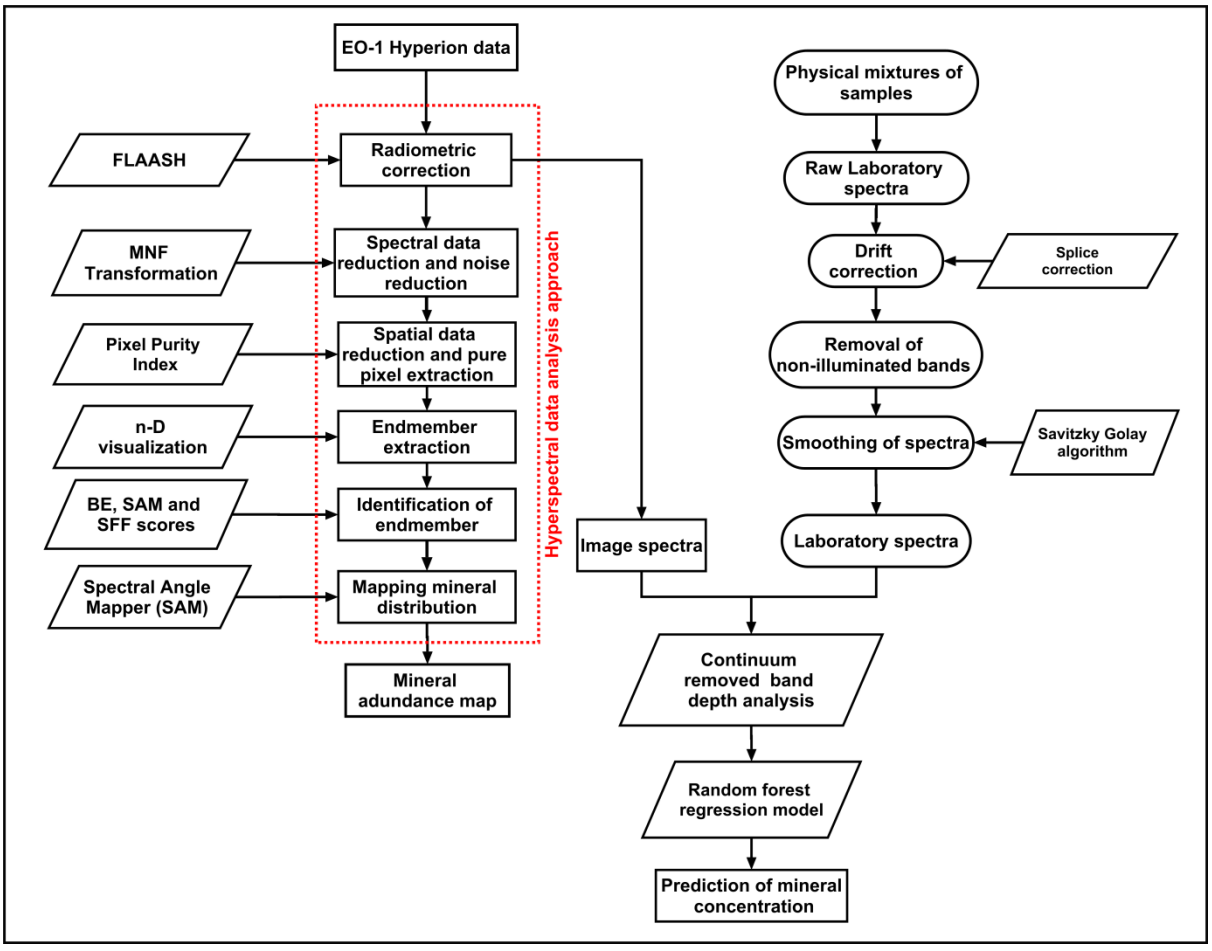

Figure 4.1: Flowchart showing the proposed methodology adopted for the present study.

4.3.1. Hyperspectral analysis of EO-1 Hyperion

The hyperspectral analysis techniques which, include six continuous processes followed by SAM image classification algorithm, were selected for mapping minerals present in beach sand using Hyperion data. Many researchers have made an attempt to integrate hyperspectral techniques for mapping minerals.[32–34] The analysis includes a series of six continuous processes such as (i) radiometric correction and extraction of reflectance values; (ii) spectral data reduction for removing noisy bands; (iii) spatial data reduction for extracting

pure pixels; (iv) extraction of endmembers from pure pixels; (v) identification of mineral classes from endmembers, and (vi) mapping of minerals using a classification algorithm [33]. The FLAASH was used for eliminating the atmospheric effects and for retrieving the reflectance values.[35] In the case of Hyperion data, prior to FLAASH correction, a series of pre-processing steps which involves (i) Bad band removal, (ii) Along track de-striping and (iii) Georeferencing,. The 242 bands of Hyperion level L1R data have been processed and only 158 bands were taken for the hyperspectral analysis. The non- illuminated bands (1-7 and 225-242), overlap region (58-78), water vapour absorption bands (120-132, 165-182, and 221-224), Hyperion bad bands (185-187) were removed from the Hyperion data.[36] The differences in calibration of Hyperion detector array based on pushbroom technology cause striping noises like visually noticeable corrupted pixels and dark vertical stripes which got de-stripped using flag mask correction utility, and also manually using the ENVI module Spatial Pixel Editor which interpolates adjacent image columns.[37] Minimum Noise Fraction (MNF) transformation was applied on de-striped bands to generate a set of uncorrelated bands from the input bands. Out of that, the most informative bands with least noise were selected based on eigen values estimated using noise statistics of input bands. Pure pixels were extracted using PPI, where it generates a PPI image showing pure pixels in bright pixels. Unique target members having a unique spectra value called endmembers are extracted from the pure pixels using n-D visualizer.[13] The true endmembers are compared with the reference spectra of minerals using the widely used spectral matching techniques like SAM, SFF, and BE. Each produces a score between 0 and 1, where 1 corresponds to the best match. The reference spectra can be measured using a spectroradiometer or otherwise extracted from the image itself. Finally, the identified mineral classes were used for classifying the satellite image using a suitable image classification algorithm. In the present study, mineral was mapped using the SAM classification where the image spectra and reference spectra were considered as unit vectors in an n-dimensional space for measuring the n-D angle between them.[38,39]

The commonly used Overall accuracy and Kappa coefficient are used for evaluating ML algorithms for classifying the Landsat 8 OLI data.[40,41] The complete elements in the error matrix are used for generating the Kappa coefficient, whereas only the diagonal elements are used in the case of overall accuracy. The Kappa statistics provide a measure of similarity between the observation datasets and the predicted or classified data using a value ranging from 0 to 1 where 1 represents the best match.[42]

4.3.2. Reflectance measurements and Continuum removed band depth analysis

High purity minerals of ilmenite, zircon, sillimanite, rutile, garnet, etc. were successfully recovered from beach sands of Varkala and Kovalam coasts of India using a judicious combination of gravity, electrostatic, and magnetic separation units. These minerals are used for preparing physical mixtures of mineral samples, as shown in Table 4.1, having a gravimetric content of 100g. Since the zircon exists in maximum compared to others in the present study area, the mixtures are prepared with zircon as the reference. The Light minerals or quartz exist as ubiquitous in beach areas, it is also added to the mixtures. Moreover, the addition of quartz causes a strong impact because it causes scattering of light in the absorption features of other minerals.[43] Since the spectra of physical mixtures were compared with satellite data showing real scenarios, the addition of quartz is very important.

Reflectance measurements of the physical mixtures of mineral samples were carried out in the laboratory using ASD Fieldspec® 3 spectroradiometer. Two sets of spectral measurements were recorded in the wavelength regions of visible-near infrared (350–1000 nm) at a spectral resolution of 3 nm and short-wave infrared (1000–2500 nm) at a spectral resolution of 10 nm.[44] The instrument consists of a sensor for recording the light reflected from the sample mixtures, which is spread on a black cloth in such a way that it covers the FOV of the sensor. A tungsten filament halogen lamp is used for illuminating the samples in which it consistently generates energy in the spectral range of 400–2500 nm. The measured spectra were subjected to a series of post–processing techniques such as splice correction of ASD Viewspec Pro^{TM}, elimination of spectral data in the wavelength range of 350nm to 400nm, and finally, the smoothing of spectra[45]. The splice correction eliminates the temperature-driven spectral drifts that occurred at 1001 and 1831 nm.[46] Savitzky–Golay smoothing algorithm is used for removing the sensor inherent noises and smoothen the spectra by maintaining the actual slope of the curve. The parameters like the degree of polynomial order is selected as 2, and a filter size of 15 is used for executing the algorithm.[47] The mean spectra in ASCII format were imported into ENVI software for generating the reference spectra for the continuum removed band depth analysis**.** The reflectance spectra of the pure zircon mineral are taken from the spectral library of minerals prepared in the laboratory using the same spectroradiometer.

Table 4.1: Prepared mineral samples with content given in wt. % of the total mass of 100 g.

Samples	**Mineral mixture**				
S1	Zircon (100%)				
S2	Zircon (75%)	Ilmenite (25%)			
S3	Zircon (50%)	Ilmenite (50%)			
S4	Zircon (25%)	Ilmenite (75%)			
S5	Zircon (25%)	Ilmenite (25%)	Sillimanite (25%)	Quartz (25%)	
S6	Zircon (50%)	Quartz (50%)			
S7	Zircon (20%)	Ilmenite (50%)	Quartz (20%)	Sillimanite (10%)	
S8	Zircon (30%)	Ilmenite (40%)	Sillimanite (10%)	Quartz (20%)	
S9	Zircon (50%)	Sillimanite (50%)			
S10	Zircon (75%)	Quartz (25%)			
S11	Zircon (75%)	Sillimanite (25%)			
S12	Zircon (25%)	Quartz (75%)			
S13	Zircon (25%)	Sillimanite (75%)			
S14	Zircon (20%)	Sillimanite (20%)	Ilmenite (20%)	Rutile (20%)	Garnet (20%)
S15	Zircon (20%)	Sillimanite (20%)	Ilmenite (20%)	Rutile (20%)	Quartz (20%)

Continuum removal is a normalization function that enhances the absorption features by removing its background information, and thereby, it allows a better comparison of different spectra under a common baseline.[48,49] The reflectance value of each absorption pit of the original data set at a particular wavelength is divided by the reflectance value of the continuum line (convex hull) corresponds to that wavelength. The output shows enhanced absorption between the values between 0 and 1.[50] The absorption feature parameters measured from the continuum-removed reflectance spectra particularly depth, width and asymmetry of absorption band are widely used for content estimation of the materials such as mining waste quantification.[18,19,51,52]

The absorption band depth is expressed as

$$\text{Absorption band depth} = 1-\frac{R_b}{R_c} \qquad (4.1)$$

Where R_b and Rc correspond to reflectance values at band bottom and continuum of the same band.[53] The band depth analysis corresponds to the strongest absorption band that was carried out on the image spectra (spectra derived from EO-1 Hyperion data) as well as on the laboratory spectra measured from the physical mixtures of mineral samples. The absorption parameters were measured using the DISPEC (version 18.03), an IDL program developed by Harald Van der Werff.[54]

4.3.3. Random forest regression modelling

The Random forest (RF) regression has been used to develop a prediction model using the relationship between the mineral concentration and their corresponding absorption parameters. Recently RF is widely used in diverse fields due to their brilliant classification results and high-speed processing of complex data structures in high dimensional feature spaces.[55,56] Mainly it is used for classifying remote sensing datasets[57–59] but recently started to use as regression technique[60–62] for predictive modelling for remote sensing purposes. RF is a machine learning algorithm that uses decision trees to make predictions[63]. Best results are obtained from the aggregation of a large number of regression trees, which is termed as 'bagging' approach [64].Here the trees are made to its maximum based on the bootstrap sample by selecting a random set of variables from the training dataset (approximately 70% of the total input data). In each tree, the RF makes a prediction for the out of bag data, which is called OOB data (approximately 30% of the total input data).The decision trees can be either classification trees or regression trees which need only two parameters, such as the number of regression trees (*ntree*) and the number of predictive variables (*mtry*). An independent dataset of 30 variables randomly selected from the laboratory spectra data was used for optimizing the parameters *ntree* and *mtry* using root mean square error (RMSE). The *ntree* was tested for 100, 300, 500, 700, and 900. The *mtry* was tested for 5,10,15,20, and 25. Finally using the best parameters of *ntree* and *mtry* having the least RMSE error, the RF regression model was applied to both the datasets of laboratory spectra and image spectra. The random forest modelling is implemented using the Python programming environment with the help of the Scikit-learn machine learning module (http://scikit-learn. org/stable/).[65]

4.4.Results and Discussion

4.4.1. Mineral Mapping using EO-1 Hyperion

The reflectance calibrated 158 bands of EO-1 Hyperion data were used for creating mineral map of the study area. The FLAASH atmospheric correction parameters are shown in Table 4.2. The reflectance calibrated bands were linearly transformed using MNF Transformation. The MNF bands having eigenvalues below one are usually noise dominant with less information.[66] It was noticed that usually first 6, 10, and 20 MNF bands were selected for classifying mineral occurrences from Hyperion data.[67–70] The MNF images clearly show that up to the MNF 15 band with the eigenvalue of 4.2756 can be taken for further processing. The first 15 MNF bands were used to generate the PPI image with the iterations of 15000 and a threshold value of 2.5 for extracting the pure pixels.

Table 4.2: FLAASH atmospheric correction parameters of Hyperion image.

Scene center location	11.7861N, 79.7993E
Sensor altitude	705km
Initial visibility	40km
Spectral polishing	Yes
Pixel size	30m
Flight date	9 February 2009
Flight time	04:55:24
Atmospheric Model	Tropical
Aerosol Model	Maritime
Water retrieval	No
Aerosol Retrieval	2-Band(K-T)
Width of bands	9
Wave length calibration	No

The pure pixels were rotated in a 15-dimensional visualizer for generating the endmembers having unique spectral characteristics. Endmembers were derived mostly from individual pure pixels rather than considering the mean of a group of pixels, which may avoid mixing endmembers and increase the accuracy of target detection and sub-pixel mapping of minerals.[70] The ROI exported from the endmembers falls over other geological units, waterbody, landcover, etc. were not considered for further processing. The endmembers that

fall exactly along the beach sediments of the coast were assigned to a particular mineral class by comparing with the spectral library of beach minerals. The spectral library consists of reference spectra of ilmenite, rutile, zircon, monazite, sillimanite, leucoxene, garnet and the light minerals (quartz). Table 4.3 shows the results of spectral matching techniques. The plots of relative reflectance of image spectra and reference spectra were shown in Figure 4.2.

Table 4.3: Spectral matching results of laboratory spectra and image spectra

Endmember	**SAM**	**SFF**	**BE**	**Score**
Zircon	0.903	0.898	0.943	2.744
Garnet	0.434	0.679	0.709	1.821
Sillimanite	0.910	0.907	0.968	2.78
Light minerals (Quartz)	0.824	0.866	0.905	2.596

The scores obtained for SAM, SFF, and BE clearly indicate that the true endmembers collected from the image show a strong correlation with the reference spectra of zircon, garnet, sillimanite/kyanite and the quartz. Thus the hyperspectral analyses could able to retrieve the endmembers of four minerals from the beach sand which exist in moderately low concentration. These four endmembers of mineral classes such as garnet, zircon, kyanite/sillimanite, and lights (quartz) were used as the training data for executing the SAM classification. Here the SAM algorithm has been used for two purposes; it is used as a spectral matching algorithm for deriving the mineral classes from true endmembers and also as a sub-pixel mineral image classification algorithm for mapping minerals. The SAM classified image of the study area is shown in Figure 4.3.

The SAM classified image was verified with the previous studies carried out on the Cuddalore coast.[30,71–73] The results clearly indicate the potential of Hyperion data for mapping low to moderate concentration of beach minerals. The Pondicherry –Cuddalore region is mainly occupied by kyanite (1.21% to 32.54%), zircon (4.0% to 20.19%), and garnet (12.03% to 31.76%), sillimanite (0 to 1.84%), and the light minerals (71.52% to 87.17) [30]. The SAM classified image could able to map zircon, garnet, sillimanite and light minerals (quartz) from the Hyperion data. The classification accuracy calculated for six locations is given in Table 4.4. The results show an overall accuracy of 88.68% and Kappa coefficient of

0.85 which is sufficient to prove the ability of Hyperion data in mapping beach minerals. The abundance of zircons indicates the influence of paleosediments and probably originated from khondalites[71]. Garnets are noticed in two types, such as colourless and pink originated from pyroxene granulite [74]. The Cuddalore region is dominated by colourless garnets. The kyanite exists as colourless, and blue originated from Miocene Cuddalore sandstone. The Cuddalore region is dominated by Blue kyanite. The high concentration of heavy minerals usually occurred due to the removal of light minerals from the beach due to the action of high energy waves [32].

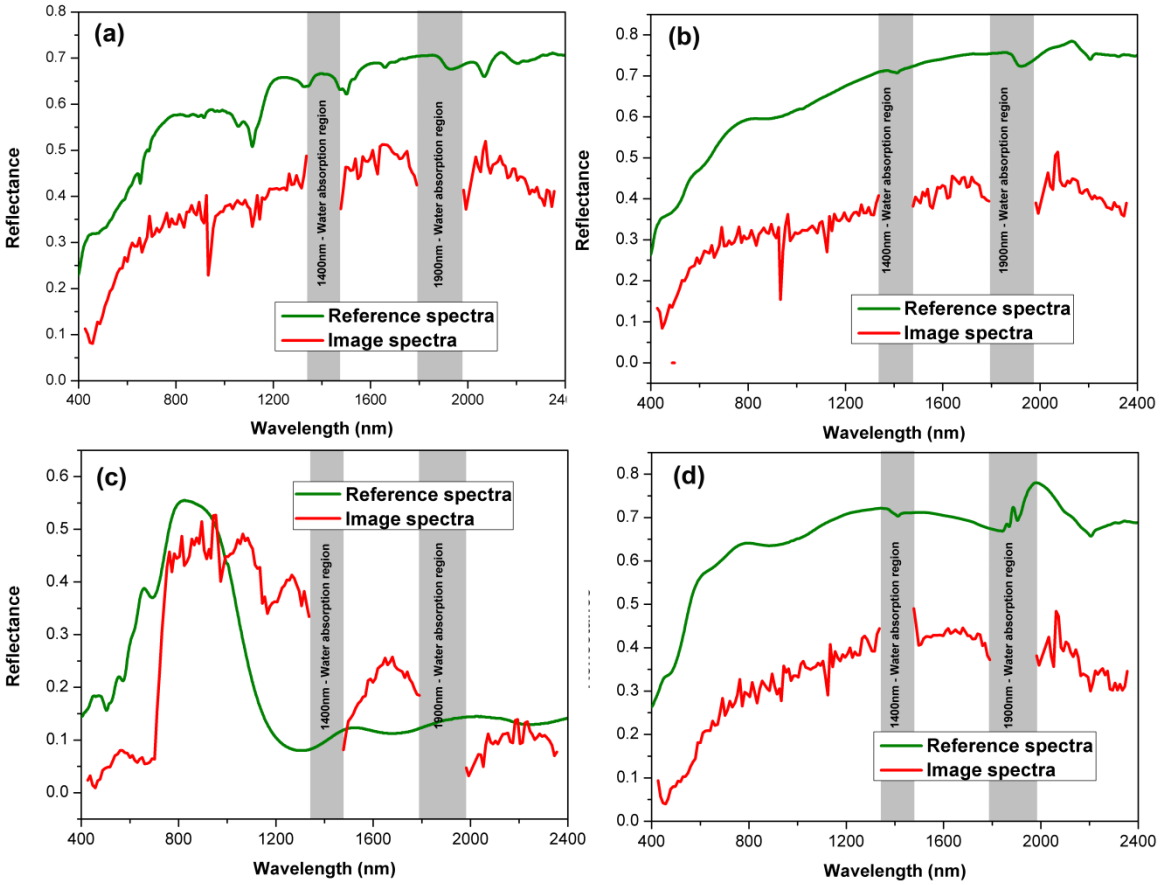

Figure 4.2: Plots of relative reflectance between reference spectra and image spectra. (a) zircon; (b) sillimanite; (c) garnet; (d) light minerals (quartz).

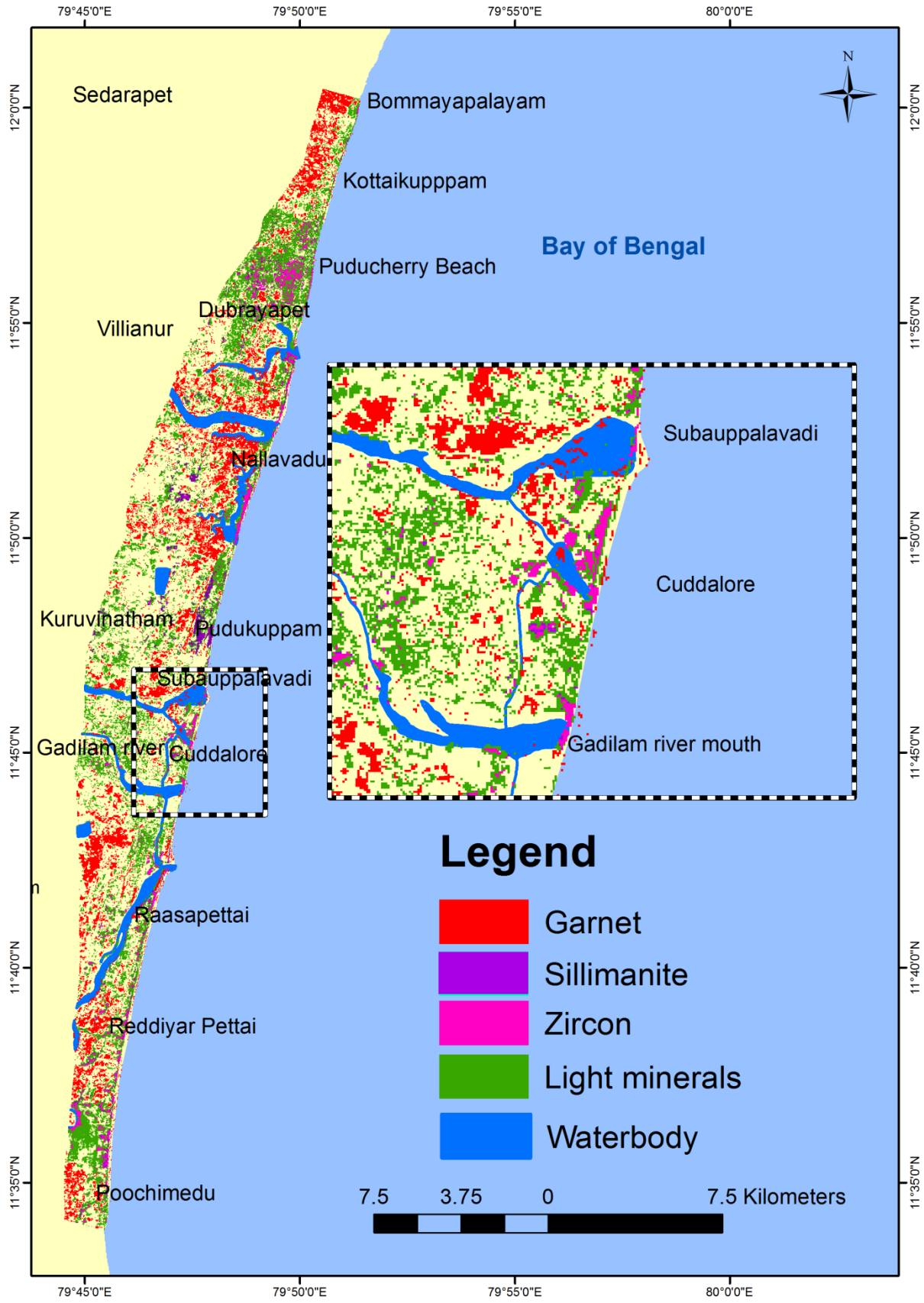

Figure 4.3: SAM classified image of EO-1 Hyperion data showing the mineral distribution along Cuddalore coast.

Table 4.4: Accuracy assessment matrix for SAM derived mineral map.

	Reference Data					
Classes	**Light minerals**	**Zircon**	**Garnet**	**Sillimanite**	**Total**	**User's accuracy**
Unclassified	2	0	1	0	3	
Light minerals	7	0	0	3	10	70
Zircon	0	16	0	0	16	100
Garnet	0	0	11	0	11	100
Sillimanite	0	0	0	13	13	100
Total	9	16	12	16	53	

Overall accuracy = 88.68%, Kappa coefficient = 0.85

4.4.2. Deriving spectral parameters using Continuum removal band depth analysis

The well-defined absorption features of zircon are needed for predicting the concentration of zircon in sample mixtures as well as in satellite data. To obtain this, continuum removal was applied to each spectrum. The Figure 4.4 shows the continuum removed spectra of zircon mineral, where it allows comparison of individual absorption features. Here the reflectance spectra are broken into two parts, broad and smoothly changing regions showing the general shape of the spectra, and another one is narrow and deep trough indicating the strong absorption features. Minerals can be easily identified using the shape, depth, and position of these absorption features.[75] Well defined absorption features for zircon mineral are noticed in the range 1075– 1150nm at a position of 1113nm. The strongest absorption feature for zircon can be correlated with UV-Vis-NIR spectroscopy of zircon samples.[76] A quantitative relation always exists between depth of absorption and the abundance of the absorber.[52] Figure 4.5 clearly shows that as the amount of zircon in the mixture increases, the absorption maxima at 1113nm becomes more visible.

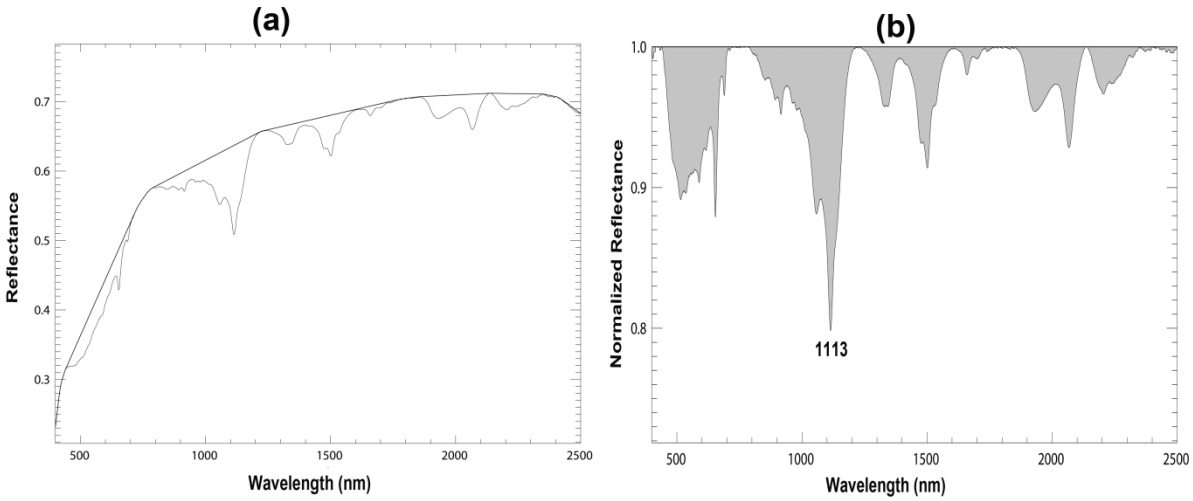

Figure 4.4: Continuum removed spectra of zircon mineral.

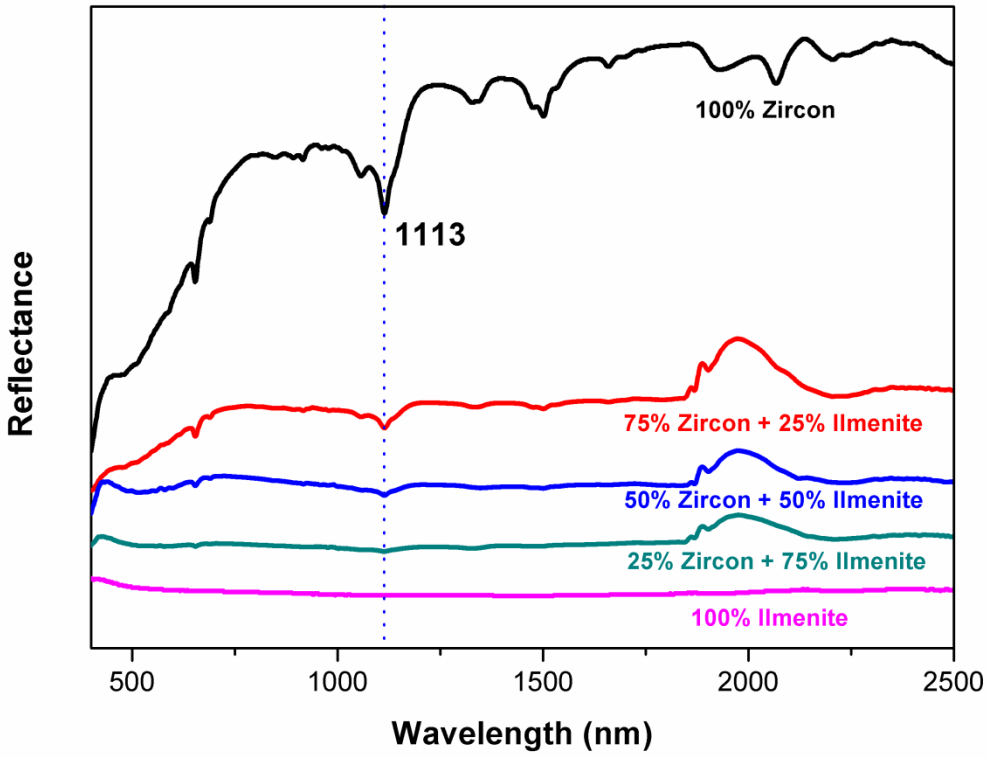

Figure 4.5: Laboratory spectra measured for different physical mixtures of samples with content given in wt. % of the total mass of 100 g.

4.4.3. Correlating mineral concentration and spectral parameters

The Figure 4.6 shows the empirical models relating absorption parameters and mineral concentration. Figure 4.6(a-b) corresponds to the relation between band depth and band area with laboratory spectra developed using physical mixtures of mineral samples. Figure 4.6(a1-

b1) corresponds to the relation between band depth and band area with image spectra derived from EO-1 Hyperion data. About 45 spectral measurements were taken from laboratory arrangement whereas from image, spectra data of 168 pixels were collected for analysing the correlation between the mineral concentration and spectral parameters. The mineralogical data for the Cuddalore coastal area is adopted from previous studies[30,71]. Analysis of both laboratory and image spectra reveals that the band depth and band area correspond to the strong absorption range of 1075– 1150nm show an increase with increasing zircon concentration. The band depth and band area derived from laboratory spectra show positive correlations of about $R^2 = 0.792$ and $R^2 = 0.784$ with increasing zircon concentration (20 to 100%). In the case of image spectra also, the band depth and band area show positive correlations of $R^2 = 0.757$ and $R^2=0.740$ with increasing zircon concentration (4 to 20.19%).

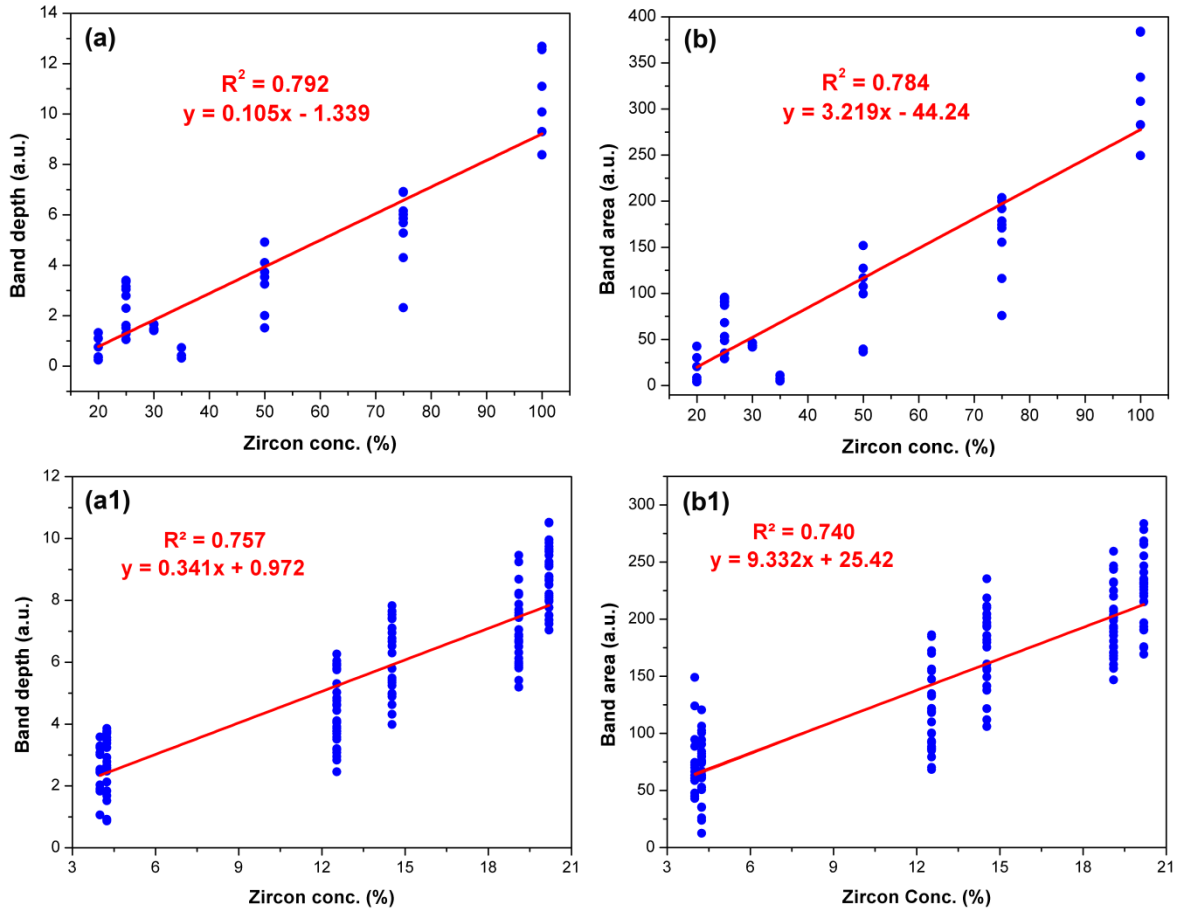

Figure 4.6: Empirical models relating absorption parameters and mineral concentration. (a-b) laboratory spectra; (a1-b1) image spectra.

In the case of laboratory spectra, the average band depth and band area of 0.686 and 18.706 were obtained for 20%, 3.294 and 96.986 for 50%, and 10.685 and 323.792 for 100%

zircon concentration respectively. In the case of image spectra, the average band depth and band area were observed as 2.573 and 73.762 for 4%, 4.34 and 117.564 for 12.54%, and 8.783 and 226.689 for 20.19% concentration values respectively. In both the cases of laboratory and image spectra, spectral parameters show a gradual and well-defined increase with the mineral concentration. It was reported that the Fe content in iron ores shows a positive correlation with band depth and band area whereas the Al content shows a negative correlation.[19] The Al-OH related absorption-band depth of spectral data of AVIRIS data show an increase in intensity with the formation of hydrothermal alteration minerals like alunite, kaolinite, montmorillonite, etc.[77] Likewise, in the present study also a strong correlation was successfully derived between zircon concentration and absorption band parameters. The increasing trends of band parameters with the increase in mineral concentration may help to derive a quantitative relationship between mineral content and spectral parameters. Also, these relationships can be used for predicting the concentration of minerals from unexplored areas using the absorption parameters measured from the satellite data.

4.4.4. Prediction of mineral concentration

The optimization results of RF parameters (*ntree* and *mtry*) are shown in Figure 4.7. The optimization was carried out using 30 variables selected from the laboratory dataset. The results clearly show that the parameters *ntree* and *mtry* clearly affects the RMSE error of the prediction. The RMSE error was low for the ntree value 500 and the *mtry* value 5-10 which is approximate to the $1/3^{rd}$ of the total variables. The higher and lower values of ntree with different *mtry* generate results with high RMSE error. So based on the calibration results, an *ntree* value of 500 and *mtry* value of $1/3^{rd}$ of the total variables were selected for the present study. Actually, these are default values chosen by many researchers for RF modelling.[62] The entire dataset will be split into 70% and 30% for calibration and validation. The calibration dataset is used to optimize and calibrate the RF regression model, whereas the validation dataset is used to validate the prediction results.[78]

The RF regression model has been successfully used for predicting the concentration of zircon using the absorption parameters derived from laboratory spectra and image spectra. About 45 datasets were derived from laboratory spectra, which were split into 30 and 15 for calibration and validation. In the case of Hyperion data, 168 data variables were used as 112 for calibration and 56 for validation. The results of RF predictive modelling showing the one-to-one relationships between the predicted and measured mineral concentration for laboratory

spectra and image spectra are shown in Figure 4.8(a) and Figure 4.8(b). The R^2 and RMSE error values are used for validating the RF models. The R^2 values obtained for laboratory spectra and image spectra were 0.959 and 0.805, which clearly shows a strong correlation between observed values and predicted values of zircon concentration. Furthermore, the low RMSE values of 0.082 and 0.156 also suggest the better predictive performance of RF method for estimating mineral concentration in beach sands. Selection of number of trees (*ntree)* and spectral variables (*mtry)* are other factors behind the yield of lower RMSE because, for predictive purposes, the less number of trees (500 in the present study) results in a minimum correlation between ranking variables.[79,80]

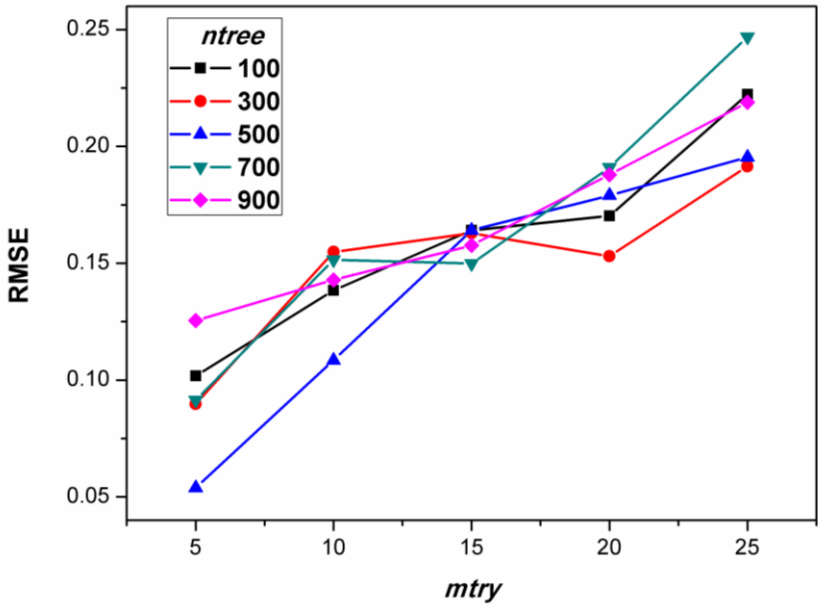

Figure 4.7: Optimization of Random forest (RF) parameters (*ntree* and *mtry*) using RMSE.

The feature-selection method of the RF algorithm is another important factor.[81] It says that the selection of absorption parameters that were showing the best relationship with the mineral concentration through a process of internal validation of out-of-bag data helps in achieving reducing the hyperspectral data redundancy. On comparing the predictive performance of both the cases, it can be concluded that with the aid of the RF regression model, the derived absorption parameters can show the best prediction of mineral concentration.

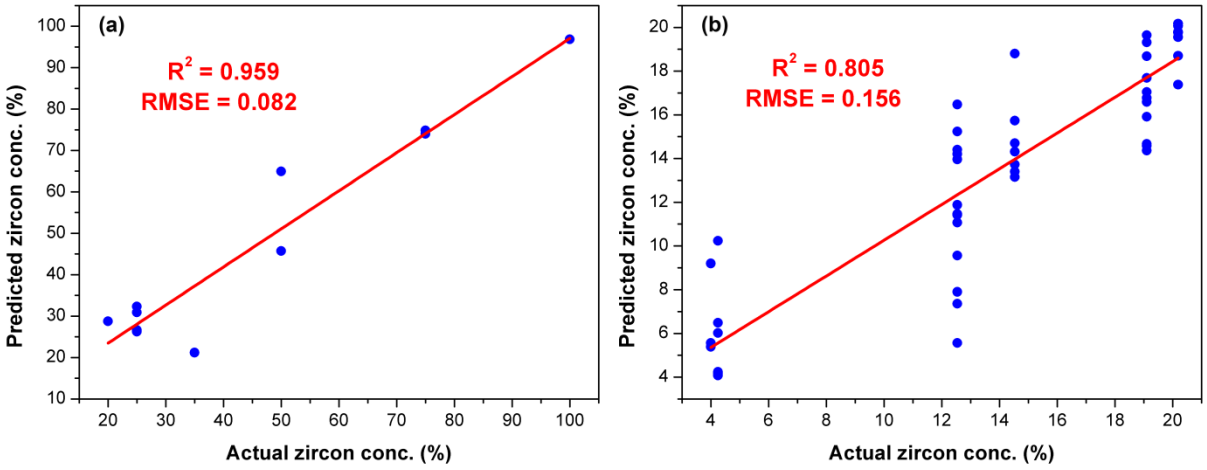

Figure 4.8: One-to-one relationships between measured and predicted zircon mineral concentration. (a) RF regression model developed using Laboratory spectra. (b) RF regression model developed using image spectra.

4.5.Conclusion

Sub-pixel mapping of strategic minerals in beach sands can be successfully achieved by applying standardized hyperspectral analysis techniques, including SAM image classification algorithm, to EO-1 Hyperion data. The results clearly depict the ability of hyperspectral data for identifying minerals of low to moderate concentration in beach sand deposits. The strong absorption parameters like band depth and band area derived from continuum removed spectra of satellite data can be used to model and predict the quantity of minerals in beach sands. The Random forest regression model has potential in estimating the concentration of minerals with reasonable prediction accuracies, using the reflectance spectra either measured in the laboratory or extracted from satellite data. Overall, it can be concluded that integration of advanced image processing techniques and hyperspectral remote sensing datasets provide solid information on potential mineral targets that facilitates eco-friendly and sustainable exploration of strategic mineral resources. Moreover, the study recommends the use of the Random forest regression model to assess the performance in the prediction of minerals (moderate to low concentration) using different remote sensing datasets.

4.6.References

(1) Carranza, E. J. M.; Hale, M. Mineral Imaging with Landsat Thematic Mapper Data for Hydrothermal Alteration Mapping in Heavily Vegetated Terrane. *Int. J. Remote Sens.* **2002**, *23* (22), 4827–4852.

(2) Abdelsalam, M. G.; Stern, R. J.; Berhane, W. G. Mapping Gossans in Arid Regions with Landsat TM and SIR-C Images: The Beddaho Alteration Zone in Northern Eritrea. *J. African Earth Sci.* **2000**, *30* (4), 903–916.

(3) Rajesh, H. M. Mapping Proterozoic Unconformity-Related Uranium Deposits in the Rockhole Area, Northern Territory, Australia Using Landsat ETM+. *Ore Geol. Rev.* **2008**, *33* (3–4), 382–396.

(4) van der Meer, F. Mineral Mapping and Landsat Thematic Mapper Image Classification Using Spectral Unmixing. *Geocarto Int.* **1997**, *12* (3), 27–40.

(5) Rejith, R. G.; Sundararajan, M. Mapping of Mafic-Ultramafic Rock Units in Late Archean Bhavani Complex, Southern India Using ASTER Thermal Bands. In *Shear Zones and Crustal Blocks of Southern India*; 2018; pp 34–40.

(6) Gemail, K.; Abd-El Rahman, N. M.; Ghiath, B. M.; Aziz, R. N. Integration of ASTER and Airborne Geophysical Data for Mineral Exploration and Environmental Mapping: A Case Study, Gabal Dara, North Eastern Desert, Egypt. *Environ. Earth Sci.* **2016**, *75* (7), 592.

(7) Gabr, S.; Ghulam, A.; Kusky, T. Detecting Areas of High-Potential Gold Mineralization Using ASTER Data. *Ore Geol. Rev.* **2010**, *38* (1–2), 59–69.

(8) Bedini, E. Mineral Mapping in the Kap Simpson Complex, Central East Greenland, Using HyMap and ASTER Remote Sensing Data. *Adv. Sp. Res.* **2011**, *47* (1), 60–73.

(9) van der Werff, H.; van der Meer, F. Sentinel-2A MSI and Landsat 8 OLI Provide Data Continuity for Geological Remote Sensing. *Remote Sens.* **2016**, *8* (11), 883.

(10) Fal, S.; Maanan, M.; Baidder, L.; Rhinane, H. THE CONTRIBUTION OF SENTINEL-2 SATELLITE IMAGES FOR GEOLOGICAL MAPPING IN THE SOUTH OF TAFILALET BASIN (EASTERN ANTI-ATLAS, MOROCCO). *ISPRS - Int. Arch. Photogramm. Remote Sens. Spat. Inf. Sci.* **2019**, *XLII-4/W12*, 75–82.

(11) Hu, B.; Xu, Y.; Wan, B.; Wu, X.; Yi, G. Hydrothermally Altered Mineral Mapping Using Synthetic Application of Sentinel-2A MSI, ASTER and Hyperion Data in the Duolong Area, Tibetan Plateau, China. *Ore Geol. Rev.* **2018**.

(12) Bishop, C. A.; Liu, J. G.; Mason, P. J. Hyperspectral Remote Sensing for Mineral

Exploration in Pulang, Yunnan Province, China. *Int. J. Remote Sens.* **2011**, *32* (9), 2409–2426.

(13) Kruse, F. A.; Boardman, J. W.; Huntington, J. F. Comparison of Airborne Hyperspectral Data and Eo-1 Hyperion for Mineral Mapping. *IEEE Trans. Geosci. Remote Sens.* **2003**, *41* (6), 1388–1400.

(14) Zeinelabdein, K. A. E.; El Nadi, A. H. H. The Use of Landsat 8 OLI Image for the Delineation of Gossanic Ridges in the Red Sea Hills of NE Sudan. *Am. J. Earth Sci.* **2014**, *1* (3), 62–67.

(15) Cui, S.; Zhou, K.; Ding, R.; Jiang, G. Estimation of Copper Concentration of Rocks Using Hyperspectral Technology. *Front. Earth Sci.* **2019**, *13* (3), 563–574.

(16) Robertson, K. M.; Milliken, R. E.; Li, S. Estimating Mineral Abundances of Clay and Gypsum Mixtures Using Radiative Transfer Models Applied to Visible-near Infrared Reflectance Spectra. *Icarus* **2016**, *277*, 171–186.

(17) Mulder, V. L.; Plötze, M.; de Bruin, S.; Schaepman, M. E.; Mavris, C.; Kokaly, R. F.; Egli, M. Quantifying Mineral Abundances of Complex Mixtures by Coupling Spectral Deconvolution of SWIR Spectra (2.1–2.4 Mm) and Regression Tree Analysis. *Geoderma* **2013**, *207–208*, 279–290.

(18) Alayet, F.; Mezned, N.; Sebai, A.; Abdeljaouad, S. Continuum Removed Band Depth Analysis for Carbonate Mining Waste Quantification Using X-Ray Diffraction and Hyperspectral Spectroscopy in the North of Tunisia. *J. Appl. Remote Sens.* **2017**, *11* (1), 016021.

(19) Magesh, N. S.; Chandrasekar, N.; Kaliraj, S. Mapping of Heavy Mineral Placers through Marine GIS Expert System: A Case Study in Kalaignanapuram Coastal Stretch, Southeast Coast of Tamil Nadu, India. *Arab. J. Geosci.* **2015**, *8* (1), 195–206.

(20) Gayathri, G. S.; Rejith, R. G.; Jeelani, S. H.; Sundararajan, M.; Aslam, M. M.; Chidambaram, S. Heavy Mineral Resources In Tamil Nadu, India: An Overview. In *Geochemistry and Mineralogy of Coastal Sediments in Tamil Nadu*; 2017; pp 110–121.

(21) Ali, M. A.; Krishnan, S.; Banerjee, D. C. Beach and Inland Heavy Mineral Sand

Investigations and Deposits in India-An Overview. *Explor. Res. At. Miner.* **2001**, *13*, 1–21.

(22) Sundararajan, M.; Bhat, K. H.; Velusamy, S.; Babu, N.; Janaki, M. E. K.; Sasibhooshanan, S.; Das, P. N. M. Characterization of Ilmenite from Kerala Coastline, India:Implications in the Production of Synthetic Rutile. *J. Miner. Mater. Charact. Eng.* **2009**, *08* (06), 427–438.

(23) Kumari, A.; Panda, R.; Jha, M. K.; Kumar, J. R.; Lee, J. Y. Process Development to Recover Rare Earth Metals from Monazite Mineral: A Review. *Miner. Eng.* **2015**, *79*, 102–115.

(24) Sinha, H. N. From Zircon to High Purity Zirconia for Ceramics. *Miner. Process. Extr. Metall. Rev.* **1992**, *9* (1), 313–325.

(25) Banerjee, G. Beach and Minerals: A New Material Resource for Glass and Ceramics. *Bull. Mater. Sci.* **1998**, *21* (4), 349–354.

(26) Sundararajan, M.; Bhat, K. H.; Velusamy, S. Investigation on Mineralogical and Chemical Characterization of Ilmenite Deposits of Northern Kerala Coast, India. *Res. J. Earth Sci.* **2010**, *2* (2), 36–40.

(27) Rajganapathi, V. C.; Jitheshkumar, N.; Sundararajan, M.; Bhat, K. H.; Velusamy, S. Grain Size Analysis and Characterization of Sedimentary Environment along Thiruchendur Coast, Tamilnadu, India. *Arab. J. Geosci.* **2013**, *6* (12), 4717–4728.

(28) Anitha, J. K.; Joseph, S.; Rejith, R. G.; Sundararajan, M. Monazite Chemistry and Its Distribution along the Coast of Neendakara–Kayamkulam Belt, Kerala, India. *SN Appl. Sci.* **2020**, *2* (5), 812.

(29) Sajimol, S.; Rejith, R. G.; Lakshumanan, C.; Sundararajan, M. Sedimentology And Geochemistry Of Heavy Mineral Deposits along the Coast of Kanyakumari District, Tamil Nadu, India. In *Geochemistry and Mineralogy of Coastal Sediments in Tamil Nadu*; 2017; pp 145–161.

(30) Suresh Gandhi, M.; Solai, A. Textural and Heavy Mineral Characteristics of Surface and Buried Sediments along the Coast between Cuddalore and Pondicherry, India. *Int. J. Earth Sci. Eng.* **2010**, *3* (6), 886–892.

(31) Angusamy, N.; Loveson, V. J.; Rajamanickam, G. V. Zircon and Ilmenite from the Beach Placers of Southern Coast of Tamil Nadu, East Coast of India. *Indian J. Mar. Sci.* **2004**, *33* (2), 138–149.

(32) Chandrasekar, N.; Mujabar, P. S.; Rajamanickam, G. V. Investigation of Heavy-Mineral Deposits Using Multispectral Satellite Data. *Int. J. Remote Sens.* **2011**, *32* (23), 8641–8655.

(33) Pal, S. K.; Majumdar, T. J.; Bhattacharya, A. K.; Bhattacharyya, R. Utilization of Landsat ETM+ Data for Mineral-Occurrences Mapping over Dalma and Dhanjori, Jharkhand, India: An Advanced Spectral Analysis Approach. *Int. J. Remote Sens.* **2011**, *32* (14), 4023–4040.

(34) Matar, S. S.; Bamousa, A. O. Integration of the ASTER Thermal Infra-Red Bands Imageries with Geological Map of Jabal Al Hasir Area, Asir Terrane, the Arabian Shield. *J. Taibah Univ. Sci.* **2013**, *7* (1), 1–7.

(35) Felde, G. W.; Anderson, G. P.; Cooley, T. W.; Matthew, M. W.; Adler-Golden, S. M.; Berk, A.; Lee, J. Analysis of Hyperion Data with the FLAASH Atmospheric Correction Algorithm. In *International Geoscience and Remote Sensing Symposium (IGARSS)*; 2003.

(36) Ganesh, B. P.; Aravindan, S.; Raja, S.; Thirunavukkarasu, A. Hyperspectral Satellite Data (Hyperion) Preprocessing—a Case Study on Banded Magnetite Quartzite in Godumalai Hill, Salem, Tamil Nadu, India. *Arab. J. Geosci.* **2013**, *6* (9), 3249–3256.

(37) Scheffler, D.; Karrasch, P. Preprocessing of Hyperspectral Images: A Comparative Study of Destriping Algorithms for EO1-Hyperion. In *Image and Signal Processing for Remote Sensing XIX*; Bruzzone, L., Ed.; 2013; p 88920H.

(38) Kruse, F. A.; Lefkoff, A. B.; Boardman, J. W.; Heidebrecht, K. B.; Shapiro, A. T.; Barloon, P. J.; Goetz, A. F. H. The Spectral Image Processing System (SIPS)—Interactive Visualization and Analysis of Imaging Spectrometer Data. *Remote Sens. Environ.* **1993**, *44* (2–3), 145–163.

(39) Felde, G. W.; Anderson, G. P.; Cooley, T. W.; Matthew, M. W.; Adler-Golden, S. M.; Berk, A.; Lee, J. Analysis of Hyperion Data with the FLAASH Atmospheric Correction Algorithm. In *IGARSS 2003. 2003 IEEE International Geoscience and*

Remote Sensing Symposium. Proceedings (IEEE Cat. No.03CH37477); IEEE, 2000; Vol. 1, pp 90–92.

(40) Cohen, J. A Coefficient of Agreement for Nominal Scales. *Educ. Psychol. Meas.* **1960**, *20* (1), 37–46.

(41) Lumpkin, G. R. Alpha-Decay Damage and Aqueous Durability of Actinide Host Phases in Natural Systems. *J. Nucl. Mater.* **2001**, *289* (1–2), 136–166.

(42) Congalton, R. G., & Green, K. *Assessing the Accuracy of Remotely Sensed Data. Principles and Practices (2 Edition)*; 2009.

(43) Clark, R. N. Spectroscopy of Rocks Andminerals, and Principles of Spectrocopy. *Remote Sens. earth Sci. Man. Remote Sens.* **1999**, *3* (3–58), 2–2.

(44) ASD. *Fieldspec® 3 User Manual*; ASD document 600540 Rev J. Boulder, CO: ASD Inc, 2010.

(45) Prasad, K. A.; Gnanappazham, L. Discrimination of Mangrove Species of Rhizophoraceae Using Laboratory Spectral Signatures. In *2014 IEEE Geoscience and Remote Sensing Symposium*; IEEE, 2014; pp 2906–2909.

(46) Beal, D.; Eamon, M. Preliminary Results of Testing and a Proposal for Radiometric Error Correction Using Dynamic, Parabolic Linear Transformations of "Stepped" Data. In *Boulder (CO): Analytical Spectral Devices*; 1996; pp 1–5.

(47) Prasad, K. A.; Gnanappazham, L.; Selvam, V.; Ramasubramanian, R.; Kar, C. S. Developing a Spectral Library of Mangrove Species of Indian East Coast Using Field Spectroscopy. *Geocarto Int.* **2015**, *30* (5), 580–599.

(48) Clark, R. N.; Roush, T. L. Reflectance Spectroscopy: Quantitative Analysis Techniques for Remote Sensing Applications. *J. Geophys. Res. Solid Earth* **1984**, *89* (B7), 6329–6340.

(49) Curtis C. Mason, R. L. F. Differentiation of Beach, Dune, and Aeolian Flat Environments by Size Analysis, Mustang Island, Texas. *SEPM J. Sediment. Res.* **1958**, *Vol. 28*.

(50) Schmidt, K. S.; Skidmore, A. K. Spectral Discrimination of Vegetation Types in a

Coastal Wetland. *Remote Sens. Environ.* **2003**, *85* (1), 92–108.

(51) Alayet, F.; Mezned, N.; Abdeljaoued, S. Continuum Removed Band Depth Analysis for Waste Detection in the North of Tunisia. In *Earth Resources and Environmental Remote Sensing/GIS Applications VI*; Michel, U., Schulz, K., Ehlers, M., Nikolakopoulos, K. G., Civco, D., Eds.; 2015; p 96441K.

(52) Kayet, N.; Pathak, K.; Chakrabarty, A.; Sahoo, S. Hyperspectral Image Analysis for Iron Mineral Exploration and Spectral Unmixing Study in Kiriburu and Meghahataburu Mining Areas, West Singbhum, Jharkhand. In *38th Asian Conference on Remote Sensing - Space Applications: Touching Human Lives, ACRS 2017*; 2017.

(53) Kokaly, R. F.; Couvillion, B. R.; Holloway, J. M.; Roberts, D. A.; Ustin, S. L.; Peterson, S. H.; Khanna, S.; Piazza, S. C. Spectroscopic Remote Sensing of the Distribution and Persistence of Oil from the Deepwater Horizon Spill in Barataria Bay Marshes. *Remote Sens. Environ.* **2013**, *129*, 210–230.

(54) Janaki Rama Suresh, G.; Sreenivas, K.; Sivasamy, R. Hyperspectral Analysis of Clay Minerals. *ISPRS - Int. Arch. Photogramm. Remote Sens. Spat. Inf. Sci.* **2014**, *XL–8*, 443–446.

(55) Tyralis, H.; Papacharalampous, G. Variable Selection in Time Series Forecasting Using Random Forests. *Algorithms* **2017**, *10* (4), 114.

(56) Pillai, N. D.; Nandy, S.; Patel, N. R.; Srinet, R.; Watham, T.; Chauhan, P. Integration of Eddy Covariance and Process-Based Model for the Intra-Annual Variability of Carbon Fluxes in an Indian Tropical Forest. *Biodivers. Conserv.* **2019**, *28* (8–9), 2123–2141.

(57) Adam, E. M.; Mutanga, O.; Rugege, D.; Ismail, R. Discriminating the Papyrus Vegetation (Cyperus Papyrus L.) and Its Co-Existent Species Using Random Forest and Hyperspectral Data Resampled to HYMAP. *Int. J. Remote Sens.* **2012**, *33* (2), 552–569.

(58) Gislason, P. O.; Benediktsson, J. A.; Sveinsson, J. R. Random Forests for Land Cover Classification. In *Pattern Recognition Letters*; 2006.

(59) Stumpf, A.; Kerle, N. Combining Random Forests and Object-Oriented Analysis for

Landslide Mapping from Very High Resolution Imagery. *Procedia Environ. Sci.* **2011**, *3*, 123–129.

(60) Abdel-Rahman, E. M.; van den Berg, M.; Way, M. J.; Ahmed, F. B. Hand-Held Spectrometry for Estimating Thrips (Fulmekiola Serrata) Incidence in Sugarcane. In *2009 IEEE International Geoscience and Remote Sensing Symposium*; IEEE, 2009; pp IV-268-IV–271.

(61) Ismail, R.; Mutanga, O. A Comparison of Regression Tree Ensembles: Predicting Sirex Noctilio Induced Water Stress in Pinus Patula Forests of KwaZulu-Natal, South Africa. *Int. J. Appl. Earth Obs. Geoinf.* **2010**, *12*, S45–S51.

(62) Mutanga, O.; Adam, E.; Cho, M. A. High Density Biomass Estimation for Wetland Vegetation Using WorldView-2 Imagery and Random Forest Regression Algorithm. *Int. J. Appl. Earth Obs. Geoinf.* **2012**, *18*, 399–406.

(63) Breiman, L. Random Forests. *Mach. Learn.* **2001**, *45* (1), 5–32.

(64) Dhanda, P.; Nandy, S.; Kushwaha, S.; Ghosh, S.; Murthy, Y. K.; Dadhwal, V. Optimizing Spaceborne LiDAR and Very High Resolution Optical Sensor Parameters for Biomass Estimation at ICESat/GLAS Footprint Level Using Regression Algorithms. *Prog. Phys. Geogr. Earth Environ.* **2017**, *41* (3), 247–267.

(65) Turner, D.; Lucieer, A.; Malenovský, Z.; King, D.; Robinson, S. A. Assessment of Antarctic Moss Health from Multi-Sensor UAS Imagery with Random Forest Modelling. *Int. J. Appl. Earth Obs. Geoinf.* **2018**, *68*, 168–179.

(66) Jensen, J. R. *Introductory Digital Image Processing: A Remote Sensing Perspective: Pearson Prentice Hall*; 2005.

(67) Waldhoff, G.; Bubenzer, O.; Bolten, A.; Koppe, W.; Bareth, G. Spectral Analysis of Aster, Hyperion, and Quickbird Data for Geomorphological and Geological Research in Egypt (Dakhla Oasis, Western Desert). In *International Archives of the Photogrammetry, Remote Sensing and Spatial Information Sciences - ISPRS Archives*; 2008.

(68) Satpathy, R.; Singh, V. K.; Parveen, R.; Jeyaseelan, A. T. Spectral Analysis of Hyperion Data for Mapping the Spatial Variation of in a Part of Latehar &Amp;

Gumla District, Jharkhand. *J. Geogr. Inf. Syst.* **2010**, *02* (04), 210–214.

(69) Kumari, S. K.; Debashish, C.; Pulakesh, D.; Jatisankar, B. Hyperion Image Analysis for Iron Ore Mapping in Gua Iron Ore Region. *Int. Res. J. Earth Sci.* **2014**, *1*, 1–6.

(70) Kruse, F. A.; Lefkoff, A. B.; Boardman, J. W.; Heidebrecht, K. B.; Shapiro, A. T.; Barloon, P. J.; Goetz, A. F. H. The Spectral Image Processing System (SIPS)—Interactive Visualization and Analysis of Imaging Spectrometer Data. *Remote Sens. Environ.* **1993**, *44* (2–3), 145–163.

(71) Angusamy, N.; Dajkumar Sahayam, J.; Suresh Gandhi, M.; Rajamanickam, G. V. Coastal Placer Deposits of Central Tamil Nadu, India. *Mar. Georesources Geotechnol.* **2005**, *23* (3), 137–174.

(72) Suresh, M.; Solai, A.; Kaveri, S.; Kanan, K.; Dhamodharan, V.; Baskar, K.; Rajamanickam, V. Post Tsunami Heavy Mineral Distribution Between Cuddalore to Kanyakumari Along the Tamil Nadu Coast, India – A Review. In *Tsunami - A Growing Disaster*; InTech, 2011.

(73) Viveganandan, S.; Lakshumanan, C.; Sundararajan, M.; Eswaramoorthi, S.; Natesan, U. Depositional Environment of Sediments along the Cuddalore Coast of Tamilnadu, India. *Indian J. Mar. Sci.* **2013**, *42* (3), 375–382.

(74) Chatterjee, S. C. *Petrography of the Igneous and Metamorphic Rocks of India*; 1974.

(75) K., T.; S., C.; S., P.; M., S.; R., T.; C., T.; Sharma, D. A.; Sinha, U. K. Geochemical and 13C Trends in Sedimentary Deposits of Coastal Pondicherry Region, East Coast of India – Insights from a Borehole Study. *Geochemistry* **2019**, 125553.

(76) Zhang, M.; Salje, E. K. H.; Ewing, R. C. Oxidation State of Uranium in Metamict and Annealed Zircon: Near-Infrared Spectroscopic Quantitative Analysis. *J. Phys. Condens. Matter* **2003**, *15* (20), 3445–3470.

(77) van der Meer, F. Analysis of Spectral Absorption Features in Hyperspectral Imagery. *Int. J. Appl. Earth Obs. Geoinf.* **2004**, *5* (1), 55–68.

(78) Ismail, R.; Mutanga, O.; Bob, U. The Use of High Resolution Airborne Imagery for the Detection of Forest Canopy Damage Caused by Sirex Noctilio. In *Proceedings International Precision Forestry Symposium*; 2006; pp 119–134.

(79) Goldstein, B. A.; Hubbard, A. E.; Cutler, A.; Barcellos, L. F. An Application of Random Forests to a Genome-Wide Association Dataset: Methodological Considerations & New Findings. *BMC Genet.* **2010**, *11* (1), 49.

(80) Abdel-Rahman, E. M.; Ahmed, F. B.; Ismail, R. Random Forest Regression and Spectral Band Selection for Estimating Sugarcane Leaf Nitrogen Concentration Using EO-1 Hyperion Hyperspectral Data. *Int. J. Remote Sens.* **2013**, *34* (2), 712–728.

(81) Lawrence, R. L.; Wood, S. D.; Sheley, R. L. Mapping Invasive Plants Using Hyperspectral Imagery and Breiman Cutler Classifications (RandomForest). *Remote Sens. Environ.* **2006**, *100* (3), 356–362.

Chapter 5

Studies on structure, chemistry and surface morphology of heavy minerals

5.1.Abstract

The beach sands of the Varkala-Kovalam coast, south-west India show good concentration of heavy minerals. The beach sand deposits mainly composed of ilmenite followed by sillimanite, monazite, rutile, zircon, leucoxene, and garnet. All these minerals from Varkala and Kovalam were successfully recovered and analysed the structure, chemistry, and surface morphology using advanced characterization techniques like Raman spectroscopy, ED-XRF, HR-ICP-MS, thermogravimetric analysis (TGA), UV-Visible-NIR spectroscopy, XPS, and SEM-EDS. The chemical composition including major oxides, trace elements, and rare earth elements present in each mineral were quantified. Surface chemistry, oxidation state of surface elements, degree of metamictization in zircon and monazite, anisotropic crystal behaviour of the minerals due to physical or chemical processes, discrimination of isomorphous series (garnet), polymorphs (Ti-oxide and $A1_2SiO_5$), opaque and non-opaque Fe–Ti oxide minerals, and finally the morphological changes due to mechanical impacts and solution activity of chemicals during the long transportation and deposition of mineral grains were also discussed. The characterisation results show good agreement with other major placer deposits in India. The study provides solid information to the scientific community and policymakers for determining the grade and potential applications of these strategic minerals.

5.2.Introduction

The beaches of India are bestowed with high concentration of strategic minerals such as ilmenite, monazite, garnet, rutile, sillimanite, zircon,etc.[1] The important placer deposits in India are Chavara (Kerala), Ratnagiri deposits (Maharashtra), Manavalakurich (Tamil Nadu), Bhimunipatnam (Andhra Pradesh), and Chatrapur (Orissa).[2] The ilmenite from Chavara in Kerala is industrially important for high TiO_2 content, which is about 60%. Many researchers have completed detailed studies including depositional environment, mineralogy and geochemical characterization of these placer deposits.[3–5] Apart from these major deposits, other beach placer deposits like the Kanykumari coast[6], Cuddalore coast[7], Thiruchendur coast[8], Valapatanam-Azhikode coast in Kerala[9], etc. were also studied in a detailed manner. All these minerals are named as “strategic” on the basics of their huge economic value due to

the wide range of applications in diverse areas.[10] The minerals are recovered from beach sands using a judicious combination of different physical, magnetic, and electrostatic separation units. Rutile and the upgraded ilmenite (synthetic rutile) with high TiO_2 content are used for the production of Titania products such as pulp, pigment, metal, etc.[11] Monazite is processed under optimized conditions of leaching, solvent extraction, precipitation, etc. for the recovery of rare earth metals.[12] High purity zirconia is extracted from zircon for ceramics and chemical industries.[13] Sillimanite as such or converted into synthetic mullite, is widely used for refractory applications and garnet as an abrasive material for glass polishing.[14] The potential applications of all these minerals truly depend on the grade of minerals, and it is determined using advanced characterization on crystal structure and chemical composition.

Advanced characterization on the crystal structure, geochemistry, optical properties, and surface morphology of beach sand minerals can be successfully achieved using a combination of robust technologies such as Raman spectroscopy, ED-XRF, HR-ICP-MS, SEM-EDS, etc. ED-XRF technique ensured the elemental composition especially the major oxides ranges from percentage to ppm level in minerals such as Ce_2O_3, P_2O_5, U, ThO_2, etc. of monazite[15], Al_2O_3, SiO_2, etc. of sillimanite[16], and also Fe_2O_3, TiO_2 etc. of garnet and ilmenite[6]. ICP-MS provides a more powerful and accurate determination of rare earth elements and also the trace elements present in ppm-level. Padmasubashini and Nandakishore determine rare earth and radioactive elements in ilmenite by ICP-MS.[17] Rajendran et al. determine rare earth elements of Indian coastal monazites using ICP-MS.[18] Raimondo et al., use LA-ICP-MS for assessing minor elements and RE elements of garnet.[19] The chemical composition of minerals such as the TiO_2 content of ilmenite and rutile, ZrO_2 in zircon, and rare earth elements in monazite plays an important role in determining their grade. Raman spectroscopic studies of heavy minerals provide an effective and detailed structural characterization of minerals under a polarizing microscope. Here it measures the vibrational properties of minerals by means of inelastic scattering of light.[20,21] The Raman studies of ilmenite structure were reported in Martian meteorite EETA79001[22], Pumice rock from El Gasco, Spain[23] and also in Ganga–Brahmaputra fluvial sediments, Bangladesh[24]. Narayanan (1950) have first reported the Raman Effect in rutile.[25] Presently, the Raman spectra are used for advanced level studies like discrimination of TiO_2 polymorphs[26,27], degree of metamictization in zircon and monazite[28], and discriminating isomorphous series of garnet and $A1_2SiO_5$ polymorphs[29,30]. XPS was used for understanding the chemistry and chemical state of surface elements of the minerals. The XPS offers evidence of absorbed D_2O, and O_2

with the Fe or Ti species on ilmenite surfaces.[31] The X-ray photoelectron spectra was used for discriminating Al_2SiO_5 polymorphs like andalusite, sillimanite, and kyanite based on the variance in chemical bonding and structural differences in the Al- and Si-coordination.[32] The abrasive property makes the garnet for preparing paints for metallic surfaces. Poon et al. use XPS for analyzing the surface chemistry of garnet and thereby is used for analysing its property for making bindings with metal surfaces. The XPS helps identify the rate of weathering of zircon by detecting the formation of Zr oxide or hydroxide at the mineral surface.[34] The optical properties of the minerals were analysed using UV–Vis–NIR absorption spectra, which provide solid information regarding various electronic transitions of metal cations and their charge transfer process. The charge transfer occurred due to Fe-O, Ti-O, and Fe-Ti transitions are responsible for strong absorption peaks of ilmenite in UV-Vis-NIR range.[35] General morphological features such as sub-rounded ilmenite grains, highly rounded monazite, prismatic sillimanite, angular garnet grains are analysed by SEM techniques.[36] Apart from these, the mechanical impacts and solution activity of chemicals during the long transportation and deposition of mineral grains results in morphological changes like the removal of blocks, irregular pits, grooves, etch V's, etc. which can be clearly seen using SEM images. Moreover, the SEM-EDS help to confirm the mineral grains by analysing its major elements.

In the present work, the crystal structure, geochemistry and surface morphology of seven common heavy minerals such as ilmenite, leucoxene, rutile, monazite, zircon, sillimanite, and garnet recovered from Varkala and Kovalam coast in Kerala, south-west India have been analysed and studied using characterization techniques such as Raman spectroscopy, ED-XRF, TGA, UV-Vis-NIR spectroscopy, and SEM-EDS.

5.3.Materials and Methods

A judicious combination of gravity, magnetic, and electrostatic separation techniques were applied to raw sand collected from Varkala and Kovalam regions of Thiruvananathapuram district for recovering high-grade heavy minerals such as ilmenite, sillimanite, monazite, zircon, rutile, leucoxene, and garnet. These two set of mineral samples recovered from the coasts of Varkala and Kovalam are used for the present study. Figure 5.1 shows the characterization techniques used for studying the structure, chemistry, and surface morphology of all these heavy minerals. X-ray diffraction analysis was carried out using a PANalytical X'Pert Pro diffractometer. The resultant diffraction patterns were processed

using X'Pert HighScore Plus software (PANalytical) to identify the recovered mineral phases. Raman measurements of the powdered mineral samples were recorded using a confocal Raman microscope (WI-Tec, Inc., Germany, alpha 300R).

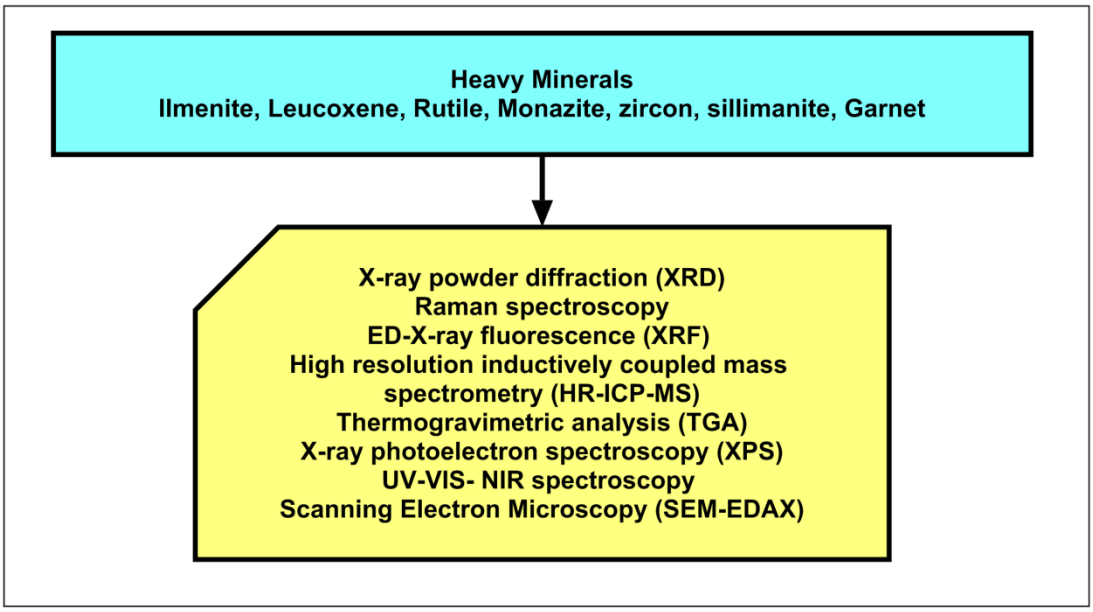

Figure 5.1: Characterization techniques used for the present study.

The trace, REE, and radioactive elements were identified using HR-ICP-MS of Nu Instruments Attom®, UK. The finely powdered mineral samples were dissolved in HF: HNO_3 acid mixture for HR-ICP-MS analysis. The bulk chemical composition was studied using Pan Analytical Epsilon 3 ED-XRF instrument having Omnion software. The SEM micrographs were taken using JEOL make model JSM5600 LV. Silicon Drift Detector−X-MaxN attached to the SEM of Carl Zeiss make EVO18 model was used for taking EDS data of minerals. Thermal gravimetric analysis of ilmenite and leucoxene were taken using a Perkin Elmer Pyris Diamond instrument with alumina as the standard and a heating rate of 10°C/min. The UV-Visible-NIR spectra were taken using Shimadzu UV-VIS-NIR spectrophotometer (UV-3600). The XPS spectra were recorded using Multilab 2000 (Thermofisher Scientific, U.K.), and the results were interpreted using MultiPak software.

5.4.Results and Discussion

5.4.1. Ilmenite and Leucoxene

Ilmenite ($FeTiO_3$) is an iron titanium oxide mineral with formula ferrous titanate, whereas leucoxene is an altered product of ilmenite.[37] The continuous process of alteration from ilmenite through pseudorutile to leucoxene, which includes processes of oxidation and

progressive removal of iron, can be expressed as $Fe_2^{3+}Ti_3O_9 \rightarrow Fe_{2-y}^{3+}Ti_3O_{9-3y}(OH)_{3y}$ where y=2 corresponds to leucoxene.[38] Usually, the Fe-Ti-Cr oxides are classified into two structural types of spinel and corundum. The ilmenite belongs to the corundum structure. The XRD patterns obtained for ilmenite and leucoxene are shown in Figure 5.2 and Figure 5.3. The excitation laser beam shows limited penetration depth for dark coloured Fe oxides. So the ilmenite is intrinsically a weak Raman scatter than other oxyanionic and Ti-Al oxide minerals.

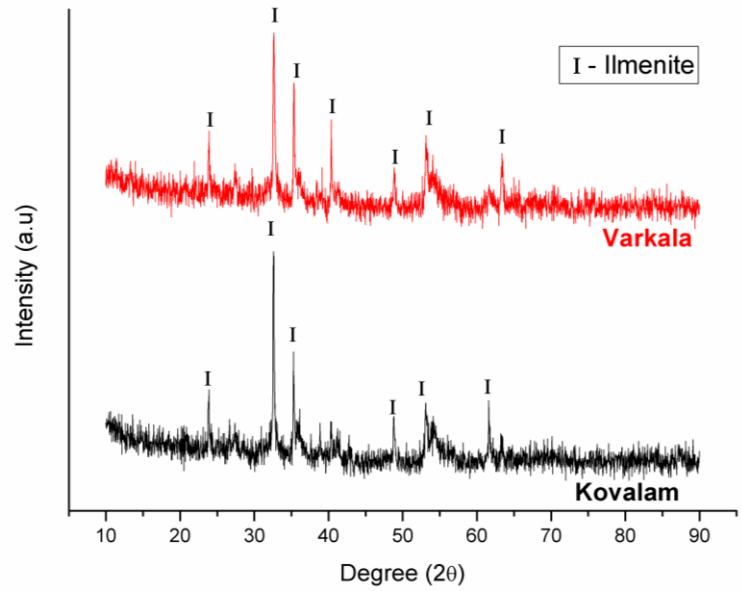

Figure 5.2: XRD patterns of ilmenite.

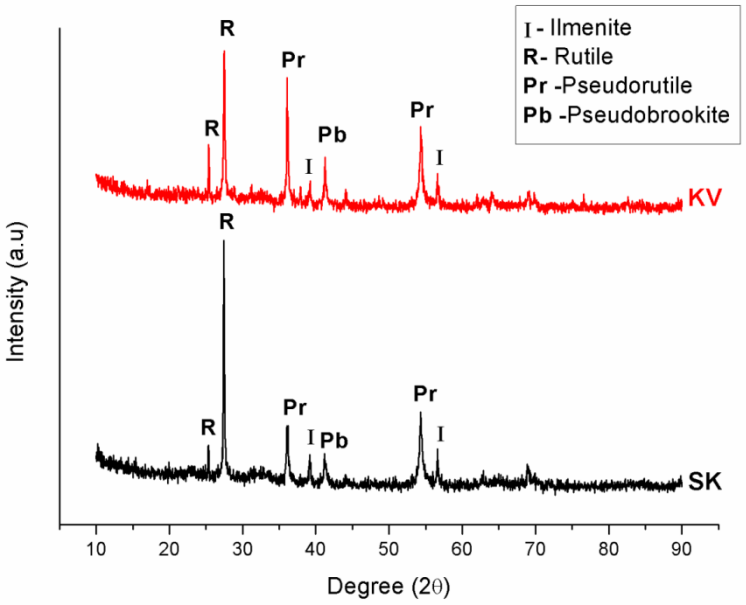

Figure 5.3: XRD patterns of leucoxene.

The intensity of the Raman signal from a mineral depends on the rigidity of the polyhedra in its structure and degree of covalency of its chemical bond. Higher the degree of covalency, then the bond produces the strongest Raman peak. The relative difference in bond strength between different types of polyhedral acts as the contributors of Raman spectral features, in which the $Ti^{4+}O_6$ Octahedra act as the main contributors of the Raman spectral features in ilmenite.[22]

Ilmenite has a Pseudo-corundum structure in which oxygen atoms form a hexagonal close-packed framework. The modes of vibrations for ilmenite is $\Gamma = 5\ A_g + 5\ E_g + 4\ A_u + 4\ E_u$ in which 10 Raman active vibrational modes (5Ag + 5Eg) can be derived based on factor group analysis. The Fe and Ti cations in ilmenite structure are well-organized among the 2/3 to fill the octahedral sites, and thereby, it forms a structural symmetry of $R\bar{3}$-C_{3i}^2.[39] The strongest peak at 678 cm^{-1} corresponds to A_g symmetry representing symmetric stretching vibration of Ti_4+O_6 octahedra and the weak peak at 236 cm-1 corresponds to Ag symmetry representing the translational motion of the Fe cation in the crystal lattice, which assist in clear discrimination of ilmenite from other opaque and non-opaque Fe–Ti–Cr oxides. [22–24] Other weaker peaks and their corresponding modes were shown in Figure 5.4 and Table 5.1.

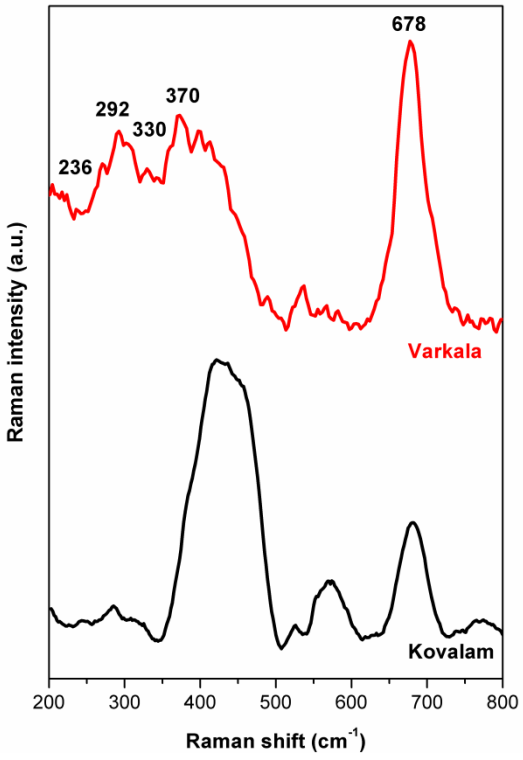

Figure 5.4: Raman spectra of ilmenite.

Table 5.1: Assignments of Raman peaks (cm^{-1}) of ilmenite structure.

Symmetry	**Assignment**	**Raman peaks (cm^{-1})**
Ag(1)	X-O stretch	678
Ag(4)	T(XO_6) translation	370
Eg(4)	T(XO_6) translation	330
Ag(5)	T(M) translation	292
Eg(5)	T(M) translation	236

The XPS bands of the ilmenite are shown in Figure 5.5. The Ti $2p_{3/2}$ and Ti $2p_{1/2}$ XPS peaks are observed at 458.23eV and 413.93 eV. The O1s get split into three components, such as 529.70eV corresponds to Ti-O, 532.10 eV corresponds to OH, and 531.05 eV corresponds to Fe-O. The $2p_{3/2}$ state of Fe splits at 710.81 eV and 713.26 eV. The $2p_{1/2}$ state of Fe can be fit at 724.39 eV. The $2p_{3/2}$ and $2p_{½}$ peaks of Fe state at around 710.81 and 724.39 eV corresponds to ferrous species, whereas at around 713.26 eV correspond to ferric species.[40]

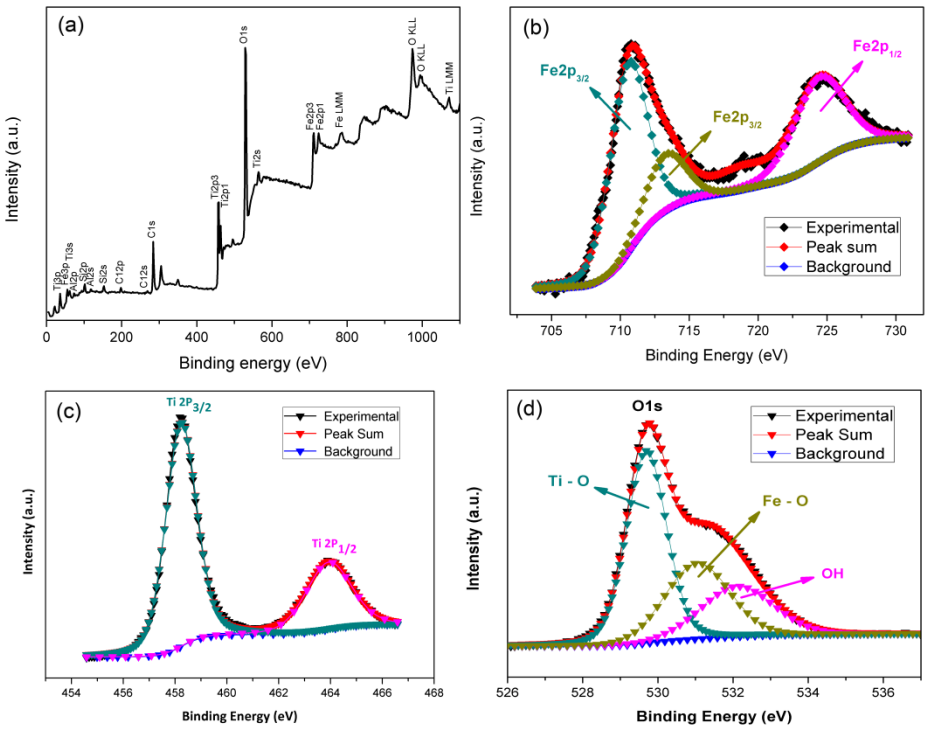

Figure 5.5: XPS spectra of ilmenite. (a) Wide scan XPS spectra, and high resolution scans of (b) Fe 2p, (c) Ti 2p, and (d) O 1s.

The TGA results of ilmenite and leucoxene are shown in Figure 5.6. The TGA curve shows weight loss, which is due to the presence of bound water or hydroxyl groups seen more in altered forms. Thus weight loss increases as the alteration increases, which is clearly noticeable in the case of leucoxene. The weight gain noticed for ilmenite above 600^{o}C corresponds to Fe^{2+}.[41] The UV-Vis-NIR spectra of ilmenite and leucoxene are shown in Figure 5.7. The strong absorption around 342-384 nm corresponds to $O^{2-} \rightarrow Ti^{4+}$ charge transfer transitions, and around 1259 nm corresponds to iron transition.[35]

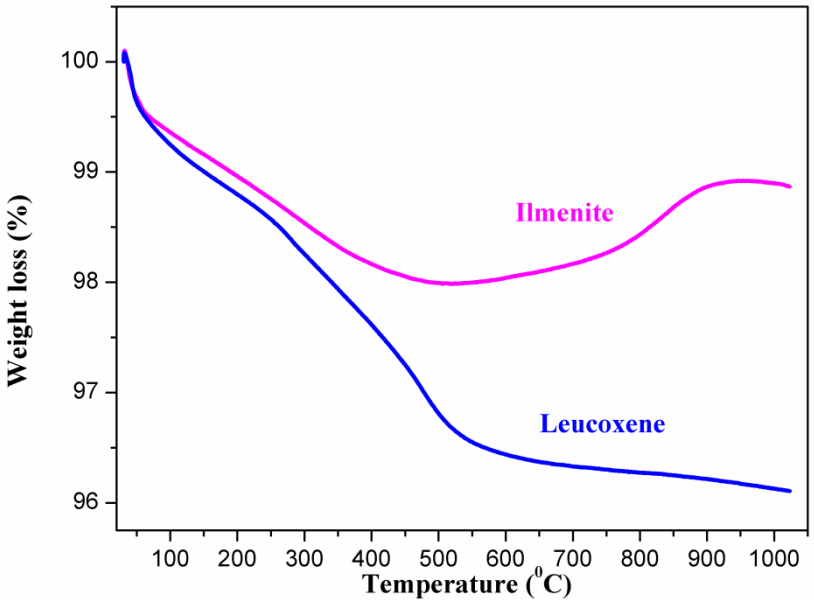

Figure 5.6: TGA results of ilmenite and leucoxene.

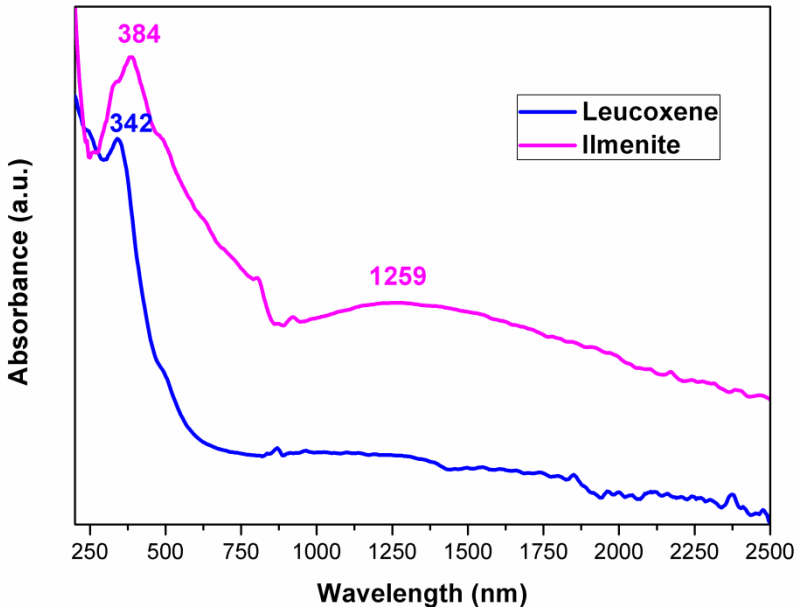

Figure 5.7: UV-Vis-NIR spectra of ilmenite and leucoxene.

The major oxides, REE and trace elements present in ilmenite are shown in Supplementary Table 5.2-5.4. The major oxides, REE, and trace elements present in leucoxene, are shown in Table 5.5-5.7. The average TiO_2 content of ilmenite and leucoxene is 54.830% and 73.556%. The average TREE content of ilmenite and leucoxene is 0.042% and 0.463%. Leucoxene from Varkala consists of 0.88% TREE, which is high compared to any other minerals other than monazite. On comparing with other placer deposits in India like Thottappally – Kayamkulam Deposit in Kerala (TiO_2 ranges 60.48-66.25%) and Manavalakurichi in Tamil Nadu (TiO_2 ranges 52.193-54.151%)[10,42], the results are comparable.

Table 5.2: Major oxides of ilmenite.

Major Oxides (%)	Varkala	Kovalam	Average
TiO_2	54.597	55.062	54.830
Fe_2O_3	41.668	40.686	41.177
SiO_2	0.568	0.55	0.559
MgO	0.518	0.574	0.546
P_2O_5	0.478	0.474	0.476
MnO	0.439	0.444	0.4415
Al_2O_3	0.239	0.747	0.493
CaO	0.168	0.173	0.1705
CdO	0.141	0.141	0.141
Others	1.184	1.149	1.1665

Table 5.3: Trace elements of ilmenite.

Trace elements (ppm)	Varkala	Kovalam	Average
V	1253.975	1249.261	1251.618
Nb	840.401	850.188	845.295
Zn	701.461	375.165	538.313
Cr	285.021	253.800	269.411
Pb	259.997	173.411	216.704
Zr	231.126	155.519	193.322
Ba	152.417	148.958	150.687

Th	134.485	81.509	107.997
Ta	87.330	96.295	91.812
Co	68.317	66.940	67.629
Sr	43.279	43.049	43.164
Ni	26.583	20.492	23.538
Cu	17.980	19.891	18.936
Ga	9.832	9.241	9.537
Hf	8.150	5.976	7.063
U	7.723	4.637	6.180
Rb	1.756	0.865	1.311
Cs	0.091	0.087	0.089
Total	4129.927	3555.284	3842.605

Table 5.4: Rare earth elements of ilmenite.

REE (ppm)	Varkala	Kovalam	Average
Ce	220.3621	85.34419	152.8531
La	105.5647	45.73811	75.65141
Sc	69.83426	71.92357	70.87891
Nd	99.4649	35.79099	67.62794
Pr	29.03324	11.09135	20.0623
Sm	15.46153	5.558739	10.51014
Y	7.079978	5.561397	6.320688
Gd	8.389168	3.401906	5.895537
Dy	2.573029	1.794721	2.183875
Yb	1.087627	1.093897	1.090762
Er	1.073025	1.021603	1.047314
Eu	0.737404	0.684271	0.710838
Tb	0.749758	0.397977	0.573868
Ho	0.409325	0.349472	0.379399
Lu	0.157865	0.158771	0.158318
Tm	0.148507	0.158635	0.153571
Total	**562.1264**	**270.0696**	**416.098**

Table 5.5: Major oxides of leucoxene.

Major Oxides (%)	Varkala	Kovalam	Average
TiO_2	74.569	72.543	73.556
Fe_2O_3	17.495	20.038	18.7665
Al_2O_3	1.993	2.007	2
SiO_2	1.618	1.708	1.663
P_2O_5	0.692	0.661	0.6765
MgO	0.443	0.537	0.49
CaO	0.282	0.261	0.2715
MnO	0.06294	0.125	0.09397
Others	2.84506	2.12	2.48253

Table 5.6: Rare earth elements of leucoxene.

REE (ppm)	Varkala	Kovalam	Average
Ce	4085.674	179.136	2132.405
La	1953.507	85.678	1019.592
Nd	1641.108	78.605	859.857
Pr	529.761	24.697	277.229
Sm	243.327	12.542	127.934
Gd	126.138	7.423	66.780
Sc	71.620	74.667	73.143
Y	62.957	13.672	38.314
Dy	26.315	4.610	15.462
Tb	9.605	0.931	5.268
Er	6.378	2.444	4.411
Eu	3.993	2.188	3.091
Ho	3.164	0.901	2.033
Yb	3.108	2.169	2.638
Tm	0.569	0.352	0.461
Lu	0.453	0.316	0.385
Total	8767.677	490.331	4629.004

Table 5.7: Trace elements of leucoxene.

Trace elements (ppm)	Varkala	Kovalam	Average
Nb	6574.076	2441.506	4507.791
Ta	2475.159	351.158	1413.158
V	2065.939	1626.037	1845.988
Th	1547.400	178.914	863.157
Zr	825.938	449.641	637.790
Cr	764.264	632.009	698.136
Pb	495.912	478.091	487.002
Zn	422.056	553.974	488.015
Ba	226.492	240.723	233.608
Sr	116.552	135.060	125.806
U	89.695	18.751	54.223
Ga	61.534	39.957	50.746
Hf	38.947	18.544	28.745
Co	24.332	30.756	27.544
Ni	18.504	20.666	19.585
Cu	18.008	19.059	18.533
Rb	1.615	1.613	1.614
Cs	0.133	0.115	0.124
Total	15766.558	7236.574	11501.566

The SEM micrographs taken for the ilmenite are shown in Figure 5.8 (a-g). Ilmenite grains are usually sub-rounded in shape with moderate relief (Figure 5.8(a-b)). Solution activities over along residence time results in formations of oriented crescentic pits (Figure 5.8(d)). Chemical reactions cause the removal of large blocks, step-like features, and undulatory wavy surfaces (Figure 5.8(d-g)). Impact "V" marks caused by etching were also noticed (Figure 5.8(e-g)). Deep grooves are also formed at an angle oriented in an irregular manner. The SEM image indicates a minimum two stages of solution activities, in which the initial stage follows parting of planes.[36] Similar morphological characteristics were shown by leucoxene (Figure 5.9). The surface morphological characteristics like pits, step-like features,

undulatory wavy surfaces, deep grooves, etc. clearly indicate the alteration of ilmenite to leucoxene.

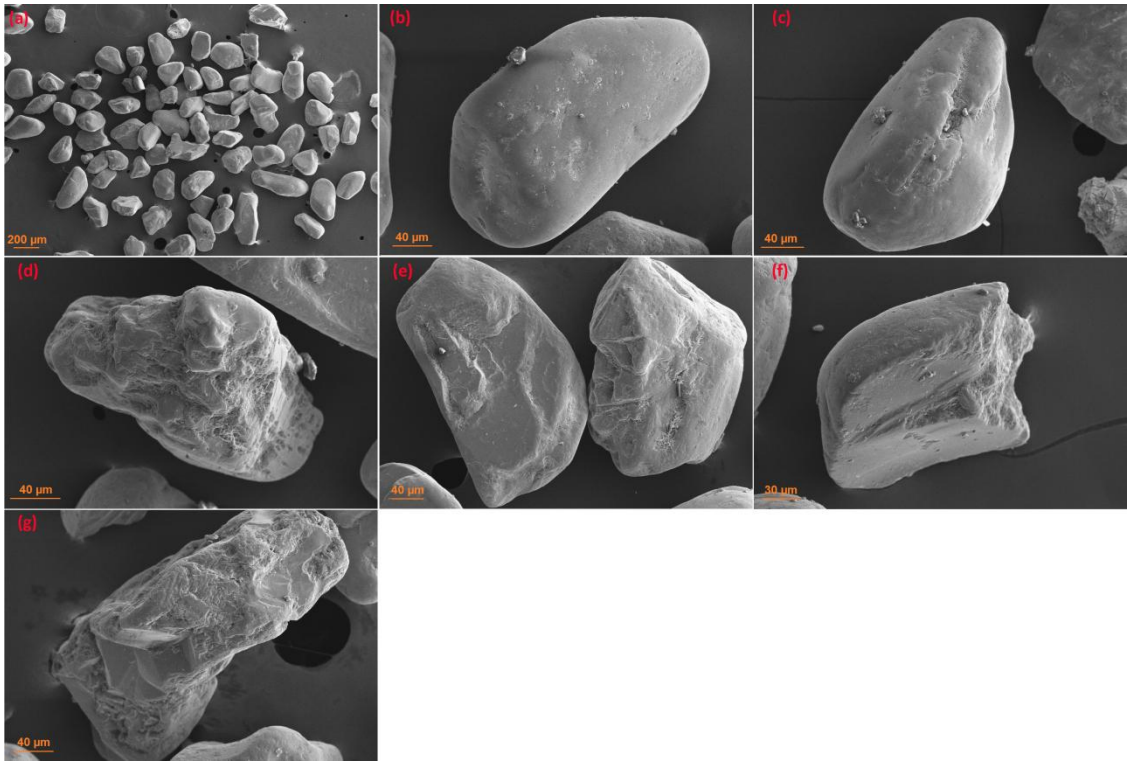

Figure 5.8: SEM images of ilmenite.

Table 5.8: Chemical composition of ilmenite by SEM-EDS.

Element	Weight (%)	Atomic (%)
Ti K	23.71	10.89
Fe K	17.6	6.93
Mg K	0.66	0.6
Al K	0.38	0.31
Si K	0.26	0.2
O K	52.59	72.28
C K	4.81	8.8

Figure 5.10, Table 5.8 and Table 5.9 show the SEM-EDS results of ilmenite and leucoxene. The results show that ilmenite and leucoxene contain Ti and Fe majorly with minor impurities of silica, alumina, and magnesium might be due to inclusions and C is due to the carbon coating.[43]

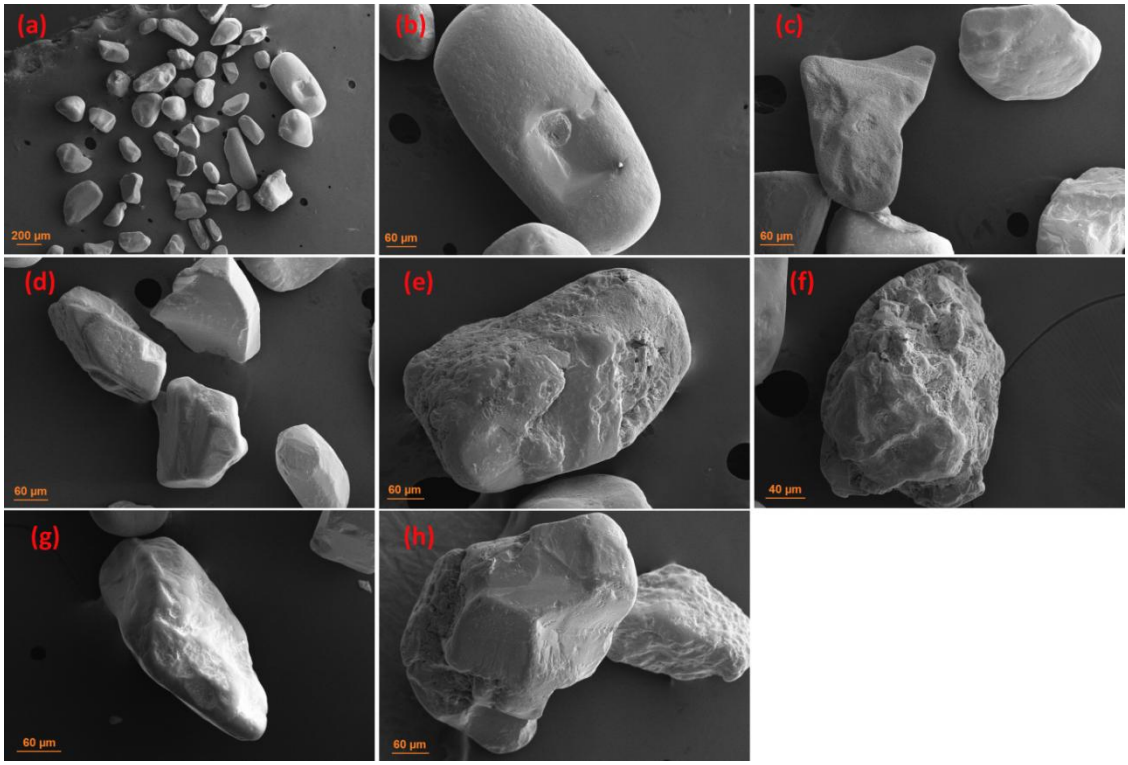

Figure 5.9: SEM images of leucoxene.

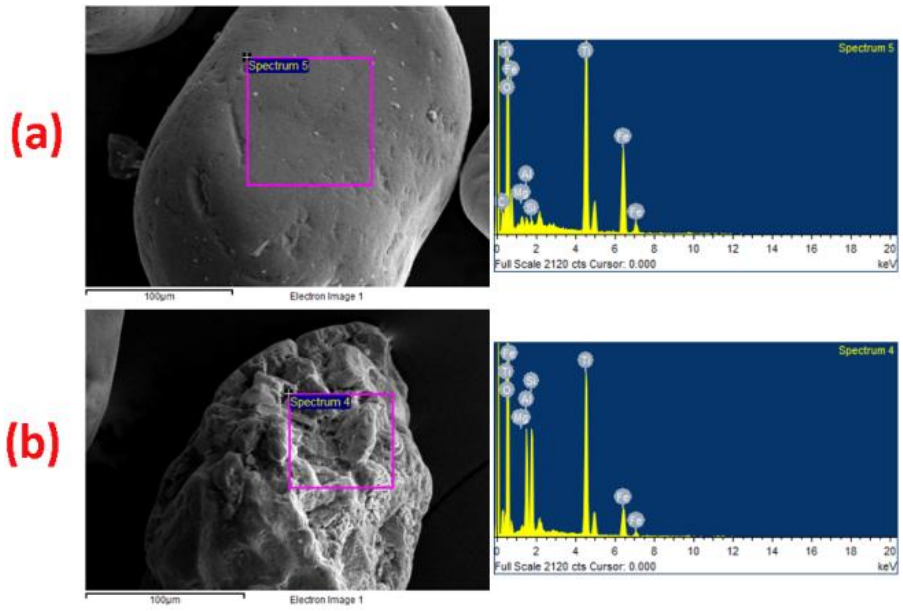

Figure 5.10: SEM-EDS results (a) Ilmenite; (b) Leucoxene.

Table 5.9: Chemical composition of leucoxene by SEM-EDS.

Element	Weight (%)	Atomic (%)
Ti K	19.97	8.68
Fe K	6.87	2.56
Mg K	0.41	0.35
Al K	5.72	4.42
Si K	5.79	4.29
O K	61.24	79.7

5.4.2. Rutile

The rutile (TiO_2) corresponds to a tetragonal system (space group D^{14}_{4h} – $P4_2/mnm$) with two TiO_2 groups per unit cell. The XRD pattern of rutile was shown in Figure 5.11. The first-order Raman scattering provides four Raman active vibrations as $A_{1g} + B_{1g} + B_{2g} + E_g$. The spectra show all the four Rama active vibrations at A_{1g}=603, B_{1g}=144, B_{2g}=827, and E_g= 443 (see Figure 5.12 and Table 5.10). The sharp and strongest peak at 443cm^{-1} belongs to doubly degenerate species E_g. The peaks at 248 and 603 also appear sharp but quite moderate. The peaks at 144 and 827 are comparatively broad and diffuse.

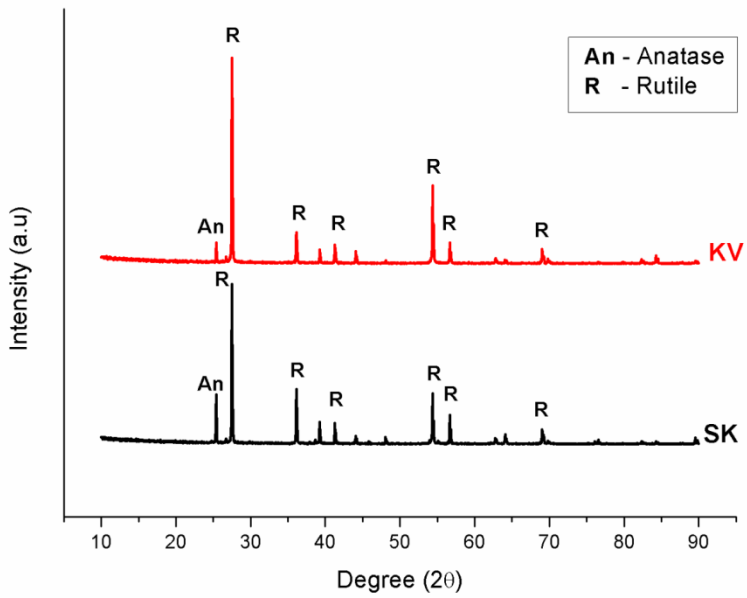

Figure 5.11: XRD pattern of rutile.

The vibrational frequency at 144 corresponds to B_{1g} mode is extremely weak due to the fact that the oxygens move strictly perpendicular around the titanium, which results in very less changes for Ti-O and O-O bond lengths. But in the case of mode B_{2g} corresponds to 827 cm^{-1}, the oxygens move simultaneously towards and away from the central titanium results in changes of Ti-O bond lengths. Hence the Raman frequency for B_{2g} is quite high compared to B_{1g}. Krishnamurti has theoretically calculated the values of A_{2g} and B_{2g} as 582 and 831, respectively.[44] The Raman spectrum of rutile exhibits a moderate peak at 603 and a very weak peak at 827.[45] The peak at ~ 248 cm^{-1} corresponds to second-order Raman scattering, but it is theoretically Raman inactive and may arise due to infra-red active doubly degenerate mode of Eu species.[46,47] Krishnamurti have suggested that infrared active EU species have been observed to be weakly Raman active in violation of selection rules due to the variation in atomic weights of the titanium isotopes.[44] All the Raman peaks obtained for the sample strictly follow the Raman modes of rutile, not with any other polymorphs such as anatase or brookite.

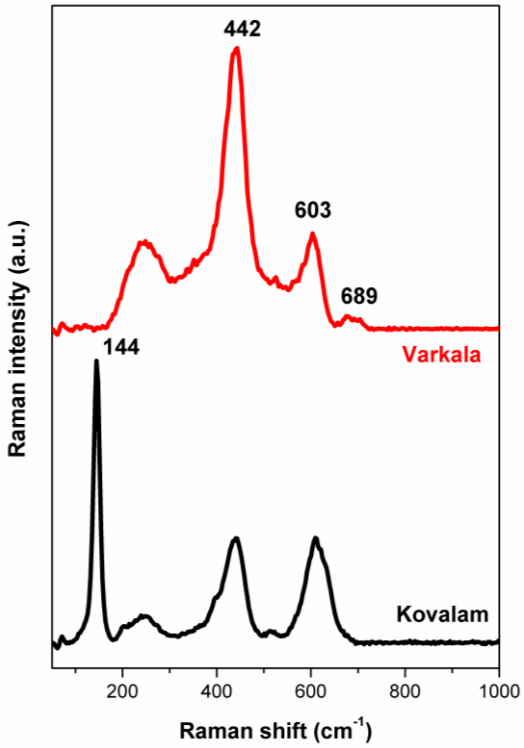

Figure 5.12: Raman spectra of rutile.

Table 5.10: Raman active vibrational frequencies (cm^{-1}) of rutile TiO_2.

Symmetry	Raman peaks (cm^{-1})
B_{1g}	144
E_g	443
A_{1g}	603
A_{2u} x A_{2u}	692
B_{2g}	827

The XPS spectra of rutile are shown in Figure 5.13. The Ti 2p are fitted as $Ti^{4+}2p_{1/2}$ at 464.14 eV and $Ti^{4+}2p_{3/2}$ at 458.45 eV.[48] The O1s shows two peaks at 529.80 eV corresponds to metallic oxide, and 532.10 eV corresponds to OH groups, chemisorbed oxygen, and organic oxygen present on the mineral surface.[49,50]

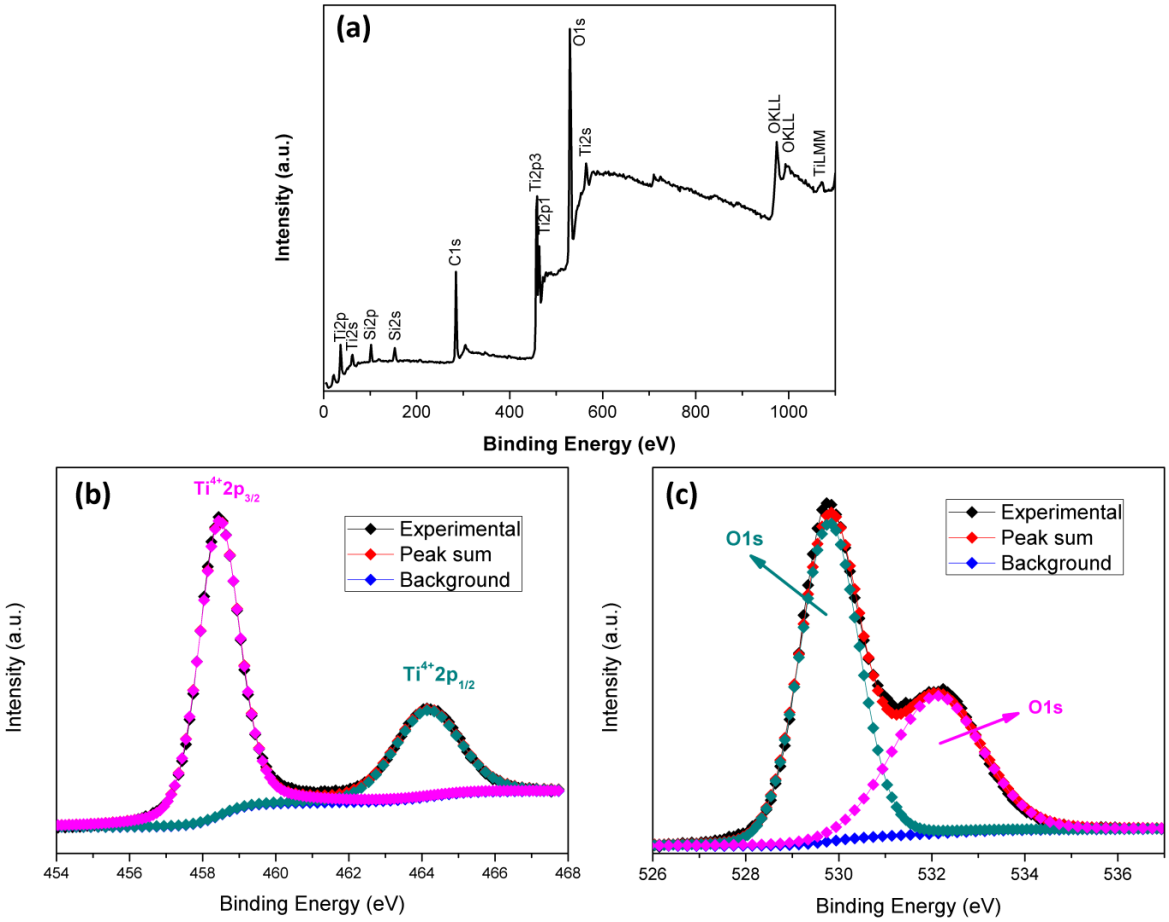

Figure 5.13: XPS results of rutile (a) Wide scan XPS spectra, and high resolution scans of (b) Ti 2p, and (c) O 1s.

The UV-Vis-NIR spectra of natural rutile are shown in Figure 5.14. The rutile (TiO_2) shows strong absorption in the UV region with a sharp peak at 362nm, which can be assigned to $O^{2-} \rightarrow Ti^{4+}$ charge transfer transitions.[35]

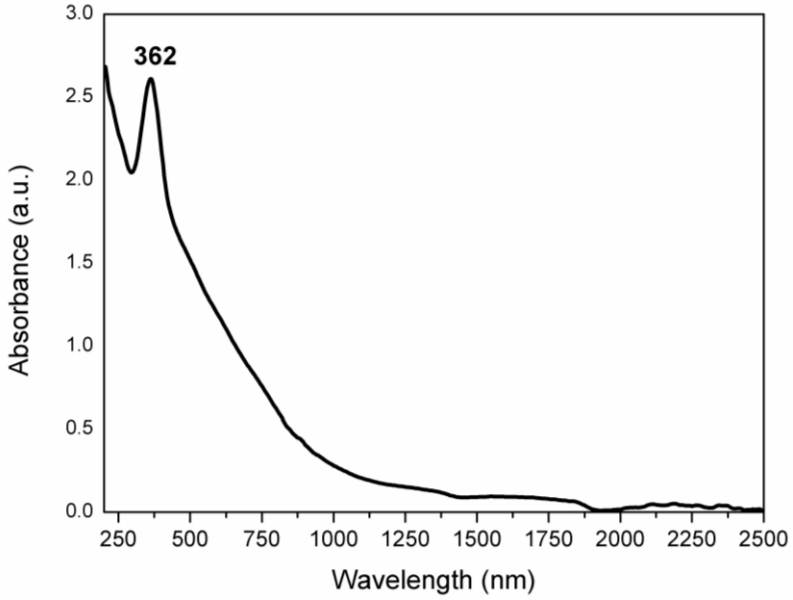

Figure 5.14: UV-Vis-NIR spectra of rutile.

The Tables 5.11- 5.13 gives the major oxides, trace elements, and RE elements present in rutile. The average TiO_2 content is 95.718%. It follows by Nb_2O_5, SiO_2, Fe_2O_3, Al_2O_3, and CaO. Apart from major oxides, the rutile usually holds trace elements in ppm level like V, Cr, Co, Ni, Cu, etc. The rutile also contains radioactive elements like Th and U in the range of 0.924ppm to 0.103ppm. The average rare earth content estimated for rutile comes around 36.117ppm with a maximum for scandium (11.163 ppm) followed by Ce, La, Nd, Y, etc. On comparing with the TiO_2 content of rutile from Bhimunipatnam–Konada coast, Andhra Pradesh ranges 97.48 to 99.13%[51], the results are comparable.

Table 5.11: Major oxides present in rutile.

Major Oxides (%)	Varkala	Kovalam	Average
TiO_2	95.921	95.515	95.718
Nb_2O_5	0.85	0.677	0.7635
SiO_2	0.593	0.996	0.7945
Fe_2O_3	0.336	0.289	0.3125
Al_2O_3	0.268	0.294	0.281
CaO	0.108	0.111	0.1095
Others	1.924	2.118	2.021

Table 5.12: Trace elements of rutile.

Trace elements (ppm)	Varkala	Kovalam	Average
V	4754.110	3597.031	4175.571
Cr	2693.311	2516.003	2604.657
Co	2270.896	2053.535	2162.216
Ni	681.682	471.153	576.417
Cu	481.990	441.372	461.681
Zn	203.668	329.187	266.427
Ga	122.097	239.105	180.601
Rb	106.440	94.022	100.231
Sr	75.909	67.791	71.850
Zr	57.837	92.684	75.261
Nb	15.657	18.565	17.111
Cs	10.329	12.164	11.247
Ba	7.555	12.353	9.954
Hf	4.287	5.002	4.645
Ta	1.062	0.852	0.957
Pb	1.034	1.390	1.212
Th	0.946	0.901	0.924
U	0.098	0.109	0.103
Total	11488.908	9953.220	10721.064

Table 5.13: Rare earth elements of rutile.

REE (ppm)	Varkala	Kovalam	Average
Sc	11.109	11.218	11.163
Ce	8.211	10.297	9.254
La	4.982	5.740	5.361
Nd	4.285	4.812	4.548
Y	2.484	1.428	1.956
Pr	1.164	1.391	1.278
Sm	0.649	0.820	0.735
Gd	0.462	0.584	0.523
Dy	0.367	0.364	0.366
Yb	0.305	0.258	0.281
Er	0.287	0.295	0.291
Eu	0.103	0.125	0.114
Ho	0.086	0.088	0.087
Tb	0.064	0.073	0.069
Tm	0.050	0.051	0.051
Lu	0.044	0.037	0.041
Total	34.653	37.580	36.117

The SEM micrographs showing the morphological characteristics of rutile are given in Figure 5.15. Usually, rutile grains are seen in highly rounded in shape with varying relief from high to moderate (Figure 5.15 (a)). Irregular pits, deep fractures of solution grooves (Figure 5.15 (c)), embayments, removal of blocks (Figure 5.15 (d and g)), etch V's are noticed on the surface. This clearly indicates intense etching formed by long exposure to chemical activity. Precipitations are also noticed, especially with the grooves. Removal of blocks made a step-like appearance (Figure 5.15 (f)) for the mineral grains.[36] The EDS results are given in Figure 5.16 and Table 5.14. The EDS results confirm that the mineral is rutile by indicating the high presence of Ti with the minor presence of Fe and other impurities such as Vanadium. The presence of V is also confirmed in ICPMS results.

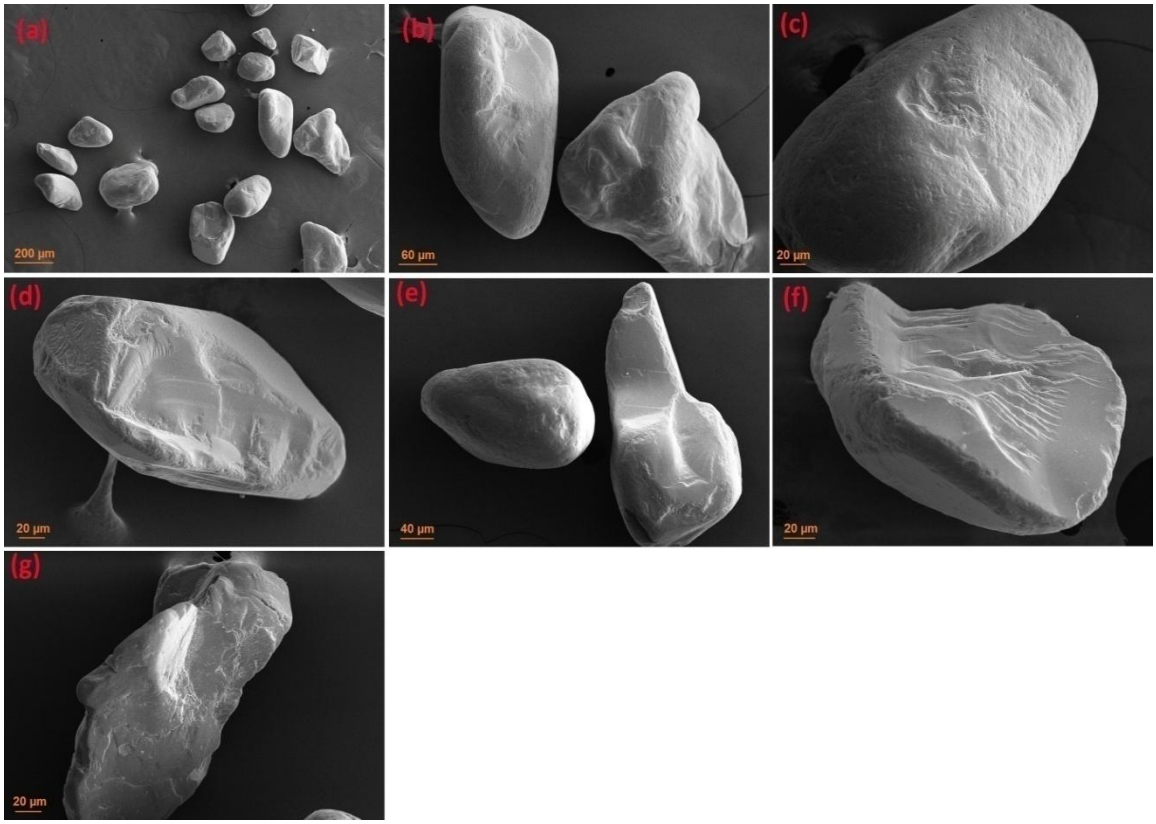

Figure 5.15: SEM images of rutile.

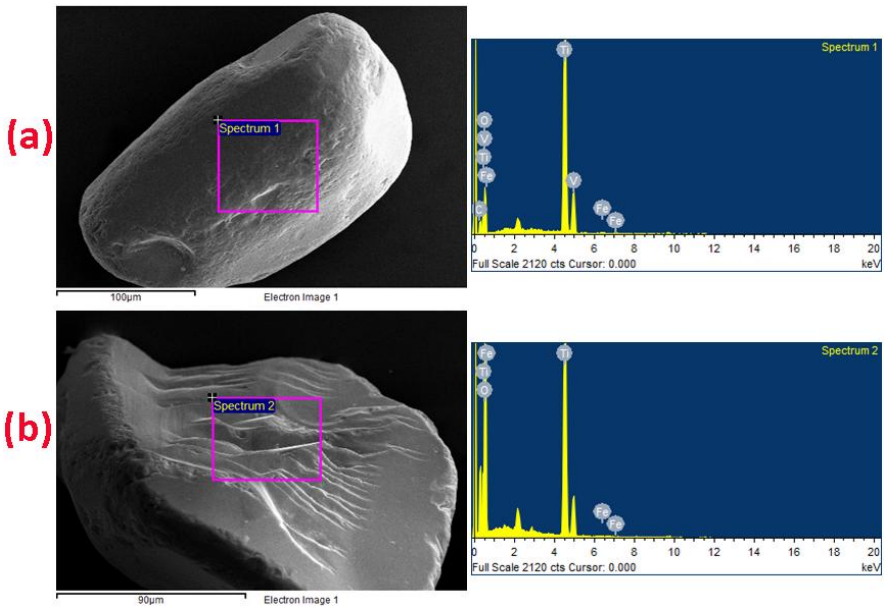

Figure 5.16: SEM-EDS results of rutile.

Table 5.14: Chemical composition of rutile by SEM-EDS.

Element	(a)		(b)	
	Weight (%)	**Atomic (%)**	**Weight (%)**	**Atomic (%)**
Ti K	56.31	29.81	34.62	15.05
Fe K	0.4	0.18	0.14	0.05
V K	1.08	0.54	-	-
O K	37.31	59.13	65.24	84.9
C K	4.9	10.34	-	-

5.4.3 Monazite

Monazite is a light rare-earth orthophosphates mineral with general formula MPO_4 where M = La to Gd. It belongs to the monoclinic system (space group C_{2h}^5) consists of four formula units per unit cell. The M and PO_4 occupy the general *C1* sites. The monazite group shows varying geochemistry due to the addition of actinide elements like Th or U, a small quantity of Pb, substitution of Ce by light REEs and also the inclusion of heavy REEs, moreover, it may results in the formation of solid solutions also with other minerals.[52] The ICP-MS analysis reveals that Chavara monazite from Kerala shows total REE contents (TREE) of 48.42% in which the light REE (LREE) is 47.37%, and heavy lanthanides (HREE) is 10594ppm. The ThO_2 and U_3O_8 content normally ranges around 10.50% and 0.04%.[18] The XRD pattern of monazite is shown in Figure 5.17. The symmetry representation analysis shows that 36 Raman-active modes (A_g+B_g) are available from the optical modes for monazite–(Ce) as $\Gamma = 18A_g + 17A_u + 18B_g + 16B_u$. The free $(PO4)_{3-}$ ion shows four normal modes, such as symmetric stretch v_1(A1), antisymmetric stretch v_3(F2), and bending v_2(E) and v_4(F2) vibrations. The Raman spectrum of monazite groups shows distinct peaks in the ranges 970-1075 cm^{-1} and below 620 cm^{-1}.[53] The Raman peaks in the range 970- 1075 $cm^{-1}$are assigned to the internal PO_4 stretching vibrations. The Raman modes of monazite were clearly shown in Figure 5.18 and Table 5.15. The PO_4 bending together with the external vibrations due to the movements of the Ce^{3+} ions and the $[PO_4]^{3-}$ units are responsible for the peaks below 620 cm^{-1}.[54] The strong peak at 972 cm^{-1} corresponds to symmetric stretching of the PO_4 tetrahedrons has a contribution from both A_g and B_g mode.

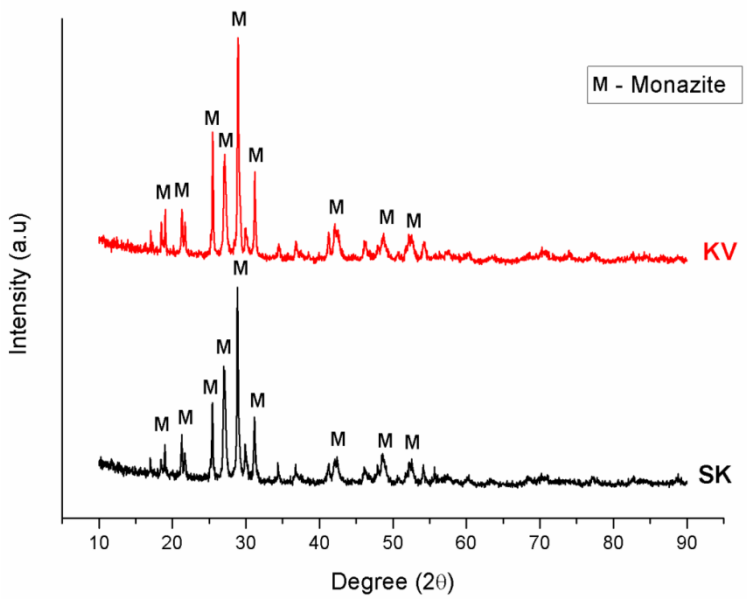

Figure 5.17: XRD pattern of monazite.

Table 5.15: Raman active frequencies (cm^{-1}) of monazite.

Symmetry	**Assignment**	**Raman peaks (cm^{-1})**
Bg	Lattice	89
Ag	Lattice	105
Ag	Lattice	151
Bg	Lattice	173
Ag	Lattice	181
Ag /Bg	Lattice	219
Ag /Bg	Lattice	227
Ag	Lattice	256
Ag	Lattice	276
Ag/Bg	Lattice	400
Ag/Bg	Lattice	419
Ag/Bg	v_2	468
Ag /Bg	v_4	621
Ag /Bg	v_1	972
Ag /Bg	v_3	1058

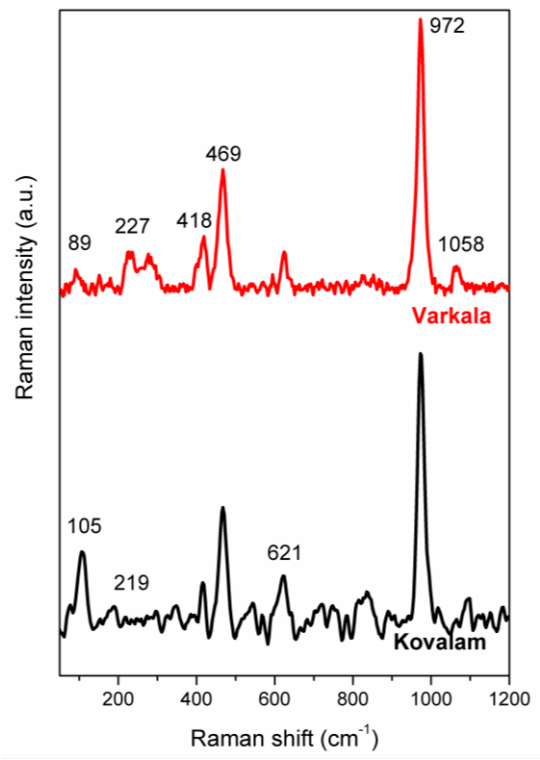

Figure 5.18: Raman peaks of monazite.

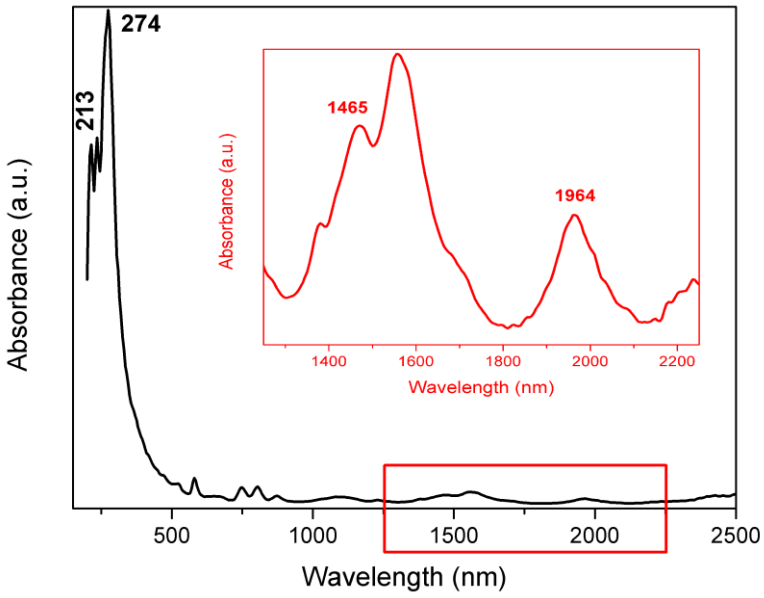

Figure 5.19: UV-Vis-NIR spectra of monazite.

The UV-Vis-NIR spectrum of monazite is shown in Figure 5.19. Two absorption bands of 213nm and 274nm in the UV region correspond to the transition of $^2F_{5/2}$ (ground state) to $^2D_{5/2}$ and $^2D_{3/2}$ levels (excited state). The weak extension noticed from 300 to 450nm corresponds to the presence of Ce^{4+}. The peaks around 1465nm and 1964nm in the NIR

region corresponds to the presence of phosphate.[55] The major oxides, rare earth elements, radioactive elements, and trace elements present in monazite are shown in Tables 5.16-5.19. The average P_2O_5 content is 23.769%, followed by SiO_2, Cao, Al_2O_3, CdO, MgO, and Fe_2O_3. The results of major oxides, especially the values of P_2O_5, SiO_2, Cao, Al_2O_3, etc. are comparable with the results obtained for monazite from Chavara in Kerala.[15] The Th and U content of Varkala monazite is 6.312% and 0.304%, and that of Kovalam monazite is 6.359% and 0.30%. The average Th and U content are 6.336% and 0.312%. The TREE elements present in Varkala and Monazite samples are 40.76% and 42.599%, with an average of 41.668%. The Ce present in maximum with an average of 20.318%, followed by La, Bd, Pr, Sm, Gd, etc. Trace elements such as Zn, Pb, Ga, Sr, Zr, etc. also present in monazite in ppm-level. The TREE for Chavara and Manavalakurichi monazite determined using ICP-MS are 48.42%, and 56.61% also show a strong correlation with the current results.[18]

Table 5.16: Major oxides of monazite.

Major Oxides (%)	**Varkala**	**Kovalam**	**Average**
P_2O_5	24.153	23.385	23.769
CaO	1.647	1.64	1.6435
SiO_2	1.309	2.906	2.1075
Al_2O_3	0.62	1.922	1.271
CdO	0.462	0.656	0.559
Fe_2O_3	0.372	0.243	0.3075
MgO	0.267	0.363	0.315
Others	71.17	68.885	70.0275

Table 5.17: Radioactive elements of monazite.

Radioactive elements (%)	**Varkala**	**Kovalam**	**Average**
Th	6.312	6.359	6.336
U	0.304	0.320	0.312
Total	6.615	6.679	6.647

Table 5.18: Rare Earth elements of monazite.

REE (%)	Varkala	Kovalam	Average
Ce	19.821	20.814	20.318
La	8.613	9.155	8.884
Nd	7.624	7.779	7.702
Pr	2.494	2.577	2.535
Sm	1.158	1.167	1.163
Gd	0.6	0.625	0.613
Y	0.235	0.27	0.252
Dy	0.104	0.113	0.108
Tb	0.045	0.05	0.047
Er	0.018	0.02	0.019
Ho	0.011	0.012	0.011
Eu	0.008	0.011	0.01
Yb	0.004	0.004	0.004
Tm	0.001	0.001	0.001
Lu	0.001	0.001	0.001
Sc	0	0.001	0.001
Total	40.736	42.599	41.668

Table 5.19: Trace elements of monazite.

Trace elements (ppm)	Varkala	Kovalam	Average
Zn	9479.575	9168.141	9323.858
Pb	6901.717	7032.331	6967.024
Ga	2082.117	2330.171	2206.144
Sr	405.924	320.950	363.437
Zr	310.761	2035.323	1173.042
Ba	309.267	380.648	344.957
Cu	161.784	106.686	134.235
Ni	60.124	78.631	69.377

Cr	20.601	17.357	18.979
V	18.450	15.625	17.038
Rb	15.030	18.137	16.584
Hf	10.565	59.074	34.820
Nb	6.953	4.113	5.533
Co	3.470	3.309	3.389
Ta	1.708	2.429	2.068
Cs	0.227	0.268	0.248
Total (%)	**1.979**	**2.157**	**2.068**

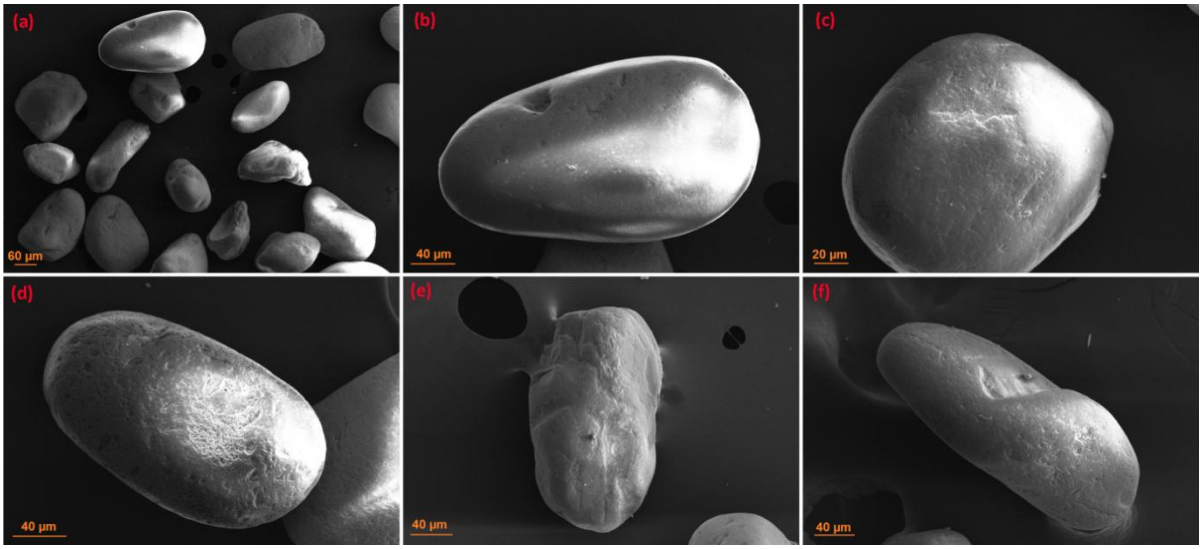

Figure 5.20: SEM images of monazite.

Figure 5.20 gives the SEM photos of monazite. Figure 5.21 and Table 5.20 show the SEM-EDS results of monazite. The monazite is usually seen as highly rounded in shape with moderate relief (Figure 5.20 (a-d)). Irregular pits oriented in different directions (Figure 5.20 (b and d)). Cleavage-controlled blocky fractures due to the removal of blocks (Figure 5.20 (e and f) were formed due to precipitation. Impact effects cause linear, curved, or irregular features, sometimes they coalesced on the surface (Figure 5.20 (e)). The morphology clearly indicates the polycyclic nature of the grains occurred due to high physical energy conditions, long transport, and solution effects of grains.[36] The high content of rare earth elements (Ce, La, and Nd), radioactive elements (Th and U), and P confirms that the minerals are monazite. The SEM-EDS also shows the minor presence of Ca, and F [15], and the presence of carbon tapes used for fixing the grains may give the values of C [56].

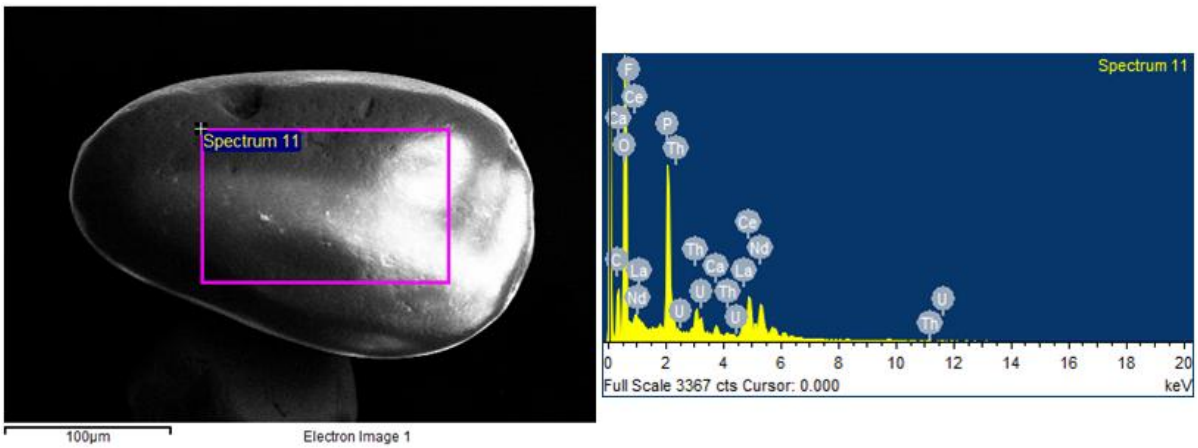

Figure 5.21: SEM-EDS results of monazite.

Table 5.20: Chemical composition of monazite by SEM-EDS.

Element	Weight (%)	Atomic (%)
Ce L	14.31	2.3
La L	6.99	1.13
Nd L	4.8	0.75
Th M	5.81	0.56
U M	0.15	0.01
P K	9.84	7.14
Ca K	0.8	0.45
F K	0.09	0.11
O K	41.89	58.87
C K	15.31	28.67

5.4.4. Zircon

Zircon having a tetragonal structure ($I4_1/amd$ and $Z = 4$)[57], formed by a chain of edge-sharing and alternating SiO_4 tetrahedra. The XRD pattern of zircon is shown in Figure 5.22. Theoretically 12 Raman active normal modes represented as $2A_{1g} + 4B_{1g} + B_{2g} + 5E_g$ in which the internal modes are $2A_{1g} + 2B_{1g} + B_{2g} + 2E_g$ and external modes are $2B_{1g}$(translatory) + $2E_g$(translatory) + E_g(rotatory). The internal modes for zircon are listed in Table 5.21 along with their assignments, and the external modes are 207, 226, 356, 397 cm^{-1} (see Figure 5.23).

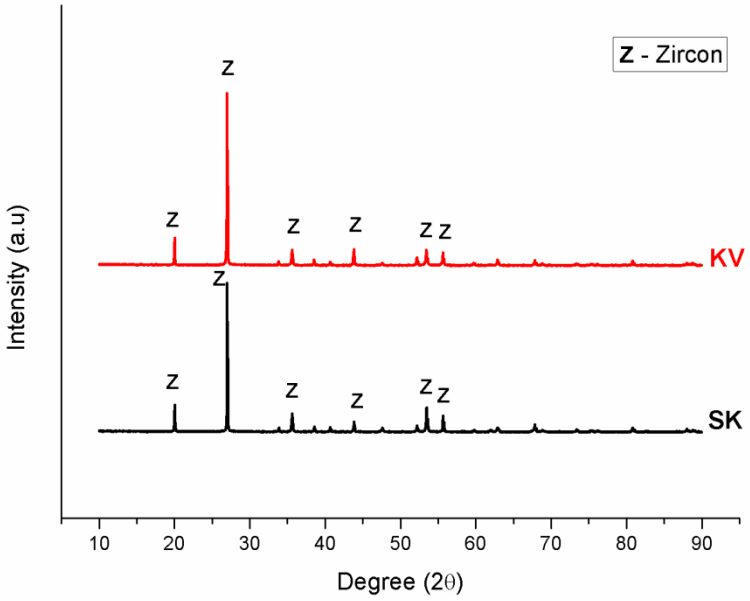

Figure 5.22: XRD pattern of zircon.

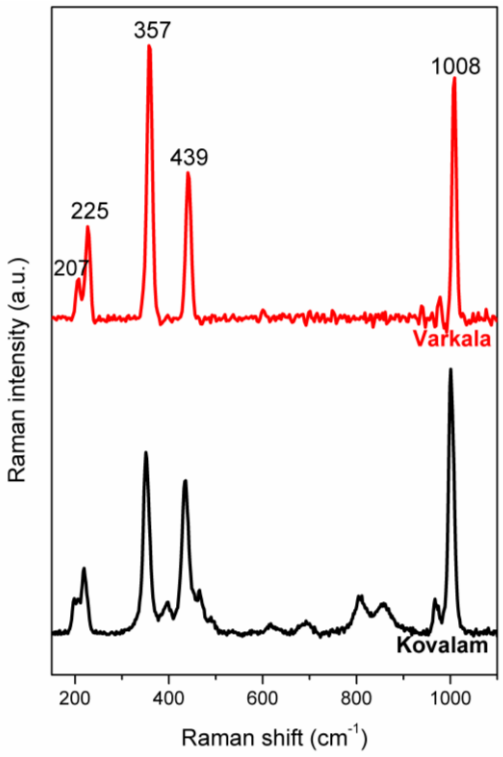

Figure 5.23: Raman peaks of zircon.

Table 5.21: Experimental Raman frequencies (cm^{-1}) of Zircon.

Symmetry	Assignment	Raman peaks (cm^{-1})
Internal modes		1008
$\mathbf{B_{1g}}$	Si–O ν_3 stretching	
$\mathbf{A_{1g}}$	Si–O ν_1 stretching	978
$\mathbf{A_{1g}}$	Si–O ν_2 bending	440
$\mathbf{B_{2g}}$	Si–O ν_2 bending	270
External modes		207, 225, 357, 395

The radioactive decay of radionuclides, and their daughter products causes heavy damage to the crystalline structure of naturally occurring zircon.[58,59] These increase in α-decay radiation dose causes the two Si-O stretching modes features between 970 and 1010 cm−1, especially the $\nu_3(SiO_4)$ frequency mode, to become weaker and broader.[20,34] Thus it results in a broad spectral feature between 850 and 1100 cm^{-1}.[60] This state of high loss in the periodic crystal structure of zircon due to the radiation damage is termed as metamictization of zircon.[61] Metamict is defined as a state of a periodic or amorphous.[62] The zircon shows a clear, well-defined peak at 1009cm^{-1} corresponds to ν3 (SiO4) stretching.[63] The well-resolved and sharp peaks indicate well-crystallized structure for zircon samples.

The XPS peaks of the zircon are shown in Figure 5.24. The Zr 3d photo-peak decomposed into $3d_{5/2}$ at 182.95 eV and $3d_{3/2}$ at 185.52 eV. The Si 2p spectra were also fitted with two Gaussian components of $Si_1$2p and $Si_2$2p at 101.10 eV and 102.27 eV.[34] The O1S represents a superposition of oxygen atoms such as O_1 and O_2 at 530.96 eV and 531.36 eV. The energy of $O_1$1s corresponds to regular atoms of the three-coordinated oxygen in $ZrSiO_4$, and that of $O_2$1s corresponds to oxygen atoms of defect oxygen atoms assigned to defect $SiO_3^{2-}$and SiO_2^0.[64]

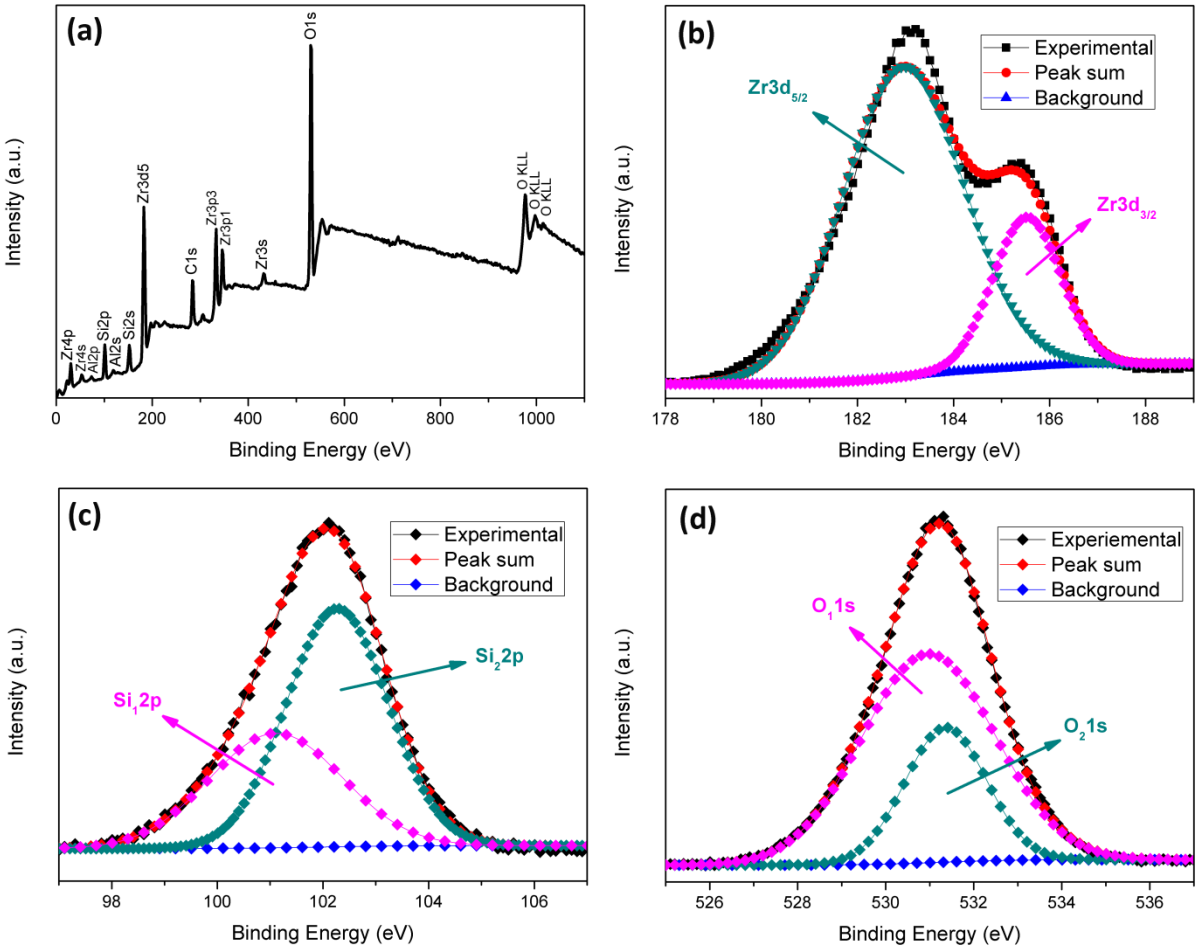

Figure 5.24: XPS results of zircon (a) Wide scan XPS spectra, and high resolution scans of (b) Zr3d, (c) Si2p, and (d) O1s.

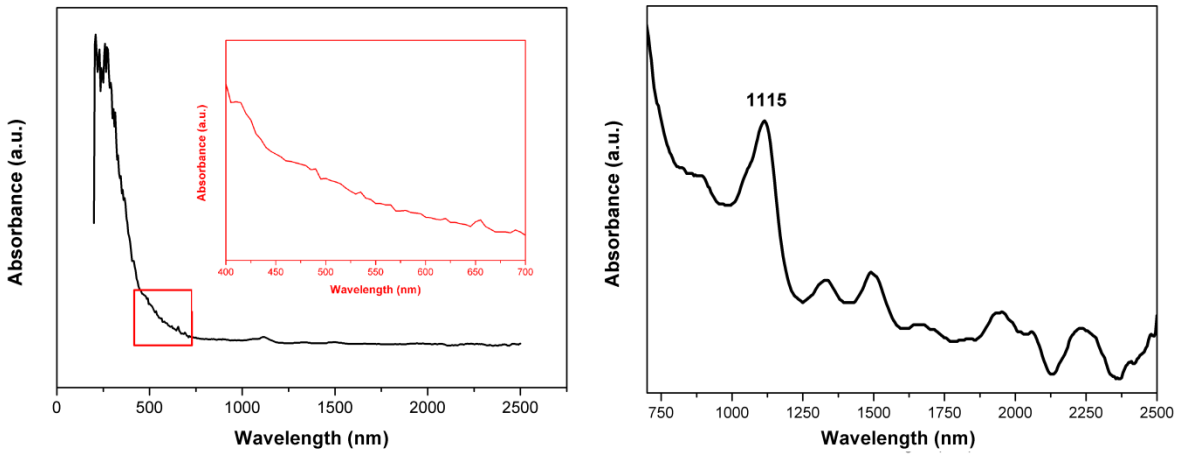

Figure 5.25: UV-Vis-NIR spectrum of zircon.

The UV-Vis-NIR spectrum of zircon is given in Figure 5.25. It helps to analyze the effect of natural radiation, and thereby the extent of metmictization occurred in zircon.

Natural radiation in detrital zircon grain results in the replacement of zirconium with uranium atoms. This can be easily identified by analyzing UV-Vis-NIR spectroscopy. The presence of U, Th, and rare earth elements cause f-f electron transition in zircon, which can be identified by sharp lines of absorption spectra below 600nm.[65] But in the case of natural zircon, these sharp lines are weak and faint, denotes less chances of radiation damage.[66] The results of Raman, XPS, and UV-Vis-NIR spectroscopy clearly denote less metamictization and a well-crystallized structure for detrital zircon grains. Moreover, the maximum absorbance is shown by the zircon at 1115nm (~1113nm of laboratory spectrum).

The major oxides, rare earth elements, and trace elements present in zircon are tabulated in Table 5.22-5.24. The average ZrO_2 content of zircon is 63.72% followed by SiO_2, Al_2O_3, TiO_2, etc. The average rare-earth content is estimated at about 1698.735ppm with a maximum for Ce (628.164ppm) followed by La, Nd, Y, Sc, Pr, etc. Few elements were present in ppm level like Zn, Pb, Hf, Th, U, Sr, etc. The results show good correlation with zircons grains from other parts of the country like zircon grains along the south-eastern part of Tamil Nadu consists of ZrO_2 in the range of 61.77 – 64.13% [67] and that from Chatrapur in Orissa is 65.90% [14].

Table 5.22: Major oxides of zircon.

Major Oxides (%)	Varkala	Kovalam	Average
ZrO_2	65.12	62.32	63.72
SiO_2	30.595	28.797	29.696
Al_2O_3	1.113	5.943	3.528
TiO_2	0.82	0.59	0.705
CaO	0.296	0.294	0.295
Fe_2O_3	0.154	0.224	0.189
Others	1.902	1.832	1.867

Table 5.23: Table REE elements of zircon.

REE (ppm)	Varkala	Kovalam	Average
Ce	605.217	651.110	628.164
La	263.110	268.412	265.761
Nd	222.091	251.125	236.608

Y	148.530	208.212	178.371
Sc	125.295	177.532	151.413
Pr	66.145	73.170	69.658
Sm	34.413	41.249	37.831
Yb	29.025	43.602	36.314
Gd	22.802	28.227	25.515
Er	20.136	29.262	24.699
Dy	19.222	25.990	22.606
Ho	5.447	7.646	6.547
Lu	4.217	6.333	5.275
Tm	3.745	5.557	4.651
Tb	3.029	3.905	3.467
Eu	1.658	2.058	1.858
Total	1574.081	1823.390	1698.735

Table 5.24: Trace elements of zircon.

Trace elements (ppm)	**Varkala**	**Kovalam**	**Average**
Zn	11137.865	10114.336	10626.101
Pb	3427.547	3425.908	3426.727
Hf	1807.852	2548.040	2177.946
Sr	402.665	359.472	381.068
Ba	336.660	392.296	364.478
Th	236.002	208.843	222.422
Cu	184.012	149.404	166.708
U	118.049	151.058	134.553
Ni	71.288	66.734	69.011
V	23.159	31.857	27.508
Cr	21.826	44.276	33.051
Rb	20.592	18.335	19.463
Nb	14.700	11.691	13.196
Ga	4.914	6.149	5.532

Co	3.980	3.251	3.615
Ta	1.754	2.422	2.088
Cs	0.221	0.232	0.226
Total	17813.086	17534.302	17673.694

Figure 5.26 shows the SEM micrographs of zircon. Zircons are usually stable and well-developed with rounded edges with high relief (Figure 5.26 (a-f)). The rounded edges show a long history of transportation. Inclusions, impact V's, and irregular pts of different shapes are seen on the surface. Zoning effects were also noticed on the grains.[36]

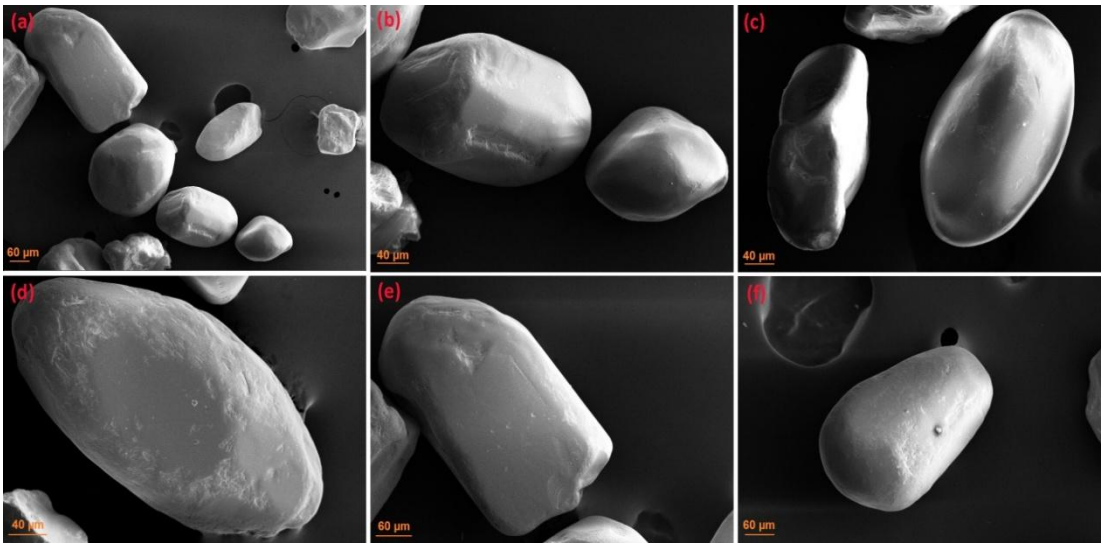

Figure 5.26: SEM images of zircon.

Figure 5.27 and Table 5.25 show the SED-EDS results of the zircon grains. The high content of Zr followed by Si confirms the mineral is zircon.[68]

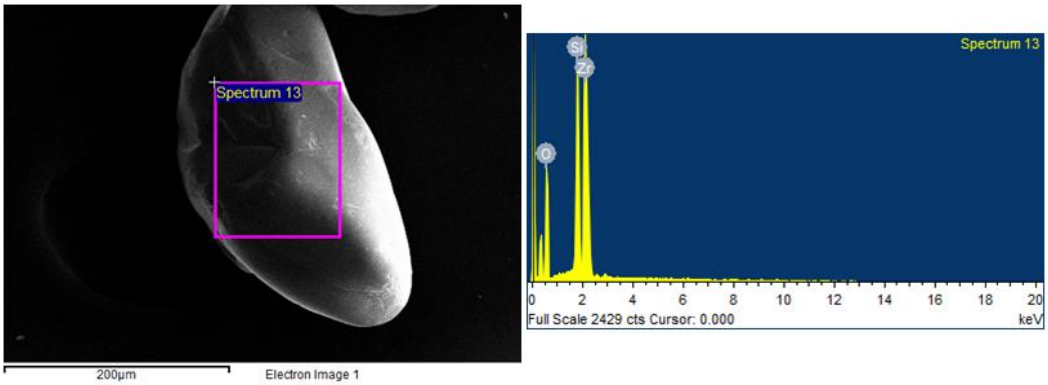

Figure 5.27: SEM-EDS results of zircon.

Table 5.25: Chemical composition of zircon by SEM-EDS.

Element	Weight (%)	Atomic (%)
Zr L	45.35	13.94
Si K	12.9	12.88
O K	41.75	73.18

5.4.5. Sillimanite

Sillimanite (Al_2SiO_5) belongs to aluminosilicates (space group Pbnm, Z =4) has an orthorhombic structure formed by chains of edge-sharing $A1O_6$ octahedra along the c-axis (Pbnm) which are also linked by SiO_4 and AlO_4 tetrahedra.[69] The XRD patterns are shown in Figure 5.28.

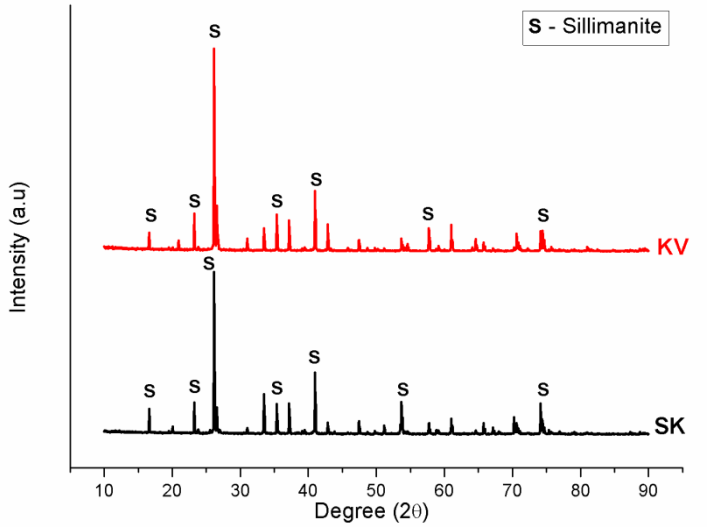

Figure 5.28: XRD pattern of sillimanite.

The modes of vibrations for sillimanite structure is Γ =13 A_g+8 B_{1g}+ 13 B_{2g}+8 B_{3g}+ l l A_u +16 B_{1u} +11 B_{2u} +16 B_{3u}. The high Raman frequencies due to the v_3 vibration of free SiO4 tetrahedron are assigned to Si-$O_{(c)}$.[70] Raman peaks around mid wave numbers are due to Al-O displacements, but the vibrations of the silicate and aluminate tetrahedra are difficult to distinguish in this region.[71] The Raman modes, their symmetry, and assignments were clearly shown in Figure 5.29 and Table 5.26. The broadening of the Raman bands will occur due to an increase in disorder of A1-Si tetrahedra. The relatively sharp Raman bands of the sillimanite suggest that low A1/Si disorder levels.[29] Furthermore, the Raman modes strictly discriminate sillimanite from other $A1_2SiO_5$ polymorphs such as andalusite and kyanite.

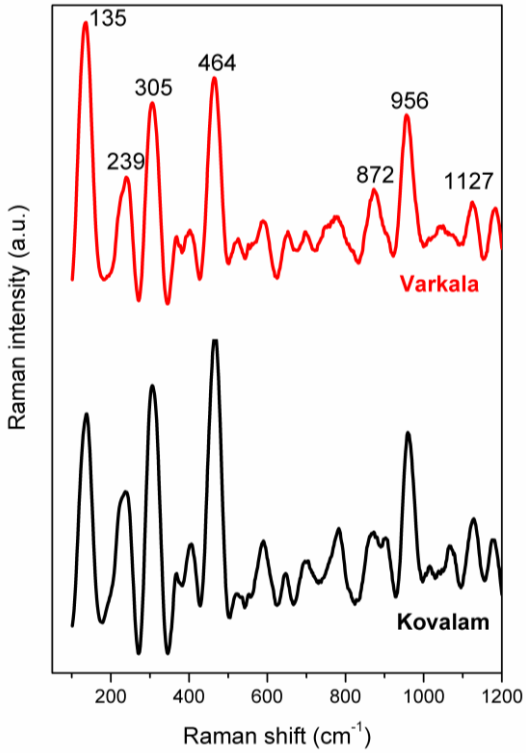

Figure 5.29: Raman peaks of sillimanite.

Table 5.26: Raman active frequencies (cm^{-1}) of sillimanite.

Symmetry	Assignment	Raman peaks (cm^{-1})
B_{2g}	v_3	1127, 1040
B_{2g}	v_1	956
B_{3g}	v_3	901
A_g, B_{2g}	v_3, v_4	872
A_g	v_1	781
A_g	T'(O_a:*xy*)	707
B_{3g}	v_4; *T'*(Al_1:*xy*)	701
A_g	v_4	525
A_g	v_2; T'(Al_l :z)	464
A_g	T'(Al_l :z; O_a:x; Al_2, O_c, O_d:xy)	402
A_g	*T'(A1₂:xy; O_a* :x)	367
A_g	R'(SiO_4:Z); *T'(O_a:xy*, $A1_2$:y)	305
B_{1g}	T'(O_a, O_b, $A1_2$:z; O^d:yz)	261

B_{1g}	T'(Al_l:xy; SiO_4:z)	239
A_g	T' ($A1_2$, SiO_4 : x)	135

The XPS results of sillimanite are shown in Figure 5.30. The Si2p usually seen as a single Gaussian peak at 102.44eV. The Si atoms in sillimanite are bonded tetrahedrally with O to form Al-O-Si linkages. The single peak clearly indicates that the electronic structure of Si linkages is not much influenced by Al atoms. The Al2p curve can be fitted into two peaks at 74.22 eV and 74.96 eV. These indicate that in sillimanite, Al atoms of sillimanite are in octahedral and tetrahedral coordination. [69] Further it suggests that Al atoms in sillimanite can be classified into two types viz., one more ionically bonded like in kyanite and another one is more covalently bonded. The O1s spectra for sillimanite can be fitted at 530.77 eV and 532.02 eV. The O atoms in sillimanite are 20 in total, where 12 are either charge-balanced or slightly over bonded whereas the remaining 8 are feebly under bonded. These make O atoms corresponds to $O_1$1s (530.77 eV) are more ionic compared to those that corresponds to $O_2$1s (532.02 eV).[32]

The UV-Vis-NIR spectrum of sillimanite is shown in Figure 5.31. The sillimanite shows strong absorbance in 255, 1938, and 2232 nm in UV-Vis-NIR region. The major oxides, rare earth elements, and trace elements present in sillimanite are tabulated in Table 5.27-5.29. The average Al_2O_3 and SiO_2 content of sillimanite are 53.718%, and 43.814% followed P_2O_5, CaO, Fe_2O_3, etc. The sillimanite also possesses rare earths. The average total rare earth (TREE) is estimated to be 222.384ppm with a maximum for Ce (100.040ppm), followed by La, Nd, Sc, Y, etc. Minor elements were also present in ppm level like Zr, V, Cr, Zn, Ga, etc. On comparing other placer deposits of India, the values of sillimanite are quite comparable. The Al_2O_3 and SiO_2 values for Kerala (Quilon) are 60.37% and 36.22%, Orissa are 57.60% and 40.30%, Tamil Nadu are 53.27% and 35.45%.[14,72]

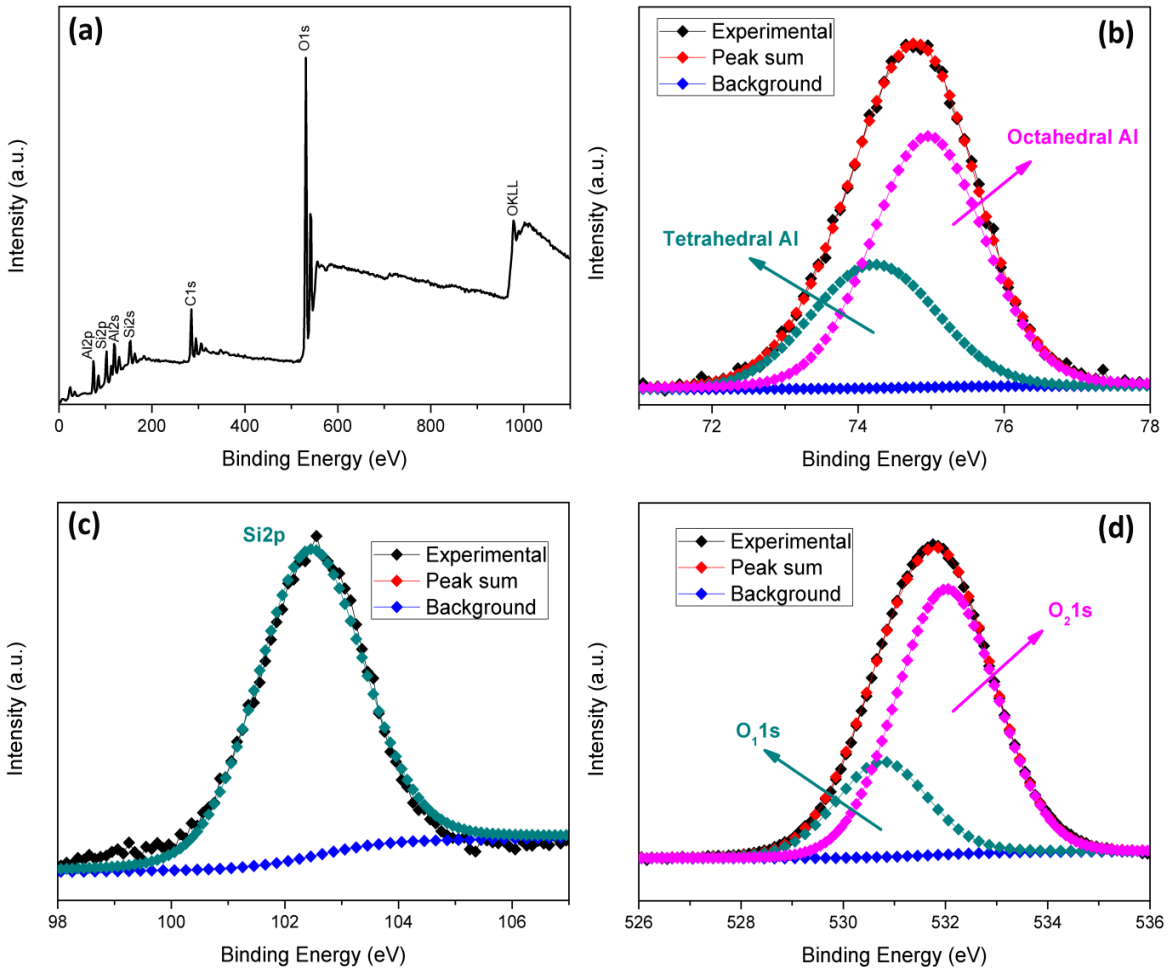

Figure 5.30: XPS peaks of sillimanite. (a) Wide scan XPS spectra, and high resolution scans of (b) Al2p, (c) Si2p, and (d) O1s.

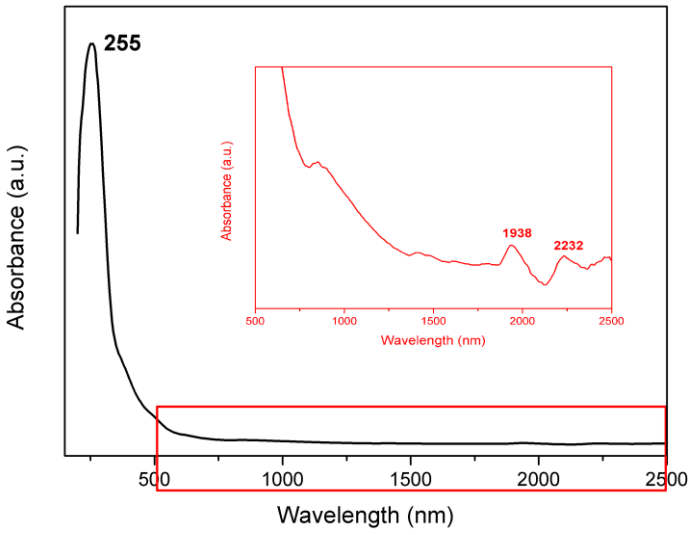

Figure 5.31: UV-Vis-NIR spectra of sillimanite.

Table 5.27: Major oxides of sillimanite.

Major Oxides (%)	Varkala	Kovalam	Average
Al_2O_3	48.589	58.846	53.718
SiO_2	48.839	38.789	43.814
P_2O_5	0.782	0.922	0.852
CaO	0.512	0.376	0.444
Fe_2O_3	0.459	0.491	0.475
Others	0.819	0.576	0.6975

Table 5.28: Rare earth elements of sillimanite.

REE (ppm)	Varkala	Kovalam	Average
Ce	6.539	193.541	100.040
Nd	3.498	83.623	43.560
La	3.262	92.053	47.657
Sc	2.211	2.664	2.438
Y	1.949	4.766	3.357
Pr	0.880	24.661	12.771
Sm	0.562	12.523	6.542
Gd	0.423	6.500	3.461
Yb	0.363	0.508	0.435
Dy	0.330	1.544	0.937
Er	0.326	0.575	0.450
Ho	0.086	0.223	0.154
Eu	0.071	0.237	0.154
Tm	0.062	0.078	0.070
Tb	0.059	0.526	0.293
Lu	0.053	0.074	0.063
Total	20.672	424.095	222.384

Table 5.29: Trace elements of sillimanite.

Trace elements (ppm)	Varkala	Kovalam	Average
Zr	557.355	471.655	514.505
V	326.035	401.858	363.946
Cr	206.921	250.224	228.573
Ba	122.796	236.752	179.774
Zn	106.884	137.595	122.240
Ga	49.302	62.624	55.963
Pb	37.546	49.127	43.336
Ta	16.636	24.315	20.475
Hf	16.051	13.988	15.020
Sr	14.296	13.653	13.975
Cu	12.020	14.061	13.040
Ni	11.070	11.635	11.353
Nb	6.243	8.666	7.454
Th	2.361	66.539	34.450
U	1.169	4.234	2.701
Rb	1.122	1.431	1.277
Co	0.710	0.861	0.785
Cs	0.087	0.111	0.099
Total	1488.604	1769.329	1628.966

The SEM images of sillimanite are given in Figure 5.32. Sillimanite grains are seen as prismatic with rounded edges (Figure 5.32 (a-e)). Conchoidal fractures with moderate relief can be seen. Removal of blocks and cleavage controlled step-like features besides the fracture plates next to crystal cleavage (Figure 5.32(g)). Irregular pits, grooves, impact V's, and solution channels formed by mechanical impact followed by chemical action. Smoothening of surface shows rolling topography. Some precipitation features are also noticed on the surface (Figure 5.32(h)).[36] The SEM-EDS results are shown in Figure 5.33 and Table 5.30. The EDS shows the concentration of Al and Si, and thereby it confirms that the mineral in sillimanite.[73]

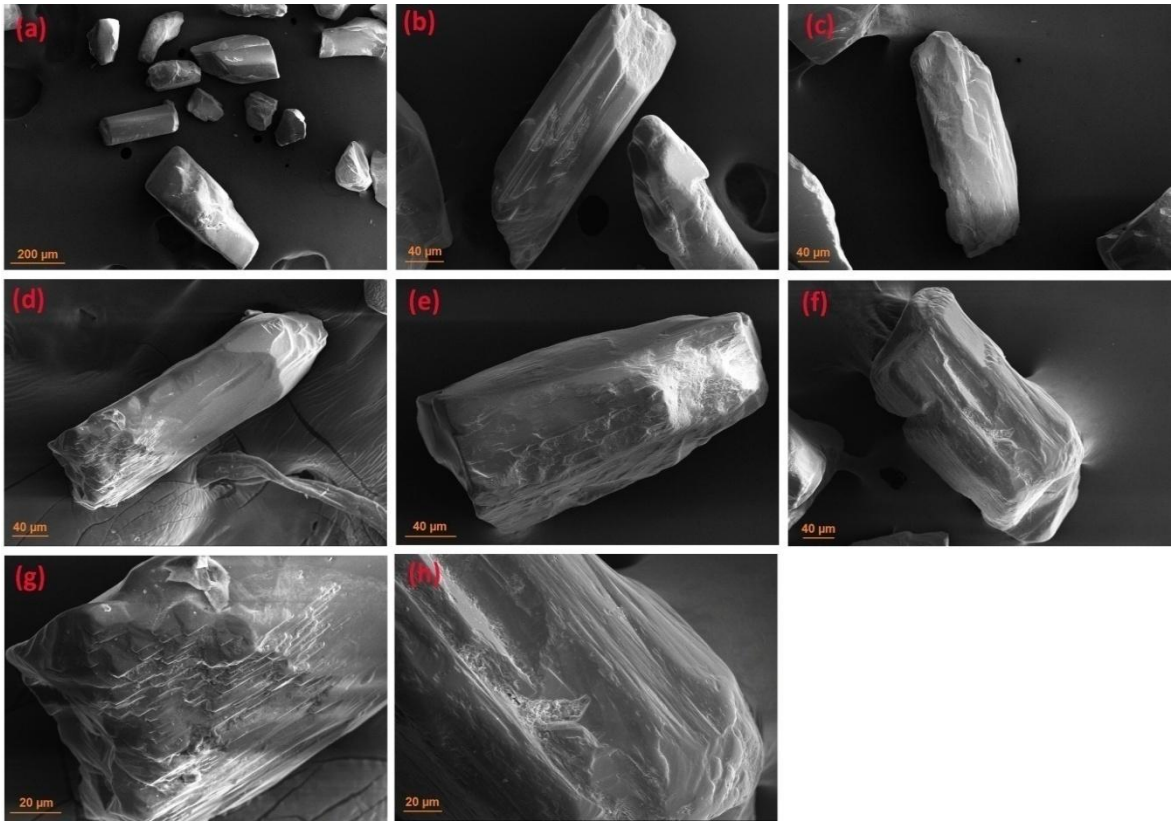

Figure 5.32: SEM images of sillimanite.

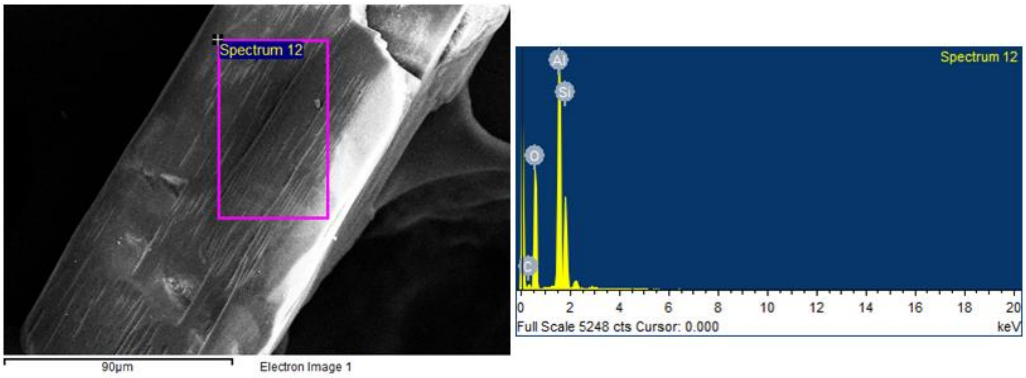

Figure 5.33 SEM-EDS results of sillimanite.

Table 5.30: Chemical composition of sillimanite by SEM-EDS.

Element	Weight (%)	Atomic (%)
Al K	25.99	17.79
Si K	13.84	9.1
O K	50.65	58.47
C K	9.52	14.64

5.4.6. Garnet

Garnet is formed by a group of silicates. The general formula is $X_3^{2+}Y_2^{3+}(SiO_4)_3$. It comprises of two groups viz. pyralspite (Y =Al; X=Mg, Fe^{2+}, Mn,) and ugrandite (X= Ca; Y = Cr, Al, Fe^{3+}).[74] The XRD pattern of garnet is given in Figure 5.34. The composition of the garnet is very close to the almandine ($Fe_3Al_2Si_3O_{12}$), which falls under pyralspite group. The Raman active modes of garnet also made clear discrimination from other silicate garnets such pyrope, spessartine, etc. Theoretically, the total number of vibrations for silicate garnets as $\Gamma = 3A_{1g}+5A_{2g}+8E_g+14F_{1g}+14F_{2g}+5A_{1u}+5A_{2u}+10E_u+17F_{1u}+16F_{2u}$, in which the total Raman active modes (A1g, Eg, and F2g) are 25 and infrared active modes (F_{1u}) are 17.

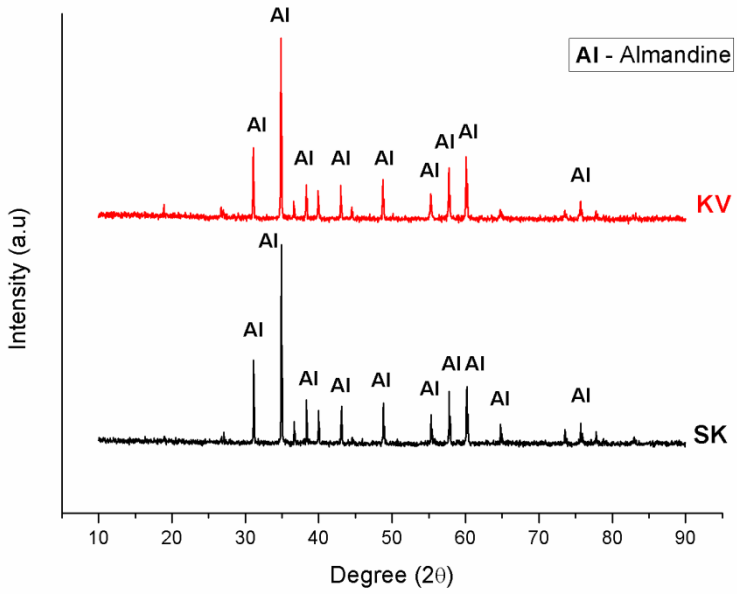

Figure 5.34: XRD pattern of garnet.

The symmetry and mode assignments for the Raman spectra of garnet are given in Figure 5.35 and Table 5.31. The intense modes at 351, 522, and 921 cm^{-1} correspond to rotational, internal bending, and stretching vibrations of the SiO_4 tetrahedra.[75] The entire tetrahedral unit contributes to the vibration of $R(SiO_4)^{4-}$ whereas only the oxygen anions are involved in the vibrations of $T(SiO_4)^{4-}$. This results in low frequencies for $T(SiO_4)_4$ modes compared to $R(SiO_4)^{4-}$. The F_{2g} modes at low frequencies fall between 170 and 280 cm^{-1}, and the weak mode in the E_g spectra at 255 cm^{-1} corresponds to $X^{2+}(x, y)$ and $X^{2+}(z)$-translations.

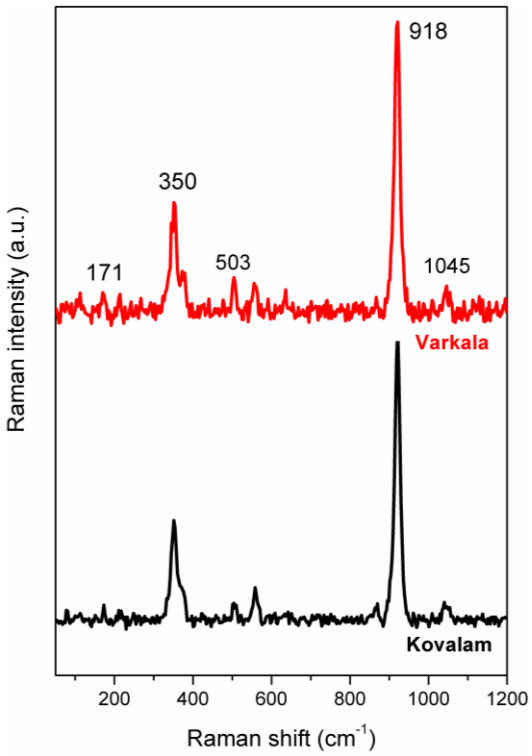

Figure 5.35: Raman peaks of garnet.

Table 5.31: Assignments of Raman peaks (cm^{-1}) of garnet.

Symmetry	Assignment	Raman peaks (cm^{-1})
$\mathbf{F_{2g}}$	(Si-O)stretching	1045
$\mathbf{A_{1g}}$		918
$\mathbf{F_{2g}}$		866
$\mathbf{F_{2g}}$	(Si-O)bending	635
$\mathbf{E_g}$		591
$\mathbf{E_g}$		522
$\mathbf{F_{2g}}$		503
$\mathbf{F_{2g}}$		476
$\mathbf{E_g}$		373
$\mathbf{F_{2g}}$	$R(SiO_4)^{4-}$	350
$\mathbf{E_g}$		323
$\mathbf{F_{2g}}$		314
$\mathbf{F_{2g}}$	$T(SiO_4)^{4-}$	171
$\mathbf{E_g}$		163

$\mathbf{E_g}$	$T(X^{2+})$	255
$\mathbf{F_{2g}}$		214

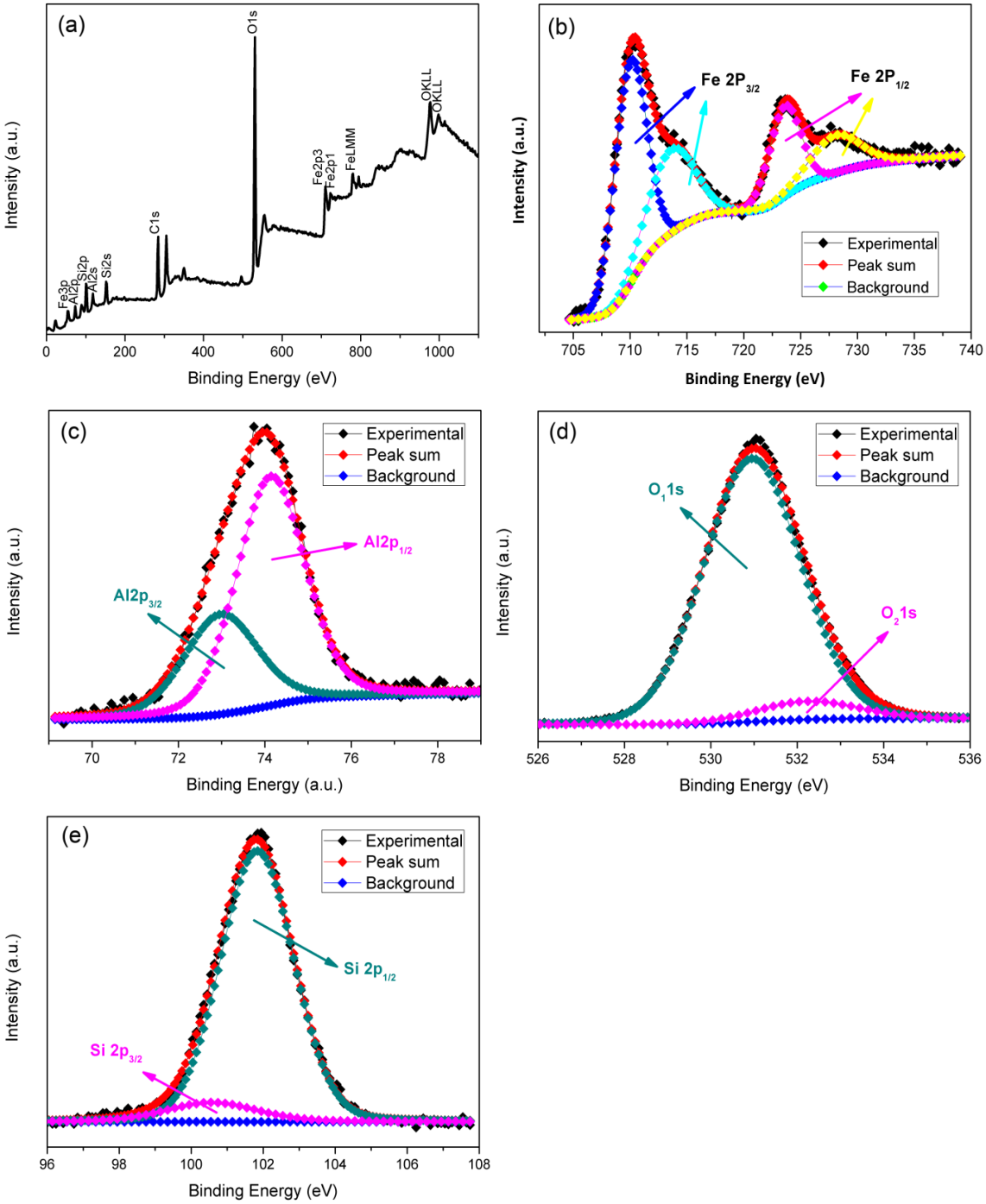

Figure 5.36: XPS results of garnet. (a) Wide scan XPS spectra, and high resolution scans of (b) Fe 2p, (c) Al2p, (d) O1s, and (e) Si2p.

The XPS results of garnet are clearly shown in Figure 5.36. The Fe state of garnet splits into two sets corresponds to ferrous and Ferric. The $2p_{3/2}$ and $2p_{1/2}$ of the ferrous state is observed at 710.20 eV and 723.79 eV. The 2p3/2 and 2p1/2 of the ferric state is observed at 714.02 eV and 728.19 eV. The Si 2p peak has been fitted into two Gaussian curves at 100.57 eV and 101.83 eV which corresponds to *Si* $2p_{3/2}$ and Si $2p_{1/2}$of the bulk aluminosilicate frame work. The O1s can be convoluted into two Gaussian peaks $O_1$1s and $O_2$1s at 530.96 eV and 532.23 eV corresponds to bulk oxide and surface oxygen species. The Al2p peak was fitted at 72.98 eV, and 74.14 eV corresponds to $2p_{3/2}$ and $2p_{1/2}$ of the bulk aluminosilicate framework.[33]

The UV-Vis-NIR spectrum of garnet is given in Figure 5.37. The intense peak at 250nm corresponds to Fe^{3+} ion in garnet. It is due to the charge transfer of Fe^{3+} ion in the octahedral site with Fe^{2+} in the dodecahedral site which also the main reason determining the colour of garnet.[76] In the NIR region, garnet shows major peaks at 1309, 1695, and 2253 nm can be attributed to the transition of eight coordinated Fe^{2+} from d_z^2 orbital ground state to $d_{x^2-y^2}$, d_{xz} and d_{yz} orbitals.[77]

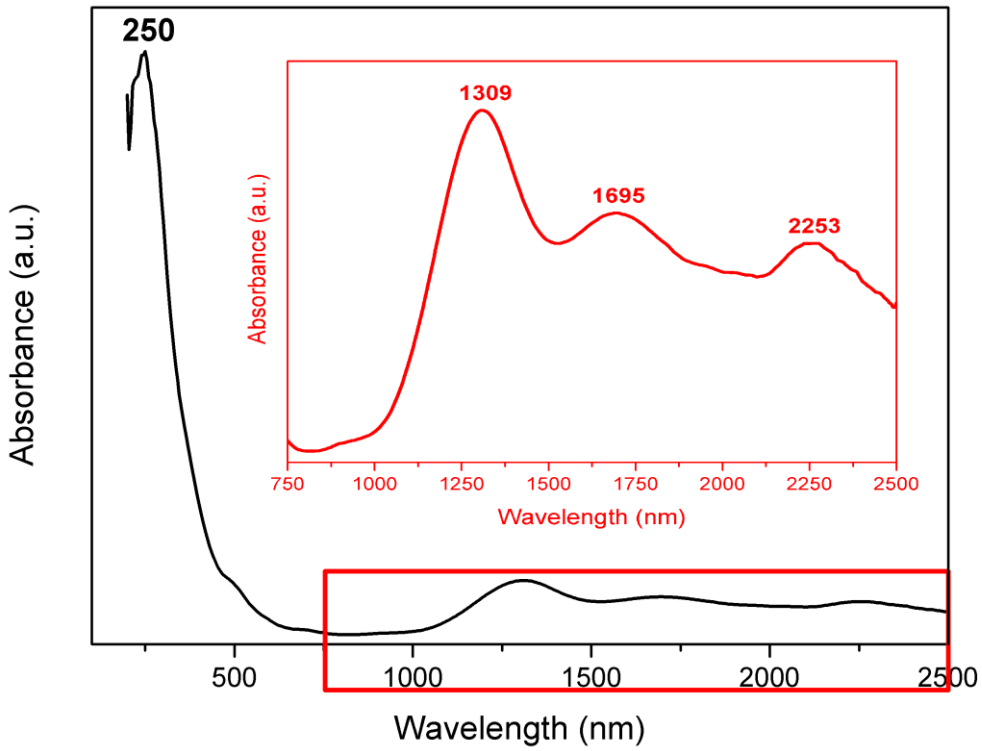

Figure 5.37 UV-Vis-NIR spectrum of garnet

The major oxides, rare earth elements and trace elements present in garnet are given in Figure 5.32-5.34. The average Fe_2O_3 is 40.0005% which followed by SiO_2 of 33.577%, Al_2O_3

of 17.33%, etc. The total rare earth elements present in garnet corresponds to 1093.529 ppm with a maximum for Ce (304.7325ppm) followed by Y, La, Nd, Sc, Pr, etc. Minor elements like Zr, Zn, Th, Ba, V, Cr, etc. also present at ppm-level. The Fe_2O_3 content using ED-XRF of garnet from the Thiruchendur coast in Tamil Nadu ranges from 36.481-39.146%.[78]

Table 5.32: Major oxides of garnet.

Major Oxides (%)	Varkala	Kovalam	Average
Fe_2O_3	40.455	39.546	40.0005
SiO_2	33.454	33.7	33.577
Al_2O_3	17.005	17.655	17.33
MgO	5.353	6.19	5.7715
CaO	1.236	1.009	1.1225
P_2O_5	0.82	0.761	0.7905
MnO	0.623	0.577	0.6
TiO2	0.202	0.128	0.165
CdO	0.153	0.14	0.1465
Others	0.699	0.294	0.4965

Table 5.33: Rare earth elements of garnet.

REE (ppm)	Varkala	Kovalam	Average
Ce	456.9274	152.5375	304.7325
Y	254.3044	194.5081	224.4063
La	213.6151	72.66331	143.1392
Nd	201.0812	69.03791	135.0595
Sc	83.39019	77.4556	80.42289
Pr	58.38995	19.75982	39.07488
Dy	42.09932	32.66968	37.3845
Gd	37.57541	25.52896	31.55218
Sm	37.4646	17.64101	27.5528
Er	29.15151	21.23576	25.19364
Yb	26.90597	18.77554	22.84076

Ho	10.28881	7.714217	9.001511
Tb	6.457932	4.976315	5.717124
Tm	4.390967	3.104704	3.747836
Lu	3.920614	2.736027	3.32832
Eu	0.505571	0.243895	0.374733
Total	1466.469	720.5884	1093.529

Table 5.34: Trace elements of garnet.

Trace elements (ppm)	Varkala	Kovalam	Average
Zr	578.461	74.248	326.355
Zn	328.703	473.623	401.163
Th	168.635	55.587	112.111
Ba	122.586	127.348	124.967
V	101.266	110.848	106.057
Cr	78.585	99.678	89.132
Pb	50.657	79.123	64.890
Ta	44.340	6.503	25.422
Co	43.338	46.577	44.958
Nb	15.898	6.627	11.262
Hf	15.170	2.149	8.660
Cu	11.941	12.764	12.352
Ni	11.244	12.507	11.875
Ga	8.541	6.365	7.453
U	7.869	2.840	5.355
Sr	6.613	8.597	7.605
Rb	1.317	1.941	1.629
Cs	0.093	0.118	0.106
Total	1595.258	1127.442	1361.350

The SEM images of the garnet are shown in Figure 5.38. Garnet grains are usually seen as highly angular with moderately high relief and show conchoidal fractures (Figure 5.38 (a-

f)). Undulatory planes and embayments are formed due to the solution effect. Large depressions with precipitation are seen on the surface due to etching. Removal of inclusions forms irregularly rounded pits (Figure 5.38 (b)). Impact "V" modified by etching forms grooves and pits.[36] Figure5.39 and Table 5.35 show the SEM-EDS results of garnet. The EDS shows a high content of Fe K ranges 23.72-27.46% confirms the garnet belongs to the almandine group.

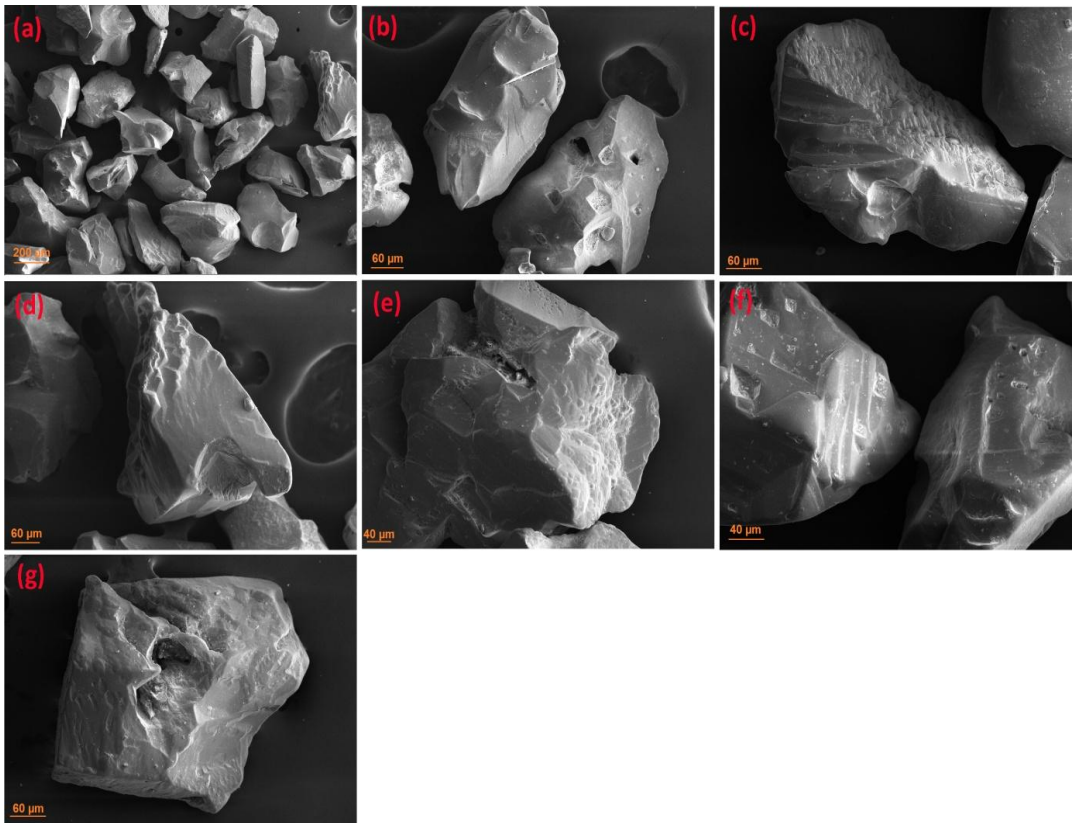

Figure 5.38: SEM images of garnet.

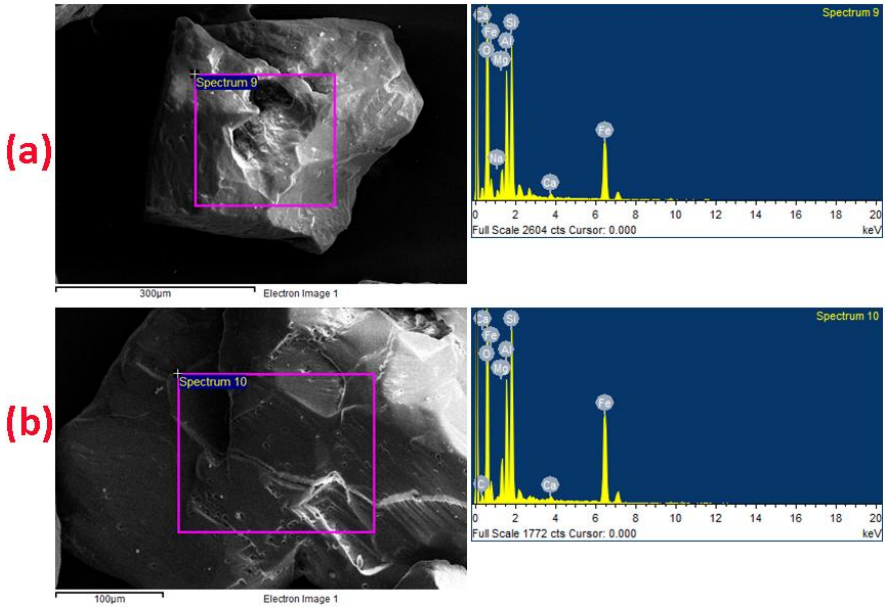

Figure 5.39: SEM-EDS results of garnet.

Table 5.35: Chemical composition of garnet by SEM-EDS.

Element	(a)		(b)	
	Weight (%)	Atomic (%)	Weight (%)	Atomic (%)
Fe K	23.72	9.81	27.46	11.14
Al K	12.35	10.57	9.31	7.81
Si K	16.3	13.41	15.16	12.22
Mg K	3.09	2.93	3.73	3.47
Ca K	0.56	0.32	0.5	0.28
Na K	1.18	1.19	-	-
O K	42.79	61.77	37.53	53.14
CK	-	-	6.32	11.93

5.4.7. Comparison with important coastal placer deposits of India

The major geochemistry of the minerals collected from Varkala-Kovalam coast were compared with the chemical data of minerals from important placer deposits in India collected from Indian Rare Earths Limited, Govt. of India (Table 5.36).

Table 5.36: Comparison of geochemical data with important coastal placer deposits of India.

Minerals	Compounds (%)	Chavara Kerala	Manavalakurichi Tamil Nadu	Chatrapur Orissa	Varkala-Kovalam
Rutile	TiO_2	95.05	94.4	94.5	95.72
Ilmenite	TiO_2	60.1	55.5	50.5	54.83
Leucoxene	TiO_2		70- 80		73.56
Sillimanite	Al_2O_3	59.3	-	56.6	53.72
Zircon	ZrO_2	65.3	65.8	64.5	63.72
Monazite	REO	-	55	-	64.17
	ThO_2	-	9.2	-	7.21
	U	-	0.30	-	0.31
Garnet	FeO	-	26	27.9	35.99
	Al_2O_3	-	21	19.8	17.33

The Chavara in Kerala, Manavalakurichi in Tamil Nadu and Chatrapur in Orissa are the three major placer deposits in India where the IREL have mineral processing units for recovering the minerals from beach sand. The major production of heavy minerals in India is controlled by these three major deposits. The major element present in each mineral which determines the grade of the minerals is compared with that of our study area. The ilmenite, leucoxene and rutile are used for the production of TiO_2, therefore the TiO2 content of these mineral is very important in determining the industrial grade. The TiO_2 content of rutile and leucoxene is 95.72% and 73.56% which comes closer to the TiO_2 content of other placer deposits. But in case of ilmenite, its TiO_2 content is observed much closer to Manavalakurichi deposits rather than the Chavara and Chatrapur. The study area Varkala-Kovalam is situated between these two deposits on the south west coast of India and has more influence from Manavalakurichi. The average Al_2O_3 and ZrO_2 values of 53.72% and 63.72% also come to other three placer deposits. Monazite acts as the primary source of rare earths. The REE, ThO_2 and U content of the monazite recovered from Varkala-Kovalam are 64.17%, 7.21% and 0.31% which are also comparable with other placer deposits in India. The type of garnet exist in India is almandine with high content of iron. Moreover, the high content of iron suggests that the garnet type is almandine. All together, the characterisation results show good agreement with other major placer deposits in India.

5.5. Conclusion

Detailed characterization of strategic heavy minerals such as ilmenite, rutile, zircon, sillimanite, garnet, and monazite recovered from the beach sands of Varkala-Kovalam coast, Kerala, south-west India has been performed in the context of a detailed study on geochemistry, crystal structure, and surface morphology. It is remarkable that the analysis provides useful information regarding the presence of rare earth elements and minor elements, degree of metamictization in zircon and monazite, surface chemistry, oxidation state of surface elements, discrimination of isomorphous series (almandine group of garnet), Ti-oxide polymorphs (anatase, brookite or rutile), $A1_2SiO_5$ polymorphs (sillimanite or kyanite), opaque and non-opaque Fe–Ti oxide minerals (ilmenite or rutile) and the anisotropic crystal behaviour of the minerals due to physical or chemical processes and finally the morphological changes due to mechanical impacts and solution activity of chemicals during the long transportation and deposition of sediments. The characterisation results show good agreement with other major placer deposits in India. The study provides solid information to the scientific community and policymakers for determining the grade and potential applications of these strategic minerals.

5.6. References

(1) Gayathri, G. S.; Rejith, R. G.; Jeelani, S. H.; Sundararajan, M.; Aslam, M. M.; Chidambaram, S. Heavy Mineral Resources In Tamil Nadu, India: An Overview. In *Geochemistry and Mineralogy of Coastal Sediments in Tamil Nadu*; 2017; pp 110–121.

(2) Ali, M. A.; Krishnan, S.; Banerjee, D. C. Beach and Inland Heavy Mineral Sand Investigations and Deposits in India-An Overview. *Explor. Res. At. Miner.* **2001**, *13*, 1–21.

(3) Behera, P. Heavy Minerals in Beach Sands of Gopalpur and Paradeep along Orissa Coastline, East Cost of India. *Indian J. Mar. Sci.* **2003**, *32* (2), 172–174.

(4) Nair, A. G.; Babu, D. S. S.; Damodaran, K. T.; Shankar, R.; Prabhu, C. N. Weathering of Ilmenite from Chavara Deposit and Its Comparison with Manavalakurichi Placer Ilmenite, Southwestern India. *Journal of Asian Earth Sciences*. 2009, pp 115–122.

(5) Valsangkar, A. B.; Fernandes, D. Pre- and Post-Monsoonal Changes in Grain Size and

Heavy Minerals in the Sediments from Kalbadevi Bay, Ratnagiri, West Coast of India. *Indian J. Mar. Sci.* **2011**, *40* (5), 657–663.

(6) Sajimol, S.; Rejith, R. G.; Lakshumanan, C.; Sundararajan, M. Sedimentology And Geochemistry Of Heavy Mineral Deposits along the Coast of Kanyakumari District, Tamil Nadu, India. In *Geochemistry and Mineralogy of Coastal Sediments in Tamil Nadu*; 2017; pp 145–161.

(7) Viveganandan, S.; Lakshumanan, C.; Sundararajan, M.; Eswaramoorthi, S.; Natesan, U. Depositional Environment of Sediments along the Cuddalore Coast of Tamilnadu, India. *Indian J. Mar. Sci.* **2013**, *42* (3), 375–382.

(8) Rajganapathi, V. C.; Jitheshkumar, N.; Sundararajan, M.; Bhat, K. H.; Velusamy, S. Grain Size Analysis and Characterization of Sedimentary Environment along Thiruchendur Coast, Tamilnadu, India. *Arab. J. Geosci.* **2013**, *6* (12), 4717–4728.

(9) Sundararajan, M.; Bhat, K. H.; Velusamy, S. Investigation on Mineralogical and Chemical Characterization of Ilmenite Deposits of Northern Kerala Coast, India. *Res. J. Earth Sci.* **2010**, *2* (2), 36–40.

(10) Rao, D. S., Vijaya Kumar, T. V., Subba Rao, S., Bhaskar Raju, G., & Prabhakar, S. Alteration Characteristics of Manavalakurichi Beach Placer Illmenite, Tamilnadu. *J. Appl. Geochemistry* **2005**, *7* (2), 195–200.

(11) Sundararajan, M.; Bhat, K. H.; Velusamy, S.; Babu, N.; Janaki, M. E. K.; Sasibhooshanan, S.; Das, P. N. M. Characterization of Ilmenite from Kerala Coastline, India:Implications in the Production of Synthetic Rutile. *J. Miner. Mater. Charact. Eng.* **2009**, *08* (06), 427–438.

(12) Kumari, A.; Panda, R.; Jha, M. K.; Kumar, J. R.; Lee, J. Y. Process Development to Recover Rare Earth Metals from Monazite Mineral: A Review. *Miner. Eng.* **2015**, *79*, 102–115.

(13) Sinha, H. N. From Zircon to High Purity Zirconia for Ceramics. *Miner. Process. Extr. Metall. Rev.* **1992**, *9* (1), 313–325. https://doi.org/10.1080/08827509208952715.

(14) Banerjee, G. Beach and Minerals: A New Material Resource for Glass and Ceramics. *Bull. Mater. Sci.* **1998**, *21* (4), 349–354.

(15) Anitha, J. K.; Joseph, S.; Rejith, R. G.; Sundararajan, M. Monazite Chemistry and Its Distribution along the Coast of Neendakara–Kayamkulam Belt, Kerala, India. *SN Appl. Sci.* **2020**, *2* (5), 812.

(16) Jin, J.; Gao, H.; Ren, Z.; Chen, Z. The Flotation of Kyanite and Sillimanite with Sodium Oleate as the Collector. *Minerals* **2016**, *6* (3), 90. https://doi.org/10.3390/min6030090.

(17) Padmasubashini, V.; Nandakishore, S. Determination of Rare Earth Elements, Yttrium, Uranium and Thorium in Ilmenite Samples by ICP-MS. *Explor. Res. At. Miner.* **2013**, No. 23, 151–157.

(18) Rajendran, J.; Balasubramanian, G.; Thampi, P. K. Determination of Rare Earth Elements in Indian Coastal Monazite by ICP-AES and ICP-MS Analysis and Their Geochemical Significance. *Curr. Sci.* **2008**, *94* (10), 1296–1302.

(19) Raimondo, T.; Payne, J.; Wade, B.; Lanari, P.; Clark, C.; Hand, M. Trace Element Mapping by LA-ICP-MS: Assessing Geochemical Mobility in Garnet. *Contrib. to Mineral. Petrol.* **2017**, *172* (4), 17.

(20) Nasdala, L.; Irmer, G.; Wolf, D. The Degree of Metamictization in Zircon: A Raman Spectroscopic Study. *Eur. J. Mineral.* **1995**, *7* (3), 471–478.

(21) Rull, F.; Martinez-Frias, J.; Rodríguez-Losada, J. A. Micro-Raman Spectroscopic Study of El Gasco Pumice, Western Spain. *J. Raman Spectrosc.* **2007**, *38* (2), 239–244.

(22) Wang, A.; Kuebler, K. E.; Jolliff, B. L.; Haskin, L. A. Raman Spectroscopy of Fe-Ti-Cr-Oxides, Case Study: Martian Meteorite EETA79001. *Am. Mineral.* **2004**, *89* (5–6), 665–680.

(23) Rull, F.; Martinez-Frias, J.; Rodríguez-Losada, J. A. Micro-Raman Spectroscopic Study of El Gasco Pumice, Western Spain. *J. Raman Spectrosc.* **2007**.

(24) Garzanti, E.; Andó, S.; France-Lanord, C.; Censi, P.; Vignola, P.; Galy, V.; Lupker, M. Mineralogical and Chemical Variability of Fluvial Sediments 2. Suspended-Load Silt (Ganga–Brahmaputra, Bangladesh). *Earth Planet. Sci. Lett.* **2011**, *302* (1–2), 107–120.

(25) Narayanan, P. S. Raman Spectrum of Rutile (TiO2). *Proc. Indian Acad. Sci. - Sect. A*

1950, *32* (4), 279.

(26) Murad, E.; Köster, H. M. Determination of the Ti Speciation in Commercial Kaolins by Raman Spectroscopy. *Clay Miner.* **1999**, *34* (3), 479–485.

(27) Frank, O.; Zukalova, M.; Laskova, B.; Kürti, J.; Koltai, J.; Kavan, L. Raman Spectra of Titanium Dioxide (Anatase, Rutile) with Identified Oxygen Isotopes (16, 17, 18). *Phys. Chem. Chem. Phys.* **2012**, *14* (42), 14567.

(28) Nasdala, L.; Akhmadaliev, S.; Artac, A.; Chanmuang N., C.; Habler, G.; Lenz, C. Irradiation Effects in Monazite–(Ce) and Zircon: Raman and Photoluminescence Study of Au-Irradiated FIB Foils. *Phys. Chem. Miner.* **2018**, *45* (9), 855–871.

(29) Mernagh, T.; Liu, L. Raman Spectra from the Al2SiO5 Polymorphs at High Pressures and Room Temperature. *Phys. Chem. Miner.* **1991**, *18* (2), 126–130.

(30) Hofmeister, A. M.; Chopelas, A. Vibrational Spectroscopy of End-Member Silicate Garnets. *Phys. Chem. Miner.* **1991**.

(31) Schulze, P. D.; Neil, T. E.; Shaffer, S. L.; Smith, R. W.; McKay, D. S. XPS Studies of Water and Oxygen on Iron- sputtered Natural Ilmenite. *J. Vac. Sci. Technol. A Vacuum, Surfaces, Film.* **1985**, *3* (1), 6–9.

(32) Ohuchi, F. S. Chemical Bonding and Electronic Structures of the Al2SiO5 Polymorphs, Andalusite, Sillimanite, and Kyanite: X-Ray Photoelectron- and Electron Energy Loss Spectroscopy Studies. *Am. Mineral.* **2006**, *91* (5–6), 740–746.

(33) Poon, J.; Madden, D. C.; Wood, M. H.; van Tol, R.; Sonke, H.; Clarke, S. M. Surface Chemistry of Almandine Garnet. *J. Phys. Chem. C* **2020**, *124* (9), 5099–5117.

(34) Balan, E.; Trocellier, P.; Jupille, J.; Fritsch, E.; Muller, J. P.; Calas, G. Surface Chemistry of Weathered Zircons. *Chem. Geol.* **2001**, *181* (1–4), 13–22.

(35) Zhou, G. W.; Don, K. L.; Young, H. K.; Chang, W. K.; Young, S. K. Preparation and Spectroscopic Characterization of Ilmenite-Type CoTiO3 Nanoparticles. *Bull. Korean Chem. Soc.* **2006**, *27* (3), 368–372.

(36) Mallik, T. K. Micromorphology of Some Placer Minerals from Kerala Beach, India. *Mar. Geol.* **1986**, *71* (3–4), 371–381.

(37) Thankappan, N.; Varangalil, N.; Kachapally Varghese, T.; Njaliplackil Philipose, K. Coastal Morphology and Beach Stability along Thiruvananthapuram, South-West Coast of India. *Nat. Hazards* **2018**, *90* (3), 1177–1199.

(38) Mücke, A.; Bhadra Chaudhuri, J. N. The Continuous Alteration of Ilmenite through Pseudorutile to Leucoxene. *Ore Geol. Rev.* **1991**, *6* (1), 25–44.

(39) Ross, N. L.; McMillan, P. The Raman Spectrum of Magnesium Silicate (MgSiO3) Ilmenite. *Am. Mineral.* **1984**.

(40) Li, F.; Zhong, H.; Zhao, G.; Wang, S.; Liu, G. Adsorption of α-Hydroxyoctyl Phosphonic Acid to Ilmenite/Water Interface and Its Application in Flotation. *Colloids Surfaces A Physicochem. Eng. Asp.* **2016**, *490*, 67–73.

(41) Suresh Babu, D. S.; Thomas, K. A.; Mohan Das, P. N.; Damodaran, A. D. Alteration of Ilmenite in the Manavalakurichi Deposit, India. *Clays Clay Miner.* **1994**, *42* (5), 567–571.

(42) Nallusamy, B.; Babu, S.; Suresh Babu, D. S. Heavy Mineral Distribution and Characterisation of Ilmenite of Kayamkulam — Thothapally Barrier Island, Southwest Coast of India. *J. Geol. Soc. India* **2013**, *81* (1), 129–140.

(43) Sundararajan, M.; Bhat, K. H.; Babu, N.; Janaki, M. E. K.; Das, P. N. M. Characterization Studies on Ilmenite of Ullal and Suratkal along Karnataka Coastline, West Coast of India. *J. Miner. Mater. Charact. Eng.* **2009**, *08* (06), 479–493.

(44) Krishnamurti, D. The Raman Spectrum of Rutile. *Proc. Indian Acad. Sci. - Sect. A* **1962**, *55* (5), 290–299.

(45) Tompsett, G. A.; Bowmaker, G. A.; Cooney, R. P.; Metson, J. B.; Rodgers, K. A.; Seakins, J. M. The Raman Spectrum of Brookite, TiO2 (Pbca, Z = 8). *J. Raman Spectrosc.* **1995**, *26* (1), 57–62.

(46) Hope, G. A.; Woods, R.; Munce, C. G. Raman Microprobe Mineral Identification. *Miner. Eng.* **2001**, *14* (12), 1565–1577.

(47) Swamy, V.; Muddle, B. C.; Dai, Q. Size-Dependent Modifications of the Raman Spectrum of Rutile TiO2. *Appl. Phys. Lett.* **2006**, *89* (16), 163118.

(48) Bharti, B.; Kumar, S.; Lee, H.-N.; Kumar, R. Formation of Oxygen Vacancies and Ti3+ State in TiO2 Thin Film and Enhanced Optical Properties by Air Plasma Treatment. *Sci. Rep.* **2016**, *6* (1), 32355.

(49) Bessergenev, V. G.; Pereira, R. J. F.; Mateus, M. C.; Khmelinskii, I. V.; Vasconcelos, D. A.; Nicula, R.; Burkel, E.; Botelho Do Rego, A. M.; Saprykin, A. I. Study of Physical and Photocatalytic Properties of Titanium Dioxide Thin Films Prepared from Complex Precursors by Chemical Vapour Deposition. *Thin Solid Films* **2006**, *503* (1–2), 29–39.

(50) Kallel, W.; Bouattour, S.; Ferreira, L. F. V.; Botelho do Rego, A. M. Synthesis, XPS and Luminescence (Investigations) of Li+ and/or Y3+ Doped Nanosized Titanium Oxide. *Mater. Chem. Phys.* **2009**, *114* (1), 304–308.

(51) Bangaku Naidu, K.; Reddy, K. S. N.; Ravi Sekhar, C.; Ganapati Rao, P.; Murali Krishna, K. N. Rutile Mineral Chemistry as a Guide to Provenance of Red Sediments and Modern Sands of Bhimunipatnam–Konada Coast, Andhra Pradesh, East Coast of India. *Natl. Acad. Sci. Lett.* **2020**, *43* (2), 145–152.

(52) Williams, M. L.; Jercinovic, M. J.; Hetherington, C. J. Microprobe Monazite Geochronology: Understanding Geologic Processes by Integrating Composition and Chronology. *Annu. Rev. Earth Planet. Sci.* **2007**, *35* (1), 137–175.

(53) Sadeghi, K.; Thanakkasaranee, S.; Lim, I.-J.; Seo, J. Calcined Marine Coral Powders as a Novel Ecofriendly Antimicrobial Agent. *Mater. Sci. Eng. C* **2020**, *107*, 110193.

(54) Simpraditpan, A.; Wirunmongkol, T.; Pavasupree, S.; Pecharapa, W. Hydrothermal Synthesis of Nanofibers from Natural Ilmenite Mineral and Their Utilization for Dye-Sensitized Solar Cell. *Integr. Ferroelectr.* **2013**, *149* (1), 135–142.

(55) Verma, S.; Bamzai, K. K. Preparation of Cerium Orthophosphate Nanosphere by Coprecipitation Route and Its Structural, Thermal, Optical, and Electrical Characterization. *J. Nanoparticles* **2014**, *2014*, 1–12.

(56) Udayakumar, S.; Rezan, S. A.; Mohd Noor, A. F.; Rama Putra, T. A.; Takip, K. M.; Hazan, R. Characterization of Malaysian Monazite Concentrate for The Recovery of Thorium Dioxide. *J. Phys. Conf. Ser.* **2018**, *1082*, 012090.

(57) Hazen, R. M.; Finger, L. M. Crystal Structure and Compressibility of Zircon at High Pressure. *Am. Mineral.* **1979**, *64* (1–2), 196–201.

(58) Lumpkin, G. R. Alpha-Decay Damage and Aqueous Durability of Actinide Host Phases in Natural Systems. *J. Nucl. Mater.* **2001**, *289* (1–2), 136–166.

(59) Weber, W. J.; Ewing, R. C.; Angell, C. A.; Arnold, G. W.; Cormack, A. N.; Delaye, J. M.; Griscom, D. L.; Hobbs, L. W.; Navrotsky, A.; Price, D. L.; Stoneham, A. M.; Weinberg, M. C. Radiation Effects in Glasses Used for Immobilization of High-Level Waste and Plutonium Disposition. *J. Mater. Res.* **1997**, *12* (8), 1948–1978.

(60) Zhang, M.; Salje, E. K. H.; Farnan, I.; Graeme-Barber, A.; Daniel, P.; Ewing, R. C.; Clark, A. M.; Leroux, H. Metamictization of Zircon: Raman Spectroscopic Study. *J. Phys. Condens. Matter* **2000**, *12* (8), 1915–1925.

(61) Holland, H. D.; Gottfried, D. The Effect of Nuclear Radiation on the Structure of Zircon. *Acta Crystallogr.* **1955**, *8* (6), 291–300.

(62) Ewing, R. C. The Metamict State: 1993 — the Centennial. *Nucl. Instruments Methods Phys. Res. Sect. B Beam Interact. with Mater. Atoms* **1994**, *91* (1–4), 22–29.

(63) Dawson, P.; Hargreave, M. M.; Wilkinson, G. R. The Vibrational Spectrum of Zircon (Zrsio 4). *J. Phys. C Solid State Phys.* **1971**, *4* (2), 240–256.

(64) Shchapova, Y. V.; Votyakov, S. L.; Kuznetsov, M. V.; Ivanovskii, A. L. Effect of Radiation Defects on the Electronic Structure of Zircon by X-Ray Photoelectron Spectroscopy Data. *J. Struct. Chem.* **2010**, *51* (4), 657–662.

(65) Chen, T.; Ai, H.; Yang, M.; Zheng, S.; Liu, Y. Brownish Red Zircon from Muling, China. *Gems Gemol.* **2011**.

(66) Nasdala, L. Spectroscopic Methods Applied to Zircon. *Rev. Mineral. Geochemistry* **2003**, *53* (1), 427–467.

(67) Angusamy, N.; Loveson, V. J.; Rajamanickam, G. V. Zircon and Ilmenite from the Beach Placers of Southern Coast of Tamil Nadu, East Coast of India. *Indian J. Mar. Sci.* **2004**, *33* (2), 138–149.

(68) Routray, S.; Rao, R. B. Beneficiation and Characterization of Detrital Zircons from

Beach Sand and Red Sediments in India. *J. Miner. Mater. Charact. Eng.* **2011**, *10* (15), 1409–1428.

(69) Winter, J. K.; Ghose, S. Thermal Expansion and High-Temperture Crystal Chemistry of the Al 2 SiO 5 Polymorphs. *Am. Mineral.* **1979**, *64* (5–6), 573–586.

(70) Salje, E.; Werneke, C. The Phase Equilibrium between Sillimanite and Andalusite as Determined from Lattice Vibrations. *Contrib. to Mineral. Petrol.* **1982**, *79* (1), 56–67.

(71) McMillan, P.; Piriou, B. The Structures and Vibrational Spectra of Crystals and Glasses in the Silica-Alumina System. *J. Non. Cryst. Solids* **1982**, *53* (3), 279–298.

(72) Tripathi, H. S.; Mukherjee, B.; Das, S. K.; Ghosh, A.; Banerjee, G. Effect of Sillimanite Beach Sand Composition on Mullitization and Properties of Al2O3-SiO2 System. *Bull. Mater. Sci.* **2003**, *26* (2), 217–220.

(73) Yugeswaran, S.; Vijay, M.; Suresh, K.; Ananthapadmanabhan, P. V.; Karoly, Z.; Szépvölgyi, J. Synthesis of Mullite from Sillimanite Dissociation through Transferred Arc Plasma Torch. *Int. J. Miner. Process.* **2011**, *99* (1–4), 54–60.

(74) Deer, W. A.; Howie, R. A.; Zussman, J. Rock-Forming Minerals. Vol. 1A. Orthosilicates. **1982**.

(75) Kolesov, B. A.; Geiger, C. A. Raman Spectra of Silicate Garnets. *Phys. Chem. Miner.* **1998**, *25* (2), 142–151.

(76) Khomenko, V. M.; Langer, K.; Wirth, R.; Weyer, B. Mie Scattering and Charge Transfer Phenomena as Causes of the UV Edge in the Absorption Spectra of Natural and Synthetic Almandine Garnets. *Phys. Chem. Miner.* **2002**, *29* (3), 201–209.

(77) Geiger, C. A. Spectroscopic Investigations Relating to the Structural, Crystal-Chemical and Lattice-Dynamic Properties of (Fe 2+ ,Mn 2+ ,Mg,Ca) 3 Al 2 Si 3 O 12 Garnet : A Review and Analysis. In *Spectroscopic methods in mineralogy*; Mineralogical Society of Great Britain and Ireland: Germany, 2004; pp 589–645.

(78) Sundararajan, M.; Nallusamy, B.; Sharath Raj, B.; Xaviour, A.; Pasha, M. A.; Aslam, M. M. Depositional Environment, X-Ray Mineralogy And Geochemistry Of Heavy Minerals From The Trichendur Coast, Tamil Nadu, India. In *Geochemistry and Mineralogy of Coastal Sediments in Tamil Nadu*; 2017; pp 52–75.

Chapter 6

Conclusion and future perspectives

6.1. Summary and Conclusion

In the present study, advanced remote sensing techniques were used for investigating the grain size and mineral distribution of beach sediments in the coast of Thiruvananthapuram district, Kerala, India using multispectral and hyperspectral data. An attempt has been also made to map other strategic minerals like the silica and deposits (Cherthala, Kerala), Fullerene bearing Barytes (Mangampet, Andhra Pradesh), Kaolin clay deposits (Thonnakkal, Kerala) and beach sediments of Cuddalore coast, Tamil Nadu using hyperspectral remote sensing techniques.

The **chapter 1** gives an introduction to remote sensing and its applications in mineral exploration. A literature review on various remote sensing techniques used for mineral exploration is discussed here in detail.

In **chapter 2**, detailed investigation on grain size and mineral distribution of beach sediments along the coast of Thiruvananthapuram, the southernmost district of Kerala, India have been carried out. The variation in grain size was studied using the spectral indices derived from the visible-NIR-TIR bands of Landsat and ASTER remote sensing data. Further, an attempt has been made to map the distribution of strategic minerals present in beach sands using standardized hyperspectral analysis techniques. Individual heavy minerals of good quality were recovered from beach sands using a combination of magnetic, electrostatic and gravity separation units. The spectral signatures of 10 strategic minerals including beach minerals, silica sand, kaolin clay deposits, and Baryte mineral were measured using ASD Fieldspec® 3 spectroradiometer and used as the reference spectra for mineral mapping. Grain Size Index maps showing the texture of beach sediments were successfully generated from the satellite imageries. The hyperspectral analysis extracts two endmembers of ilmenite and light minerals (quartz) from the Landsat and ASTER imagery, which could be successfully, mapped using the SAM classification algorithm. The same procedure was used for mapping silica deposits from Landsat and ASTER data. The Fullerene bearing Barytes (Mangampet, Andhra Pradesh) and Kaolin deposits (Thonnakkal, Kerala) were successfully derived from Landsat data using hyperspectral analysis followed by MTMF classification method. The satellite-

derived maps have been validated with the results of laboratory analysis and field data which show strong correlation almost in all locations.

In **chapter 3**, four widely used MLAs such as RFC, ANN, SVM, and MLC were compared for their efficiency in mapping beach minerals and silica sand deposits using Landsat 8 OLI imagery. The image pixels correspond to sampling locations were selected as the training sites. The random forest classifier (RFC) and Support vector machine (SVM) shows the highest Kappa coefficient and overall accuracy for mapping beach sediments and silica sand deposits.

In **chapter 4**, EO-1 Hyperion data was used for mapping the strategic minerals of Cuddalore coast, Tamil Nadu using the hyperspectral analysis techniques followed by SAM classification. The endmembers of garnet, zircon, sillimanite and light minerals (quartz) were derived from the satellite data and compared with spectral library of minerals. The band depth analysis of continuum removed laboratory spectra and image spectra helps to derive a strong correlation between band parameters and the corresponding mineral concentration. This relation was used to quantify minerals with the help of Random Forest Regression technique. Thus the concentration of zircon mineral along the coast of Cuddalore, Tamil Nadu was quantified using EO-1 Hyperion data.

In **chapter 5**, detailed characterisation on structure, chemistry and surface morphology of beach minerals recovered from the beach sands of Varkala-Kovalam coast was carried out using advanced characterisation techniques. The crystal structure of the minerals was analysed using Raman spectroscopy and X-ray diffraction. The ED-XRF, HR-ICP-MS, SEM-EDS and XPS were used to analyze chemical composition and rare earth chemistry. Thermal properties of the samples were determined using TGA analysis. The surface morphological features of minerals were also analysed using SEM. The characterisation results show good agreement with the reported values for other major placer deposits in India.

Summary of the thesis work with valid conclusions obtained from the present work are given in the **Chapter 6** which also includes the future perspectives.

The major conclusions obtained from the present study are:

- Effective recovery of heavy minerals from beach sediments was achieved by judicious combination of magnetic, electrostatic and gravity separation techniques.
- A spectral library comprises of 10 strategic minerals comprising of beach minerals, kaolin clay mineral and baryte mineral were developed using laboratory spectral signatures.
- Grain Size Index maps showing the texture of beach sediments were successfully generated using the satellite imageries.
- Potential targets of heavy mineral occurrences were derived using hyperspectral analysis of Landsat 8 OLI, ASTER and EO-1 Hyperion imageries.
- Machine learning algorithms like Random Forest classifier (RFC) and support vector machine (SVM) applied to Landsat 8 OLI imagery shows the best results for mapping beach minerals and silica sand deposits
- The band parameters derived from continuum removed spectra shows a strong correlation with the corresponding mineral concentration.
- The concentration of zircon mineral along the coast of Cuddaore, Tamil Nadu was quantified using continuum removed band depth analysis and RF regression technique applied to EO-1 Hyperion data.
- The characterisation results of beach minerals from Varkala-Kovalam coast show good agreement with the reported values for other major placer deposits in India.

6.2. Future perspectives

- Mapping shallow subsurface to identify mineral occurrence using ground penetration radar (GPR).
- Developing spectral library of other strategic minerals in India.
- GIS- based 3d visualization of subsurface mineral occurrences.
- Application of microwave and thermal remote sensing in mapping strategic minerals and ore deposit targeting.

List of Publications

Peer-reviewed journals

1. **Rejith, R. G**., Sundararajan, M., Gnanappazham, L., & Loveson, V. J. (2020). Satellite-based spectral mapping (ASTER and landsat data) of mineralogical signatures of beach sediments: a precursor insight. *Geocarto International*, 1–24. https://doi.org/10.1080/10106049.2020.1750061
2. **Rejith, R. G**., & Sundararajan, M. (2019). Mapping of mineral resources and lithological units: a review of remote sensing techniques. *International Journal of Image and Data Fusion*, 10(2), 79-106 https://doi.org/10.1080/19479832.2019.1589585
3. **Rejith, R. G**., Sundararajan, M., & Kaliraj, S. (2018). A Geo-processing Modeling of Deltaic Suspended Sediment Variability. *Journal of Geovisualization and Spatial Analysis*, 2(2), 13. https://doi.org/10.1007/s41651-018-0020-z
4. **Rejith, R. G**., & Sundararajan, M. (2018). Combined magnetic, electrostatic, and gravity separation techniques for recovering strategic heavy minerals from beach sands. *Marine Georesources & Geotechnology*, 36(8), 959-965. https://doi.org/10.1080/1064119X.2017.1403523
5. Athira, L., Sundararajan, M., Renjith, R. A., **Rejith, R. G**., Mohammed-Aslam, M. A., & Singh, U. (2020). A review of scandium–hafnium doped TiO_2 nanocrystals. *SN Applied Sciences*, *2*(5), 814. https://doi.org/10.1007/s42452-020-2508-7
6. Anitha, J. K., Joseph, S., **Rejith, R. G**., & Sundararajan, M. (2020). Monazite chemistry and its distribution along the coast of Neendakara–Kayamkulam belt, Kerala, India. *SN Applied Sciences*, *2*(5), 812. https://doi.org/10.1007/s42452-020-2594-6
7. Gayathri G S, Sundararajan M, **Rejith R G**, Sreela S R, Silambarasan S, Pruthiviraj N (2020) Texture and Mineralogy of beach sediments of Chavara and Manavalakurichi, South India- A comparative analysis. *Indian Journal of Geo Marine Sciences* (accepted for publication- Ref: IJMS/MS/4202/18)
8. Amritha, A., Sundararajan, M., **Rejith, R. G**., & Mohammed-Aslam, M. A. (2019). La-Ce doped TiO2 nanocrystals: a review on synthesis, characterization and photocatalytic activity. *SN Applied Sciences*, *1(11):1441*. https://doi.org/10.1007/s42452-019-1455-7

Book Chapters

9. **Rejith, R. G.,** S. Anirudhan & M. Sundararajan (2019). Delineation of Groundwater potential zones in hard rock terrain using integrated Remote sensing, GIS and MCDM techniques: a case study from Vamanapuram river basin, Kerala, India. In: GIS and Geostatistical Techniques for Groundwater Science-Elseiver (ISBN: 978-0-12-815413-7). 25, 349-363.
10. **Rejith, R. G.,** & Sundararajan, M (2018). Mapping of mafic-ultramafic rock units in late Archean Bhavani Complex, southern India using ASTER thermal bands. In: Shear Zones and Crustal Blocks of Southern India Vol 5. Proc. of the 5^{th} UGC-SAP-DRS II & CTESS seminar, Dept of Geology, University of Kerala, India, 5, 34-40.(ISBN 978-81-923449-9-7)
11. Gayathri, G. S., **Rejith, R. G**., Jeelani, S. H., Sundararajan, M., Aslam, M. M., & Chidambaram (2017). Heavy Mineral Resources in Tamil Nadu, India: An Overview. In: Geochemistry and Mineralogy of Coastal Sediments in Tamil Nadu (ISBN: 978-81-933440-8-8). 8, 110-121.
12. Sajimol, S., **Rejith, R. G**., Lakshumanan, C., & Sundararajan, M. (2017). Sedimentology and Geochemistry of Heavy Mineral Deposits Along The Coast Of Kanyakumari District, Tamil Nadu, India. In: Geochemistry and Mineralogy of Coastal Sediments in Tamil Nadu (ISBN: 978-81-933440-8-8). 10, 145-161.
13. **Rejith, R. G.,** Sundararajan, M., Venkatesan. S., Mohammed-Aslam, M. A(2020). Remote sensing for exploring heavy mineral deposits: a case study of Chavara and Manavalakurichi deposits, southwest coast of India. In: Remote Sensing of Ocean and Coastal Environments 1st Edition-Elsevier (ISBN: 9780128196045) 11. (Accepted for publication).
14. Renjith, R. A., **Rejith, R. G**., Sundararajan, M (2020). Evaluation of coastal sediments: an appraisal of geochemistry using ED-XRF and GIS techniques. In: Remote Sensing of Ocean and Coastal Environments 1st Edition-Elsevier (ISBN: 9780128196045) 7. (Accepted for publication).
15. Shravanraj. K., **Rejith, R. G.,** Sundararajan, M (2020). Evaluation of heavy metals in coastal aquifers and seawater: an appraisal of geochemistry using ICPMS and remote sensing. In: Remote Sensing of Ocean and Coastal Environments 1st Edition-Elsevier (ISBN: 9780128196045) 10. (Accepted for publication).

List of conference presentations

Oral Presentations

1. **Rejith, R. G.,** & Sundararajan, M (2018). "Mapping of mafic-ultramafic rock units in late Archean Bhavani Complex, southern India using ASTER thermal bands) in UGCSAPDRS II & CTESS seminar on Shear Zones and Crustal Blocks of Southern India organized by Dept. of Geology, University of Kerala, India on February 15-16, 2018, 5, 34-40.

2. **Rejith, R. G.,** & Sundararajan, M (2018). "Analysis of multispectral satellite data for mapping strategic minerals in beach placer deposits: A GIS and remote sensing perspective " in the Research Scholars Symposium on Materials Science and Engineering organized by The Indian Institute of Metals, Trivandrum chapter on April 6, 2018 at CSIR-NIIST, Trivandrum.

Poster Presentations

3. **Rejith R G.**, M Sundararajan, R A Renjith (2019) "Rare earth chemistry and crystal structure of detrital monazite and zircon grains from beach placers of India" presented during the Science, Technology And Applications Of Rare Earths (STAR-2019) symposium organized by Rare Earth Association of India (REAI) and Indian Institute of Metals (IIM) in association with *Department of Atomic Energy* (*DAE*) on December 05 – 07, 2019 **(Best Poster Award)**.
4. **Rejith R G.**, M Sundararajan (2019). "Geo-exploration of strategic mineral deposits using Remote sensing and GIS techniques" in DST- INSPIRE Fellowship Review Meet organized at the Gandhi Institute of Technology and Management (GITAM), Bengaluru campus held during 13-15 June 2019.
5. **Rejith R G.**, M Sundararajan, R A Renjith, K H Bhat (2018). "SEM-EDAX characterisation of Ilmenite mineral from Chavara deposit, India" in National Conference on Emerging Trends in Science, Technology & Application of Electron Microscopy (STAEM-2018) jointly organized by CSIR-NIIST and Academy of Microscope Science and Technology (AMST), India on December 19 – 21, 2018, 93 **(Best Poster Award)**.

6. **Rejith, R. G.,** Sundararajan, M., & K. H. Bhat (2018). "Raman spectroscopic studies of Fe-Ti oxide heavy minerals" in the 3rd International Conference on Advanced Materials and manufacturing Processes for strategic Sectors 2018 (ICAMPS 2018)" organized by The Indian Institute of Metals (IIM), Trivandrum.
7. **Rejith, R. G.,** Sundararajan, M., & K. H. Bhat (2018). "Investigation on structure and chemistry of monazite mineral using Raman spectroscopy" in the International Conference on Science, Technology and Applications of Rare Earths (ICSTAR 2015) organized by Rare Earths Association of India (REAI) and Indian Institute of Mineral Engineers, Tamil Nadu chapter, 128.
8. **Rejith, R. G.,** & Sundararajan, M (2018). "Raman spectra to study the structure and chemistry of heavy minerals recovered from Kappil-Varkala Coast, South Kerala, India" in the National Seminar on Effects of Paleo and Anthropogenic Events on Earth System organized by Department of Geology, Periyar University and Geological Society of India, 70-71.